Universitat Autònoma de Barcelona

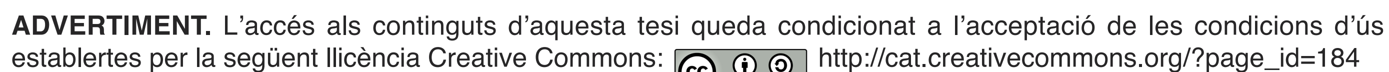

ADVERTIMENT. L'accés als continguts d'aquesta tesi queda condicionat a l'acceptació de les condicions d'ús establertes per la següent llicència Creative Commons: http://cat.creativecommons.org/?page_id=184

ADVERTENCIA. El acceso a los contenidos de esta tesis queda condicionado a la aceptación de las condiciones de uso establecidas por la siguiente licencia Creative Commons: http://es.creativecommons.org/blog/licencias/

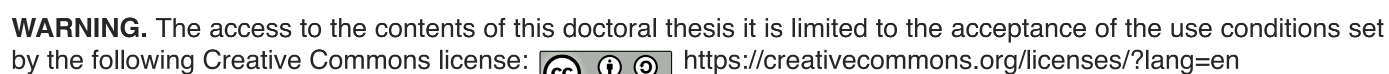

WARNING. The access to the contents of this doctoral thesis it is limited to the acceptance of the use conditions set by the following Creative Commons license: https://creativecommons.org/licenses/?lang=en

Universitat Autònoma
de Barcelona

Photoresistance and electroresistance in ferroelectric tunnel junctions based on $BaTiO_3$ and $Hf_{0.5}Zr_{0.5}O_2$

XIAO LONG

September 2022

Doctoral Thesis

SUPERVISORS

Prof. Josep Fontcuberta Griñó

Dr. Ignasi Fina Martínez

Institut de Ciència de Materials de Barcelona ICMAB-CSIC

Laboratory of Multifunctional Oxides and Complex Structures

TUTOR

Prof. Josep Fontcuberta Griñó

Institut de Ciència de Materials de Barcelona ICMAB-CSIC

Laboratory of Multifunctional Oxides and Complex Structures

ICMAB
INSTITUT DE CIÈNCIA DE MATERIALS DE BARCELONA

CSIC
CONSEJO SUPERIOR DE INVESTIGACIONES CIENTÍFICAS

Se ve el arcoíris después de la tormenta

Prof. Josep Fontcuberta Griñó and **Dr. Ignasi Fina Martínez**, research professor and tenured scientist, respectively, at the Institut de Ciència de Materials de Barcelona - Consejo Superior de Investigaciones Científicas.

CERTIFY

that **XIAO LONG** carried out under their direction the research work entitled "Photoresistance and electroresistance in ferroelectric tunnel junctions based on $BaTiO_3$ and $Hf_{0.5}Zr_{0.5}O_2$". This work has been developed within a PhD program in Materials Science at the Universitat Autònoma de Barcelona at the department of physics. For that record they sign the certificate.

Bellaterra, September 2022

Prof. Josep Fontcuberta Griñó

Dr. Ignasi Fina Martínez

Acknowledgements

The conclusion of this thesis is not merely a triumph to me, but also should be a triumph that belongs to everyone who helped me during last four years. Firstly, I must deliver the highest gratitude and respect to my two supervisors. I admire Prof. Josep Fontcuberta for his profound knowledge in various fields and his rigorous attitude and extraordinary passion towards science. Also, I salute to Dr. Ignasi Fina for his outstanding competence in many aspects and his diligence and self-discipline. Both of them have been very magnificent for manifesting us a paradigm of being a mature and responsible researcher.

I am deeply thankful for the sample fabrication to Raul Solanas and Dr. Mengdi Qian. I would like to thank the support by Dr. Florencio Sánchez on materials and systems selection to accomplish with the aims of the present thesis, and to Dr. Jike Lyu for devoting efforts in PLD parameter tuning for epitaxial HZO. I greatly appreciate the efforts of STEM characterization and data analysis by Dr. Jaume Gazques and Dr. Saúl Estandía. Also, thanks to Anna Crespi, the technician of the X-ray lab in ICMAB, for her technique support.

In addition, I give my courtesy to Guillaume Sauthier of the photoemission spectroscopy facility in ICN2 for his great assistance and patience.

A pleasing academic atmosphere was created together by all MULFOX group members. Much obliged to Dr. Gervasi Herranz for organizing the weekly group meeting, from where I have learnt how to effectively communicate with the other researchers. Special thanks to Huan Tan for conducting experimental data acquisition and analysis of the PFM, and to Dr. Milena Sulzbach and Dr. Alberto Quintana for sharing very constructive suggestions in my work.

Besides, I would like to extend my gratitude to other companions to whom I have extensive interactions, they are Dr. Ferran Vallés, Dr. Mikko Kataja, Dr. Rafael Cichelero, Dr. Yu Chen, Dr. Nico Dix, Dr. Alejandro Fernández, Dr. Mathieu Mirjolet, Dr. Artur Romanov, Dr. Juri Banchewski, Dr. Xiaodong Zhang, Tingfeng Song, Yunwei Sheng, Jiahui Jia, and Tetiana Zakusylo.

Thanks to the financial support from the Spanish Ministry of Science and Innovation (10.13039/501100011033), through the Severo Ochoa FUNFUTURE (project CEX2019-000917-S funded by MCIN/AEI), project TED2021-130453B-C21 funded by MCIN/AEI and European Union NextGenerationEU/PRTR, and projects TED2021-130453B-C21, PID2020-118479RB-I00, PID2020-112548RB-I00 and PID2019-107727RB-I00 funded by MCIN/AEI, and from CSIC through the i-LINK (LINKA20338) program are acknowledged. Project supported by a 2020 Leonardo Grant for Researchers and Cultural Creators, BBVA Foundation, and AGAUR Generalitat de Catalunya (2017 SGR 1377). Personally, I am financially supported by the China Scholarship Council (CSC) under grant No.201806100207.

Finally, I am grateful for the timely aid from many affiliations of Chinese government during the global pandemic. As a Chinese citizen I am able to live with dignity and have opportunities to pursue my dream, due to a thriving and prospering patria which has always been standing with its people.

"Be alone, that is the secret of invention;

Be alone, that is when ideas are born."

—— Nikola Tesla

Abstract

Informational technology development is approaching a crucial bottleneck due to the limitation of Von-Neumann architecture, for data storage and logic functions. Meanwhile, nowadays the DRAM and NAND flash memories have shown drawbacks such as data volatility, limitations of speed and endurance problem. Newly emerging non-volatile memories (NVMs) have become prominent candidates for the upcoming era of artificial intelligence and neuromorphic computing.

One promising type of NVMs is the ferroelectric tunnel junction (FTJ), which has a simple capacitor structure, consisting of an ultrathin ferroelectric layer, allowing tunnel transport, sandwiched between two metallic electrodes. The switching of ferroelectric polarization between two directions (P_{DOWN} and P_{UP}) modulates the barrier properties at the interface with electrodes, which consequent changes of conductance, i.e. the tunnel electroresistance (ER) effect. Contrary to early ferroelectric memories, ER is pivotal because it allows data reading in FTJs without perturbing its polarization (memory) state. It is claimed that FTJs have great potential to preserve high/low resistive state (HRS and LRS) over long time (> 10 years), and reversible switching between HRS/LRS after large read/write cycles (> 10^6 times).

HfO_2-based oxides can be made ferroelectric and polycrystalline related compounds are extensively used for fabricating high performance NVMs, due to its high compatibility to CMOS technique. Here, thin films of HfO_2 doped with Zr ($Hf_{0.5}Zr_{0.5}O_3$, HZO) were epitaxially grown by pulsed laser deposition and used to build FTJs. In spite of the epitaxial nature of the obtained films, it turns out that films contain the presence of grain boundaries among ferroelectric

(orthorhombic) and non-ferroelectric (monoclinic) phases. It follows that under voltage application, polarization reversal in ferroelectric grains occurs but conductive channels along the grain boundaries can be also opened. While suitable capping layer had been earlier proposed to mitigate the role of the mentioned grain boundaries on charge transport and leakage, named ionic motion channels, in relatively thick films (> 5 nm), it remained to be seen if the same approach could be operative in thinner HZO barriers. This has been a first objective of this PhD manuscript. A second one, intimately linked to the previous one, is that, after suitable large voltage application, quite often the FTJs display an abrupt reduction of resistance (soft breakdown) that definitely affects its ER and thus its potential use a ferroelectric memory. Therefore, the ferroelectric and ER characteristics after the breakdown has been investigated.

In the approaches described above, the state of the ferroelectric memory is set by a suitable electric field (voltage) that selects the polarization direction and thus the resistance state (high/low, HRS/LRS). However, current trends in ferroelectric memories pushes for alternative writing schemes. Optical writing is one of the possible options. Unfortunately, for devices to be operated at visible light range, HZO is not appropriate due to its exceedingly large bandgap. In contrast, $BaTiO_3$ films commonly display photoabsorption at visible light range and thus are potential candidates for this operation mode. Therefore, to achieve optically tunable NVMs, barium titanate (BTO) was chosen. Herein, 4 nm thick BTO FTJs were fabricated. The presence of imprint electric field breaks the symmetry between P_{UP} and P_{DOWN}, favoring one of the states. In our case imprint was found to favor P_{DOWN}. Polarization switching induced by light from P_{UP} to P_{DOWN} was observed and subsequently, an optically induced LRS to HRS switching. If a $SrTiO_3$ layer was inserted between the ferroelectric layer

(STO/BTO) and the electrode, it was found that the electrical/optical control of resistance can be operated more stably and repeatedly. Further investigations were conducted to understand the physical origin of light-induced resistive switching. It is observed that the time-dependent response depends on laser power and BTO thickness, which have provided valuable insights on the microscopic mechanism of light-induced polarization reversal. In brief, data indicates that the resistive change from LRS to HRS is related to photovoltaic effect.

The study in this thesis provides engineering strategies to improve or optimize FTJs performances. As well, it will be a guidance to implement optically tunable artificial synaptic function with FTJs.

Resumen

El desarrollo de la tecnología de la información se acerca a un cuello de botella crucial debido a la limitación de la arquitectura de Von-Neumann para el almacenamiento de datos y las funciones lógicas. Mientras tanto, hoy en día las memorias flash DRAM y NAND han mostrado inconvenientes como la baja retención de la información, tiempos de conmutación lentos y problemas de robustez. Otras memorias no volátiles (NVMs) emergentes se han convertido en candidatas para la próxima era de computación neuromórfica.

Un tipo de NVM es la unión túnel ferroeléctrica (FTJ), que tiene una estructura de condensador simple, que consiste en una capa ferroeléctrica ultradelgada, que permite el transporte por efecto túnel, intercalada entre dos electrodos metálicos. La conmutación de la polarización ferroeléctrica entre dos direcciones (P_{DOWN} y P_{UP}) modula las propiedades de barrera en la intercara con los electrodos, lo que consecuentemente causa cambios de conductancia, es decir, da lugar a electrorresistencia (ER). A diferencia de otros tipos de memorias ferroeléctricas, la lectura del estado de memoria en las FTJ no perturba su estado de polarización (estado de memoria). Las FTJs muestran buena retención durante mucho tiempo (> 10 años) y mayor robustez después ciclos de lectura/escritura (> 10^6 veces).

Los óxidos basados en HfO_2 dopado muestran ferroelectricidad en forma de lámina ultradelgada (<20 nm). En forma policristalina se pueden utilizar para fabricar NVMs, debido a su alta compatibilidad con la tecnologia CMOS. En el presente trabajo, capas delgadas de HfO_2 dopadas con Zr ($Hf_{0.5}Zr_{0.5}O_3$, HZO) se crecieron epitaxialmente mediante la técnica de deposición por láser pulsado

y se usaron para construir FTJ. A pesar de la naturaleza epitaxial de las capas obtenidas, las capas contienen fronteras de grano entre las fases ferroeléctrica (ortorrómbica) y no ferroeléctrica (monoclínica) del material. De ello se deduce que, puede ocurre la inversión de polarización en los granos ferroeléctricos, pero también se pueden crear canales conductores a lo largo de las fronteras de los granos. Si bien anteriormente se había propuesto que el uso de una capa protectora adecuada es útil para mitigar la contribución de la conducción eléctrica en las fronteras de grano, denominados canales de movimiento iónico, en capas relativamente gruesas (> 5 nm), quedaba por ver si la misma estrategia podría ser operativo en barreras HZO más delgadas. Este ha sido el primer objetivo de esta tesis doctoral. Un segundo objetivo, íntimamente ligado al anterior, es que la aplicación de alto voltaje en FTJs causa una reducción de su resistencia (suave ruptura) que afecta su ER y por ende a su potencial uso como memoria ferroeléctrica. Por lo tanto, entender las propiedades de unión después de la ruptura es de alta relevancia y ha centrado parte de la investigación realizada durante el desarrollo de la presente tesis.

En los enfoques descritos anteriormente, el estado de la memoria ferroeléctrica se establece mediante un campo eléctrico (voltaje) que selecciona la dirección de polarización y, por lo tanto, el estado de resistencia (alto/bajo, HRS/LRS). Sin embargo, investigar esquemas de escritura alternativos es de potencial interés. La escritura óptica es una de las opciones posibles. Desafortunadamente, para los dispositivos que funcionan en el rango de luz visible, HZO no es apropiado debido a que su ancho de banda es excesivamente grande. Por el contrario, capas de $BaTiO_3$ comúnmente muestran fotoabsorción en el rango del visible y, por lo tanto, son candidatas potenciales para este modo de operación. Se fabricaron FTJ BTO de 4 nm de espesor, los campos eléctricos internos

rompen la degeneración entre P_{UP} y P_{DOWN} a favor de uno de los estados. En nuestro caso, se encontró que se favorecía a P_{DOWN}. Se observó el cambio de polarización inducido por la luz de P_{UP} a P_{DOWN} y, posteriormente, se observó un cambio de baja a alta resistencia inducido ópticamente. Se observó un comportamiento similar en dispositivos donde se insertó una capa delgada de $SrTiO_3$ entre la capa ferroeléctrica (STO/BTO) y el electrodo. Se encontró que el control eléctrico/óptico de la resistencia se puede operar de manera más estable. Se muestra que los FTJs de STO/BTO muestran un comportamiento memristivo, es decir la resistencia cambia gradualmente de LRS a HRS por estímulo óptico en condiciones apropiadas. Se realizaron más investigaciones para comprender el origen físico de la conmutación resistiva inducida por la luz. Se ha observado que la dependencia temporal del cambio de resistencia viene determinada por la potencia del láser y el grosor del BTO, lo que ha proporcionado información valiosa sobre el mecanismo microscópico de la inversión de la polarización inducida por la luz. Se ha concluido que el cambio resistivo de LRS a HRS está relacionado con el efecto fotovoltaico.

Los estudios incluidos en la presente tesis son de interés ya que proporcionan estrategias de ingeniería de materiales interesantes para mejorar u optimizar el rendimiento de los FTJs.

Resum

El desenvolupament de la tecnologia de la informació s'acosta a un coll d'ampolla. Avui dia les memòries FLASH DRAM i NAND han mostrat inconvenients com la baixa retenció de la informació, temps de commutació lents i problemes de robustesa. Altres memòries no volàtils (NVMs) emergents s'han convertit en candidates per a la propera era de computació neuromòrfica.

Un tipus de NVM és la unió túnel ferroelèctrica (FTJ), que té una estructura de condensador simple, que consisteix en una capa ferroelèctrica ultraprima, que permet el transport per efecte túnel, intercalada entre dos elèctrodes metàl·lics. La commutació de la polarització ferroelèctrica entre dues direccions (P_{DOWN} i P_{UP}) modula les propietats de la barrera a la intercara amb els elèctrodes, cosa que conseqüentment causa canvis de conductància, és a dir, dóna lloc a electroresistència (ER). A diferència d'altres tipus de memòries ferroelèctriques, la lectura de l'estat de memòria de les FTJ no pertorba el seu estat de polarització (estat de memòria). Les FTJs mostren bona retenció durant molt de temps (> 10 anys) i més robustesa després cicles de lectura/escriptura (> 106 vegades).

Els òxids basats en HfO_2 dopat mostren ferroelectricitat en forma de làmina ultraprima (<20 nm). En forma policristalina es poden utilitzar per fabricar NVMs, per la seva alta compatibilitat amb la tecnologia CMOS. En aquest treball, capes primes de HfO_2 dopades amb Zr ($Hf_{0.5}Zr_{0.5}O_3$, HZO) es van créixer epitaxialment mitjançant la tècnica de dipòsit per làser pulsat i es van fer servir per construir FTJ. Tot i la naturalesa epitaxial de les capes obtingudes, les capes contenen fronteres de gra entre les fases ferroelèctrica (ortorròmbica) i no ferroelèctrica (monoclínica) del material. D'això se'n dedueix que la

conmutació de la polarització en els grans ferroelèctrics succeix, però també es poden crear canals conductors al llarg de les fronteres dels grans. Si bé anteriorment s'havia proposat que l'ús d'una capa protectora adequada és útil per mitigar la contribució de la conducció elèctrica a les fronteres de gra, anomenats canals de moviment iònic, en capes relativament gruixudes (> 5 nm), quedava per veure si la mateixa estratègia podria ser emprada en barreres HZO més primes. Aquest ha estat el primer objectiu daquesta tesi doctoral. Un segon objectiu, íntimament lligat a l'anterior, és que l'aplicació d'alt voltatge a FTJs causa una reducció de la seva resistència (suau ruptura) que afecta a la ER i per tant al seu ús potencial com a memòria ferroelèctrica. Per tant, entendre les propietats de la unió després de la ruptura és d’alta rellevància i ha centrat part de la recerca realitzada durant el desenvolupament de la present tesi.

Tipicament, l'estat de la memòria ferroelèctrica s'estableix mitjançant un camp elèctric (voltatge) que selecciona la direcció de polarització i, per tant, l'estat de resistència (alt/baix, HRS/LRS). Tot i això, investigar esquemes d'escriptura alternatius és de potencial interès. L'escriptura òptica és una de les opcions possibles. Malauradament, per als dispositius que funcionen en el rang de llum visible, HZO no és apropiat pel fet que el seu ampla de banda és excessivament gran. Per contra, capes de $BaTiO_3$ comunament mostren fotoabsorció al rang del visible i, per tant, són candidates per a aquest mode d'operació. Es van fabricar FTJ BTO de 4 nm de gruix, els camps elèctrics interns trenquen la degeneració entre P_{UP} i P_{DOWN} a favor d'un dels estats. En el nostre cas, es va trobar que s'afavoria P_{DOWN}. Es va observar el canvi de polarització induït per la llum de P_{UP} a P_{DOWN} i, posteriorment, es va observar un canvi de baixa a alta resistència induït òpticament. Es va observar un comportament similar en dispositius on es va inserir una capa prima de $SrTiO_3$ entre la capa ferroelèctrica

(STO/BTO) i l'elèctrode. Es va trobar que el control elèctric/òptic de la resistència es pot operar de manera més estable. Es mostra que els FTJs de STO/BTO mostren un comportament memristiu, és a dir, la resistència canvia gradualment de LRS a HRS per estímul òptic en condicions apropiades. Es van fer més investigacions per comprendre l'origen físic de la commutació resistiva induïda per llum. S'ha observat que la dependència temporal del canvi de resistència ve determinada per la potència de la llum i el gruix del BTO, cosa que ha proporcionat informació valuosa sobre el mecanisme microscòpic de la inversió de la polarització induïda per la llum. Hem conclòs que el canvi resistiu de LRS a HRS està relacionat amb l'efecte fotovoltaic.

Els estudis inclosos en aquesta tesi són d'interès ja que proporcionen estratègies d'enginyeria novedoses per la optimització de memories ferroeléctricas.

Structure of this thesis

Chapter 1: This chapter firstly introduces the motivation of this study. Two major objectives are introduced: non-volatile ferroelectric memory and tunable non-volatile ferroelectric memory.

Chapter 2: This chapter contains a description of the experimental methods used to characterize ferroelectric tunnel junctions. It contains sections devoted to sample preparation, electrical and structural characterization.

Chapter 3: We have presented an enhanced endurance and stability by applying dielectric capping layer to ultrathin HZO FTJs. This chapter is extensively based on the published work "Long, X., Tan, H., Estandía, S., Gazquez, J., Sánchez, F., Fina, I., & Fontcuberta, J. (2022). Enhanced electroresistance endurance of capped $Hf_{0.5}Zr_{0.5}O_2$ ultrathin epitaxial tunnel barriers. *APL Materials*, 10(3), 031114."

Chapter 4: We have investigated the ferroelectric electroresistance after forming conductive filament channel in Si compatible HZO FTJs. This chapter is extensively based the work "Ferroelectric electroresistance after breakdown in Epitaxial $Hf_{0.5}Zr_{0.5}O_2$ Tunnel Junctions", submitted to *ACS Applied Electronic Materials*.

Chapter 5: Here we demonstrate optical control of resistive switch in BTO FTJs as well as BTO/STO heterostructure junctions. This chapter is extensively based on the published work "Long, X., Tan, H., Sánchez, F., Fina, I., & Fontcuberta, J. (2021). Non-volatile optical switch of resistance in photoferroelectric tunnel junctions. *Nature Communications*, 12(1), 1–9."

Chapter 6: As an extension to Chapter 5, here the physical origin of light induced resistive switch has been investigated. This chapter is extensively based on the work "Disentangling electronic and thermal contributions to the observed light-induced resistance switching in $BaTiO_3$ ferroelectric tunnel junction", submitted to *Journal of Applied Physics*.

Contents

Acknowledgements iv

Abstract vii

Chapter 1. Introduction 21

1.1 Motivation 21

1.1.1 Development of non-volatile memory 21

1.1.2 Artificial synapse with non-volatile memory 23

1.2 Objectives 29

1.2.1 Non-volatile Ferroelectric Memory 30

1.2.2 Tunable Non-volatile Ferroelectric Memory 35

Chapter 2. Experimental Methods 42

2.1 Sample preparation 42

2.1.1 Pulsed laser deposition 43

2.1.2 Top electrode sputtering 44

2.2 Electric characterization 46

2.2.1 Measurement setup 46

2.2.2 Electro-Resistance measurement 49

2.2.3 Ferroelectric characterization 55

2.2.4 Photovoltaic characterization 60

2.2.5 Miscellaneous 62

2.3 Complementary characterization techniques 67

2.3.1 X-ray Photoelectron Spectroscopy 67

2.3.2 X-ray diffraction 78

2.3.3 Piezoresponse Force Microscopy 80

2.3.4 Scanning Transmission Electron Microscopy 81

Chapter 3. Capping layer impact on ultrathin HZO FTJs........83
3.1 Synopsis........84
3.2 Sample........84
3.3 Results........85
3.3.1 I-V dependence on capping layer........85
3.3.2 ER dependence on capping layer........86
3.3.3 Enhanced yield/endurance with capping layer........89
3.3.4 Composition and microstructural characterization........93
3.4 Conclusion........97
3.5 Appendix........98
Chapter 4. Electroresistance after breakdown in HZO FTJs........103
4.1 Synopsis........104
4.2 Sample........104
4.3 Results........105
4.3.1 X-ray diffraction characterization........105
4.3.2 Transport and ferroelectric characterization........107
4.3.3 Impedance measurement and analysis........112
4.4 Conclusion........117
4.5 Appendix........117
Chapter 5. Optical control of resistive switch in BTO FTJs........125
5.1 Synopsis........126
5.2 Sample........127
5.3 Results........127
5.3.1 Light induced polarization switching........127
5.3.2 Electric field and light control of ER........129
5.3.3 Enhanced optical control of ER........134
5.4 Conclusion........140

5.5 Appendix 141

Chapter 6. Disentangle physical origin of light induced resistive switch . 164

6.1 Synopsis 165

6.2 Sample 165

6.3 Results 166

6.3.1 Light-induced ER suppression 166

6.3.2 Resistive switching dependence on wavelength 167

6.3.3 Photoresponse dependence on wavelength 169

6.3.4 Response speed dependence 171

6.4 Conclusion 174

6.5 Appendix 175

Chapter 7. Conclusion 184

Chapter 8. Outlook 186

Bibliography 187

List of Samples 197

List of Figures 198

List of Tables 212

List of Abbreviations 213

List of Publications 215

List of Communications 216

Chapter 1. Introduction

1.1 Motivation

The rapid development of informational technology has nearly reached its "bottleneck" in several aspects, for example, the limitation of Moore's Law[3–6] and disadvantages of conventional Von-Neumann architecture[7–10] rising from increasing energy consumption and increasing computation complexity. In addition, there is an urgent demand for advanced non-volatile data storage unit.[4,11,12] During the last decades industry has witnessed newly emerging NVMs, and among them, the FTJ has shown huge potential in applications of data storage and artificial synapse.[2,13,14] Despite of its simple capacitor's structure, it has a great extent of versatility. Therefore, this thesis aims to investigate non-volatile and tunable FTJ memory.

1.1.1 Development of non-volatile memory

In this section, we focus on the development of NVM. The concept of "non-volatile" has been explicitly defined as "the ability to retain data for 10 years".[15] In contrast, the so called "volatile memory", which fades the stored data when power supply is turned off and needs to be refreshed periodically to retain the data, is also defined. The random-access memory (RAM) is a typical volatile memory. Dynamic random-access memory (DRAM) is one of its types and DRAM advantages are cheap cost, high density on chip, and fast speed of read/write operations (< 10 ns).[4,16] The RAM is synchronous with the CPU in

speed, nevertheless it does not support non-volatile storage. Dating back to the 1980s, computing technology required a fast and non-volatile memory to overcome a “memory gap”[15,17] problem, because non-volatile storage unit (at that era magnetic disk) was asynchronous with the logic unit, and the speed gap between them was almost six orders of magnitude. Since the year 2009 flash memory technique was developed to fill that “gap”. One of the most extensively applied flash is the NAND flash, which has advantages such as a fast speed (microsecond or nanosecond scale) and low fabrication cost.[4,18–20] A flash memory consists of many floating gate transistors, and data storage is realized by changing the charge quantity in a floating gate. During the process, voltage is applied to eject charges in and out through a gate oxide film which isolates floating gate to prevent charges loss. Repeatedly write and erase steps results in a degradation of gate oxide film, and lead to severe drawbacks in retention and endurance. In addition, other problems related to size, speed and power consumption, have also been pointed out and the applicability of flash memory is still limited.[4,21,22] The emerging NVMs in recent years with promising materials and architectures are expected to overcome some of the mentioned limitations. A hierarchy of memory classification is shown in Figure 1.1, where the emerging NVMs include a variety of types: resistive random access memory (ReRAM), phase change memory (PCM), magnetic random access memory (MRAM), spin-transfer torque random access memory (STT-RAM), ferroelectric random access memory (FeRAM), Ferroelectric field effect transistors (FeFET) and ferroelectric tunnel junction (FTJ). The three ferroelectric memories FeRAM, FeFET and FTJ are also grouped as non-volatile ferroelectric memory (FeNVM). It is presumed that future NVMs would simultaneously combine advantages in many aspects, for example, fast

writing/reading speed, large density, low power consumption, and non-volatility. With rapid development of artificial intelligence in recent year, NVMs with memristive behaviors have been regarded as the one of the best candidates for artificial synapse.

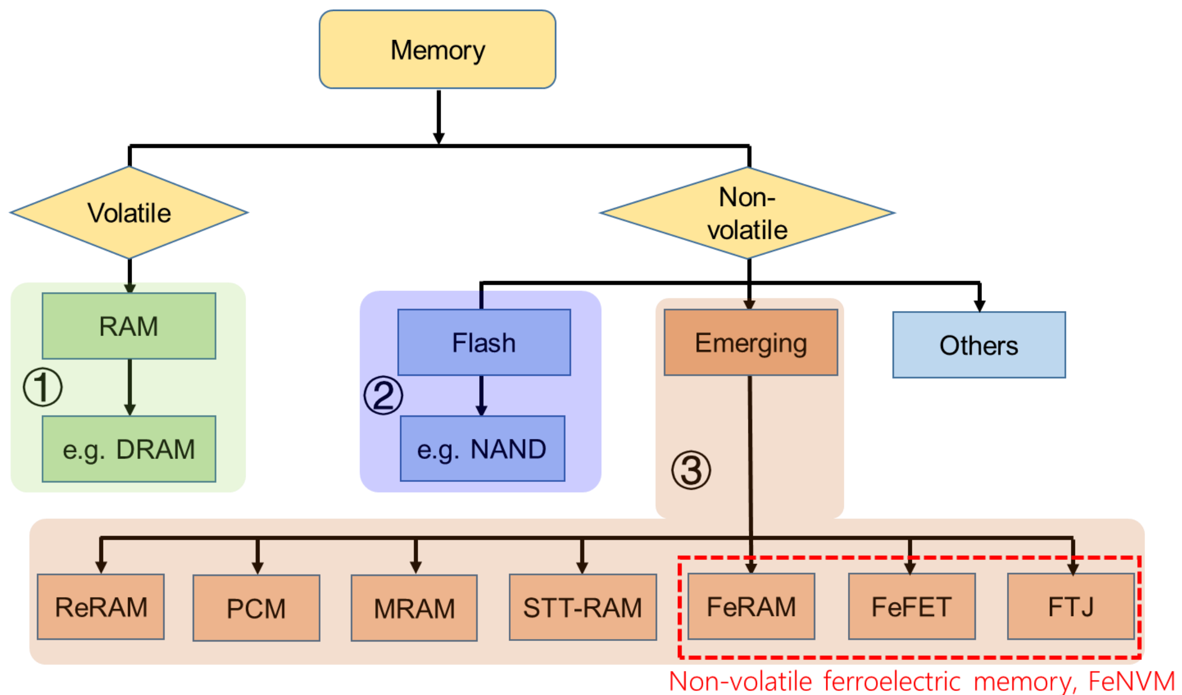

Figure 1.1 Hierarchy of the memory classification, depicted according to these references[4,17,23–25] *Three categories are marked with colored background: (1) Typical volatile memory; (2) Non-volatile memory with mature technique; (3) Emerging non-volatile memory, with a subset of "FeNVM" marked with dash line box.*

1.1.2 Artificial synapse with non-volatile memory

In biology the concept "synapse" indicates a specific structure that allows a neuron to pass chemical or electrical signals to another neuron or a target cell that responds to a stimulus.[26] As illustrated in Figure 1.2, chemical signal (e.g.

calcium or sodium ions previously enclosed in vesicle) is emitted by pre-neuron, transmits through synaptic cleft (a 20 ~ 40 nm gap) and then will be received by post-neuron.[27,28] The capability to enhance or weaken the synapse connection by changing the "weight" of synapse (strength of a connection between two nodes) is called synaptic plasticity, which is believed to be responsible for learning and memory process in the brain.[29] Neuromorphic computing has been regarded as a solution to avoid the drawbacks of traditional Von Neumann architecture by emulating the brain function. Similar to the biological brain which consists of billions of synapses, neuromorphic computing function must be realized based on enormous numbers of a basic unit. As shown in Figure 1.2, a two terminal capacitor structure has been adopted as a basic artificial synaptic unit, in which a top electrode emulates the pre-neuron, a bottom electrode as the post-neuron and an insulator serves as the synaptic cleft. In this simple structure, conductivity (or resistance) represents the strength of connection between two neuron nodes,[30] in other words it acts as the "weight". Then in order to emulate the plasticity, analog-like transition of conductance (resistance) must be implemented, in which the conductance (resistance) changes continuously based on the history of applied electrical pulse or other stimulus.[31,32] Such a memristive behavior is essential for artificial synapse application, thus requires NVMs to be tunable by stimulus. Actually a variety of non-volatile memories have been mentioned as appropriate candidates for the in-memory computing,[33] such as the ReRAM, PCM, MRAM and FTJ. Next, we will focus on important features of artificial synapse: potentiation/depression and the spike-time dependent plasticity (STDP), by giving examples to explain how they are emulated.

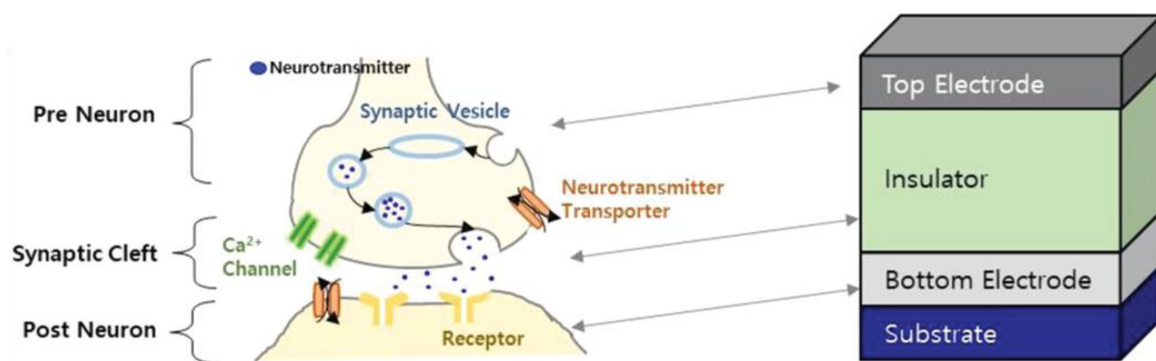

Figure 1.2 Comparison between biological synapse and artificial synapse. Taken from ref.[34]

Potentiation/Depression: A primary feature of artificial synapse is the potentiation/depression ability, in which the potentiation means an increase of the device's conductance while depression is corresponding to a decrease of its conductance, and the changes are modulated continuously by writing pulse numbers (N_P). As example, we show in Figure 1.3, two groups of writing pulses (each group $N_P = 12$) with the same amplitude but opposite polarity, applied to an ultrathin $Hf_{0.5}Zr_{0.5}O_2$ (HZO) FTJ, and the corresponding resistance measurements, collected by Milena Cervo during her PhD at ICMAB.[35] Writing with the first group of pulses (writing voltage, $V_W > 0$), the resistance increases (conductance decreases) gradually with the N_P, showing a depression process. On the contrary, writing with the other group ($V_W < 0$), the resistance decreases (conductance increases) gradually with N_P, showing a potentiation process.

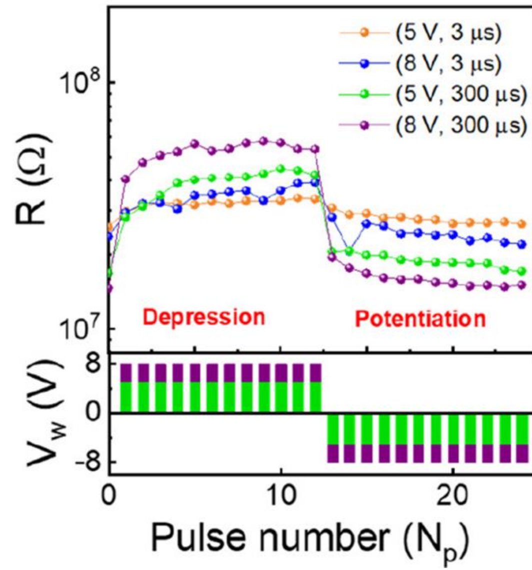

Figure 1.3 Resistance dependence on the number of pulses (N_P) in ultrathin HZO FTJ, mimicking the potentiation/depression process. Taken from ref.[35]

In addition, potentiation/depression feature can also be induced synergistically by optical/electrical stimulus. Figure 1.4 shows in a $WS_2/PbZr_xTi_{1-x}O_3$ (PZT) optoelectronic synapse (taken from ref[36]) conductance firstly increases by applying a series of light pulses (λ = 532 nm, power 10 µW, duration time 100 ms), which represents a optically induced potentiation process. Then with repetition of negative voltage pulses (V_W = -3.5 V, duration time 5 µs) its conductance diminishes, which an electrically enabled depression process. The authors have explored the underlying mechanism of light induced conductance change by conducting photo-assisted piezoresponse force microscopy (ph-PFM). The polarization underneath the WS_2 flake was gradually switched from an initial polarization upward direction (P_{UP}) to a downward direction (P_{DOWN}), while light-induced polarization reversal does not occur from P_{DWON} to P_{UP}. This can be explained by using a recently proposed theory considering the

interplay between photoinduced charges in 2D semiconductors and polarization charges in ferroelectrics.[37] As verified with PFM, the WS_2/PZT structure has shown a preference to P_{DOWN}, indicating that there is a downward built-in electric field (E_{bi}). As a result, photogenerated positive charges accumulate at WS_2/PZT interface. Then these charges screen a pre-set P_{UP} polarization and lead to a polarization reversal from P_{UP} to P_{DOWN}, driven by E_{bi}. However, a reversal from P_{DOWN} to P_{UP} is not permitted due to a downward orientation of E_{bi}.[37] Since the conductance in WS_2 is modulated by polarization, thus a gradual conductance increase can be implemented by optical stimulus, while electrical stimulus are needed to decrease the conductance.

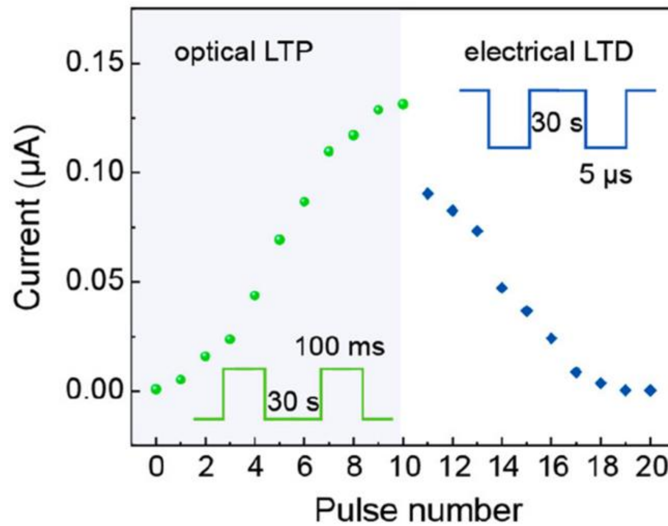

Figure 1.4 Potentiation/depression process implemented synergistically by electrical/optical stimulus, in a WS_2/PZT optoelectronic synapse. This device is a three terminal transistor, where Au source/drain were fabricated through photolithography, e-beam evaporation and lift-off. The current flowing through WS_2 channel was detected. Electrical pulses applied at the bottom gate $SrRuO_3$ (SRO), optical pulses illuminated at the WS_2 region. Taken from ref.[36]

Spike-time dependent plasticity: Another important feature for neuromorphic application is the spike-time dependent plasticity, through which the synaptic strength evolves depending on the time interval between stimulus (e.g. electrical signals) from a pre and post-neuron ($\Delta t = t_{pre} - t_{post}$).[38–40] The implementation of STDP in artificial neural networks has been regarded as an crucial approach to realize self-adaptive electronic architectures, since it does not needs any external control on synaptic strengths or any previous knowledge.[41] Now we briefly explain the STDP process by using the sketch in Figure 1.5 (a). Electrical signals coming from both pre- and post-neurons transmit to the synapse cleft, and a superposition of the two waves can be different depending on the time interval at their arrival. In the case when pre-neuron spike occurs earlier before the post-neuron spike ($\Delta t > 0$), the synaptic connection will be strengthened, corresponding to an increase of conductance ($\Delta G > 0$) in an artificial synapse. In the opposite case when pre-neuron spike is exited later than the post-neuron ($\Delta t < 0$), then synaptic connection will be weakened, in correspondence to a decrease of conductance ($\Delta G < 0$) in an artificial synapse. An experimental STDP data is shown in Figure 1.5 (b) (taken from ref[41]), where the conductance change (ΔG) was plotted as a function of time interval (Δt). Notice that in the STDP measurement only closely timed spikes (when $|\Delta t|$ is short) will produce a conductance change, whereas long time delay compared to the pulse width does not cause any substantial change.

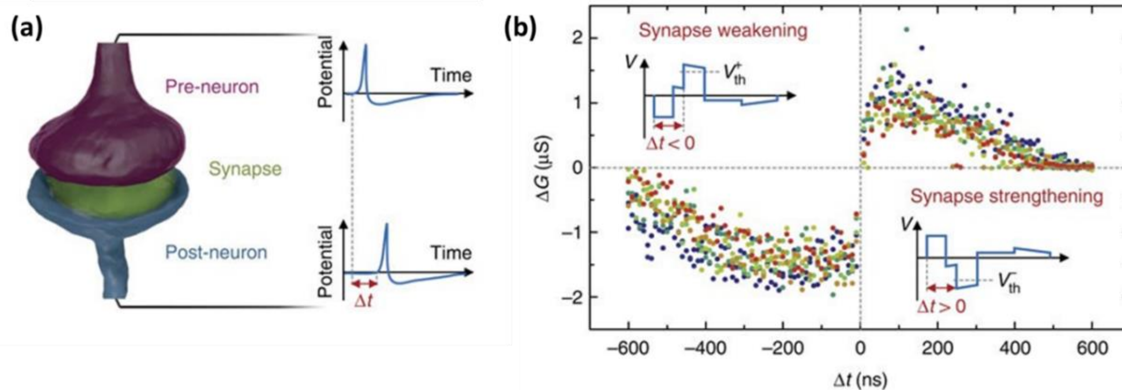

Figure 1.5 (a) Sketch of pre- and post-neurons connected by a synapse. The synaptic transmission is modulated by the time interval (Δt) of two neuron spikes. (b) Measurements of STDP in a $BiFeO_3$ (BFO) FTJ. Modulation of the device conductance (ΔG) as a function of the delay (Δt) between pre- and post-synaptic spikes. Taken from ref.[41]

1.2 Objectives

In this thesis, two major objectives have been pursued:

(i) Firstly, a series of investigations have been done on non-volatile ferroelectric memories using HZO as a ferroelectric layer. Two different blocks of experiments and results will be reported. a) Ultrathin HZO films grown on single crystalline perovskite substrates and using dielectric layers (named "capping layer") between the HZO and the top electrode (Chapter 3), and b) ultrathin HZO layers grown on appropriately buffered Silicon substrates (Chapter 4). Comparison of data collected in Chapters 3 and 4, allowed to obtain a fresh insight into the different mechanisms contributing to electroresistance in ultrathin ferroelectric layers.

(ii) Secondly, to achieve optically tunable non-volatile ferroelectric memory, BTO was chosen, because although it has an intrinsic band gap larger than the energy of photons in the visible range, it displays a substantial photoresponse at visible, due to defect-induced in-gap states. An optical/electrical controlled resistive switching has been observed with STO/BTO heterostructure (Chapter 5). A detailed investigations into the physical origin of light-induced resistive switching have been performed (Chapter 6).

1.2.1 Non-volatile Ferroelectric Memory

Non-volatile ferroelectric memories can be categorized into three categories: (1) FeRAM, which is a transistor connecting its source node to a ferroelectric capacitor, a so called 1T1C cell. (2) FeFET, which is a transistor that uses a ferroelectric oxide layer to separate the gate and channel. (3) FTJ, which is a ferroelectric capacitor with a "metal-ferroelectric-metal" structure. The basic idea of FTJ was proposed by Esaki et al.[42] in 1971, but it was at the first decade of new millennium that interest was renewed to exploit the powerful Esaki's concept, due to technological progress and new studies[43–47] upon nanometers-thick ferroelectric films.[48] In this thesis, FTJ are studied as promising NMV device due to its relatively simple structure, high scalability, large ON/OFF ratio, high speed, ultra-low power consumption and high fatigue.[13,25,49–52] Next, the working mechanism of FTJs are introduced, as well as the promising materials to be used and the engineering of FTJs that may improve their performance.

Resistive switching in FTJs: To be brief, the reversal of polarization induces modulation of tunnel barrier profile thus consequently leads to a non-volatile

switching of conductance between a high (ON) and a low (OFF) level in a FTJ, the so called tunneling electroresistance (TER) effect. The microscopic mechanism for resistance switching under polarization reversal can be explained as follows. Near ferroelectric/metal (FE/M_i, i = 1,2) interface, electrons from electrodes will be either attracted or repelled due to spontaneous polarization, which causes charge accumulation or depletion. Charges distribute over a finite depth or the so called "screening length", as defined in the Thomas-Fermi model.[53] The screening length differs depending on the microscopic properties of metals and interfaces.[54] For example, in a very good metal the screening length can be as short as tenth of nanometers, while in semiconductors it can be tens of nanometers.[25] The different screening lengths within the metal electrodes at each interface (FE/M1 and FE/M2) will lead to an asymmetric potential profile. When polarization is reversed the asymmetry of the electronic potential profile is also reversed, resulting in average in different barrier height being unequal (Φ_+ and Φ_-), as sketched in Figure 1.6. The tunnel current through a barrier depends exponentially on the square root of barrier height,[55] therefore two distinct resistance state (HRS, LRS) exist. To quantitatively express the difference between HRS and LRS (OFF state and ON state), the concept electroresistance is introduced with a mathematical relation ER = (HRS - LRS)/LRS, or calculated by using tunnel current (I_{ON} - I_{OFF})/I_{OFF}. Memristive behavior can be obtained, if intermediate resistance state between HRS and LRS are stabilized corresponding to different polarization states.

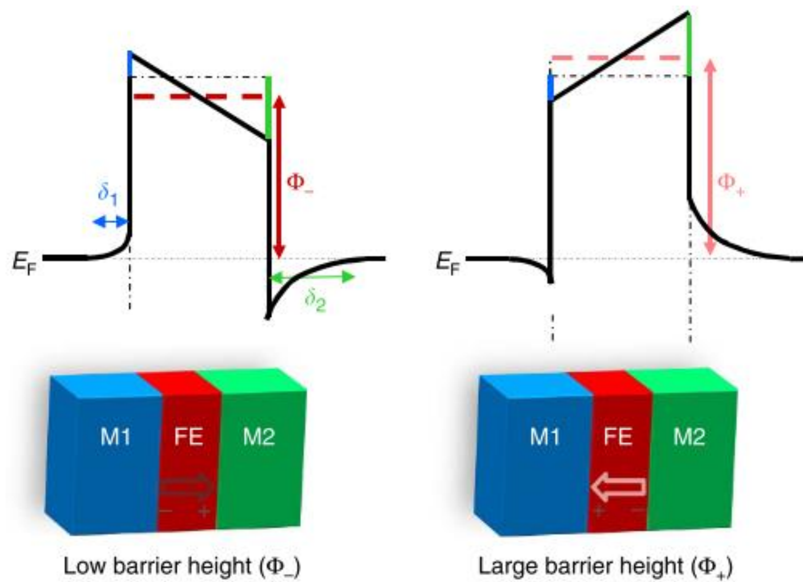

Figure 1.6 Energy barrier profile of a metal 1/ferroelectric/metal 2 (M1/FE/M2) structure, showing different change distribution (screening length δ1, δ2) in interfacial region for two polarization direction (right and left). As a consequence, the average barrier height changes (between Φ_- and Φ_+) lead to a change in the tunneling resistance. Taken from ref.[25]

Ferroelectric doped HfO_2 and $BatiO_3$: FTJs fabrication based on different ferroelectric materials have been studied up to now. In this thesis we have focused on HZO and BTO.

Since the late 1990s, hafnium oxide (HfO_2) has attracted interest due to its high dielectric permittivity and good compatibility with semiconductor processes.[2] As reported in many works,[56][57] thin films (usually < 20 nm) of doped HfO_2 are showing ferroelectric character. Thin films are commonly grown by atomic layer deposition (ALD) technique. This technique allows good conformality and scalability. However, the as-grown films are polycrystalline and require further annealing process. Epitaxial HfO_2 films prepared by pulse laser deposition (PLD) are of interest as their properties can be better controlled than

those of polycrystalline films.[58] Ferroelectric HfO_2 can be obtained by doping with several elements such as Al, Y, Zr, Gd, La, etc.[57,59–61] The doping allows the stabilization of the orthorhombic phase, which is ferroelectric. Among all studied dopants, Zr is interesting because good ferroelectric properties are obtained. The fine control of the Zr contents allows tunability of properties evolving from paraelectric (when $x \approx 0$) to ferroelectric ($x \approx 0.5$) and to antiferroelectric ($x \approx 0.8$).[62] In this thesis, HZO film will be studied so their ferroelectric properties are maximized. Epitaxial grown HZO films with orthorhombic phase with [111] out-of-plane orientation has been achieved on many substrates, including perovskite single crystals, such as strontium titanate ($SrTiO_3$, STO), gadolinium scandate ($GdScO_3$, GSO), etc. Interestingly Lyu et al.[63] has reported that epitaxial HZO can also be successfully grown on Si (001) substrate using a complex stack of buffer layers. In addition, Estandía et al.[58] has pointed out that the selection of perovskite substrates, and more precisely their cell parameter, plays a fundamental role on the stabilization of the orthorhombic (o-HZO, which is ferroelectric, as mentioned) or monoclinic (m-HZO, which is paraelectric) and determine their coexistence and relative abundance.

Nevertheless due to its large band gap (E_g = 5.75 eV),[64] HZO can hardly respond to light stimulus, so it is not a good choice for optical tunable non-volatile memory. This is why in the Thesis, the photoresponsive ER has not be explored in HZO, but only in BTO, as described below.

In recent years, the interest of optical control of ferroelectric polarization has been studied in several systems,[65] including BTO.[66] The BTO is an archetypal ferroelectric material. At room-temperature, where the tetragonal phase is stable,

the Ti^{4+} cation has two stable positions in BTO unit cell (along c-axis) which results in two stable spontaneous polarization state. Within the context of this PhD manuscript, it is important to remind that bulk BTO has a phase transition from the paraelectric at high-temperature phase to the tetragonal (ferroelectric) phase at about ~130 ºC.[67] Experimental observations of TER effect in ultrathin BTO were obtained by scanning probe microscopy by using conductive tip and metallic oxide respectively as top and bottom electrodes[49,50,68] and also in BTO FTJs with different bottom and top electrodes.[25,69,70] It has been also reported that, in BTO, ferroelectric polarization can be affected by light stimuli (see details in the following section), this is discussed in Chapter 5 and Chapter 6, where optically tunable FTJs are studied.

Engineering in FTJs: in order to manipulate tunneling electroresistance in FTJs more efficiently, various approaches have been proposed: interfaces and electrodes modification. Composite tunneling barrier combine a switchable ferroelectric and a dielectric ultrathin layer.[71] In an asymmetric metal/dielectric/ferroelectric/metal structure, the electrostatic potential of dielectric layer can be switched between a low and high level via the polarization reversal. And the dielectric barrier increases the asymmetry of the barrier change between the ON and OFF states and thus enhances the TER effect.[71,72] In other words, from these theoretical studies it was predicted that a composite barrier would result in lager TER ratio $((I_{ON} - I_{OFF})/I_{OFF})$ compared to single barrier. And it has been experimentally corroborated by Wang et al. using a BTO/STO composite barrier sandwiched between Au/Ti and SRO electrode.[73] By optimizing the relative thickness ration of BTO and STO films

within a total thickness of 10 unit cells (u.c.), a maximum TER ratio of approximately 36000% has been achieved in BTO (6 u.c.)/STO (4 u.c.), which is almost 10 times larger than a single BTO layer.[73] In addition, as reported by Sulzbach et al.,[74] adding extra dielectric layer also helps to mitigate detrimental influences by ionic motion in HZO FTJs. In this thesis dielectric/ferroelectric composite barriers will be studied.

1.2.2 Tunable Non-volatile Ferroelectric Memory

In this section, we focus on FTJs in which resistance can be tuned optically. In the following paragraphs we will start from mechanism of light induced polarization change. Then relevant works will be introduced as examples to elaborate how to achieve optical resistive control in FTJs.

Light effects on ferroelectric polarization: As described above, the key to modulate a ferroelectric tunnel barrier is to control the polarization. An idea came out since the 1980s, as researchers conceived to control ferroelectric polarization by photo absorption and concomitant generated photo carriers.[75] In 2012, Wang et al.[76] suggested that photogenerated charge carriers can be an effective screening mechanism of surface polarization charge. Photoscreening effect significantly increases by manipulating surface states in BTO films with dissociated water adsorbates.[77] Afterwards, Wang et al.[78] pointed out that synergetic effect of built-in electric field (E_{bi}) and photogenerated charges help to reverse polarization from P_{DOWN} (opposite to E_{bi} direction) to P_{UP} (along E_{bi} direction). As sketched the process in a LSMO/PZT stack in Figure 1.7 (e), there exists a E_{bi} with direction from LSMO to PZT near the LSMO/PZT interface.

The sample was illuminated with 400nm wavelength light (~3.1 eV) of which the photon energy is higher than the band gap of LSMO (1.0 ~ 1.3 eV)[79] while lower than the PZT (~3.25 eV).[78] Photogenerated electron-hole pairs in LSMO are separated by the E_{bi} at the LSMO/PZT interface, then a pre-written P_{DOWN} pulls positive charges to the PZT upper surface and results in a photovoltage along the opposite direction to polarization,[80] thus forces it recovering from P_{DOWN} to P_{UP}.[78] Ferroelectric domain switching was checked with PFM after illuminating sample with different light power and irradiation time, as shown in the images of Figure 1.7 (a)-(d). From the PFM results we can clearly observe a gradual process over time that black region (written with -3 V bias, corresponding to polarization up) vanishes and turns to bright region (written with +3 V bias, corresponding to polarization down), when light power ≥ 5.5 mW/cm^2. And this process will be accelerated when using higher light power. Specifically, when using lower light power, e.g. 3.5 or 4.3 mW/mm^2, nearly no substantial changes occurred. Furthermore, the authors found that the reversed fraction in the PFM images versus irradiation time fits well with the classic Kolmorogov-Avrami-Ishibashi (KAI) model,[81–83] which genuinely reflects domain switching kinetics under illumination. Apart from an electrical manner, it has been pointed out that thermal effect caused by high power laser irradiation is another possible way to vanish and switch polarization.[84] In Chapter 6 of this thesis we described in details about how to distinguish if a light induced polarization change is due to electrical or thermal mechanisms.

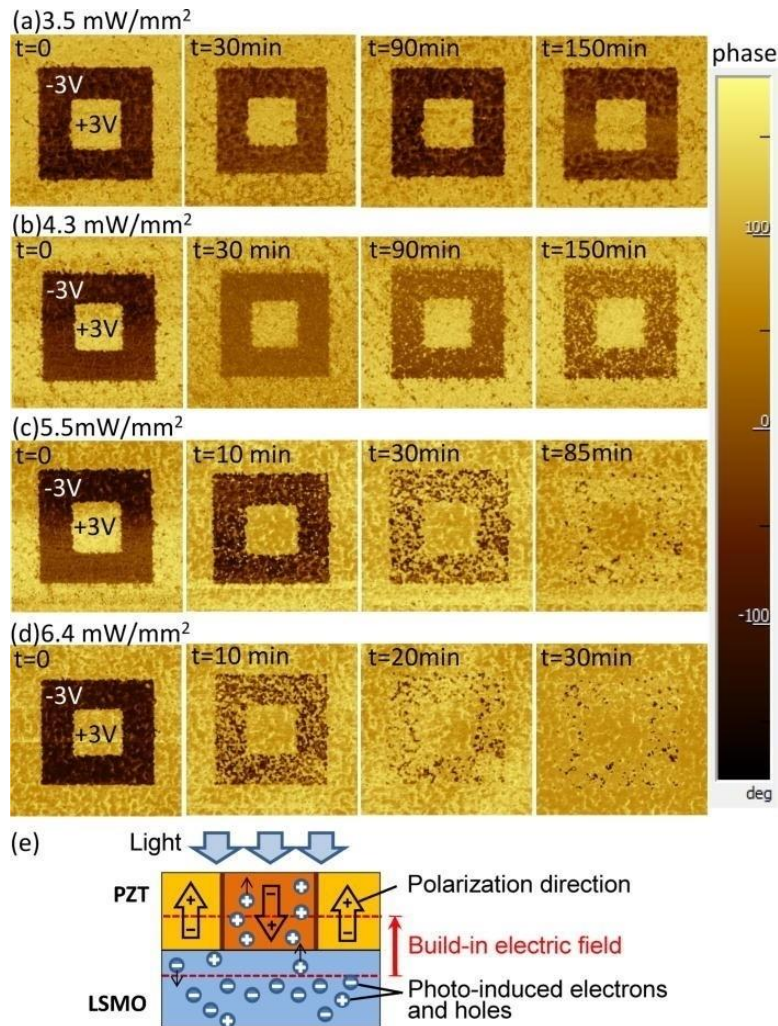

Figure 1.7 (a)-(d) Dependence of the domain variation on the power intensity and irradiation time; (e) Schematic of the mechanism of photovoltaic effect in the heterojunction composed of LSMO and poled PZT. Taken from ref.[78]

Optically tunable FTJs: In recent years, plenty of attentions have been focused on polarization switching via light absorption at 2D semiconductor materials[37,85] acting as electrodes (e.g. transition-metal dichalcogenides, such as MoS_2), or using other auxiliary methods.[86,87] In 2018, Li et al.[37] have reported a $MoS_2/BaTiO_3/SrRuO_3$ tunnel junction. In this junction, epitaxial BTO thin film was grown on SRO (bottom electrode) with 6 to 12 unit cells,

and 2D semiconductor MoS_2 flake on the BTO acting as a top electrode. The junction structure and experimental setup is shown in Figure 1.8 (a). PFM phase and amplitude images in Figure 1.8 (b)(d) and (c)(e) show that by illumination with ultraviolet (UV) light the polarization underneath MoS_2 electrode is switched from polarization up to down. Light absorption mainly occurs on MoS_2, which is absorbing in the visible range. Besides, tunnel current has been measured respectively in dark and after UV illumination, with a DC bias of 0.5V. It changes from an original tunnel current ~10 pA (corresponding to an initial polarization up) to 40 ~ 80 pA after illuminated (polarization down) with UV, indicating that this heterostructure FTJ is optically tunable in its resistance state.

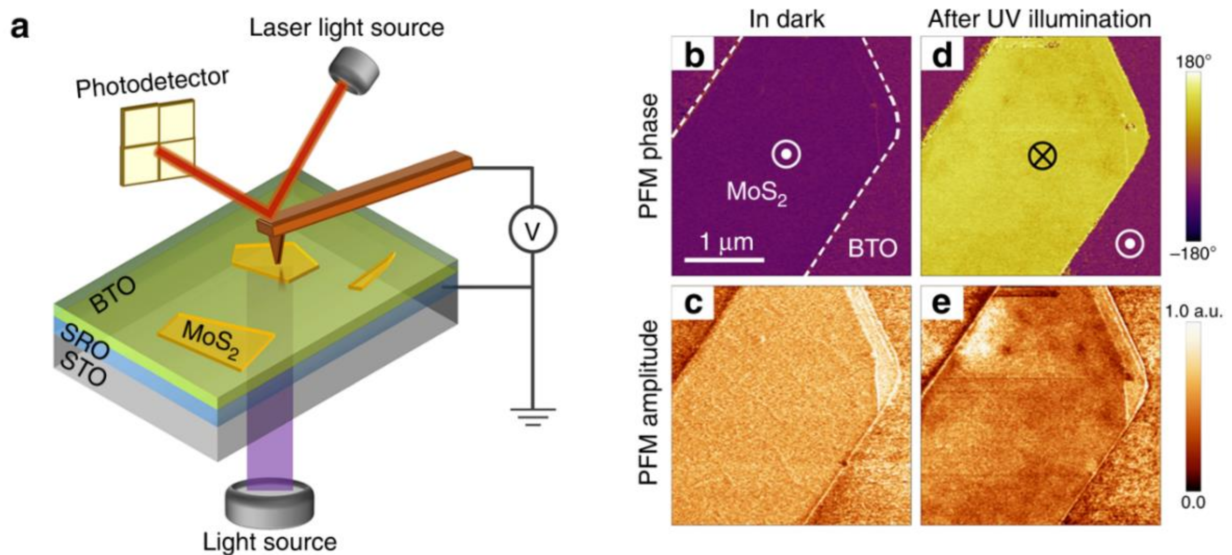

Figure 1.8 (a) Schematic diagram of sample structure and experimental geometry; (b)(d) The PFM phase and (c)(e) amplitude images obtained before and after UV illumination. Taken from ref.[37]

Apart from utilizing 2D semiconductor as electrode, it is possible to implement polarization reversal through another way, the so-called tip-enhanced photovoltaic (PV) effect, which depends on the large PV effect generated at the tip on the surface ferroelectric under illumination resulting in a localized electric filed larger than the coercive field.[84] In 2018 Yang et al.[86] reported light-induced polarization switching with tip-enhanced PV effect in an epitaxial SRO (100 nm)/BFO (150 nm) stack on a $TbScO_3$ (TSO) substrate. More interestingly, the authors found that a certain measurement configuration would allow photocurrent to change its polarity, so that the photovoltage between Pt nanoscale tip (radius ≈ 30 nm) and bottom SRO electrode changes its polarity. In 2019, Luo et al.[87] reported a light controlled binary resistance switching memory which consists of a FTJ (LSMO/PZT/Pt-tip (radius ≈ 30 nm)) and a PV cell (Pt/BFO/Pt), as shown the connection configuration in Figure 1.9 (a). The FTJ part has an ultrathin 3 nm PZT ferroelectric film, and during the optical writing process it is connected to the PV cell which contains two planar Pt stripes on top of BFO (thickness ~150 nm). The distance between two Pt stripes is 150 μm. When illuminating PV cell with blue laser (λ = 405 nm), the photogenerated current is collected along the BFO $[010]_{pc}$ direction (pc denotes pseudocubic). The polarity of photocurrent switches when light polarization changes between -45° and 45°, as shown in Figure 1.9 (b). As a consequence the electric filed in FTJ switches its direction, as shown the inset sketches in Figure 1.9 (b). When reading the resistive state, the PV cell must be detached from the FTJ part.[88] As shown in Figure 1.9 (c), resistance was recorded after repeatedly written with polarized light (-45°, 45°) to obtain photovoltage sign change, which depend on crystal orientation and size.[87] These effects will depend on the fact that in a planar Pt/BFO/Pt system, photocurrent decreases

drastically either by diminishing the thickness of BFO,[89] or by shrinking the gap between Pt electrodes.[90] Also as mentioned, optical writing and electrical reading must be operated in separated circuits, thus it increases complexity to the device structure and fabrication cost.

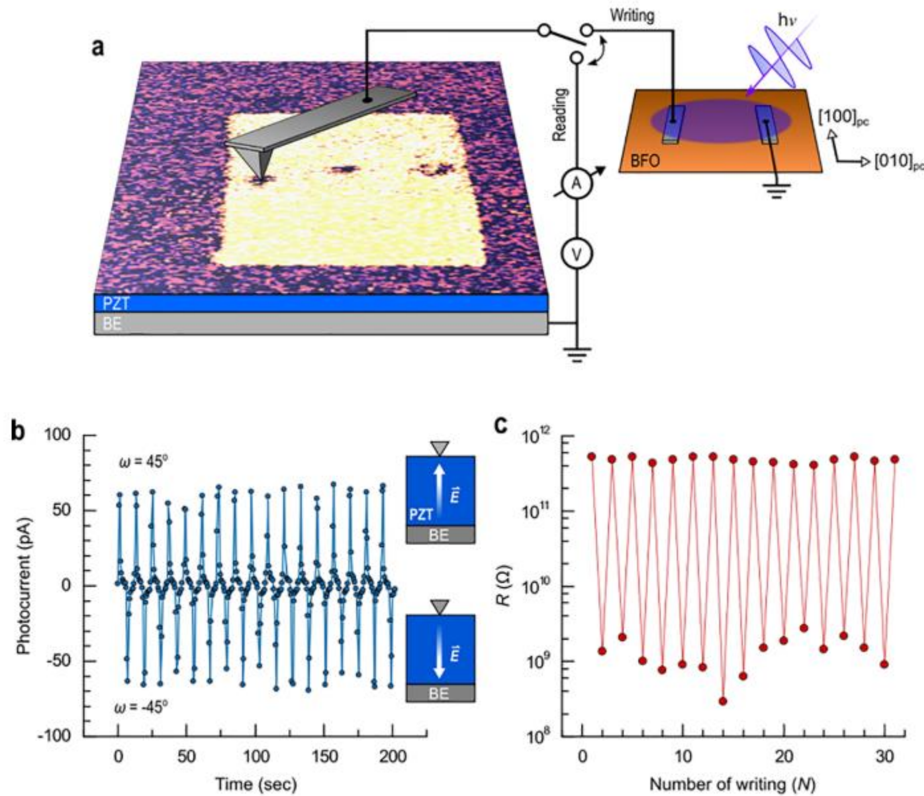

Figure 1.9 (a) Schematic illustration of the device showing the light-controlled resistance state writing and the electrical reading. The PFM image shows ferroelectric P_{UP} and P_{DOWN} in PZT layer. Note that LSMO/PZT/Pt-tip FTJ is connected to a PV cell (Pt/BFO/Pt); (b) Switching the polarity of the photocurrent by rotating the light polarization between −45° and 45°. (c) Resulting resistance states in the FTJ after the photodriven AFM tip writing, indicating a resistive switching memory function. Taken from ref.[87]

Despite the memory devices described above are fascinating for advanced optoelectronic application, however they have a lot of drawbacks, such as high

structural complexity, poor scalability, and incompatibility with massive chip fabrication. Thus, it is interesting to study structures that do not require the use of 2D materials, therefore light is absorbed in the ferroelectric. Here in this thesis, we summarize results obtained in optically tunable FTJ with LSMO/STO/BTO/Pt heterostructure, which shows robust electric/optical cycling performance, and a large ER approximately equals to $2 \times 10^{3}\,\%$, as show in Chapter 5.

Chapter 2. Experimental Methods

In this chapter, sample preparation and characterization techniques are described. Regarding sample preparation pulsed laser deposition (PLD), for sample growing, and DC sputtering, for top electrode growing, are described. Afterwards, the used electrical characterization methods and tools, central part of the present thesis, are described in detail. Compositional characterization performed by means X-ray photoelectron spectroscopy (XPS) is also described. Finally, complementary characterization methods and tools are also described: X-ray diffraction (XRD), Piezoresponse force microscopy (PFM), and scanning transmission electron microscopy (STEM).

2.1 Sample preparation

Figure 2.1(a) sketches a stack of substrate/bottom electrode/ferroelectric and top electrodes. In specific chapters of the theses dielectric layer between top electrode and ferroelectric layers [Figure 2.1(b)] or between the ferroelectric and the bottom electrode layer [Figure 2.1(c)] was inserted, bottom electrode, ferroelectric and dielectric layers were fabricated in a single PLD process. Top metal electrode were grown using stencil mask by DC sputtering.

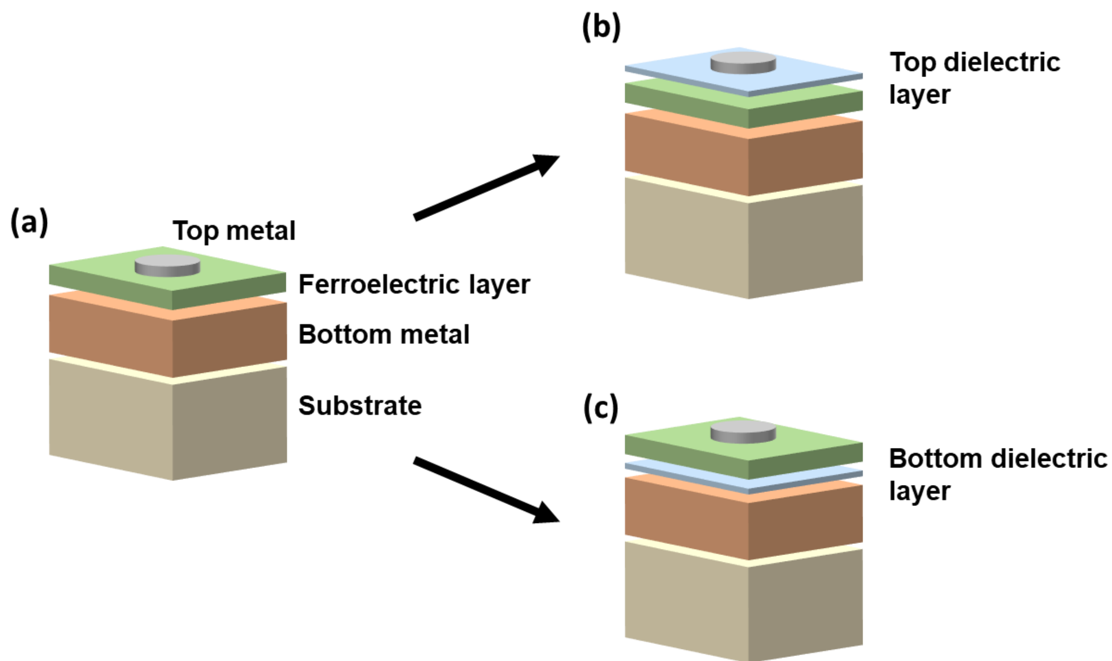

Figure 2.1 Sketch of a plano-parallel capacitor: (a) basic M1/FE/M2 structure and derived structure (b) M1/FE/DE/M2 and (c) M1/DE/FE/M2 with extra dielectric layer inserted. Here M1 represents bottom electrode and M2 represents top electrode.

2.1.1 Pulsed laser deposition

The PLD is ideal technique for the growth of complex oxide heterostructure allowing well controlled interfaces.[91] In Figure 2.2(a), the PLD setup is sketched. In the present thesis all the oxide films were grown by the Thin Film Laboratory at Institut de Ciència de Materials de Barcelona (ICMAB). The PLD system is provided by Twente Solid State Technology company (Demcon TSST, Netherland). In this technique, a KrF excimer laser generates pulsed UV laser beam with wavelength λ = 248 nm and pulse width of 10 ~ 40 ns, with a power fluence of 2 J·cm^{-2}. Growth by PLD involves the 3 stages: (1) Laser ablation

and plasma formation (see Figure 2.2 (b); (2) Plasma plume propagation; (3) Deposition and film growth.

The film thickness is controlled by the number of laser pulses. Nominal growth rate has been calibrated in selected samples by Laue interference peaks in the XRD scans patterns fitting, which will be introduced in details in the following section 2.3.2. More details about this technique are found elsewhere.[92]

All films included in this thesis were grown by PLD service of ICMAB, with the growth conditions (especially oxygen pressure $P(O_2)$ and substrate temperature T_s) described in each chapter of the thesis.

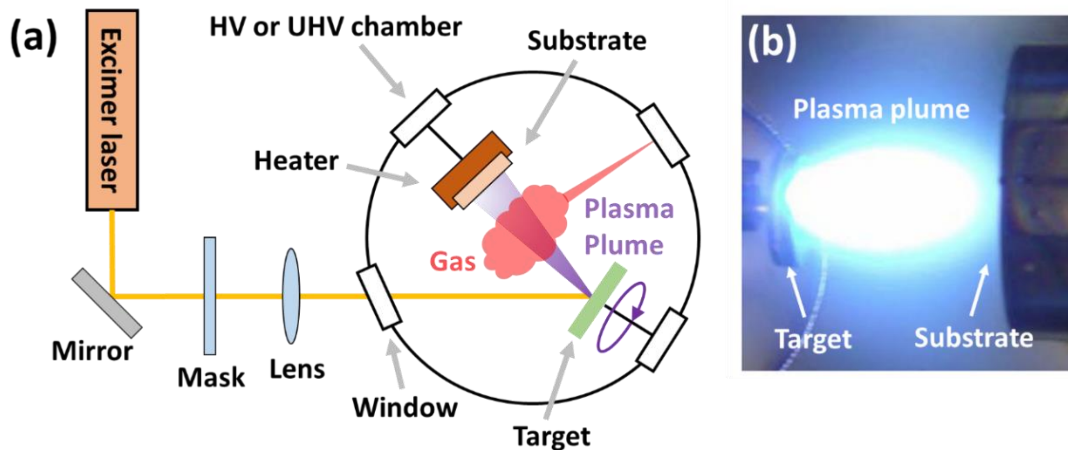

Figure 2.2 Pulsed laser deposition system utilized in ICMAB thin film laboratory: (a) A diagram of the PLD equipment structure and its working mechanism. (b) Plasma plume generated by ablating ceramic target with laser.

2.1.2 Top electrode sputtering

Top electrodes are deposited by DC sputtering. In the present thesis, Pt contacts are deposited on the surface of the oxide film described above. The sputtering system is provided by Twente Solid State Technology company (Demcon TSST,

Netherland). The Pt was considered as appropriate top metal for ferroelectric and transport measurement, due to its stability.[93] The magnetron sputtering set-up sketch is shown in Figure 2.3 (a). The target (Pt) is placed to cathode while the sample (for example STO//LSMO/BTO stack) is placed to anode. The chamber is at vacuum level of (~5×10^{-3} mbar) in a dynamic argon gas flux. Details on DC sputtering technique can be found elsewhere.[94]

To define top electrode array with designated shape and dimension deposition is done through a shadow mask. Two types of electrodes have been used as shown in Figure 2.3 (b) circular electrodes with diameters 20 μm and (c) square electrodes 60 μm × 60 μm.

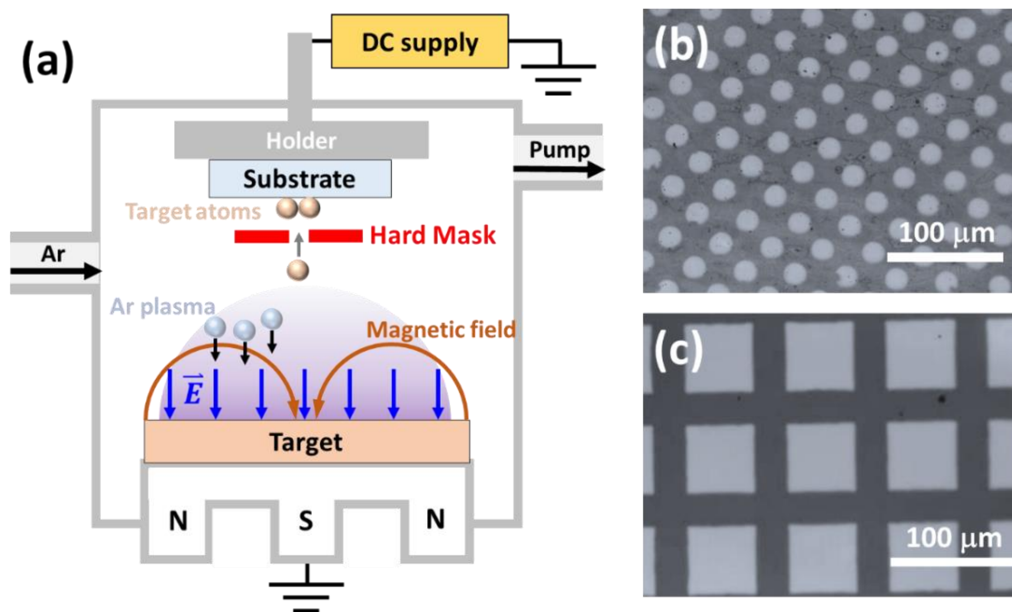

Figure 2.3 (a) Sketch of typical DC magnetron sputtering process. Optical microscopy of Pt electrode with different shape and size: (b) Circular with diameter of 20 μm; (c) Square with dimension of 60 μm × 60 μm.

2.2 Electric characterization

In this section, the electric characterization methods and set-up used are described. First, the experimental set-up and electric contact configurations are described. These are commonly used to perform electroresistance and ferroelectric characterization, which will be described afterwards.

2.2.1 Measurement setup

Here we will introduce the electrical characterization setup, including the electric characterization set-up, probe station, and the contact configuration.

Electric characterization set-up: AixACCT TFAnalyzer 2000 platform is used to perform the electric characterization. as shown in Figure 2.4. The system contains a main modulus (MM) and a FE-module. The latter consists in an electronic circuitry dedicated to condition the measured signal and the final applied voltage. Cables from probe station are connected to FE-module by two ports: “voltage source” for applying the output voltage to the measuring tip (sample) and “current input” for current measurement. The FE-module is connected to the main computer by four ports: the “I/O”, “Power”, “Out” and “In”. “I/O” serves as communication port mainly used to select the amplifiers for sensing current within FE-module, as required by the MM. The “Power” port sources the power of the FE-module. The “Out” port is connected to an inner function generator that applies V(t) signal, which signal conditioning takes place in the FE-module. “In” port is a terminal connected to an inner oscilloscope within MM, and it is used to monitor a voltage proportional to

current as in the "current input" of the FE-module. This system enables applying a V(t) signal with voltage amplitude up to 25 V between 500 μHz and 200 kHz.

Probe station: As shown in Figure 2.4, a probe station (light blue background) is connected with the TFAnalyzer 2000 system through two coaxial cables. Usually a Lakeshore EMPX-HP multifunctional probe station was utilized. Samples can be mounted on a stage illuminated by a controllable light source for a better inspection through a camera. Contact probes can be positioned on a desired region, usually the electrode area, by using suitable micropositioners The probes are ZN50-03-W tips made of tungsten, with radius of 3μm. All coaxial cables shields are connected to earth ground.

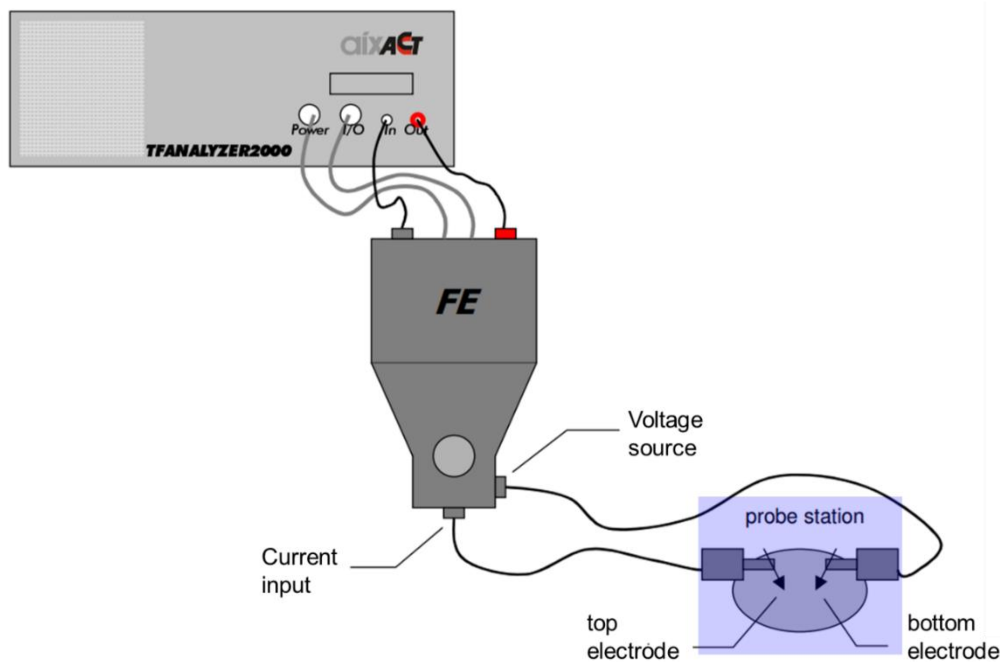

Figure 2.4 Wirings scheme for FE-module (taken from aixACT TFAnalyzer 2000 manual[95]). In our work, a Lakeshore EMPX-HP multifunctional probe station (marked with light blue background in scheme) was used to mount and connect samples, more details can be found elsewhere[96]. Coaxial cables connecting between devices and probe station are using earth ground on the shield. Sample is connected by using virtual ground on its bottom electrode.

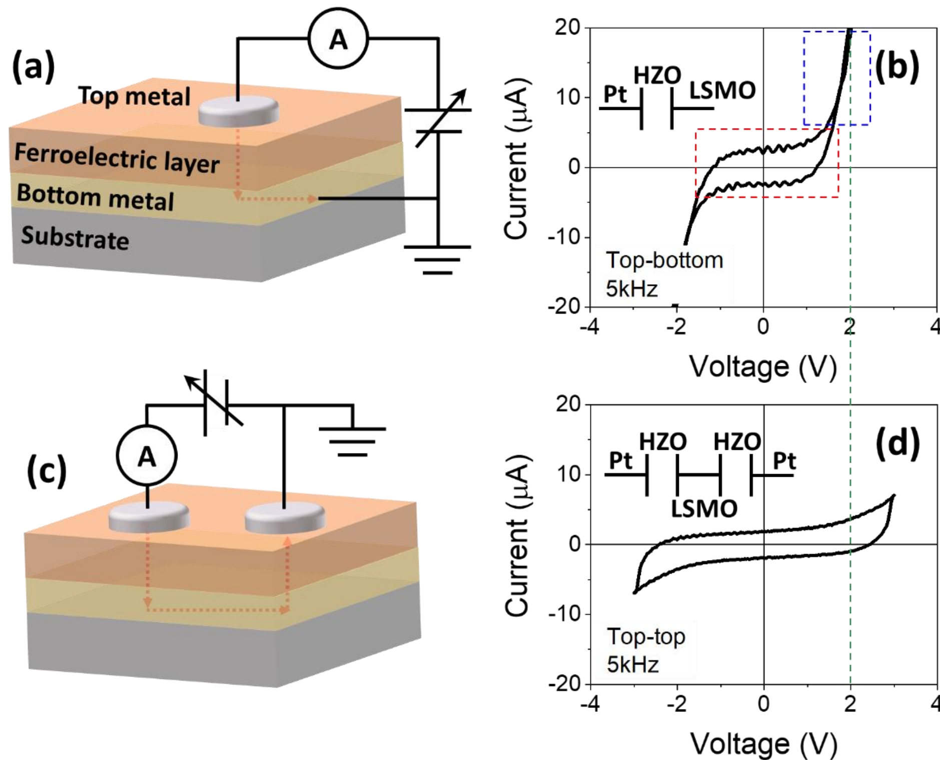

Figure 2.5 Electrode connection configuration for (a) top-bottom and (c) top-top; I-V data and equivalent circuit of each configuration (b)top-bottom and (d)top-top in an example of LSMO/2.2 nm-HZO/Pt junction.

Electric contact configuration: Two configurations has been used for electric characterization: top-bottom and top-top. In the top-bottom configuration, sketch shown in Figure 2.5 (a), the voltage signal is applied to the top metal (electrode), while the bottom metal (electrode) is contacted using silver paste to the ground. In this case, the configuration is equivalent to a connection with a single capacitor (M1/FE/M2 structure). See the sketch of the circuit in the inset of Figure 2.5 (b). In Figure 2.5 (b), the I-V collected at maximum applied voltage of 2 V and 5 kHz in this configuration a representative sample is plotted. The detected current is mainly contributed by: charge/discharge current of a

capacitor (plateau at low voltage enclosed by a red square) and the leakage current (increasing current near maximum applied voltage enclosed by a blue square). Note also that the measured current is not symmetric.

In top-top configuration, sketch shown in Figure 2.5 (c), two top electrodes are connected. One probe is connected to the ground and the other to the voltage source. Therefore, the configuration is equivalent to a series connection of two identical capacitors short-circuited by the bottom electrode, see the sketch of the circuit in the inset of Figure 2.5 (d). In Figure 2.5 (d), the I-V collected also at maximum applied voltage of 3 V and 5 kHz in top-top configuration is plotted. The shape of the curve is similar. The leakage current and asymmetry are substantially diminished, due to the doubled barrier thickness and the symmetric nature of the configuration. Therefore, this configuration is suitable for very leaky capacitors, e.g. tunneling barriers.

2.2.2 Electro-Resistance measurement

In this section we describe ER characterization methods are described. In the following sections we will introduce the ER measurement protocol, and other variations depending on the writing voltage (V_W) and writing time (τ_W). ER loop, retention and endurance characterization protocols are also described.

2.2.2.1 I-V dependence on prepoling pulse

A pre-poling V-t pulse with a trapezoid shape is applied to top electrode. As shown in Figure 2.6 (a), the trapezoid V-t pulse was defined with voltage amplitude (V_W), with a fixed rising time equals to plateau time (τ_W). After a delay time (τ_D, by default set to 1 s), a bipolar V-t triangular pulse (1 s duration) is applied and the current measured allowing to extract the I-V characteristics. The resistance is extracted at read voltage (V_R). Representative measurement is shown in Figure 2.6 (b). Notice that after pre-poling the junction with $V_W = +8$ V the detected current (red data dots) is lower than that after pre-poling with $V_W = -8$ V (blue data dots), at the dash line where $V_R = 0.5$ V. This implies that the junction has 2 distinct resistance states (HRS and LRS) after pre-poling with positive or negative bias. Resistance value is extracted at $V_R = 0.5$ V for both HRS and LRS states. The ER is calculated with the equation as follows:

$$\mathrm{ER} = \frac{HRS - LRS}{LRS} \times 100\% \qquad \textit{Equation 2.1}$$

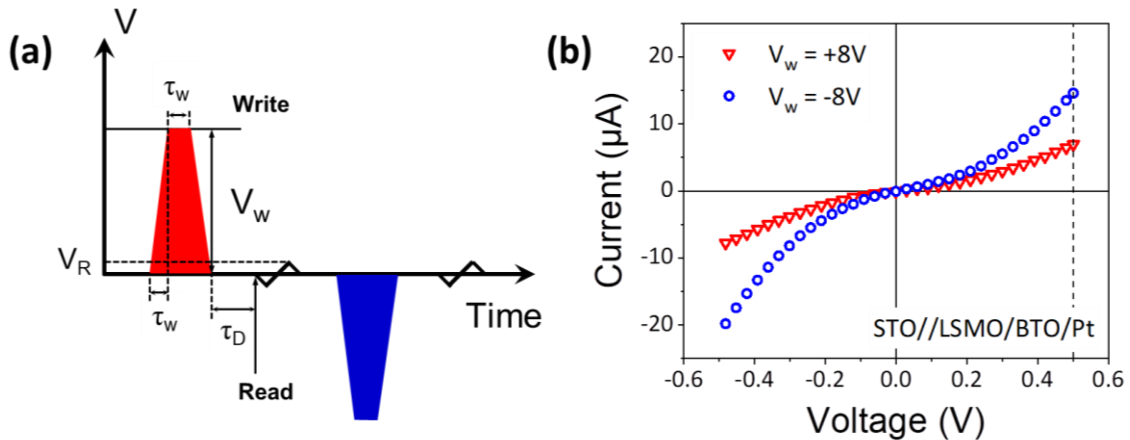

Figure 2.6 (a)Sketch of V-t pulses applied on a ferroelectric junction for tunnel resistance measurement. (b) Reading I-V recorded after pre-poling with V_W = +8 V and -8 V pulse (τ_W = 100 μs) in STO//LSMO/4nm-BTO/Pt junction. The tunnel resistance is calculated by V_R = 0.5 V, indicated with a black dash line.

2.2.2.2 V_W and τ_W dependence

V_W dependence: To characterize the V_W dependence the sequence shown in Figure 2.7 (a) is applied. Bipolar pulses of V_W are applied while the absolute amplitude gradually increases. Notice that the measurement starts from a non-prepoled initial state, which means the initial state of the sample is the as-grown one. Representative resistance dependence on V_W is shown in Figure 2.7 (b). ER in 2 different regions are distinguished: (1) ER increases gradually from V_W = 1 V to 10 V, HRS and LRS values maintain in the same order of magnitude (range between 10^7 and 10^8 Ω); (2) when V_W > 10 V both HRS and LRS decreases almost one order of magnitude, which indicates to an abrupt change in conductivity. Therefore, V_W dependence measurement helps to reveal a threshold voltage (V_{th}). The origin of the find different regions is discussed in dedicated chapters.

τ_W dependence: To characterize the τ_W dependence the sequence shown in Figure 2.7 (c) is used, for example: 1μs → 10μs →…→ 2ms. Representative τ_W dependence is shown in Figure 2.7 (d), resistance was recorded as a function of the τ_W (with fixed V_W = ±5 V). As we can find that ER constantly increases with τ_W and does not show any tendency of saturation. This protocol also gives hints on the driving mechanisms of the found ER.

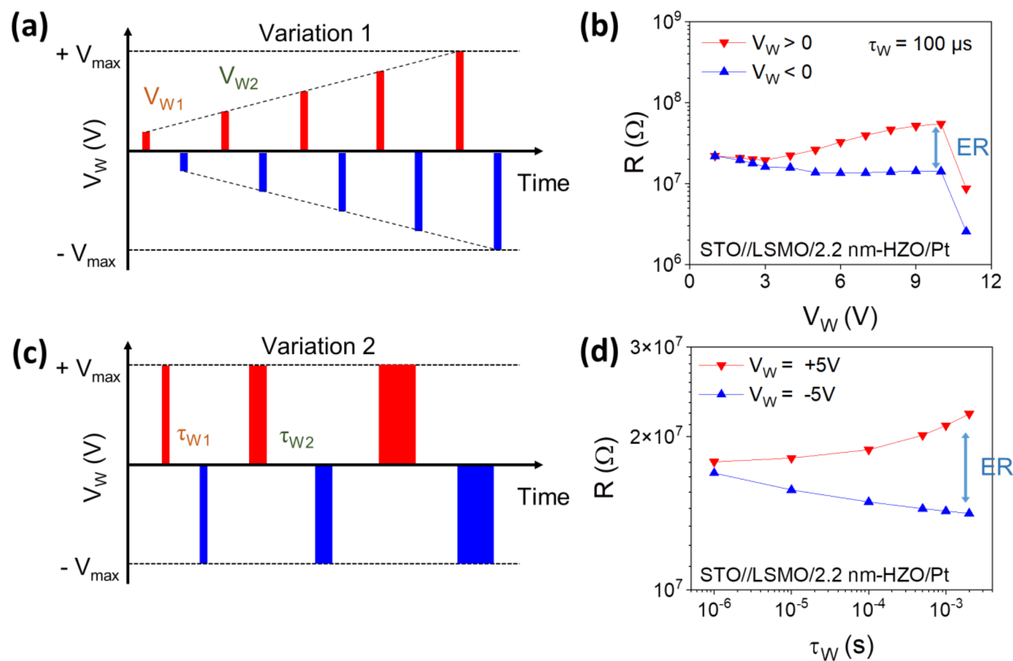

Figure 2.7 (a) Sketch of variation 1; (b) Resistance dependence on writing pulse amplitude V_W obtained from the sequence (a).(c) Sketch of variation 2; (d) Resistance dependence on writing time τ_W obtained from the sequence (c).

2.2.2.3 ER loop

ER loop is the most common method to characterize ER. The sequence shown in Figure 2.8 (a) is used, V_W pulses vary its amplitude from $-V_{max} \rightarrow 0 \rightarrow +V_{max} \rightarrow 0 \rightarrow -V_{max}$. In a representative example shown in Figure 2.8 (b), first the LRS is set by applying the negative maximum bias ($-V_{max} = -5$ V), marked by blue point. Then the V_W amplitude gradually increases following the sequence in Figure 2.8 (a). When it increases up to a threshold value V_C^+ (indicated with brown dash line), the resistance rises up and reaches a HRS, marked as red point in Figure 2.8 (b). Similarly, for decreasing V_W at the negative threshold V_C^- (indicated with purple dash line), the initial LRS is set and the loop is closed.

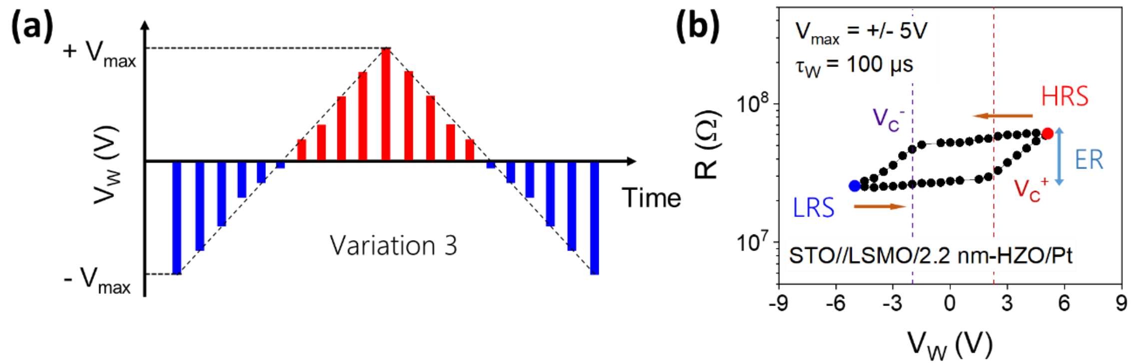

Figure 2.8 (a) Sketch of variation 3, (b) Representative resistance loop obtained from the sequence in (a), with fixed τ_W = 100 µs and V_{max} = +/- 5 V.

2.2.2.4 Endurance

To assess the stability of the junction, cycling between HRS and LRS states is performed. As shown in Figure 2.9 (a), a sequence of writing pulses with alternating positive and negative V_W is applied, and after each pulse resistance is measured at V_R = 0.5V. The pulse number can be up to hundreds or even thousands. Note that each pulse has fixed V_W and τ_W. For the representative example shown in Figure 2.9 (b). Stability up to 100 is observed followed by a decrease of resistance.

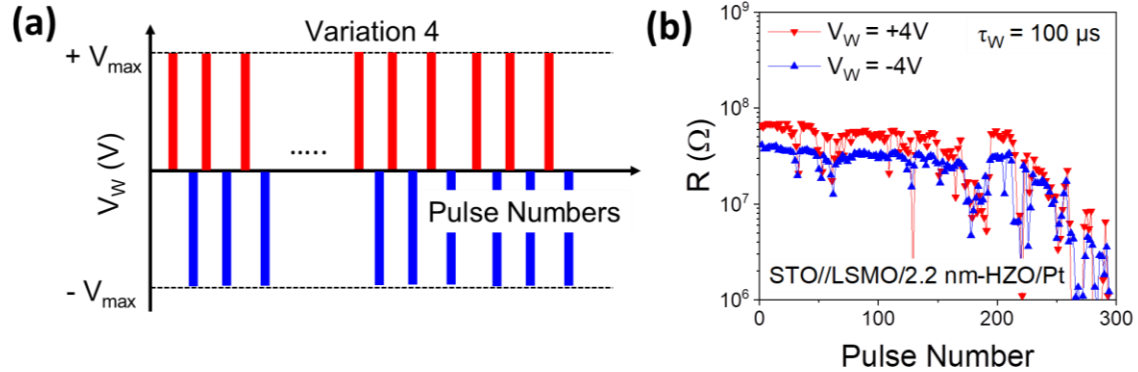

Figure 2.9 (a) Sketch of variation 4: a sequence of writing pulses with alternating positive and negative V_W and fixed τ_W. (b) Endurance measurement obtained by following the sequence in (a) with 300 pulses.

2.2.2.5 Retention

To assess the retention, the resistance as a function of τ_D is recorded. Recall here that τ_D is the time interval between a writing and reading signals, as shown in Figure 2.10 (a). The sample is pre-poled with a writing pulse of V_W and τ_W, then after a chosen retention time (τ_{D1}, τ_{D2},..,τ_{Di}) a triangular bipolar pulse with is measured to read the resistance at V_R = 0.5V. Finally, the resistance versus τ_D is plotted for both positive and negative writing pulse. A representative example of STO//LSMO/2.2 nm-HZO/Pt junction is shown in Figure 2.10 (b). In this case, the R-τ_D data pre-poled with V_W = +5 V represents how HRS changes by the time (see red dots line in Figure 2.10 (b)), while when pre-poled with V_W = -5 V represents the LRS changes by the time (see blue dots line in Figure 2.10 (b)). Then it is shown that the device remains in the HRS or LRS after a τ_D > 1000 s.

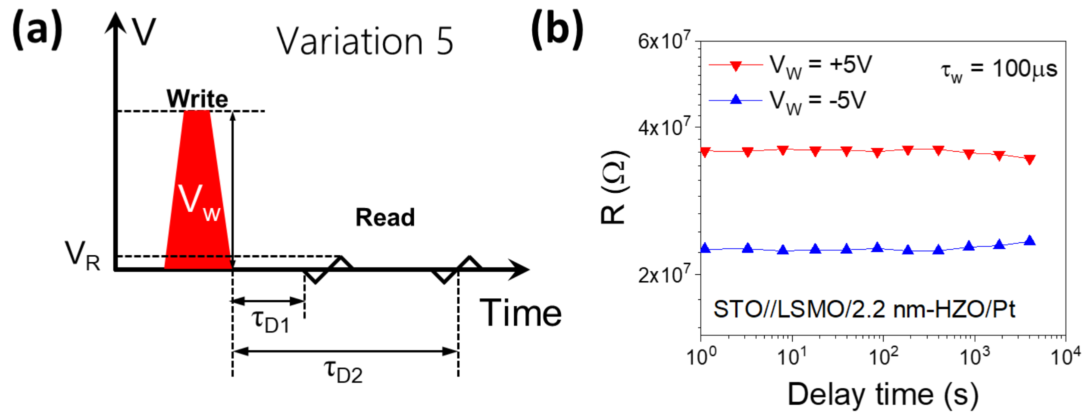

Figure 2.10 (a) Sketch of variation 5: recording I-V after writing pulse with different delay time (τ_{D1} and τ_{D2}). (b) The evolution of resistance in maximum delay time 5000 s. Both HRS and LRS were recorded.

2.2.3 Ferroelectric characterization

2.2.3.1 Dynamic Hysteresis Mode

The dynamic hysteresis mode (DHM) is used to measure P-V hysteresis loops. As shown in Figure 2.11 (a), the pulse sequence involves four bipolar triangular excitation signals with a frequency ν_0 and time interval τ_D. In this protocol ferroelectric film is pre-poled into a polarization state with the first triangular signal (filled with color gray) and the third signal (no color filling). The polarization is calculated from the integration of the current measured during the second half of the second triangular signal (filled with color green) and the second half of the fourth triangular signal (filled with color purple) normalized to the electrode area. A sketch of I-V curve obtained from the sequence is shown in Figure 2.11 (b). The current contributed by dielectric displacement current (I_{DE}) and the switching current (I_{FE}, see the two peaks) are identified. Then

finally, the polarization versus voltage hysteresis loop (Figure 2.11 (c)) can be obtained. The saturated polarization (P_S) and remnant polarization (P_R) can be obtained from the loop.

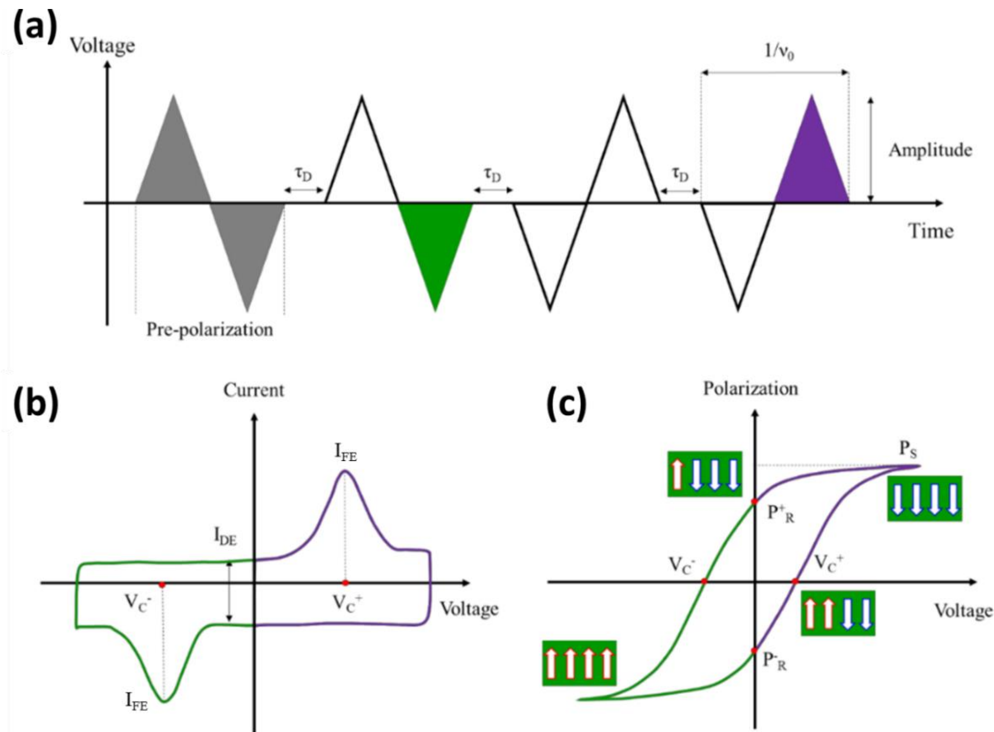

Figure 2.11 (a) Sketch of the voltage pulse sequence used for measurement with frequency v_0 using DHM mode (b) I-V curve obtained from (a). It is possible to identify coercive voltages (V_C^-, V_C^+) and dielectric displacement current (I_{DE}) and switching current (I_{FE}). (c) The integration of current in time results in the polarization curve P-V. Taken from ref.[97]

2.2.3.2 Dynamic Leakage Current Compensation

As explained in DHM mode, P-V hysteresis loop is calculated based on I-V curve. In some cases, the leakage contribution overlaps with displacement current, contributing to the calculated polarization.[98] Dielectric leakage current compensation (DLCC)[99] allows to minimize leakage influence according to

two assumptions: (1) the dielectric displacement current (I_{DE}) and switching current (I_{FE}) varies linearly with the frequency; (2) the leakage current $I_{leakage}$ is independent of frequency and only depending on the voltage. Then the system estimates a subtraction of $I_{leakage}$ by measuring in DHM mode at two different frequencies (ν_0, $\nu_0/2$), so the dielectric displacement (I_{DE}) and switching current (I_{FE}) remain.

2.2.3.3 PUND technique

Another technique that is usually used to obtain reliable P-V hysteresis character is the Positive-Up-Negative-Down (PUND)[100–102]. A sketch of a typical PUND sequence is shown in Figure 2.12 (a), it involves 5 triangular pulses with the same amplitude ($> V_C$) and writing time. Sample is firstly pre-poled to one direction with a negative pulse (marked with "X"). Then in the next second positive pulse (marked with "P"), polarization is switched to the opposite direction, and both ferroelectric contribution (I_{FE}) and non-ferroelectric ones (I_{DE}, $I_{leakage}$) are measured. In the following third pulse (marked as "U"), since there is not any switching current, only current contributed by non-ferroelectric terms (I_{DE}, $I_{leakage}$) is measured. The measured I-V corresponding to pulse "P" and "U" are shown in Figure 2.12 (b) respectively with color red and yellow, indicating a significant difference in current. The same occurs from the fourth pulse (marked as "N") to the fifth pulse (marked as "D"). Finally, the switching current can be compensated by subtracting (I_P - I_U, I_N - I_D), as shown in .Figure 2.12 (c), and then P-V loop can calculated by current integration.

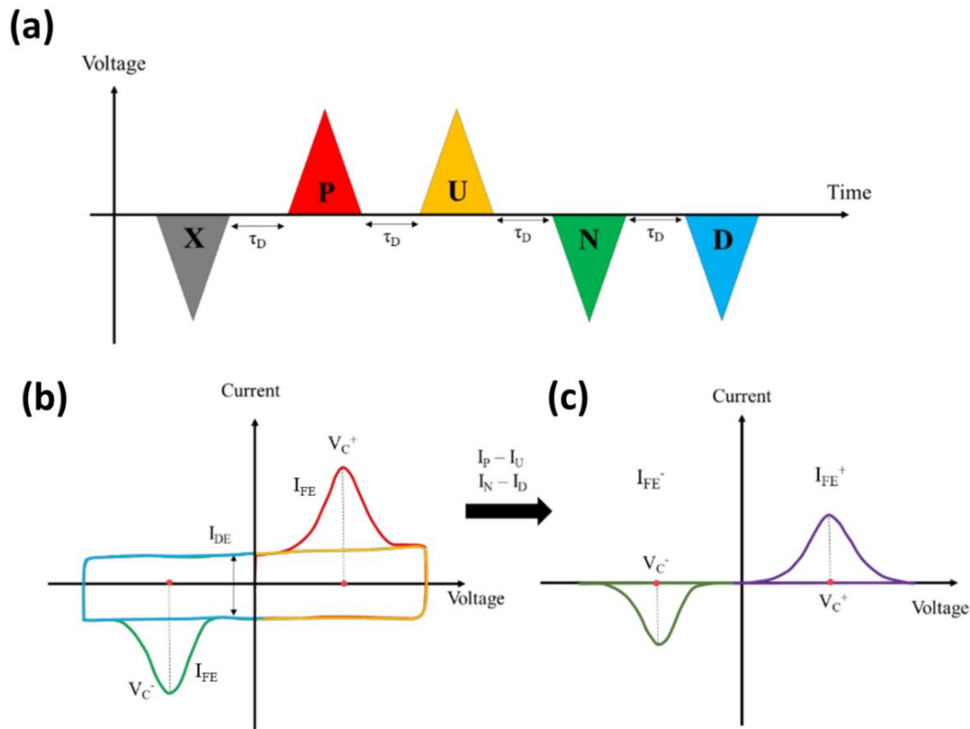

Figure 2.12 (a) Typical pulse sequence of the PUND technique, τ_D is the delay time interval between one pulse and another; (b) Representation of current response corresponding to PUND sequence; (c). Final I-V curve obtained by (I_P - I_U) and (I_N - I_D). Now the only current contribution visible is related to ferroelectric switching. Taken from ref.[97]

2.2.3.4 Cycle training

A cycle training is a treatment to the sample by using bipolar square pulses of a designated cycle number (N_C) at a given frequency ($\nu_{rectangular}$) and voltage amplitude. Meanwhile in this theses[35,103], it has been observed that a cycle training drastically decreases the conductivity of ultrathin HZO film and increases the ER of ultrathin FTJs. Examples can be taken from a STO//LSMO/2.2 nm-HZO/STO1/Pt junction, which has a 1 nm STO dielectric capping layer above HZO film. The sketch of a cycle training is shown in Figure

2.13 (a), in which $N_C = 10^4$ times and $\nu_{rectangular} = 5$ kHz and voltage amplitude V_{max} = +/- 2.5V. Here we chose a proper cycling number N_C. Then I-V curve with V_{max} = +/-2.5V 1Hz was firstly recorded before cycling, the so called "pristine" state. Then after a cycle train, I-V curve was recorded again with the same parameter, and a brief comparison of pristine and after cycling was plotted in Figure 2.13 (b), which shows a change in resistivity. An enhancement of ER after the cycle training is also observed, see Figure 2.13 (c). The ER of the ultrathin HZO FTJ roughly equals to 9% in the pristine state, while it increases up to ER ≈137%. It is ascribed that the a electric field induced phase transformation leads to the change of resistivity and ER[35]. The origin of this training effect is discussed in Chapter 3.

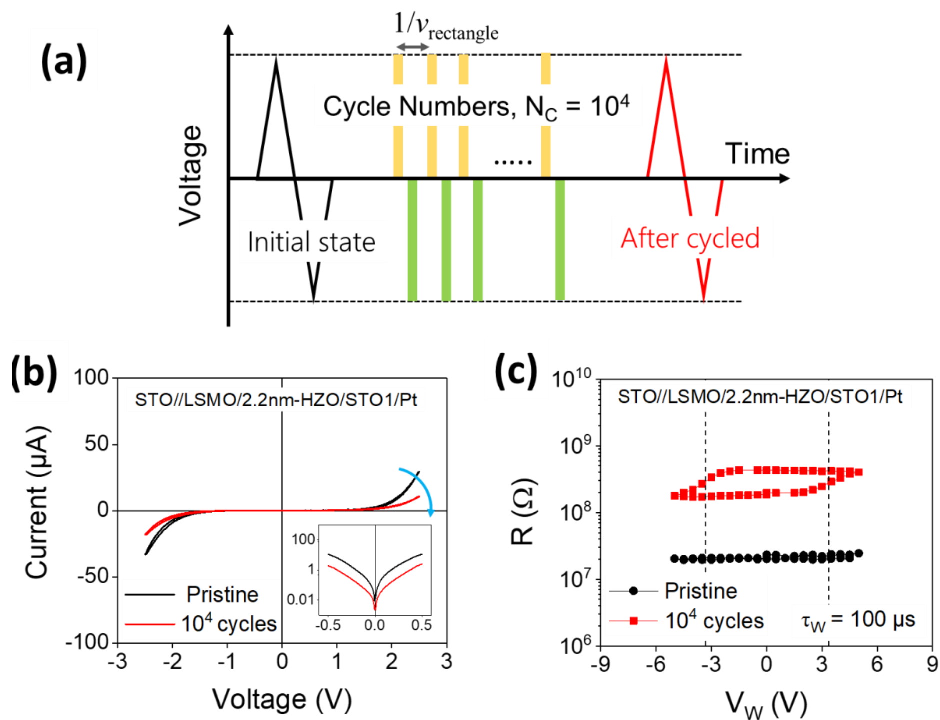

Figure 2.13 (a) Sketch of pulses applied in a cycle training; (b) Representative I-V curves measured with triangular signal 2.5V 1Hz in pristine state and after cycling 10^4 times, inset is the log scale current versus voltage in small range -0.5 V ~ +0.5 V; (c) Representative ER loops measured in pristine state and after

cycling 10^4 times, with maximum writing voltage V_{max} = +/- 5 V and writing time τ_W = 100 μs.

2.2.4 Photovoltaic characterization

Response to the optical stimuli of resistance and ferroelectric polarization is discussed in Chapter 5 and Chapter 6. In the present section, the optical excitation set-up and the used protocols are described.

2.2.4.1 Optical set-up

Optical illumination is performed blue light ($\lambda = 405$ nm) and red light ($\lambda = 405$ nm) with maximum illuminating power density of ≈ 9 W/cm^2 driven by a CPX400SA DC power (AimTTi Co.). The laser source is installed on the anti-vibration experimental table with a fixed inclination (45°). The diameter illumination spot is ~250 µm, thus covering the whole capacitor area Figure 2.14 (a).

2.2.4.2 Photoresponse measurement

Photocurrent measured in representative LSMO/BTO/Pt junction is shown in Figure 2.14 (b). Notice that in this figure optical illumination period is marked with light blue background. The recorded current abruptly rises up at the

moment when light on and it drastically drops when light off, showing a clear and reproducible photoresponse step.

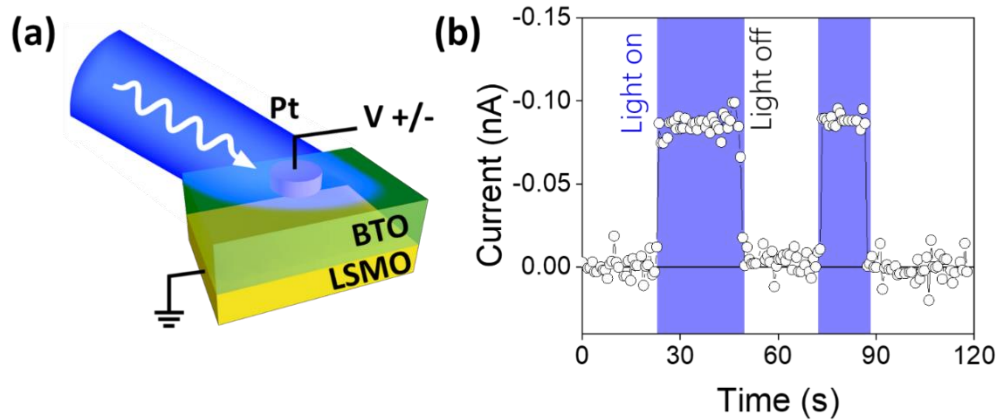

Figure 2.14 (a) Sketch of measurement under blue laser illumination in an example of STO//LSMO/BTO/Pt junction. (b) Photoresponse in LSMO/BTO/Pt junction, light blue region indicates an epoch between light on and light off. The laser power is fixed at 9 W/cm^2.

2.2.4.3 I-V curves under illumination

Another method to study photoresponse is to measure I-V curve under illumination. As shown in Figure 2.15, the I-V curves are recorded under a small bias range (from -0.1 V to +0.1 V). Notice that the I-V curve intercepts with I and V axis, which are defined as the "short circuit current" (I_{sc}) and "open circuit voltage" (V_{oc}) respectively. In dark $V_{oc} \approx 0$ V and $I_{sc} \approx 0$ nA; while under illumination $V_{oc} \approx 0.05$ V and $I_{sc} \approx 0.05$ nA, showing obvious photovoltaic effect.

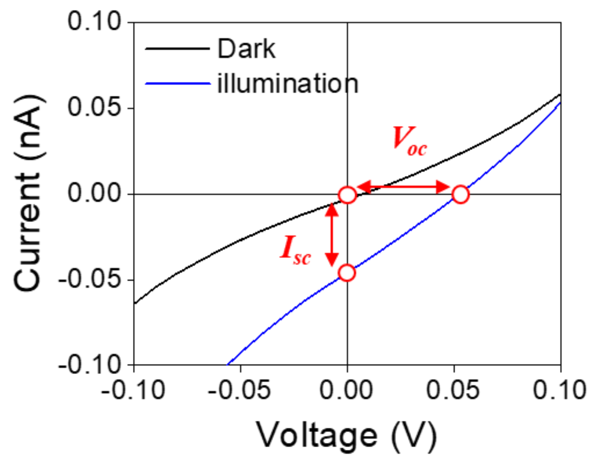

Figure 2.15 Current-voltage curves obtained with and without illumination (black line in dark, blue line illuminated with blue light 9 W/cm^2). Red arrows indicate intercept shift in both axis, which represents the open-circuit voltage (V_{oc}) and short-circuit current (I_{sc}) respectively. Data collected in a LSMO/STO/BTO/Pt heterostructure junction.

2.2.5 Miscellaneous

2.2.5.1 Impedance spectroscopy

Electrical impedance is the opposition to alternating current (AC) presented by combined effect of resistance and reactance in a circuit.[104] Unlike the resistance under direct current (DC), the impedance possesses both magnitude and phase angle, thus it represents a ratio of the complex representation of the sinusoidal voltage to the complex representation of current,[105] which depends upon the frequency of AC signal. Among those basic electric elements shown in Figure 2.16, only resistor allows current directly proportional to the voltage at all period of time, while for ideal capacitor and inductor the current does not

change synchronously with the applied electric field. The phase angle (denoted as θ) is defined as a shift between the voltage sinusoidal wave and its induced current signal. From Figure 2.16 we know that in a circuit of pure resistor θ_R = 0°, while in a circuit of pure capacitor θ_C = -90°, and in the case of inductor θ_L = 90°. Thus a complex number Z can be introduced to represent the impedance of a complicated circuit with combinations of basic electrical elements R, C, L:

$$Z = R + jX \quad \textit{Equation 2.2}$$

where the real part R represents the resistance contributed by pure resistor element, while the imaginary part X represents the reactance contributed by capacitor and inductor element ($X = |X_L - X_C|$), and j is the imaginary unit. In our study, an impedance meter (HP4192LF, Agilent Co.) is utilized to record (Z, θ) varying by frequency from 0.01 Hz to 2 MHz, and the amplitude of AC oscillation signal is 300 mV. According to Figure 2.17 (a), both real (Z' = R) and imaginary part (Z'' = X) can be calculated by the machine, then we will obtain a Nyquist plot (Z'' versus Z') as shown in Figure 2.17 (b). Different types of electrical element and their combination behaves differently in Z''-Z' character. Notice that non-ideal capacitor is denoted as a constant phase element (CPE), which has a projection on both Z'' and Z' axis. By deconstructing the Z''-Z' data, impedance meter will estimate the intrinsic capacitance value (C_i) of sample, and if C measured as function of bias then it is the so-called "C-V" measurement. Further equivalent circuit analysis can also be conducted with software Zview2 by fitting raw data within a proper frequency range, with maximum iteration of fitting was 1000 times. More details about equivalent circuit analysis are presented in Chapter 4.

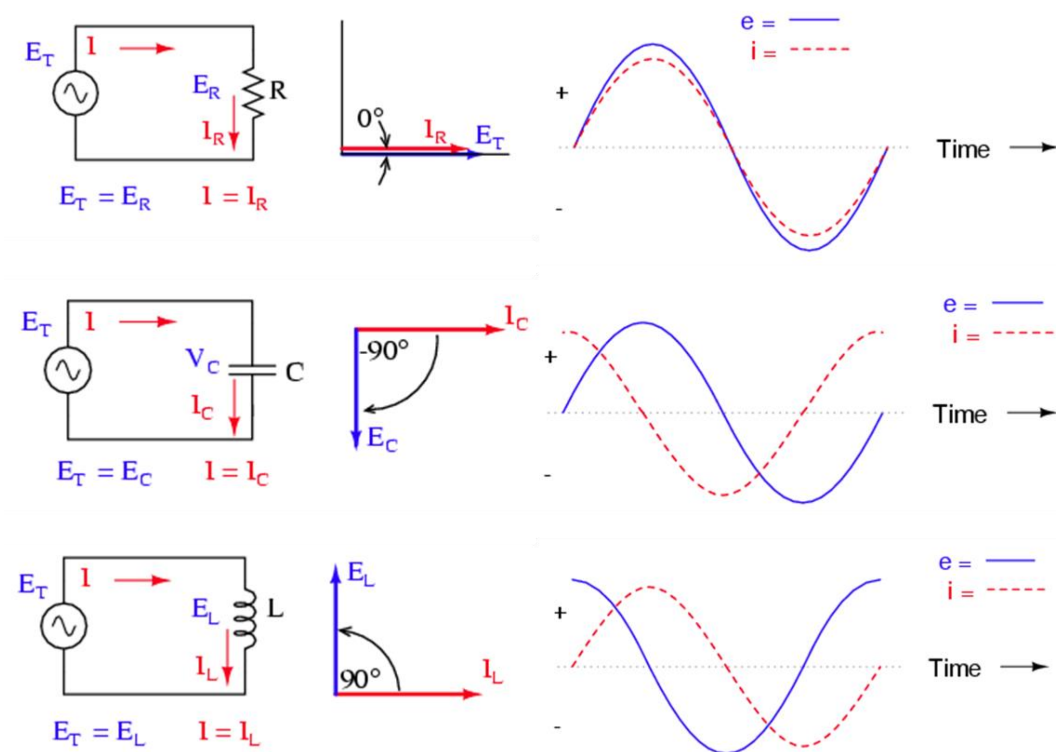

Figure 2.16 Sketches of AC circuit, phase angle and waveform for pure resistor (R), capacitor (C) and inductor (L). Taken from ref.[106]

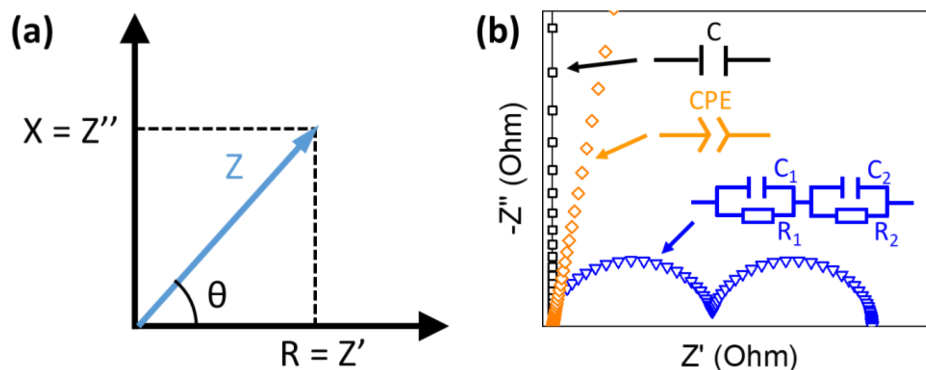

Figure 2.17 (a) A sketch of a complex impedance panel. (b)Typical Nyquist plot (Z''-Z') for ideal capacitor (C), non-ideal capacitor (constant phase element, CPE), and a complicated circuit with parallel resistor and capacitor (R1//C1-R2//C2). Inset with their circuit.

2.2.5.2 Four-probe resistivity measurement

In order to determine the resistivity of thin films in our study, a four-probe measurement (Van der Pauw method) was carried out, by contacting needles on each corners of a square region (length of edge s ≈ 5mm) on the sample as shown in Figure 2.18 (a). With a four-probe systems, we can more precisely measure a real voltage drop across a desired layer, rather than a miscalculation by involving voltage drops on contacts or cables, etc. Input current signal was applied to two contacts on one edge, by using a Keithley 2400 source meter, and meanwhile recording the output voltage (a voltage drops between the other two contacts). In fact the Van der Pauw theorem allows resistivity measurement of arbitrary shape, but sample must be homogeneous, isotropic, thin (ration of thickness versus length $t/s < 1/5$) and without isolated holes[107,108]. Taking a multilayer stack as an example, which was epitaxial grown on a STO (001) with 30 nm bottom metal LSMO and 4 nm insulator BTO above it. Experiment was conducted by deploying probes on sample surface, the contacts are marked with number 1,2,3,4 as shown in the inset sketch in Figure 2.18 (b). First a constant current signal was applied between contacts 1 and 2 (denoted as $I_{1,2}$), so a voltage drop was detected between contact 4 and 3 (denoted as $V_{4,3}$). But considering contacts 4 and 3 were connected to a voltage meter (Keithley 2400), thus no current was flowing in/out the machine through these two contacts, in other words no voltage drop lost on contacts. The potential difference $V_{4,3}$ was due to a current flow in LSMO layer underneath contact 4 and 3 (denoted as $I'_{4,3}$). The resistance in LSMO between contacts 4 and 3 can be calculated by $V_{4,3}/I'_{4,3}$. Although the value of $I'_{4,3}$ is unknown, but it is related to the known

value $I_{1,2}$, and their relation can be mathematically expressed depending on geometry[107]. By gradually changing $I_{1,2}$ from -1 mA to +1 mA, then $V_{4,3}$ varies linearly (see orange data point) indicating that it is ohmic contact. Then doing the same operation by changing the position (input $I_{2,3}$ and output $V_{1,4}$), linear data points (black ones) is shown in Figure 2.18 (b), which roughly overlaps with the orange ones. Finally, the resistivity of the bottom metal layer ρ_{LSMO}(≈ 1mΩ·cm) can be calculated using a simpler equation for infinite 2D sheet[107]:

$$\rho = t \times \frac{\pi}{\ln 2} \times \frac{V}{I} \qquad \text{Equation 2.3}$$

where t is the thickness of LSMO layer, and ration V/I can be extracted directly from the slop. The four-probe measurement was also conducted under laser illumination, see Chapter 5.

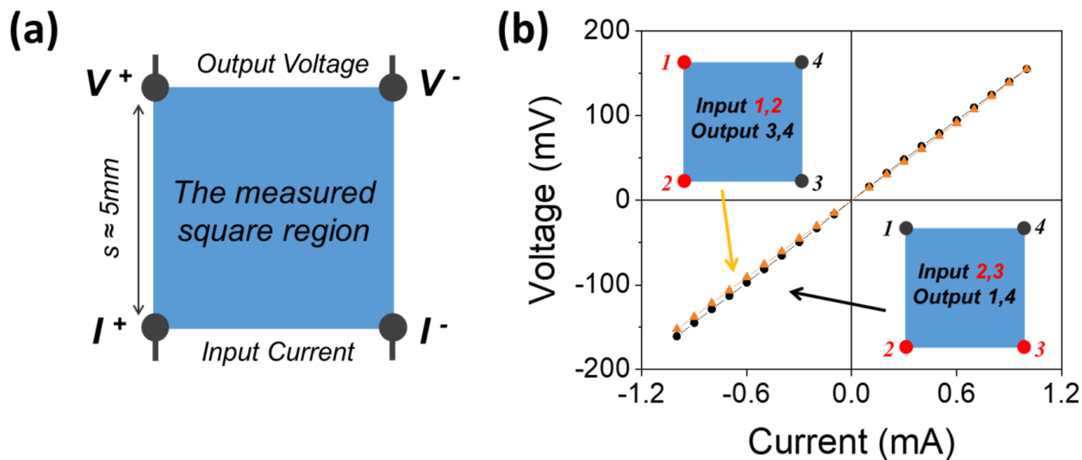

Figure 2.18 (a) Scheme of a four-probe configuration; (b) Representative data of a STO//30 nm-LSMO/4 nm-BTO stack: Recording $V_{4,3}$ as a function of $I_{1,2}$ (orange data points); Or recording $V_{1,4}$ as a function of $I_{2,3}$ (black data points). Inset in (b) shows how measurement was conducted on different position.

2.3 Complementary characterization techniques

In this thesis, complementing the electric characterization, other techniques have been used: X-ray photoelectron spectrum (XPS), X-ray diffraction (XRD), Piezoresponse force microscopy (PFM), and scanning transmission electron microscope (STEM).

2.3.1 X-ray Photoelectron Spectroscopy

The XPS has been regarded as a powerful tool to investigate interfaces[109]. In this section fundamental principles, experimental details and the analysis methodology is introduced.

2.3.1.1 Principle of the technique

A sketch of basic components of a XPS system is shown in Figure 2.19. X-ray is produced by bombarding Al anode with a raster scanned electron gun. Then combining with a quartz crystal, X-ray is monochromatized (beam energy 1486.6 eV). Afterwards, photoelectrons emitted after light interacts with the sample are detected. Usually it can be imagined as a simple three-stage process[110]: (1) X-ray photons interact with the electrons in atomic shell and photoelectrons (and Auger electrons) are generated; (2) the generated electrons partially move through the bulk to surface and are subject to various scattering processes (inelastic scattering), thus loss their kinetic energy; (3) electrons

reaching the surface are emitted in the vacuum after surmounting the work function threshold. Then the binding energy (E_b) can be calculated based on the following equation:

$$E_b = h\nu - E_{kin} - \Phi \qquad \textit{Equation 2.4}$$

where $h\nu$ is the characteristic X-ray energy, E_{kin} is the detected kinetic energy of photoelectrons, and Φ is the work function. Note that in fact Φ results from the work function of both the machine (the so called "analyzer work function") Φ_A and the sample Φ_S. The sample surface is electrically connected to the spectrometer, using a metallic clamp. The work function Φ_A is calibrated and compensated in the XPS system. Thus, the relevant energy relation can be further simplified as follows:

$$E_b = h\nu - E_{kin} \qquad \textit{Equation 2.5}$$

As we know that although electrons on core level does not participate in any chemical reaction, their binding energy shifts when changes occur in valence band (valence state), and this is the so called "chemical shift". Taking an example of hafnium atom, its electron structure is expressed as [Xe] $4f^{14}$ $5d^2$ $6s^2$, in which 5d and 6s orbitals are valence levels while 4f is the core level. The binding energy of Hf 4f7/2 increases when valence levels lose more electrons: 14.13 eV (Hf metallic) → 16.28 eV (Hf^{3+}) → 17.58 eV (Hf^{4+}). It provides explicitly identification of different extent of oxidation or reduction.

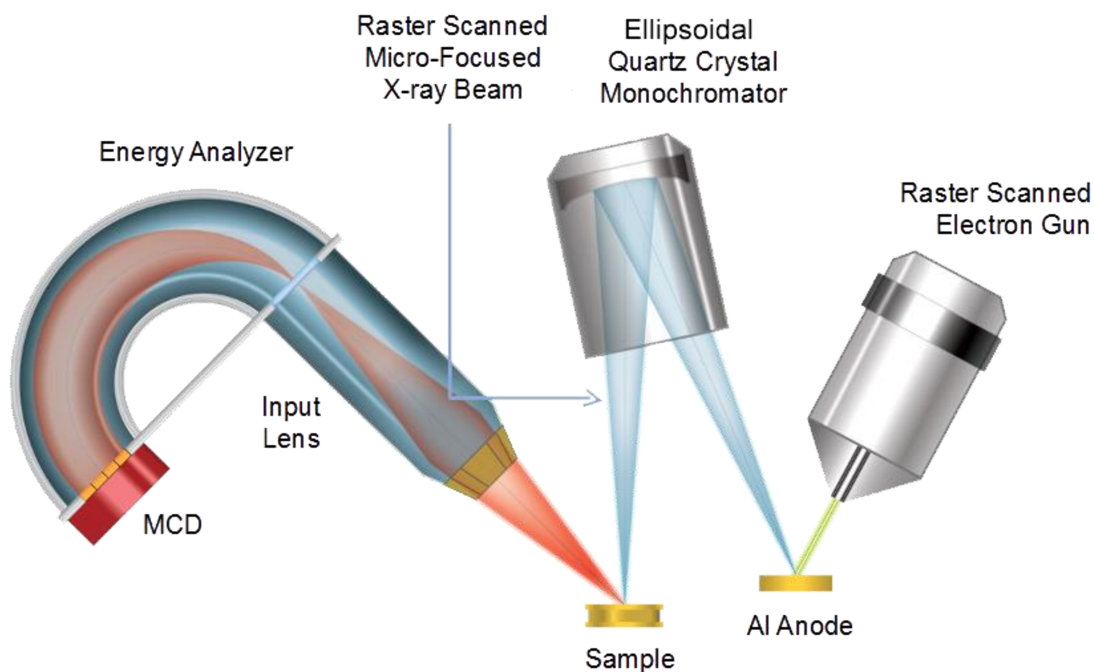

Figure 2.19 Sketch of basic components of XPS system, where MCD is acronym of multi-channel detector. Taken from ref.[111]

2.3.1.2 Experimental details

The results obtained by XPS can be very dependent on three aspects: (1) the X-ray beam on sample projection; (2) the X-ray beam position; (3) the protocol during the pumping process. Apart from that, there is an optional step called "electron flood gun" treatment which helps to remove a potential charge influence. After measurement, a calibration of raw energy data is important for a comparison of binding energy between different samples. Furthermore, the probe depth can be modified by adjusting the relative position (emission angle) of detector to sample, which makes it possible to inspect either deep or shallow regions in a sample.

Measurement setup and preparation: In this thesis, all XPS measurements were performed with a Phoibos 150 analyzer (SPECS GmbH, Berlin Germany) in ultra-high vacuum conditions (base pressure 5×10^{-10} mbar) with a monochromatic Al Kα X-ray source (hv = 1486.6 eV). Measurements were carried out by Dr. Guillaume Sauthier at the Institut Català de Nanociència i Nanotecnologia (ICN2). Samples with Pt electrode deposited on the surface were mounted on the holder by metallic screws. Then X-ray beam should be focused onto the sample surface and cover a desired region. As shown in Figure 2.20, size of our sample is aprox. 5 mm × 5 mm and the projection of X-ray beam is an ellipse with a proper dimension that can either cover the electrode zone or be accommodated in the space between electrode and the edge. In the present thesis, Pt electrodes region has been avoided. Pumping time has been set to 1 hour for all samples.

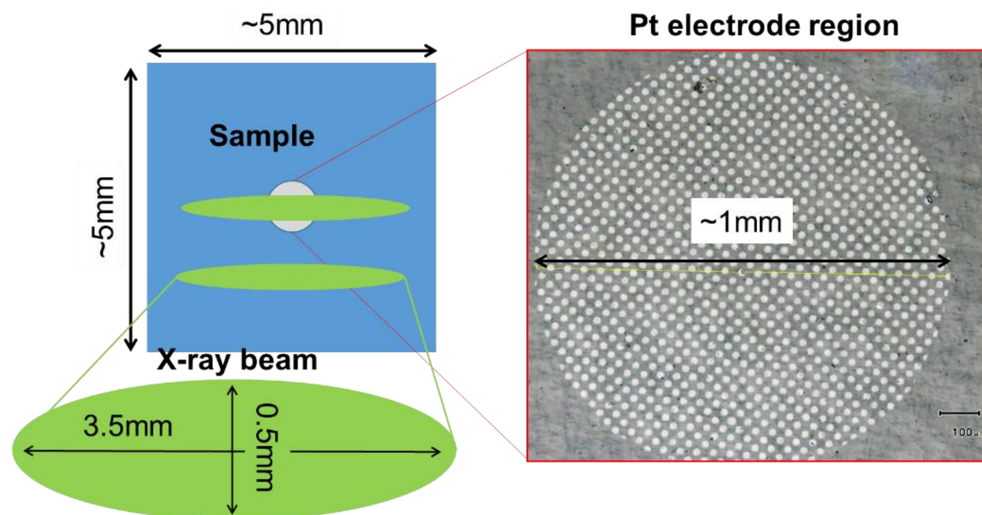

Figure 2.20 Sketch of X-ray beam projection (ellipse, long diameter 3.5 mm, short diameter 0.5mm) on sample (square, ~5 mm × 5 mm), optical microscopic photo shows the central Pt electrode array region (diameter ~1mm).

Flood gun treatment: Flood gun treatment consist on low-energy electrons reaching the surface to compensate for extra charge. This extra charge results in a shift of the collected energy spectra along the energy axis. It has been previously examined by other researchers[112,113] that charge compensation depends on flood gun conditions (voltage, current). Table 2.1 summarizes position of the C 1s peak and its shift (ΔE_b) respect to its tabulated position (E_g = 284.8 eV) depending on different flood gun treatments with time equals to one hour, during the whole measurement process. It can be seen that ΔE_b depends on flood gun conditions, being it smaller for larger input power. For voltage above 7 V and above 0.15 mA the ΔE_b is residual. In Figure 2.21 (a,b) spectra of different samples without and with flood gun treatment are shown. The C 1s peaks are not coincident if no flood gun treatment is done [Figure 2.21 (a)].Instead, it is more close to the expected position, see Figure 2.21 (b), if flood treatment is done. Therefore, as shown in our case, flood gun treatment is efficient to reduce extra surface charging.

Table 2.1 The measured C 1s binding energy (E_b , eV) depending on different flood gun condition, and the relative shift (ΔE_b) compared to a standard C 1s peak (E_b =284.8 eV). Tests done on sample GSO//HZO/AlO_x.

Flood gun condition	C 1s position (E_b, eV)	ΔE_b (eV, to standard C 1s)
No flood gun	285.4	0.6
5V 0.1mA	285.31	0.51
5V 0.15mA	285.3	0.5
7V 0.15mA	285	0.2
9V 0.2mA	285	0.2
10V 0.3mA	285	0.2

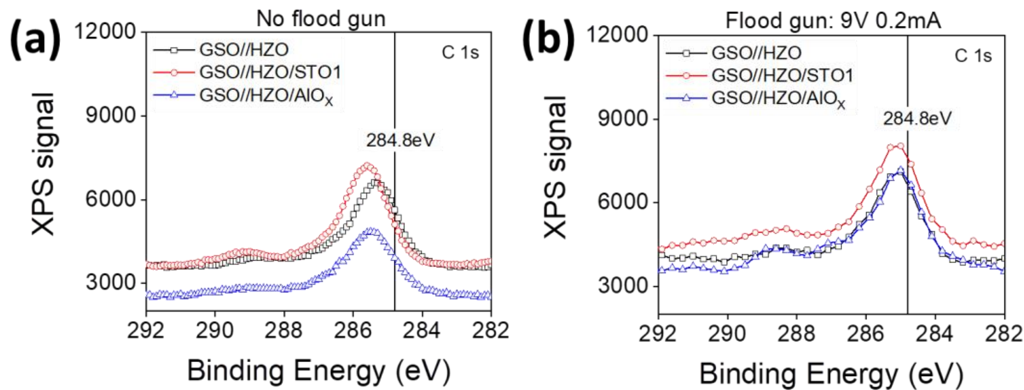

Figure 2.21 A comparison of C 1s peak position shift (to standard C 1s E_b = 284.8 eV): (a) Without flood gun treatment; (b) With flood gun treatment: 9 V 0.2 mA. Tests done on the same group of samples, grown on GSO (001) (pseudocubic setting) substrates.

Emission angle dependent XPS: As illustrated in Figure 2.19, the detector can be placed at certain angle to the normal direction to the sample plane. This emission angle, or sometimes called "takeoff angle", is usually varied in order to modulate the probe depth.[109,114,115] Photoelectrons are generated by X-ray everywhere in a thin film (depth < 10 nm). The photoelectrons travel through the material at expense of reducing its kinetic energy and eventually recombine, Precisely the intensity of detected electrons dependence on sample depth can be expressed by the "Beer-Lambert Law":

$$I_S = I_0 e^{-l/\lambda_{SD}} \qquad \text{Equation 2.6}$$

Here I_0 is the initial intensity of photoelectron, and l represents the distance that photoelectrons travel until reaching the sample surface. The inelastic mean free path (Seah and Dench model)[110] λ_{SD} can be expressed as:

$$\lambda_{SD} = \frac{538a}{E^2} + 0.41a^{3/2}E^{1/2} \qquad \text{Equation 2.7}$$

in which E is the kinetic energy in eV (corresponding to binding energy of core level), while a is mean atomic distance which relates to the intrinsic properties of material (mole mass and density). The inelastic mean free path is a key parameter to describe inelastic scattering.[116] Specifically, the value of inelastic free path for a Hf 4f can be taken as $\lambda_{SD.}$=2.5 nm.[109] In addition, probe depth depends on the emission angle. Then if detector is placed at certain angle, the probed depth will vary as $d = l{\cdot}cos\theta$, as illustrated in Figure 2.22 (a).Hence maximum probe depth diminishes by increasing emission angle, as shown in Figure 2.22 (b) for the case of Hf 4f. At depth = 1 nm only 39% of the generated electrons reach the detector if placed at normal incidence Instead, 70% of the generated electrons at 1 nm are detected if θ = 60°, as shown in Figure 2.22 (c) and (d), respectively. In Chapter 3, we used this angular dependence to better understand the composition dependence on depth.

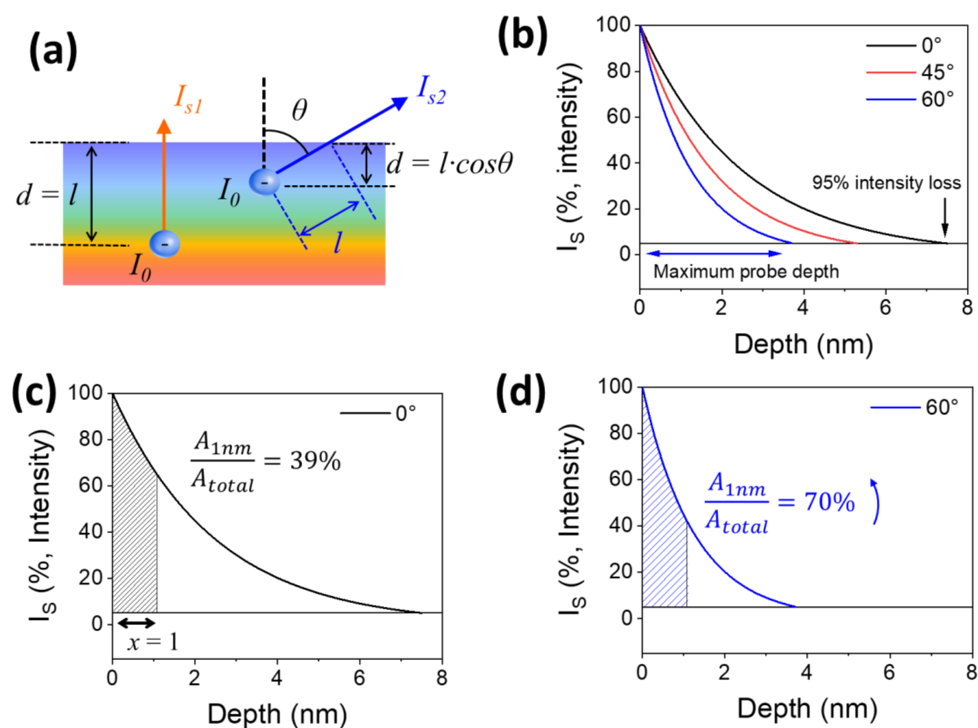

Figure 2.22 (a) Sketch of XPS probe depth with emission angle $\theta = 0°$ and $\theta \neq 0°$, where l represents a distance that photoelectrons travel through the sample, while d represents a probe depth vertical to sample plane; (b) Emission angle dependence ($\theta = 0°, 45°, 60°$) of the attenuated intensity (I_S) respect its value at the surface (c) Integral calculation based on I_S - depth curve ($\theta = 0°$), a proportion of 1 nm shallow area dividing total area is estimated to be 39%; (d) Similar calculation done based on I_S - depth curve ($\theta = 60°$).

2.3.1.3 Data analysis

Binding energy correction: First binding energy is corrected by using either the C 1s line at 284.8 eV or Pt 4f 7/2 line at 71 eV. The carbon is coming from contamination attached on samples as they were exposed to air. Also, as mentioned above in 2.3.1.2, Pt has been deposited on some part of sample surface. Since Pt is one of the least reactive metal, it can be chosen as a reference. In Figure 2.23 we show both C 1s and Pt 4f core level spectrum, standard position are marked with vertical solid lines in each panels. The doublet peaks of Pt 4f (marked as 4f 5/2 and 4f 7/2) in Figure 2.23 (b,d) are due to spin orbit splitting. Unpaired electron left after photoemission has either a parallel or antiparallel orientation to orbital momentum (spin-orbit coupling), thus makes kinetic energy different[110]. Notice that C 1s peak in Figure 2.23 (a) visibly shifts to higher binding energy compared to its standard binding energy line, which is ascribed as an effect by positive surface charges. However, the Pt 4f peak is nearly at the right position (71 eV) as shown in Figure 2.23 (b). Apparently, C 1s and Pt 4f are not equally charged, it seems that positive charges are somehow neutralized for platinum while not for carbon. These variations can be due to different charging in the Pt region (which is at the center)

compared with the C 1s, which can cover all the sample. Note that this energy shift is necessary even in the case that the flood gun is used.

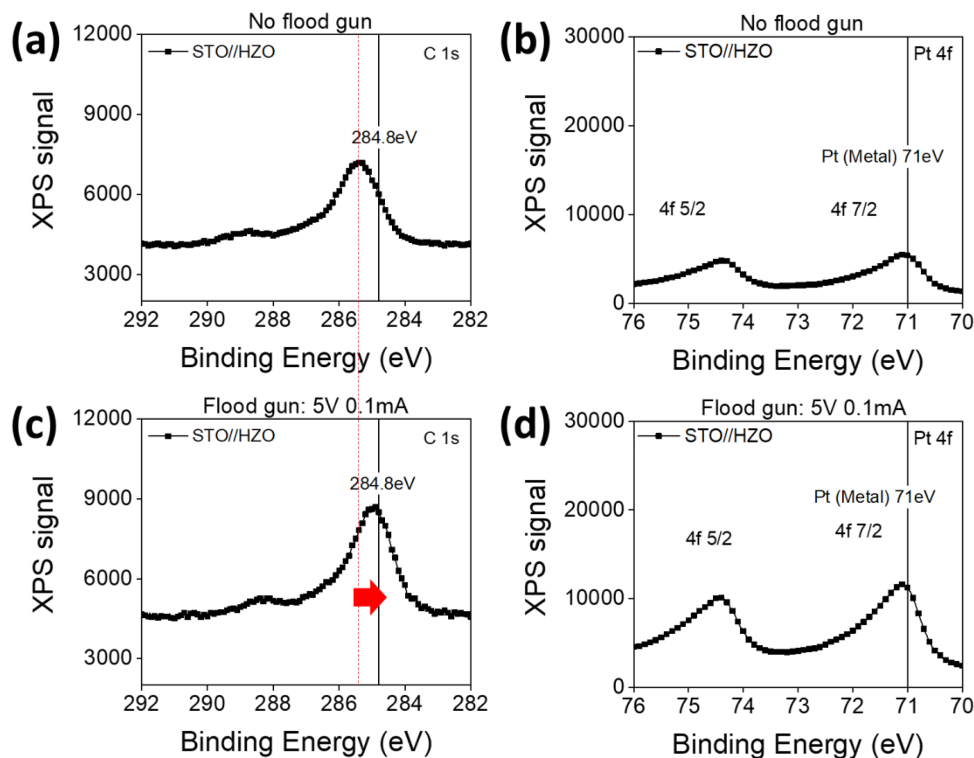

Figure 2.23 Core level spectrum measured without flood gun treatment: (a) C 1s, (b) Pt 4f. And after treated with electron flood gun (5V 0.1mA): (c) C 1s, (d) Pt 4f. The solid line in (a) (c) is corresponding to the standard binding energy of C 1s (284.8 eV). Red dash line represents the original C 1s peak position without flood gun treatment, with red arrow indicating a binding energy shift after the flood gun treatment. Solid line in (b) (d) is corresponding to the standard binding energy of Pt 4f 7/2 (metallic, 71 eV). Doublet peaks in Pt 4f are due to spin orbit splitting.

Subtraction & Normalization: Further treatment to raw data have been done for more precise analysis, including the background subtraction and normalization. Due to inelastic scattering mentioned above, there are more photoelectrons identified as "low kinetic energy" by the measurement system.

These result in the "steps" observed the spectrum. Taking the example of Hf 4f core level spectrum, the background at high binding energy side is higher than at the low binding energy side, as we can see $I_1 > I_2$ in Figure 2.24 (a). Thus, the background signal on both sides must be aligned to the same level. So we used a Shirley algorithm (this is a subtraction method of the used CasaXPS software) to subtract the background (see the blue line in Figure 2.24 (a)). Then for the better comparison between samples with were the different peaks belonging to different species show different intensity due to the presence of capping layers or different thickness, we did a normalization of the peak to its maximum intensity (I_{max}). The Hf peaks of representative samples are shown in the upper panel of Figure 2.24 (b). In the bottom panel of Figure 2.24 (b), the Shirley background shapes for different representative samples are shown. Note that while comparing different samples similar Shirley backgrounds are expected.

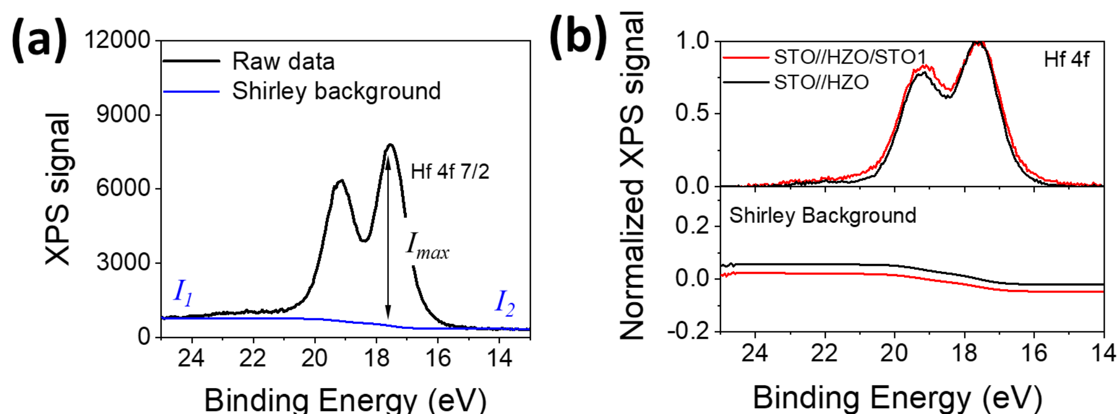

Figure 2.24 (a) Hf 4f core level spectrum of representative sample, raw data and Shirley background. I_1 and I_2 are the background intensity at two sides. I_{max} indicates the peak to background intensity. (b) XPS signal after normalization, Hf 4f spectrum of two different representative samples in the upper panel, and the corresponding Shirley background lines are shown in the bottom panel.

Deconvolution: The XPS spectrum of a metallic cation (Hf 4+, Zr 4+, etc.) can contain contribution of other species. The purpose of an XPS deconvolution is to acquire information of each individual component. The deconvolution curve fitting is performed using Gaussian/Lorentzian ration fixed at 70:30. The full width at half maximum (FWHM) is constrained at the same value with ±0.2 eV fluctuation, and peak position is constrained at standard position according to related references. The fitting is done with CasaXPS software after a proper background subtraction. Taking Hf 4f 7/2 peak as example, the Hf 4+ is at E_b = 17.58 eV, and the reduced specie Hf 3+ should appear at E_b = 16.28 eV in principle. The upper panel in Figure 2.25 is a deconvolution which only contains Hf 4+ (red curves) and apparently the fitting curve (bold black) does not fit well to the raw data points at low energy tail (16 eV to 14 eV). On the contrary, if Hf 3+ component (blue curves filled with color) is added then the fitting quality is improved. By calculating the fraction of Hf 3+ signal dividing total signal that we are able to quantitatively estimate how much percentage (%) of Hf 3+ exists in a certain sample.

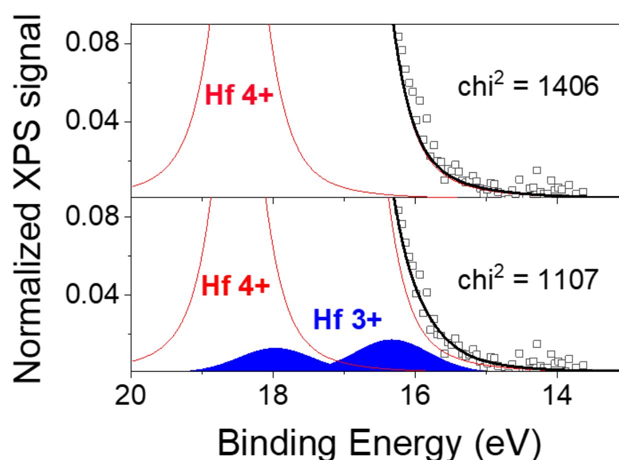

Figure 2.25 XPS fitting quality with different fitting method: upper panel, without Hf 3+; bottom panel, with Hf 3+. The open square data points are the raw data.

2.3.2 X-ray diffraction

The XRD is a widely-used tool to investigate phase composition, thickness and crystal orientation of epitaxial films. The foundation of this technique is based on the XRD.[117] Its principle can be well described with Bragg's law:

$$n\lambda = 2d\sin\theta \qquad \textit{Equation 2.8}$$

where λ is the X-ray wavelength (≈1 Å, comparable to the space in a crystal structure), d is the distance between two adjacent crystal planes, and θ is the X-ray incident angle. -Then the path difference between two X-ray equals to an integer (n = 1, 2, 3 …) multiple of wavelength then by changing the incident angle θ diffraction signal formed from interference will be detected.

θ-2θ scans: the incident angle θ is adjusted by rotating the axis ω (Figure 2.26), meanwhile the motion of the detector (2θ) keeps coupled with the incident beam during the scan, then the diffraction intensity is collected as a function of θ. It is regarded as a proper way to obtain d_{hlk} (*h, k, l* are the plane index) spacing of planes parallel to the surface for a (001) orientation, corresponding to a scan along the (00*l*) family of planes[118]. The θ-2θ scan in this thesis was performed by Siemens D5000 diffractometer with wavelength of λ (Kα1) = 1.54056 Å and λ (Kα2) = 1.54439 Å. The step time is set with 0.2s at each step and the step size is 0.02°.

2θ-χ frame: A GADDS diffractometer (Cu Kα1) equipped with a 2D detector was used to acquire 2θ-χ frames in our work. The dispersion along χ provides information about the film orientation spreading [94].

Pole figures: During this measurement, the system will constrain ω angle at a chosen direction of sample., while other two angles Φ. Here again a 2D detector is used. Pole figure measurement is used to confirm epitaxial relationship of multilayers and to check other possible minor orientations which cannot be distinguished with conventional methods[94]. In Chapter 4 we used a GADDS diffractometer (Cu Kα1) to acquire pole figures around Si, CeO_2, YSZ, LSMO (111) and o-HZO (-111) asymmetric reflection.

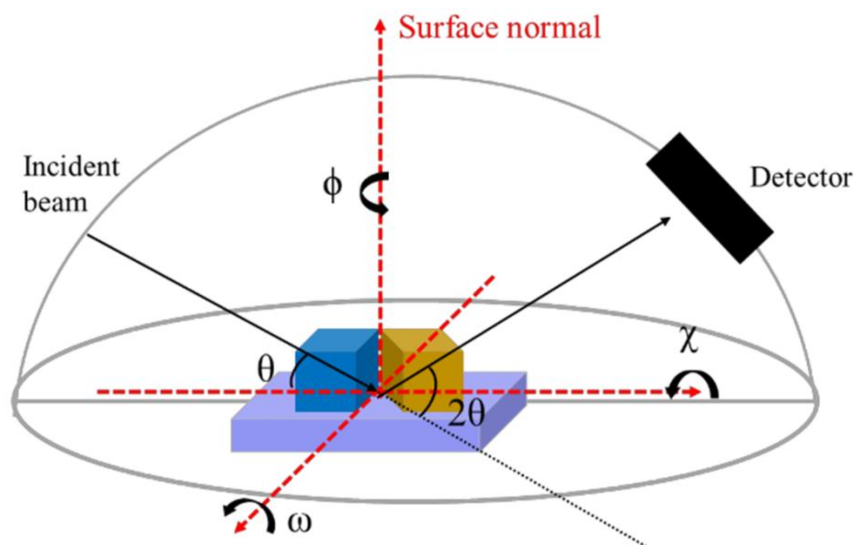

Figure 2.26 Axes and degrees of freedom for rotation in an XRD measurement. Taken from ref.[97]

Thickness calibration with Laue reflection:

Laue fringes in the θ-2θ scans has been used to calibrate and/or measure sample thickness. XRD pattern of a BTO thin film grown on STO (001) substrate is shown in Figure 2.27. Simulations of Laue interference peaks around BTO (002) reflection has been done (see red oscillation) according the dependence of an equation[119] shown as below:

$$I(Q)=\left(\frac{\sin\left(\frac{QN_c}{2}\right)}{\sin\left(\frac{Qc}{2}\right)}\right)^2 \qquad \textit{Equation 2.9}$$

where $Q=4\pi\sin(\theta)/\lambda$ is the reciprocal space vector, N_c is the number of unit cells along out-of-plan direction and c is the interplanar space. For BTO a simulation that well describes the raw data is that using a thickness of 9.8 nm.

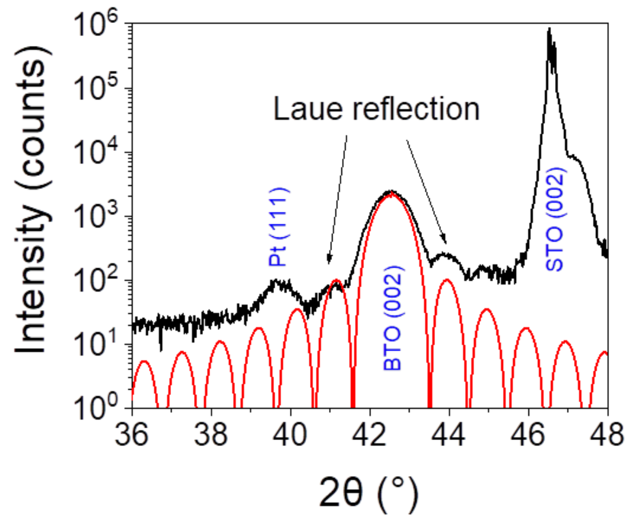

Figure 2.27 XRD pattern of epitaxial BTO film with 300 pulses by PLD. Sample was grown on a STO (001) substrate, Pt was deposited on the surface. Red line is a simulation of Laue interference fringes.

2.3.3 Piezoresponse Force Microscopy

The PFM technique enables non-destructive visualization and control of ferroelectric domain, as well as direct measurements of local physical characteristics of ferroelectrics[120]. By measuring the magnitude and phase from piezoelectric response with PFM, we are able know the polarization state.

The response amplitude is a measure of effective piezoelectric coefficient d_{zz}, which is related to the polarization magnitude, while the polarization direction can be determined from the PFM phase signal[121,122]. In this thesis, all PFM measurements were performed with an MFP-3D ASYLUM RESARCH microscope (Oxford Instrument Co.), using the AppNano silicon (n-type) cantilever with Pt coating (ANSCM-PT-50). The tip radius of the cantilever is less than 25 nm. All required measurements and analysis were conducted by Huan Tan with the equipment located at ICMAB as part of her Ph.D. research project.

2.3.4 Scanning Transmission Electron Microscopy

The STEM is a very powerful and highly versatile instrument capable of atomic resolution imaging and nanoscale analysis[123]. In this technique electron beam is focused by a deflect coil (magnetic lens) in order to have a Å-sized probe[124], then electron beam scanned over and transmitted sample to forms an image, showing internal microstructural features such as grain boundary, second phase, etc[125]. Here in this thesis, high angle dark field imaging (HAADF) was adopted, which is possible to create atomic resolution where contrast is depending on the atomic number (a Z-contrast image)[126]. Also a coupled energy electron loss spectroscopy (EELS) was used, which provides information about elemental distribution at a very low spatial scale (several nanometers)[127]. All analysis about STEM images and EELS maps was done in collaboration with Dr. Saul Estandía and Dr. Jaume Gàzquez from MULFOX group at ICMAB. The microscope used for characterization was a JEOL JEM-ARM200CF operated

at 200 kV, equipped with a CEOS GmbH aberration corrector and a GIF quantum ER spectrometer, at University Complutense of Madrid, Spain. The STEM images were acquired in HAADF imaging mode, and EELS chemical maps were obtained by integrating the characteristic edges of each element at each location. Specimens were prepared using a FEI Helios NanoLab 650. More technical details of STEM can be found elsewhere[128].

Chapter 3. Capping layer impact on ultrathin HZO FTJs

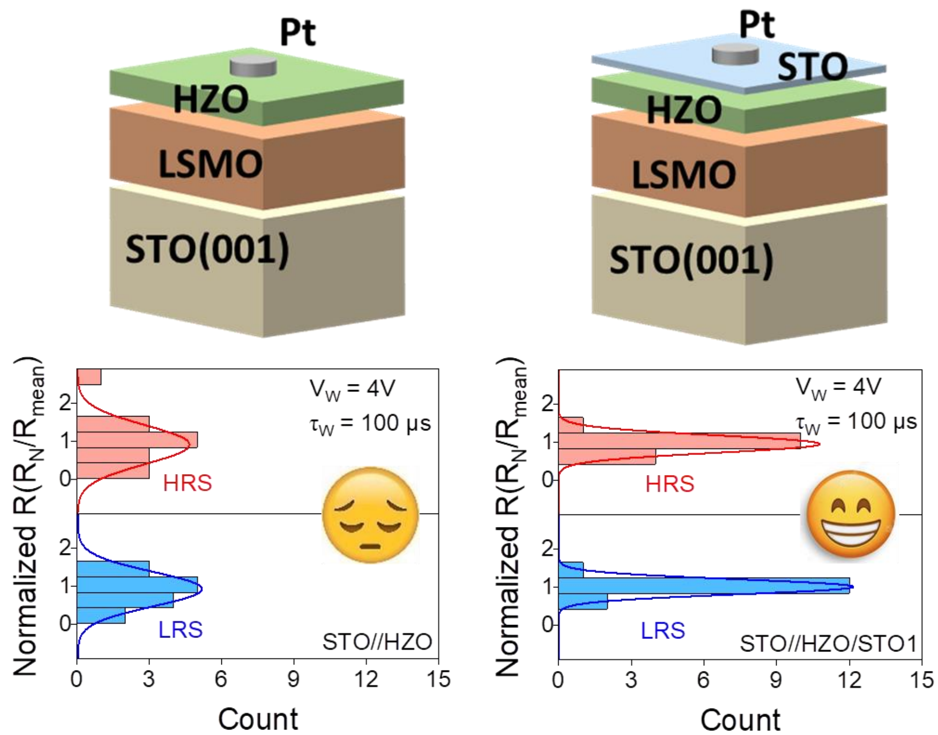

The results of this chapter have been published in “Long, X., Tan, H., Estandía, S., Gazquez, J., Sánchez, F., Fina, I., & Fontcuberta, J. (2022). Enhanced electroresistance endurance of capped $Hf_{0.5}Zr_{0.5}O_2$ ultrathin epitaxial tunnel barriers. *APL Materials*, 10(3), 031114.” from where the figure above is adapted.

3.1 Synopsis

Here in this chapter, it will be shown that capping an ultrathin ferroelectric HZO film (≈ 2 nm) grown on STO and GSO with 1 nm of STO leads to more robust ferroelectric tunnel junctions, where ER displays a larger endurance and higher yield. XPS and STEM data were used to obtain insights into the mechanisms leading to the higher performance of capped devices. It is argued that the primary role of the capping layer is to block conducting channels across grain boundaries.

3.2 Sample

Epitaxial HZO films of 2.2 nm nominal thickness were grown on STO (001)-oriented and GSO (001)-oriented (using pseudo-cubic setting) single crystalline substrates (5 × 5 mm^2) buffered with $La_{2/3}Sr_{1/3}MnO_3$ (LSMO, 22 nm thick) conducting electrodes by pulsed laser deposition (PLD), as described elsewhere.[129] HZO was subsequently capped with a STO layer deposited by ablating a $SrTiO_3$ target at $P(O_2)$ = 0.02 mbar and T_s = 700 °C and cooled to room temperature under $P(O_2)$ = 0.2 mbar. The thickness (t) of the STO capping layer was chosen to be t ≈ 1 nm as controlled by the number of laser pulses on the basis of calibrated growth rates previously determined. Circular Pt top electrodes of 20 μm of diameter and 20 nm of thickness were grown at room temperature through shadow masks by sputtering.

3.3 Results

3.3.1 I-V dependence on capping layer

The junction structure of bare and capped samples is sketched in Figure 3.1 (a)-(c). The reference sample, i.e., in which no dielectric material was deposited between the HZO layer and Pt, is labeled HZO. Films grown on STO and GSO substrates are labeled STO//HZO and GSO//HZO. Ferroelectric characterization by the piezoelectric force microscopy technique of samples grown on STO is shown in the Appendix. 3.1. Samples grown on GSO have been characterized in detail elsewhere.[35] The samples with STO capping (1 nm) are named STO//HZO/STO1 and GSO//HZO/STO1. The I-V curves collected from pristine junctions in STO//HZO and after training cycles are shown in Figure 3.1 (d). It can be observed [insets in Figure 3.1 (d)] that in agreement with earlier reports,[35] the resistance increases after voltage training. A similar trend is observed in the STO//HZO/STO1 capped samples (see Appendix. 3.2), and a less perceptible resistance increase is observed in the GSO//HZO and GSO//HZO/STO1 films (see Appendix. 3.3). Of higher interest here is the impact of the capping layer on the junction resistance. In Figure 3.1 (e) and (f) (main panels and insets), we show the I-V curves collected on trained STO//HZO, STO//HZO/STO1, and GSO//HZO/STO1 samples. It can be readily appreciated that irrespective of the substrate, the resistance after the training is larger in the capped samples (STO//HZO/STO1 and

GSO//HZO/STO1) than in the bare (STO, GSO)//HZO samples, which is consistent with the dielectric nature of the thin STO capping layer.

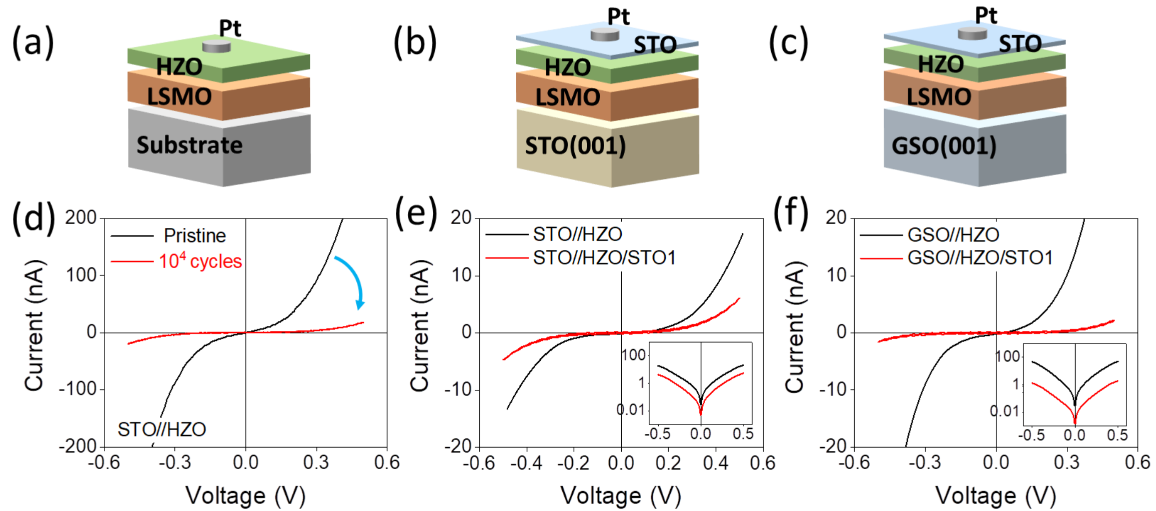

Figure 3.1(a)–(c) Sketches of the junction structure without/with dielectric capping. (d) Illustrative example of the training effect. The I–V characteristics before/after training in the STO//HZO sample. (e) and (f) I–V characteristics of STO//HZO and STO//HZO/STO1 and GSO//HZO and GSO//HZO/STO1 substrates, respectively. Data shown in panels (e) and (f) have been collected in trained devices. The insets in (e) and (f) display data in the semi-log scale.

3.3.2 ER dependence on capping layer

Different resistance states can we written on the junctions by applying writing voltage pulses of different amplitude and polarity. In Figure 3.2 (a), we show the data obtained from STO//HZO (black symbols) and STO//HZO/STO1 (red symbols) devices, electrically written with V_W up to ±20 V and using τ_W = 100 μs. It can be appreciated in Figure 3.2 (a) that a sharp drop of resistance occurs for STO//HZO at some critical writing voltage ($V_{W,C}$ ≈ 10 V). A similar behavior had been reported earlier in thicker HZO (≈ 4.5 nm) films grown on

STO, and it was attributed to a voltage threshold between the polarization-controlled resistance and ionic motion.[130] Obviously, the capped STO//HZO/STO1 (red symbols) sample displays a larger resistance than the uncapped sample. Contrasting with the observations in relatively thicker HZO films (4.5 nm), in this ultrathin HZO barriers, the capping layer does not produce any perceptible increase in $V_{W,C}$.[74] On the other hand, the resistance of GSO//HZO remains robust at least up to $V_W = \pm 20$ V [Figure 3.2 (b)], which is in agreement with the claim that HZO films on GSO substrates have a reduced density of grain boundaries. In addition, the STO capping (GSO//HZO/STO1) increases the overall resistance of the junction.

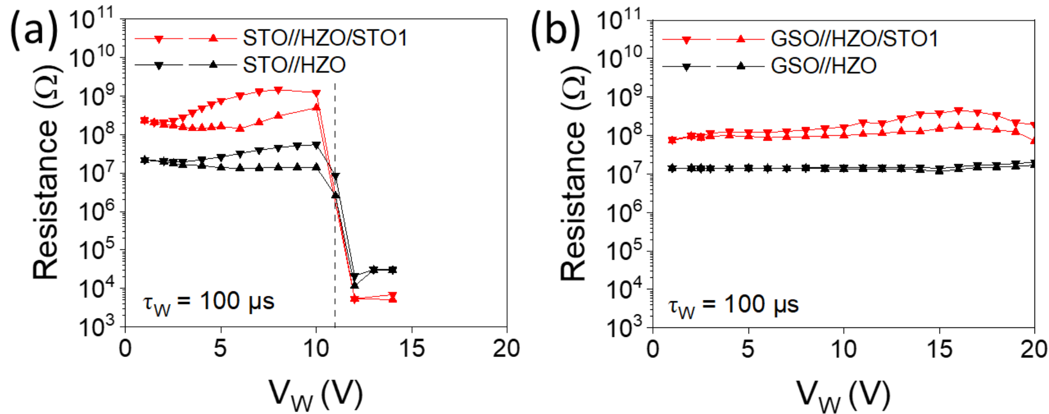

Figure 3.2 (a) and (b) Resistance vs writing voltage (V_W) of bare and capped HZO samples grown on STO and GSO substrates, respectively. Up/Down symbols indicate positive/negative writing voltages, respectively.

Figure 3.3 (a) and (b) display the ER R(Vw) loops collected on trained STO//HZO and STO//HZO/STO1 samples, with $-V_{max} < V_W < V_{max}$, with V_{max} = 2.5 V and V_{max} = 5 V , respectively, and writing times τ_W = 100 μs. Obvious ON/OFF (low resistance/high resistance, LRS/HRS) states develop at about V_W ≈ 2.5 V in all samples. Several relevant observations can be made from the data

in Figure 3.3 (a) and (b): (a) the electroresistance increases with the writing voltage and (b) the insertion of the STO capping layer produces an obvious increase in the junction resistance. As inferred from the data in Figure 3.3 (a) and (b), the ER values range from 112 % (STO//HZO) to 183 % (STO//HZO/STO1). Ambriz-Vargas et al. measured the electroresistance of HZO barriers of similar thickness sandwiched between TiN and Pt. These authors reported ER values as large as 1500%.[131,132] However, the resistance of the junctions[132] was intriguingly smaller by some orders of magnitude than in the present case, challenging understanding and comparison. Recent results obtained in epitaxial films, similarly grown on LSMO and using Pt as top electrodes, show similar resistance values.[133] In polycrystalline HZO, resistance values as large as those measured in epitaxial films are only observed in thicker films.[134] This is consistent with the claimed contribution of grain boundaries to electrical transport.

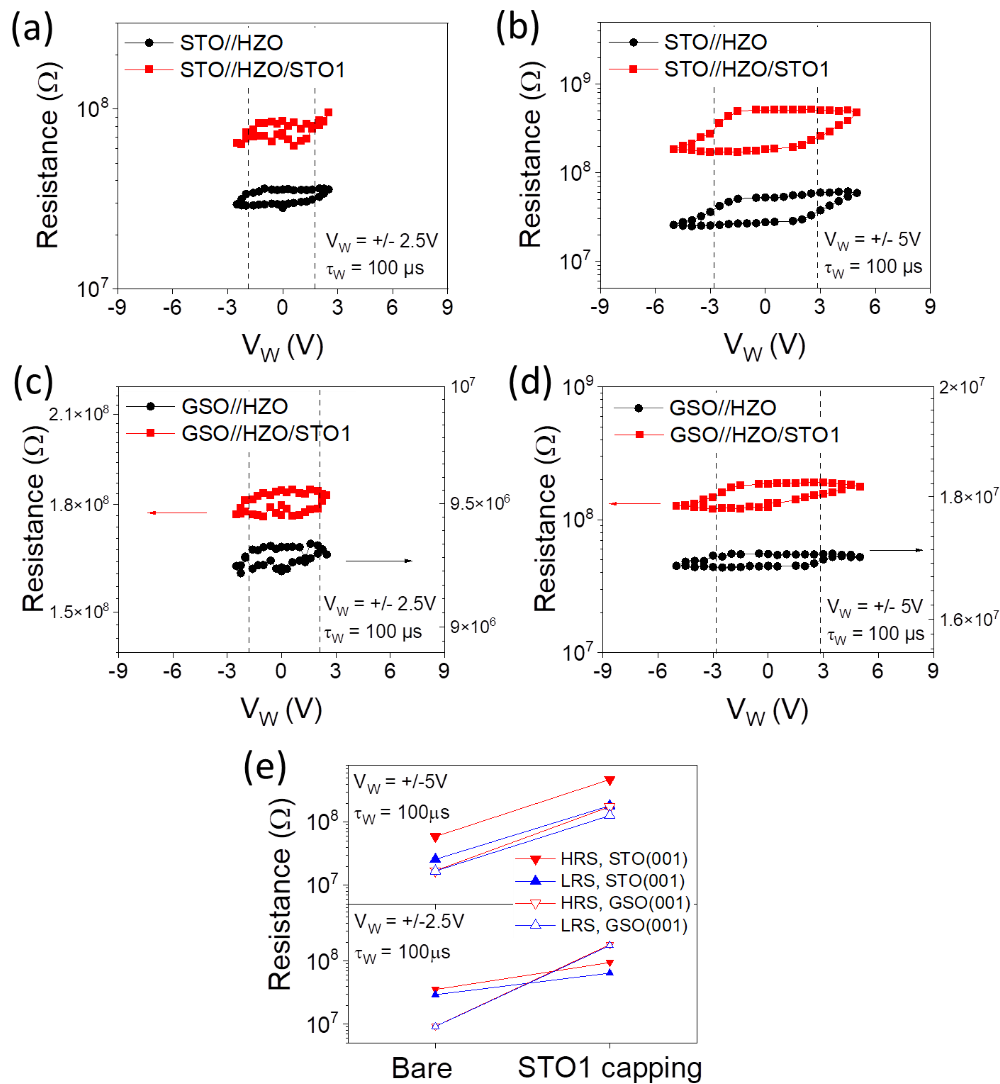

Figure 3.3 Electroresistance of HZO and HZO/STO1 grown on (a) and (b) STO and (c) and (d) GSO, electrically written with V_{max} = 2.5 V (a) and (c) and V_{max} = 5 V (b) and (d), respectively. (e) Comparison of LRS and HRS states obtained after V_W writing of bare and capped samples.

3.3.3 Enhanced yield/endurance with capping layer

Figure 3.3 (c) and (d) show the electroresistance of GSO//HZO and GSO//HZO/STO1 samples. It can be appreciated that the impact of the writing

voltage is similar to that observed for HZO on STO substrates [Figure 3.3 (a) and (b)]. However, it is apparent that the beneficial role of the STO capping is less perceptible. This observation suggests that the STO capping layer has a major impact on the charge transport along grain boundaries which are more abundant in STO//HZO than in GSO//HZO. Note that GSO//HZO shows smaller resistance (9.3 ~ 17 MΩ) and electroresistance (0.8 % ~ 1.2 %) than similar samples reported elsewhere,[35] probably due to the strong thickness dependence of tunneling current and small differences on the samples' thickness. Data reported above show that STO capping of both STO//HZO and GSO//HZO samples increases the overall device resistance as summarized in Figure 3.3 (e), where LRS and HRS for samples with and without the capping layer grown on both STO and GSO substrates are shown.

Next, we turn to inspect the role of the capping layer on the variability of ER from junction to junction (up to 15 junctions have been measured) on the same sample. Raw data of ON and OFF (LRS and and HRS) resistance states written on junctions on bare STO//HZO and on STO//HZO/STO1, respectively, are included in the Appendix. 3.4. The most illustrative results are depicted in Figure 3.4 (a) and (b) where we show the distribution R_N/R_{mean} of the recorded values, where R_{mean} is the mean value of the resistance distribution $\{R_N\}$ for STO/HZO and STO//HZO/STO1. The data clearly show that capping with the STO dielectric allows us to reduce the spread of resistance values of the tunnel junctions in the device. Note that ER has been measured with the contact tip directly placed onto the electrodes. Therefore, it cannot be excluded that the observed higher reproducibility of the resistance states in the capped devices might also be affected by the different mechanical stabilities of the capped device. Simultaneously, the endurance is definitely enhanced as illustrated in

Figure 3.4 (c) and (d). Indeed, the obvious degradation of the LRS/HRS states and their resistance contrast in the junctions on the bare STO//HZO [Figure 3.4 (c)] film is dramatically improved by the STO capping [Figure 3.4 (d)]. Note that in the STO//HZO/STO1 samples, the resistance increases while cycling, probably owing to the same mechanism that produces the increase in the resistance during device training. Similarly, as observed in Figure 3.5 (a) and (b), the spread of resistance values among different HZO junctions grown on GSO is also reduced by STO capping. The corresponding raw data are included in the Appendix. 3.5. Instead, the endurance of junctions on GSO/HZO/STO1 [Figure 3.5 (d)] is similar to the uncapped GSO/HZO sample [not perceptible ER is observed in Figure 3.5 (c)].

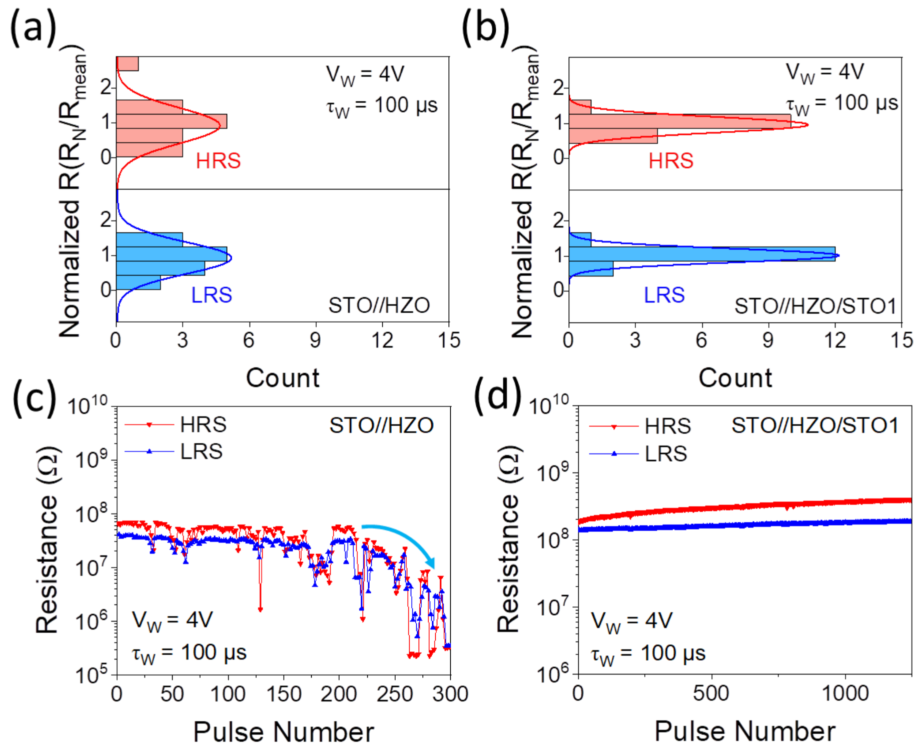

Figure 3.4 (a) and (b) Distribution of the normalized LRS and HRS resistance values (R_N/R_{mean}) measured in a set of 15 junctions on STO//HZO and STO//HZO/STO1 samples, respectively. R_{mean} is the mean value of the $\{R_N\}$

distribution. (c) and (d) Endurance of the representative junctions on STO//HZO and STO//HZO/STO1 samples, respectively, measured up to 300 writing/reading cycles for the STO//HZO sample and 1250 for the STO//HZO/STO1.

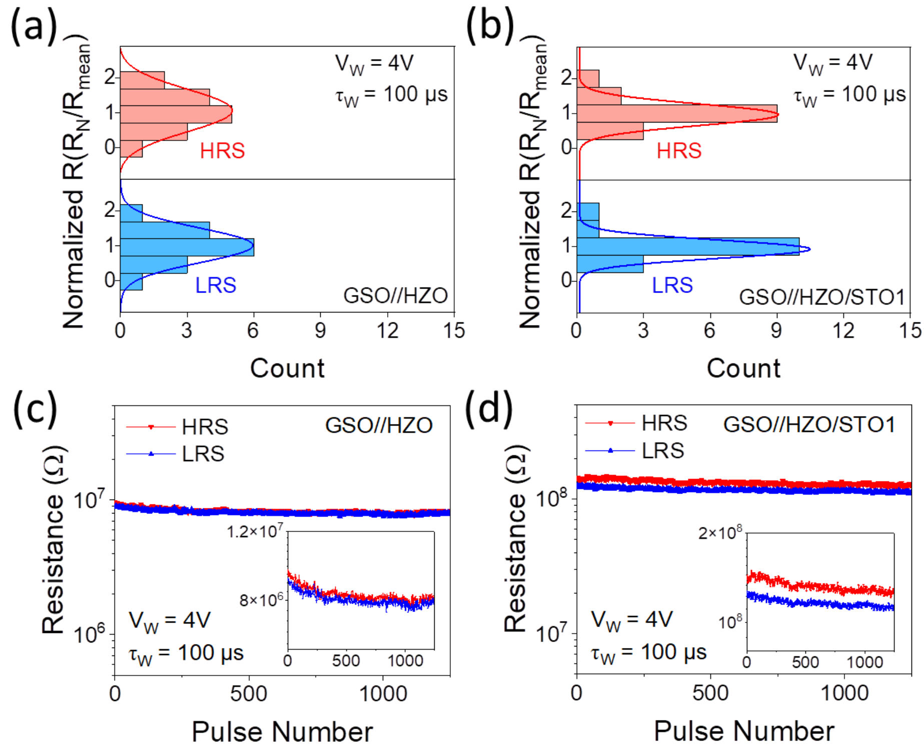

Figure 3.5 (a) and (b) Distribution of the normalized LRS and HRS resistance values (R_N/R_{mean}) measured in a representative set of junctions on GSO//HZO and GSO//HZO/STO1 samples, respectively. (c) and (d) Endurance of the representative junctions on GSO//HZO and GSO//HZO/STO1 samples, respectively, measured up to 1250 writing/reading cycles. Data with zoomed-in view of scales are shown in the insets of (c) and (d).

3.3.4 Composition and microstructural characterization

Aiming at inspecting the electronic configuration of the atomic species at the surface of the bare STO//HZO and STO//HZO/STO1 and GSO//HZO and GSO//HZO/STO1 samples, we have collected the corresponding XPS spectra. To be able to probe different depths under the HZO surface, data have been collected at various emission angles θ (θ = 0°, 45°, and 60°) with respect to the sample normal direction. In Figure 3.6 and (b), we show the Hf-4fcore level spectra of STO//HZO and STO//HZO/STO1 samples. The spin–orbit doublet dominates all spectra, with the Hf-$4f_{7/2}$ line at a binding energy (BE) BE = 17.58 eV, corresponding to Hf^{4+} in stoichiometric HfO_2 compounds.[109,133] The intensity of the Hf 4f lines in STO//HZO/STO is weaker than in the bare STO//HZO sample due to the attenuation of the escaping electrons at the upper STO capping layer. Therefore, to allow for a comparison of the shape of the XPS at different emission angles and on different samples, the measured intensity has been normalized to the maximum of the Hf-$4f_{7/2}$ line. The weak singlet visible at BE = 22.6 eV originates from O 2s core levels. Interestingly, in STO//HZO, the intensity of the O 2s line is clearly more pronounced at normal incidence than at oblique incidence, suggesting that the surface of STO//HZO is somehow oxygen depressed. Remarkably, in STO//HZO/STO1 [Figure 3.6 (b)], this angular emission dependence of the O 2s line disappears, and the explored sample depth appears to be homogeneous in its oxygen contents. To what extent this change reflects a modification (enrichment) of oxygen concentration in the top layers of HZO in the capped sample or simply results from the additional contribution of the O 2s signal from the STO capping cannot be discriminated by these experiments.

On the other hand, the inspection of the lower binding energy edge of Hf 4f is interesting, as the possible presence of reduced Hf species, such as Hf^{3+}, could lead to the emergence of the corresponding core levels, as observed in HfO_{2-x}.[135] Data in Figure 3.6 (a) and (b) show the XPS Hf-4f spectra of the bare HZO film and HZO/STO films. The vertical dashed lines indicate the expected positions of Hf^{4+} and Hf^{3+} lines. A comparison of data in Figure 3.6 (a) and (b) reveals a tiny but perceptible difference in the low energy tail, where the position of Hf^{3+} is expected, which is definitely more pronounced in the capped sample. The Hf-4f core level XPS spectra of GSO//HZO and GSO//HZO/STO show smaller differences (see Appendix. 3.6). Moreover, angular emission dependent data in Figure 3.6 (b) suggest that the Hf^{3+} contribution to the tail is more pronounced when approaching grazing incidence. This can be clearly appreciated in Figure 3.6 (d)-(f), where the deconvolution of the XPS lines into Hf^{4+} and Hf^{3+} (and O-2s) lines is indicated. The observed Hf^{3+}/Hf^{4+} variation implies a richer Hf^{3+} fraction at the HZO/STO interface. Consequently, the interface would be more reduced, maybe due to oxygen scavenging by the grown STO layer (Hf^{3+} contribution quantification is included in the Appendix. 3.7).

The Ti 2p spectra of the capping STO layer have also been recorded at various emission angles [Figure 3.6 (c)]. The Ti 2p spectra displays the spin-orbit doublet $2p_{3/2}$ and $2p_{1/2}$, where the EB ($2p_{3/2}$) = 458.7 eV is characteristic of Ti^{4+}, and the data recorded at various emission angles are coincident. No features suggesting the presence of Ti^{3+} can be detected at any emission angle. The Ti 2p spectra of the STO capping layer are also virtually indistinguishable from those of the bare STO substrates. At this point, it is pertinent to recall that the earlier electron energy loss spectrum (EELS) recorded on (thickness of 4.5 nm)

HZO films capped with STO suggested the presence of Ti^{3+} reduced species at the capping layer,[74] which are not visible in the XPS data of the present HZO/STO heterostructure. In any event, as shown in the following, the capping layer has the benefit of producing a conformal coating of the HZO layer.

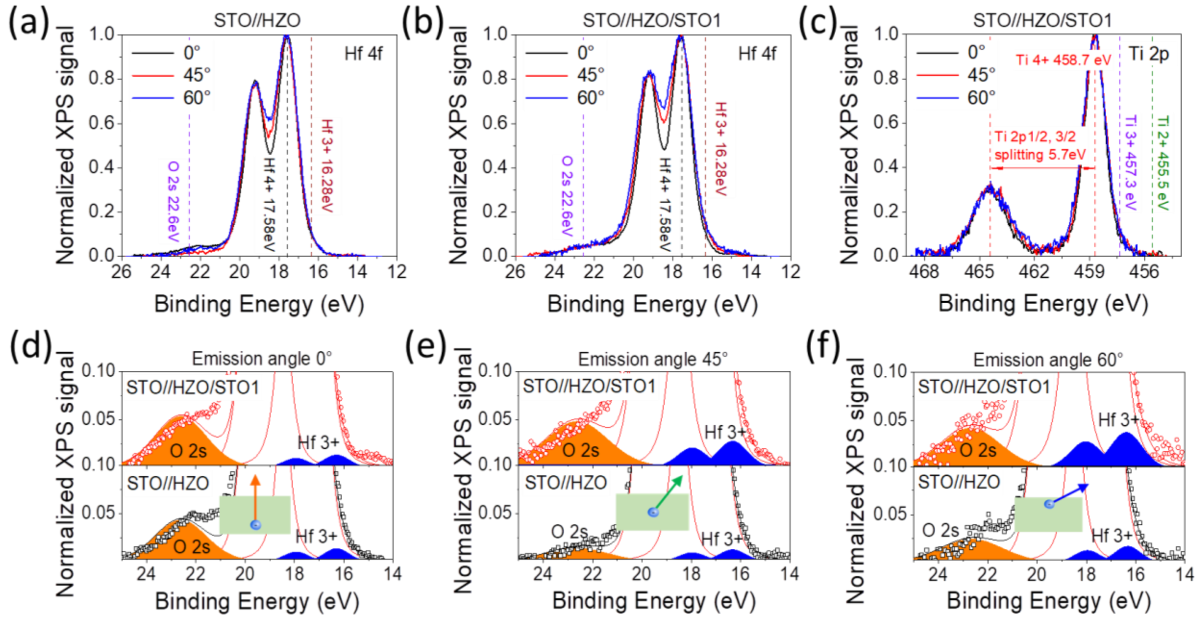

Figure 3.6 XPS Hf 4f core spectra of STO//HZO (a) and STO//HZO/STO1 (b) samples recorded at various emission angles. The vertical dashed lines indicate the expected positions of the Hf-4f$_{7/2}$ line of Hf^{4+} and Hf^{3+} and the position of the O 2s line. (c) XPS Ti 2p spectra collected at various emission angles. The vertical dashed lines indicate the expected positions of the Hf-4f$_{7/2}$ line of Hf^{4+} and Hf^{3+} and the position of the O 2s line. (d)-(f) Zoomed-in view of the XPS spectra recorded at different emission angles, with the deconvolution of Hf^{4+} and Hf^{3+} (blue areas) and O 2s (orange area) lines for STO//HZO (bottom panels) and STO//HZO/STO1 (top panels) samples.

The high spatial resolution provided by aberration corrected STEM allows us to observe the conformal covering of the HZO film by the 1 nm-thick STO capping film. Figure 3.7 (a) shows a cross-sectional high angle annular dark field (HAADF) image where the LSMO bottom electrode (grown on STO), the

HZO film, the STO (1 nm) capping film, and the Pt top electrode can be observed from the bottom to the top of the image. In particular, the conformal covering of HZO by the STO (1 nm) layer becomes evident by superimposing the Ti L-edge chemical map integrated from the corresponding electron energy loss spectrum (EELS) to the HAADF image, as shown in the right side inset of Figure 3.7 (a). Note that the STO capping layer conformably covers the boundaries between the grains (GBs) in the HZO film. Further proof of the high-quality of the stack is provided in Figure 3.7 (b), where the HAADF image and the corresponding Pt-M, Sr-L, Ti-L, Hf-M, and Zr-L EELS chemical maps of a wider horizontal area are shown. The image resolution does not allow us to disclose the crystalline state of the top STO layer. However, STEM images of similar capping on relatively thicker HZO films (4.8 nm) grown under nominally identical conditions allowed us to observe the crystalline nature of the STO capping layer. Therefore, it is likely that the top STO layer here, in addition to being conformally covering the HZO, is also crystalline. Note that in the capped samples, the interface (STO/Pt) should be different than for the uncapped (HZO/Pt) due to defect chemistry, electronic reconstructions, and/or band alignments. Available data, including EELS and STEM, do not allow addressing this issue.

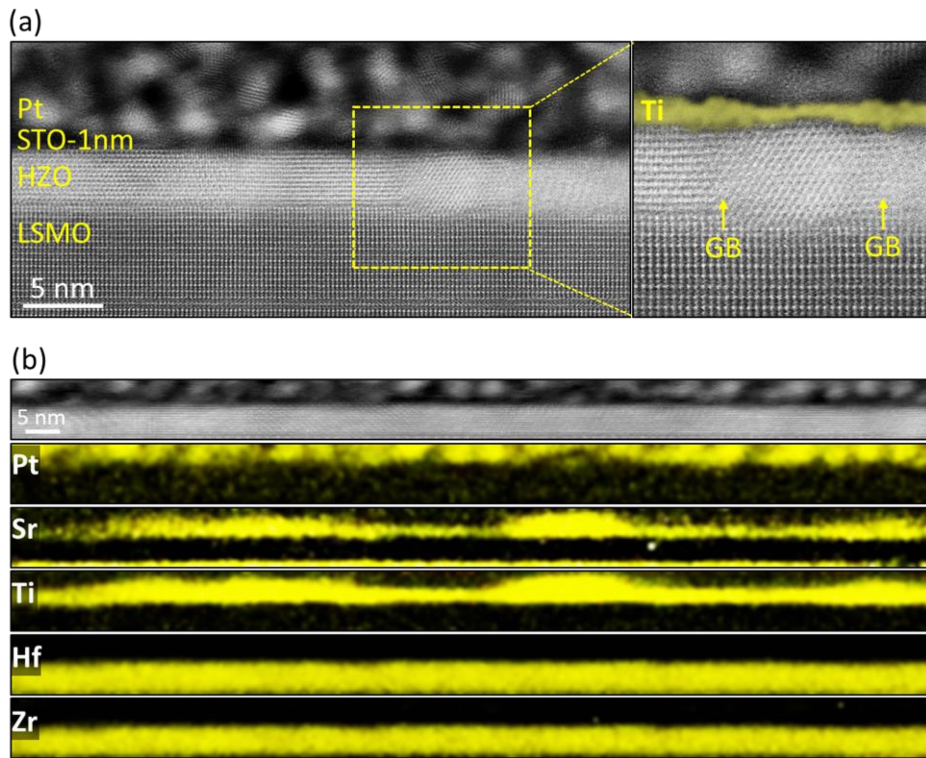

Figure 3.7 (a) STO//HZO/STO1 film. A HAADF image of the LSMO bottom electrode, the HZO film, the STO-1 nm capping film, and the Pt top electrode. In order to clearly image the conformal covering of the HZO film by STO, the right side inset shows an enlarged region with the corresponding Ti L-edge chemical map (in faded yellow) from EELS superimposed onto the HAADF image. The location of the grain boundaries (GBs) is marked with yellow arrows. (b) From the top to the bottom, the HAADF image, Pt, Sr, Ti, Hf, and Zr chemical maps corresponding to a larger horizontal area than the one shown in (a).

3.4 Conclusion

In summary, we have shown that relatively large capacitors (diameter of 20 μm) prepared on epitaxial ultrathin films of HZO, only ≈ 2.2 nm thick, grown on single crystalline STO and GSO substrates display a pronounced ER that

exceeds 150 % at room temperature. Capping these ultrathin films with a dielectric layer (here, STO) of about 1 nm increases the junction resistance. Importantly, the STO capping layer allows us to obtain a higher junction yield in a given sample and a reduction in the spread of the obtained resistance values. Moreover, the endurance of HZO in both structures is clearly enhanced. The picture that emerges is that the capping layer primarily blocks conducting channels across the grain boundaries that exist in the film due to either the presence of different variants of the ferroelectric o-phase or the spurious m-phase, and promotes a higher fraction of reduced species near the top HZO/STO interface region, as observed by XPS. In polycrystalline films, a larger abundance of grain boundaries is to be expected and consequently, a similar strategy can help to mitigate their detrimental contribution to ER and to improve the device performance, crucial for applications.

3.5 Appendix

Appendix. 3.1

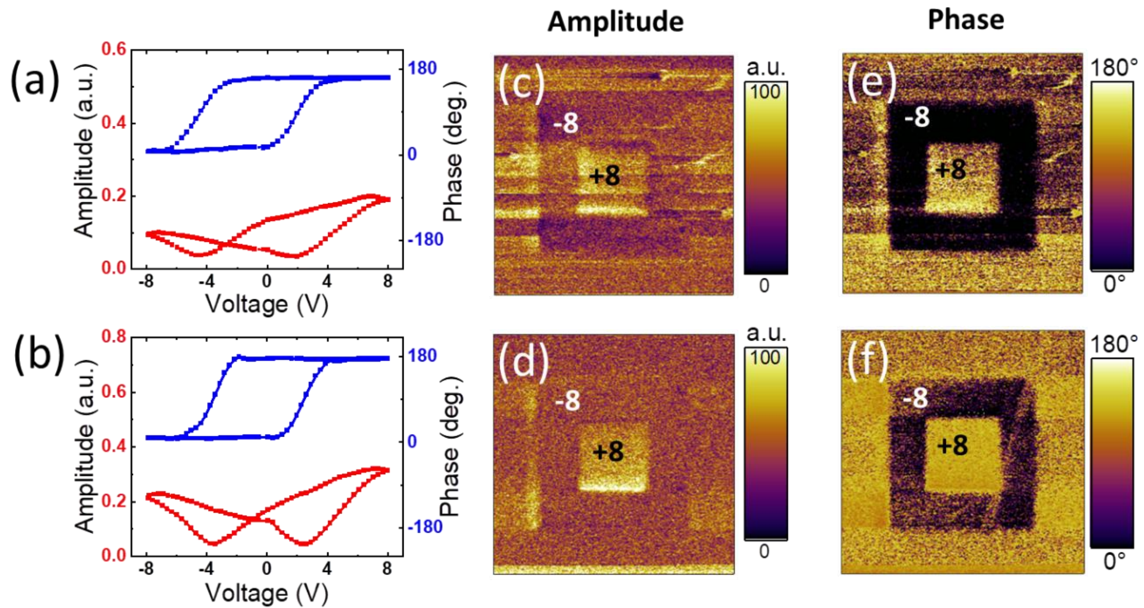

Figure 3.8 (a,b) PFM amplitude and phase loops for the STO//HZO and STO//HZO/STO1 samples. Note that the horizontal shift of the loop along the negative voltage indicates the presence of ferroelectric imprint field. It appears larger than in the case that the ER loops shown in Figure 3a, b, which are measured with large metallic top electrodes, due to the worse contact of the PFM tip. (c,d) PFM amplitude images for the STO//HZO and STO//HZO/STO1 samples after writing with ± 8 V in the indicated regions. The outer region corresponds to the pristine state. (e,f) PFM phase images for the STO//HZO and STO//HZO/STO1 samples showing 180° phase contrast. The performed characterization is fully consistent with the ferroelectric character of these ultrathin films. Note that the fact that similar response is observed in sample where the surface is HZO or STO denotes the absence of important surface chemistry effects, because both materials are expected to have a very different response on this regard. Piezoelectric force microscopy (PFM) measurements were performed with an MFP-3D microscope (Oxford Instrument Co.) using the Budget Sensors silicon (n-type) cantilevers with Pt coating (Multi75E- G). To achieve better sensitivity, the dual AC resonance tracking (DART) method was employed. [B. J. Rodriguez, C. Callahan, S. V. Kalinin, and R. Proksch, Dual-frequency resonance-tracking atomic force microscopy, Nanotechnology 18, 475504 (2007)].[136] PFM voltage hysteresis loops were always performed at remanence using a dwell time of 100 ms.

Appendix. 3.2

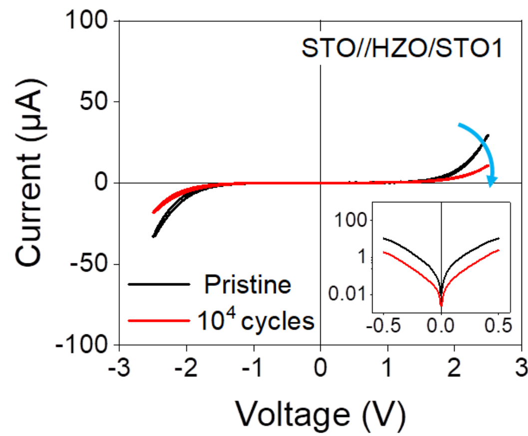

Figure 3.9 I-V of pristine and trained stated of a device in STO//HZO/STO1 sample.

Appendix. 3.3

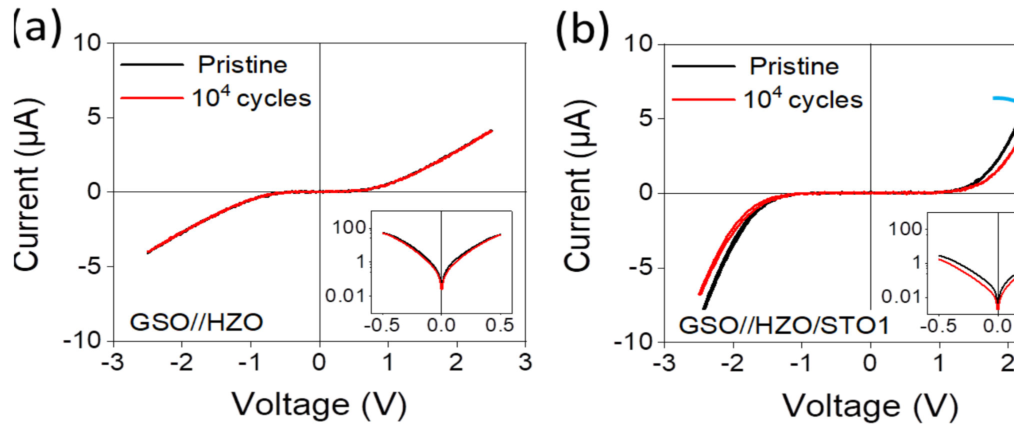

Figure 3.10 I-V of pristine and trained stated of a device in (a) GSO//HZO and (b) GSO//HZO/STO1 samples, respectively.

Appendix. 3.4

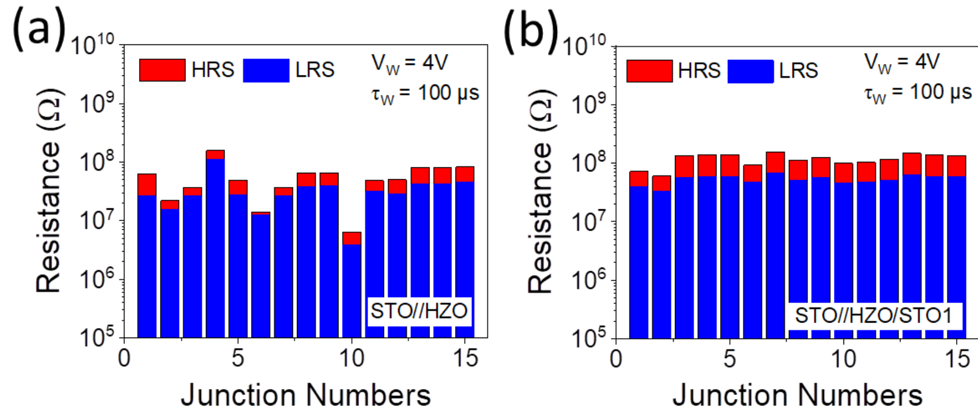

Figure 3.11 Resistance ON (LRS) and OFF (HRS) of 15 junctions of (a) STO//HZO and (b) STO//HZO/STO1 samples, respectively.

Appendix. 3.5

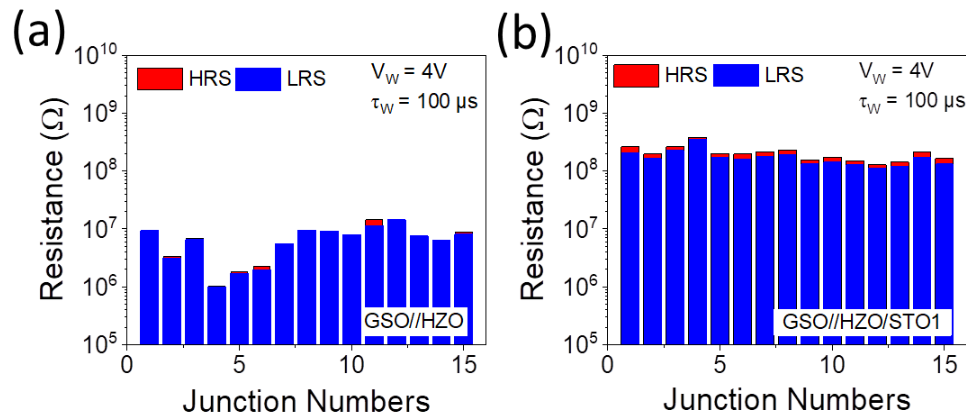

Figure 3.12 Resistance ON (LRS) and OFF (HRS) of 15 junctions of (a) GSO//HZO and (b) GSO//HZO/STO1.

Appendix. 3.6

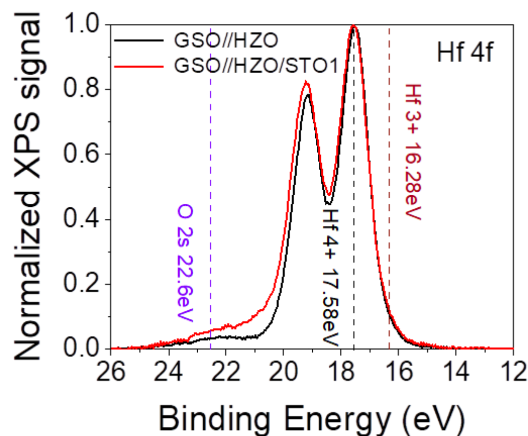

Figure 3.13 Hf 4f XPS spectra of GSO//HZO and GSO//HZO/STO1.

Appendix. 3.7

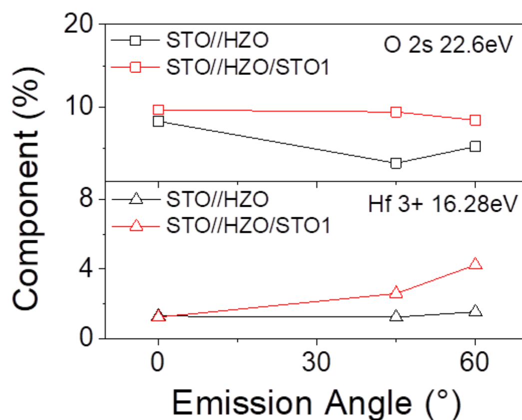

Figure 3.14 Dependence on emission angle of oxygen and Hf 3+ contributions. Whereas oxygen shows a no dependence, Hf is more reduced at the surface in the capped sample.

Chapter 4. Electroresistance after breakdown in HZO FTJs

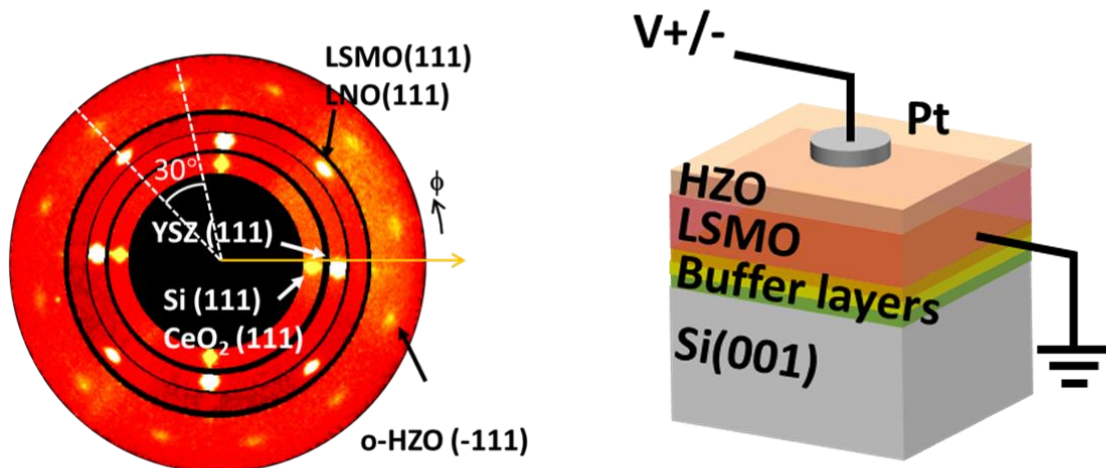

The results of this chapter have been submitted, work entitled "Ferroelectric electroresistance after breakdown in Epitaxial $Hf_{0.5}Zr_{0.5}O_2$ Tunnel Junctions", from where the figure above is adapted.

4.1 Synopsis

In this chapter, we focus on electroresistance of 4.6 nm epitaxial HZO tunnel junctions on Si substrate. Pristine films show a sizeable electroresistance (ER ≈ 57 %) between HRS and LRS respectively and ferroelectric characterization shows that electroresistance results from ferroelectric switching. A soft-breakdown is induced by the application of a suitable voltage pulse, which leads to a drop of the resistance of the device of about 5 orders of magnitude. Despite of the high conductivity, appropriate measurements allow to identify signatures of ferroelectric switching and related ER. In addition, impedance spectroscopy allows to disclose the nature of the conductive channels in the reported epitaxial devices and to determine the changes occurred at and under the electrodes.

4.2 Sample

The multilayer [Figure 4.1 (a)] was fabricated in a single process by pulsed laser deposition (PLD). A complex stack of buffer layers was deposited on Si to achieve subsequent epitaxial growth of HZO. Yttria stabilized zirconium oxide (YSZ), CeO_2, are both grown at the same substrate temperature T_s = 800 ℃ and oxygen pressure $P(O_2) = 4 \times 10^{-4}$ mbar and $LaNiO_3$ is grown at T_s = 700 ℃ and $P(O_2)$ = 0.15 mbar. LSMO, which serves as template for HZO growth and as bottom metallic electrode, was deposited at T_s = 700 ℃ and $P(O_2)$ = 0.1 mbar. HZO was deposited at T_s = 800 ℃ and $P(O_2)$ = 0.1 mbar at a laser repetition

rate of 2 Hz. Top Pt electrodes (20 μm of diameter and 20 nm of thickness) were grown ex-situ at room temperature using a stencil mask by DC sputtering. More details about growth conditions and structural characterization can be found elsewhere.[63]

4.3 Results

4.3.1 X-ray diffraction characterization

The XRD 2θ-χ frame measured using a 2D detector [Figure 4.1 (b)] shows a HZO(111) spot ascribed to the orthorhombic ferroelectric phase. The extracted θ-2θ scan integrated within $\chi = \pm 10°$ angular range, included in the inset, displays the apparent HZO (111) peak. Note that the peak is broad due to the ultrathin character of the layer. θ-2θ scan using point detector (see Appendix. 4.1) were used to determine that a lattice spacing of ≈ 2.962 Å between HZO (111) planes. The 2θ-χ frame does not show presence of any other spurious phase although precedent transmission electron microscopy studies[58] have identified traces of minority monoclinic paraelectric phase. YSZ (002), CeO_2 (002) and LNO (001) spots from the buffer layer are also visible. The LSMO (001) reflection overlaps with that of the LNO which are not resolved in the 2θ-χ scans, although it is distinguishable in the θ-2θ scan using point detector (see Appendix. 4.1). 2θ–φ frame of YSZ (111), CeO_2/Si (111) and LNO/LSMO (111) and HZO (-111) reflections belonging to the different layers is shown in Figure 4.1 (c). The four peaks of YSZ (111) and CeO2/Si (111) are clearly visible. 45°

rotation of the peaks of LNO/LSMO (111) respect to YSZ (111)/CeO_2/Si (111) indicate that the cell of LNO/LSMO is rotated by 45°. LSMO has a fourfold symmetry, and three HZO domains are formed as reported elsewhere.[137] Summarizing, the HZO film is epitaxial and mostly orthorhombic with a minor contribution of a spurious non-ferroelectric monoclinic HZO phase.

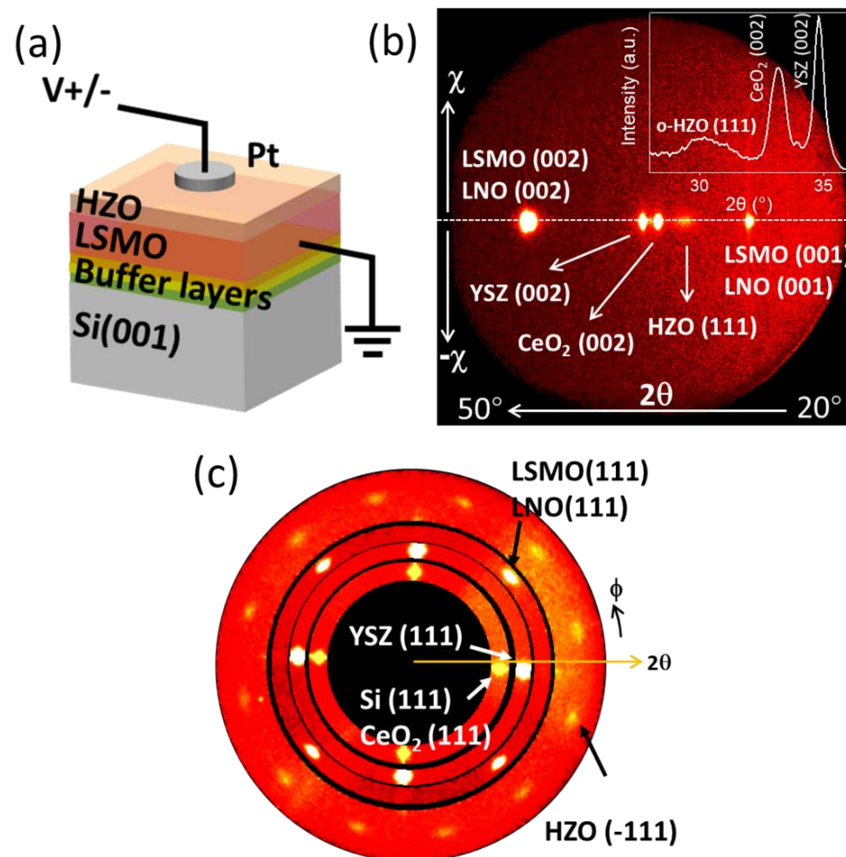

Figure 4.1 (a) Sketch of the 4.6 nm HZO film on LSMO on buffered Si with Pt top electrodes and its electrical contact configuration. (b) XRD 2θ-χ frame and integrated scan of the sample. Integrated along χ scan (±5° around χ = 0°) zoom around HZO (111) is also included, corresponding to θ-2θ scan. (c) XRD pole figure around asymmetric Si, CeO_2 YSZ, LSMO (111) and o-HZO (−111) reflections.

4.3.2 Transport and ferroelectric characterization

Figure 4.2 (a) shows the I-V curves collected up to ±4 V (black), ±8 V (red) and ±6 V (blue), sequentially. It can be observed that during the first loop the conductivity is small and only some hysteresis (negative voltage) is observed. During the second pulse collected up to 8 V, it can be observed a sudden increase of conductivity at near V_{th} = -5 V resembling the conductance increase occurring during the filament formation process in non-ferroelectric HfO_2 films.[138] If increasing voltage is applied following the positive polarity path (green line) no abrupt current increase is observed, instead a reversible hysteresis. Finally, the loop collected up to 6 V shows larger conductivity and clear reversible hysteresis. In Figure 4.2 (b), loop recorded up to 8 V, following the same protocol than for Figure 4.2 (a), is shown while measuring at 1 and 5 kHz. Although the measured current in the loop collected at 5 kHz is larger than at 1 kHz due to the displacive current contribution, no significant changes in the hysteretic behavior of the I-V curves are observed. In Figure 4.2 (c), we show the resistance measured after application of V_W = -1, +1, -2, +2, -3 V, …, using the pulses of the indicated duration. It can be observed that for a 10 μs pulse, which equivalent frequency is 100 kHz, the resistance suddenly decreases at V_{th} = ±5 V, which is consistent with the change of conductance observed in Figure 4.2 (a) and (b). A similar change of resistance has been earlier observed and claimed to be due to ionic motion and concomitant formation of conductive channels.[130] The sudden change of resistance has been also observed in thinner HZO films (t = 2.2 nm, 3.6 nm) (see Appendix. 4.2). However, a somewhat larger $|V_{th}|$ is required in thinner films, probably due to a reduction of defect density by diminishing the HZO thickness. When shorter pulses are applied (5

and 1 μs in Figure 4.2 (c)), the change of resistance is more gradual and occurs at larger V_{th}. The dependence of Vth on pulse width, in the μs time range, is an additional indication of the ionic character of the filament formation.

Next, we explore the ER induced by V_W with $|V_W| < |V_{th}|$, before and after soft-breakdown. Figure 4.2 (d, top) displays the $R(V_W)$ loop collected in the pristine state (without applying any previous electric stimuli to the junction). It can be observed that the electroresistance loop $R(V_W)$ is reversible as expected if ER is due to ferroelectric polarization switching. ER = (HRS - LRS)/LRS, where HRS and LRS are the high and low resistance, is ≈ 53 %, which similar, albeit somewhat smaller, than reported values for similar HZO junctions grown on perovskite substrates, probably due to the different microstructure of the films.[130] Figure 4.2 (d, bottom) displays the $R(V_W)$ loops measured after soft-breakdown, as evident in the much reduced resistance of the device. It can be appreciated that the $R(V_W)$ is still reversible, suggesting that indeed polarization reversal rules the observed ER, which is sizeable although it has decreased down to 3.2 %. Comparing the two $R(V_W)$ loops in Figure 4.2 (d), it is appreciated that that $R(V_W)$ switches from LRS to HRS (and vice versa) at similar voltages (≈ 2 V), suggesting that the coercive field of the ferroelectric HZO has not been modified by the formation of filamentary channels at the soft-breakdown voltage (V_{th}). The observation that both $R(V_W)$ loops in Figure 4.2 (d) are similarly shifted towards the left, indicates the presence of ferroelectric imprint field pointing down, as commonly observed in similar films and ascribed to the presence of defects,[139] that also persists after soft-breakdown. Thinner HZO films (t = 2.2 nm, 3.6 nm) show similar ER loops before and after the breakdown (see Appendix. 4.3).

Before, breakdown stability and good retention of the HRS and LRS states have been reported elsewhere in similar films.[130] After breakdown HRS and LRS are also stable as shown in Appendix. 4.4. Analysis of the I-V curves at low voltage shows that these are compatible with the presence of conduction due to tunneling before and after the breakdown as shown in Appendix. 4.5.

The I-V curves collected in the pristine state [Figure 4.2 (e), right axis] show ferroelectric switching current peak demonstrating the ferroelectric nature of the film, with a background displacive current that naturally increases with measuring frequency. Correspondingly, the P-V loop determined from the integration of the I(V(t)) data (5 kHz) shows clear hysteretic behavior with well-defined ferroelectric switching with remnant polarization 39 $\mu C/cm^2$ and coercive voltage $V_C \approx 1.5$ V. As the ER loop, the P-V loop is also shifted towards the left indicating the presence of downwards (towards LSMO) imprint. Note that the remnant polarization value is overestimated due to leakage contribution visible by the round shape of the loop near maximum applied voltage.[101] Figure 4.2 (f), display the I-V curve collected after the breakdown. It can be first observed that the junctions are more conducting (notice the different current scales in Figure 4.2 (e) and (f)) as expected from the more conducting character of the junction after the breakdown. A remarkable aperture of the I-V loop is also observed. In the Figure 4.2 (f) we include I-V loops collected at increasing frequencies. It can be observed that the mentioned aperture increases with the frequency, reflecting the displacive current contribution and therefore that it is related to the presence of surface charge variation in the capacitor, as observed before breakdown [Figure 4.2 (e)]. Interestingly, in Figure 4.2 (f) it can be appreciated that the $V > 0$ branch of the

loop collected at the highest frequency (10 kHz), displays a current peak, superimposed to the increasing with V current, which indicates ferroelectric switching. The polarization switching peak on the negative V < 0 branch of I-V is not distinguishable due to the large leakage and the presence of imprint field pointing down. Therefore, transport and ferroelectric characterization shows that stable ER and ferroelectricity are present before and after the breakdown and indicates that both show similar features indicating their connection.

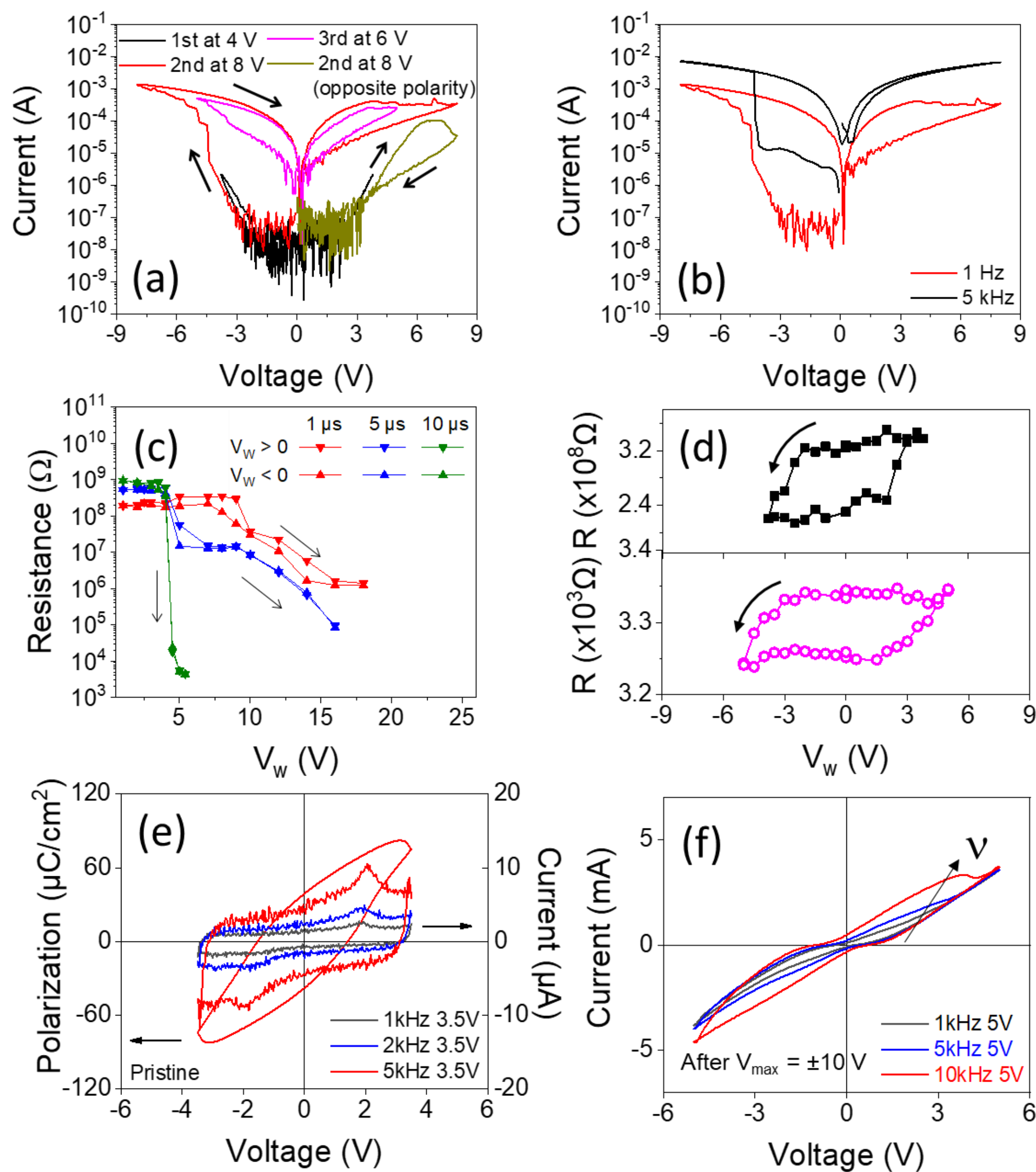

Figure 4.2 (a) I-V loops collected before using at indicated voltages in a consecutive manner. (b) I-V loops collected at different frequency. (c) R(V_W) data of samples with increasing different V_W pulse amplitude and indicated τ_W.(d) ER loop before (top) and after breakdown (bottom). The ER loops are collected at V_{max} = 3.8 V and 5 V respectively (e) P-V and I-V loops collected in the pristine state. (f) I-V loop collected after breakdown.

4.3.3 Impedance measurement and analysis

To get a further insight into the nature of the conductive channels formed after soft-breakdown, capacitance measurements have been performed. Figure 4.3 (a) displays the capacitance as a function of frequency (*f*) recorded in the pristine state of the junction. In the accessible experimental range (3 MHz > 3 kHz), the capacitance (≈ 30 pF) is virtually independent on frequency. Instead, after breakdown, C(*f*) displays a non-monotonic variation and two plateaus emerge, signaling the presence of two different contributions to the dielectric permittivity.[140] Typically, at high frequency, the intrinsic contribution dominates.[141] At low frequency high capacitance is observed, which is usually ascribed to interface effects.[141]

A complementary information can be derived from the Nyquist diagrams (Figure 4.3 (b)) of the impedance before and after breakdown. The arrows in Figure 4.3 (b) indicate increasing frequency. Before the breakdown, an almost vertical straight line indicates that the observed response corresponds to a single capacitor. Data fitting using a single capacitor in series with a resistance (line through data points) gives a capacitance of C_b = 32 pF. The series resistance accounts for the extrinsic contact and wiring contributions. Using $C = \varepsilon_r \varepsilon_0 * A/t$, where A and t are the device area and thickness, respectively, derive $\varepsilon_r \approx 54$ similar to that reported on similar films.[63] After the breakdown two semicircles are observed (Figure 4.3 (b)).

Data before and after breakdown can be well fitted (line through data points) using a simple model circuit of a series arrangement of two parallel resistance/capacitor systems (C_b,R_b) and (C_i,R_i), where the subindex refers to a

bulk (b) and interface (i) contribution as in Maxwell-Wagner model.[140] Here an additional series resistance term has been also included. Before breakdown only single capacitance contribution is observed [see sketch in Figure 4.3 (c)] that we attribute to C_b with very large parallel R_b. Data fit leads to C_b = 33 pF that corresponds to $\varepsilon_r \approx 54$, using the nominal (A and t) geometrical values. After the breakdown the two contributions become apparent. The bulk one (C_b = 19 pF and R_b = 4 kΩ) shows a decrease in both capacitance and parallel resistance compared to that extracted from data of pristine sample [Figure 4.3 (d)]. The interface contributions lead to C_i = 47 nF and R_i = 1 kΩ. Note here that the interface contribution is likely to be present before breakdown although it is not observed in the impedance spectra due to the predominant bulk contribution. After breakdown, the ε_r extracted from the C_i capacitance value (47 nF) of the low frequency contribution is exceedingly large (7.8×10^4) evidencing its extrinsic origin. For the high frequency contribution C_b = 19 pF and $\varepsilon_r \approx 31$ are obtained. Note that similar C(*f*) data trends have been observed in samples with different HZO thickness (t = 3.6 nm, 2.2 nm), as shown in Appendix. 4.6.

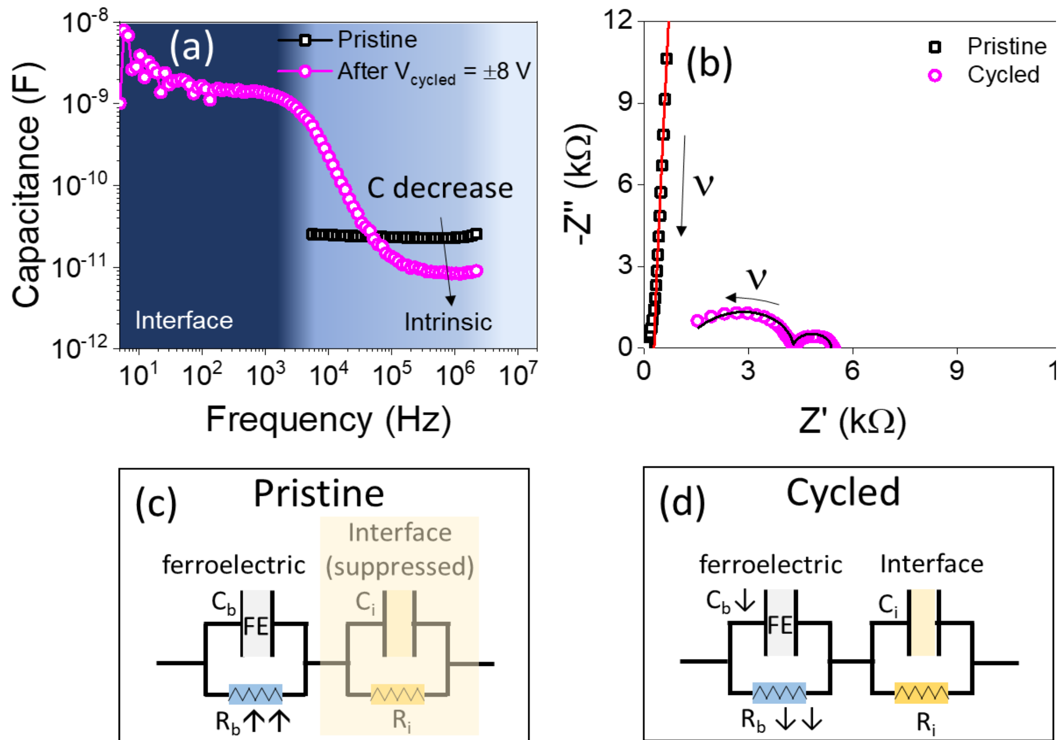

Figure 4.3 (a) Capacitance as a function of frequency in the pristine and cycled states. (b) Nyquist plot of the impedance of pristine and after cycling. Equivalent circuit model for (c) pristine state when ferroelectric capacitor is insulating (Rb ↑↑) and (d) after cycled when ferroelectric capacitor becomes leaky (Rb ↓↓).

The reduction from $\varepsilon_r \approx 54$ to 31 of the bulk contribution to the permittivity of the material after the breakdown, can result from the device heating due to the injected current leading to subsequent orthorhombic-monoclinic HZO phase change. However, XRD temperature experiments of similar films with similar composition have shown that orthorhombic phase is stable at least up to 1000 K,[142] which is much larger to the evaluated temperature increase in similar devices.[143] Therefore, an intrinsic permittivity decrease is unlikely to occur. Alternatively, if the permittivity after the breakdown is fixed to the its value

before breakdown, then, assuming the same contact area A, the effective thickness of the capacitor would be increased up to ≈ 7.7 nm. Similar thickness increase is obtained from C_b contribution derived from C(*f*) of thinner samples as shown by Figure 4.4 (a), where the dependence of the extracted thickness from data fitting is plotted for samples of different thickness. However, such dramatic thickness increase after breakdown does not appear to be well grounded. Therefore, data suggest that after breakdown, most likely the actual area of the capacitor has been modified; more precisely, reduced to account for the observed reduction of C_b. Figure 4.4 (b) shows a wide view optical microscopy image of several top Pt electrodes on the sample. The zoom included in Figure 4.4 (c) shows devices (encircled in yellow) after the breakdown. It can be observed that, at their borders, a darker region appears, which we ascribed to the formation of a higher conductivity region under electrode edges, suggesting that the effective area of the dielectric is indeed reduced. Similar behavior has been observed in other ferroelectric capacitors.[144] Consistently, according to the PFM images [see Appendix. 4.7], the piezoelectric response at the electrode borders is weaker that at its center. To sum up, the sketch of the device after the breakdown is shown in Figure 4.4 (d). It illustrates that, upon soft-breakdown, the ferroelectric intrinsic contribution is preserved, while a conductive region (non-ferroelectric) develops near the electrode borders, probably resulting from the higher electric field at electrode edges. In Figure 4.4 (a), the thickness extracted considering the device area after the breakdown, evaluated as the brighter region in the broken devices of Figure 4.4 (d), is shown as a function of the nominal thickness for three different samples. It is observed that the thickness obtained after the correction is in good agreement with the expected value (red line). Therefore, it

can be concluded that the formation of a conductive ring and the concomitant reduction of the effective area of the ferroelectric results in a decrease of overall resistance and a decrease of the device capacitance, while the dielectric properties of the unperturbed area remain robustly insulating.

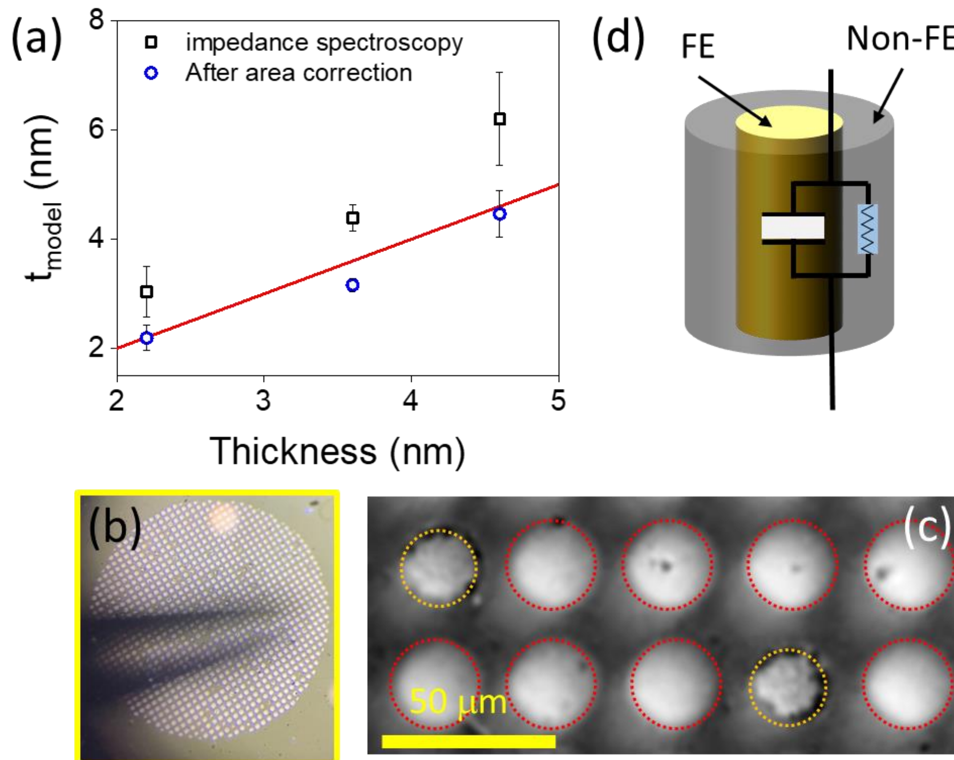

Figure 4.4 (a) Thickness extracted from the data fitting using the procedure indicated in the text versus the nominal thickness of different samples before and after correcting the device are using the area extracted from broken devices shown in panel (c). (b) Wide view of the Pt electrodes. (c) Zoom of the Pt top electrodes. In yellow, broken devices. (d) Sketch of the two ferroelectric and non-ferroelectric contributions extracted from capacitance measurements analysis.

4.4 Conclusion

In conclusion, the I-V curves and electroresistance data of HZO capacitors indicate that a soft breakdown occurs. Data indicate that ferroelectric-polarization related electroresistance exists before breakdown and it persist after breakdown. Besides, a significant reduction of device capacitance is observed after breakdown. Analysis of the frequency-dependent capacitance before and after breakdown, allows to conclude that the formation of a conductive channel under electrodes results in a reduction of the functional effective area and accounts for both the reduction of capacitance and the reduction of its parallel resistance component. Further characterization including optic and PFM response, indicate that the conductive channel forms a ring at the borders of the electrodes. The performed characterization should contribute to the further understanding of the coexisting contributions in ferroelectric HfO_2 tunneling or other devices and also to their better design. In particular, we have demonstrated that targeted capacitance characterization can help to disclose the presence of extrinsic effects. In addition, the observed modulation of the overall resistance level can be useful to develop more optimal device engineering strategies.

4.5 Appendix

Appendix. 4.1

Figure 4.5 shows XRD θ-2θ scans of the as-prepared stack of Si (001)/buffer layer/LSMO/HZO. The pattern shows (00*l*) reflections corresponding to the Si

substrate and the LSMO, LNO, CeO_2 and YSZ layers. o-HZO (111) peak position is around $2\theta \approx 30.14°$ (see the zoomed panel on the right side), indicating that the inter-planar space of $d_{o\text{-}HZO(111)} \approx 2.962$ Å. Notice also that LSMO (00*l*) overlaps with one of the buffer layer LNO (00*l*).

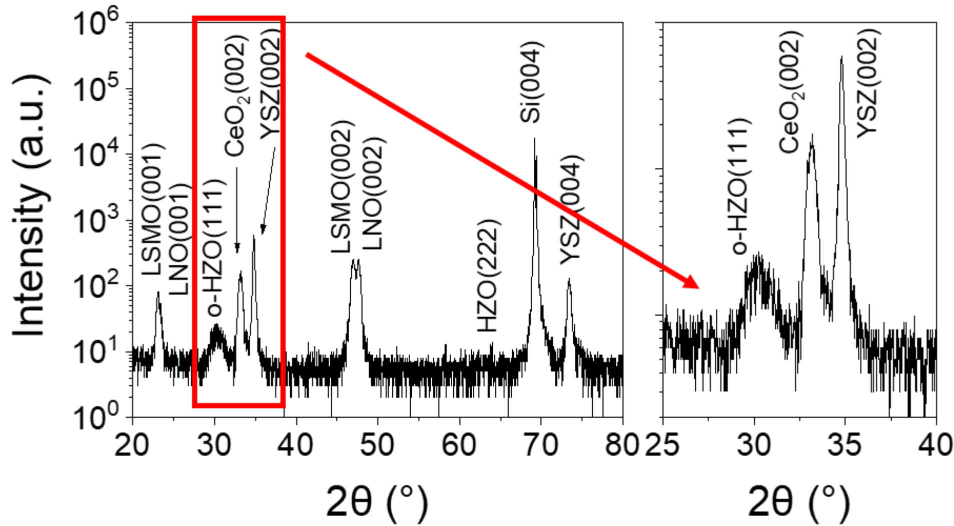

Figure 4.5 XRD θ-2θ scans of a Si(001)/buffer layer/LSMO/HZO stack in range of 2θ = 20° ~ 80°, with a zoomed region around the HZO (111) (2θ = 25° ~ 40°).

Appendix. 4.2

Resistance data was recorded as a function of writing voltage respectively for HRS and LRS for samples with different HZO thickness (Figure 4.6). This measurement was conducted by prepoling samples following a sequence: $V_W = \pm 1$ V, ±2 V, ± 2.5 V, etc. For samples of t = 4.6 nm and t = 3.6 nm, this V_{th} is roughly around ±4.5 V; however, for the thinnest sample t = 2.2 nm, $V_{th} \approx \pm 7$V. The tendency of increasing threshold voltage with HZO thickness is consistent with the information shown in Figure 4.6.

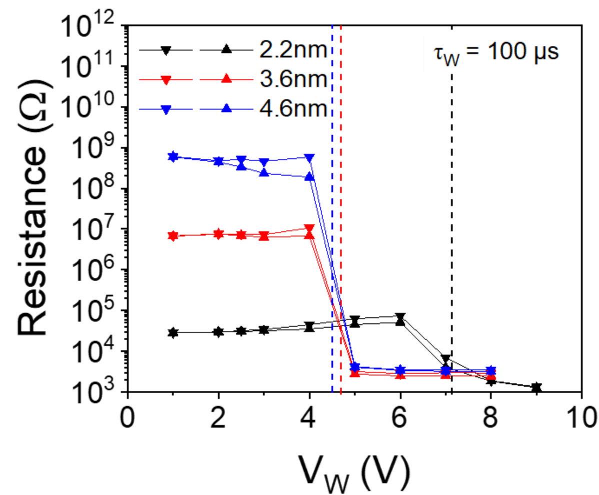

Figure 4.6 R(V_W) data of samples with different HZO thickness (t = 2.2, 3.6, 4.6 nm). The down triangle symbol (▽) represents positive prepoling while the up triangle symbol (△) represents negative prepoling. The writing time for all prepoling are the same τ_W = 100 μs.

Appendix. 4.3

R(V_W) loops before and after the soft-breakdown are shown for samples of t = 3.6 nm and 2.2 nm in Figure 4.7 (a) and (b), respectively. The ER in the sample t = 3.6 nm changes from ER = 26 % to ER = 9.8 % [Figure 4.7 (a)], while in sample t = 2.2 nm it changes from ER = 33 % to ER = 1.6 % [Figure 4.7 (b)].

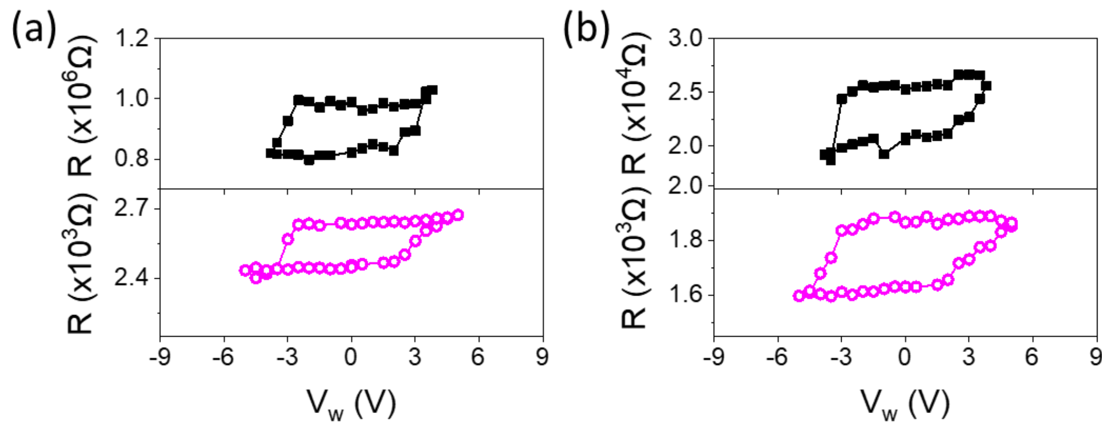

Figure 4.7 R-V loops collected up to V_{max} = 3.8V, 8V and 5V sequentially in samples with different HZO thickness (a) 3.6 nm and (b) 2.2 nm. And zoomed loops of the 1st (top) and 3rd (bottom) collected respectively for two samples (a) 3.6 nm and (b) 2.2 nm.

Appendix. 4.4

The HRS and LRS states dependence on τ_W is shown in Figure 4.8 (a). It can be observed that for V_W of 5 V the HRS and LRS are well-defined and stable as expected from the fact that these result from different ferroelectric polarization states as discussed in the main text. This is ascribed to the presence of ionic mechanisms involved on the resistance drop. For V_W = 8 V, the HRS and LRS states start to open above 100 µs, highlighted as the slow region. This aperture is most probably related to the ionic motion, which is expected to be more prominent while applying longer pulses as already observed in other ferroelectric films. Regarding endurance experiments for V_W = 5 and 8 V and fix τ_W = 100 µs, the resistance contrasts up to 200 cycles is stable [Figure 4.8 (b)], although for V_W = 8 V the variability is larger.

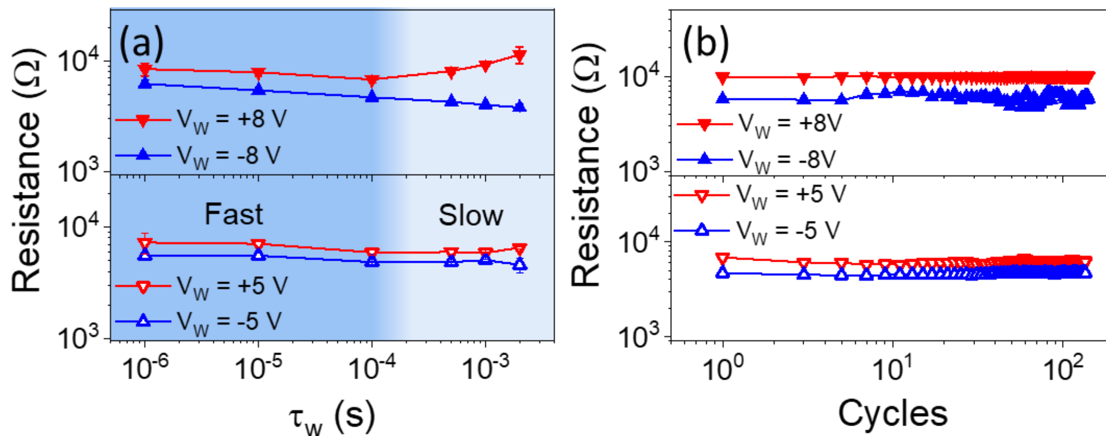

Figure 4.8 (a) Resistance after application of V_W of indicated amplitude versus τ_W. (b) Resistance after application of V_W of indicated amplitude versus cycles of amplitude V_W , τ_W = 100 μs in the collected data of (a) and (b).

Appendix. 4.5

We now try to disclose the conduction mechanisms in the explored system. Figure 4.9 (a) shows the dependence of the resistance states versus thickness. The observed exponential dependence suggests tunneling current as a possible conductance mechanism. After the breakdown, although final values of resistance show some dispersion accounted by the error bar of the plot, which has been calculated by the standard deviation of the collected resistance values, a similar exponential dependence is observed. Similar conclusion can be extracted from the I-V characteristics analysis. In Figure 4.9 (b), the I-V curves after prepoling the sample with + or - 5 V (as indicated) are shown. It can be observed that the curves show sigmoidal shape. Lines through data points correspond to the Brinkman model fitting.[50] The obtained parameters are summarized in see Table 4.1, which show reasonable agreement with the literature.[74,145,146] In Figure 4.9 (c), the I-V curves after prepoling the sample with + or - 5 V after breakdown are shown. It can be observed that the contrast between both curves is smaller in agreement with the observed smaller ER. After breakdown, it can be observed larger conductivity, which indicates the presence of a metallic-like channel. In fact, Brinkman model fitting results in smaller barrier height and thickness, as expected by the fact that the conductive channel would cause an extrinsic reduction of these parameters (Table 4.1). The obtained parameters from data fitting are nearer to the expected ones, if a parallel resistance is considered (Table 4.1).

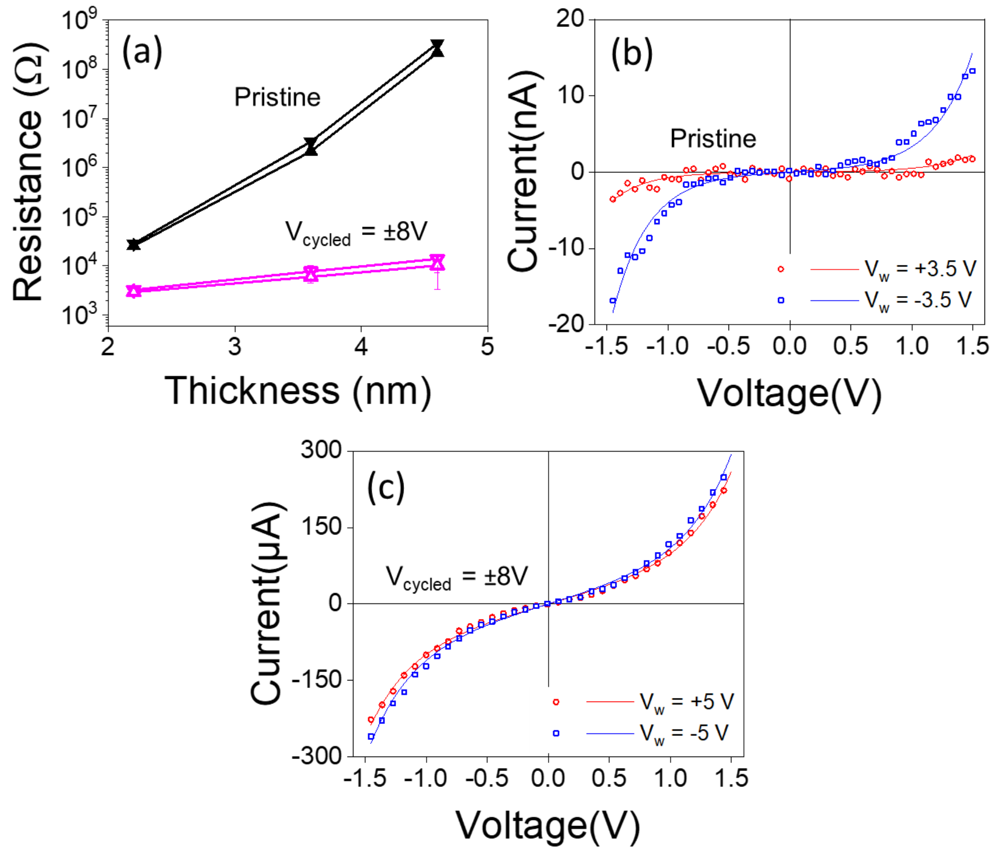

Figure 4.9 (a,b) I-V curves collected respectively after writing with V_W = +3.5 V and V_W = -3.5 V as indicated for the (b) pristine state, and V_W = +5 V and V_W = -5 V for (c) after V_{cycled} = ±8 V. (c) Dependence of ON and OFF resistance states on the HZO thickness for pristine and after V_{cycled} = ±8 V.

Table 4.1 Barrier parameters extracted from fittings are shown in Figure 4.9 (b)(c), including effective thickness (t_{eff}), barrier height for both interfaces (Φ_{LSMO} and Φ_{Pt}), and the fitting quality chi^2. Exclusively for status after breakdown, both conventional Brinkman model and an improved Brinkman model with parallel resistance (fixed R = 18kΩ).

Break	State	Φ_{LSMO} (eV)	Φ_{Pt} (eV)	t_{eff} (nm)	chi2
Before	LRS -3.5 V	2.06	2.85	4.6	9.51×10^{-9}
Before	HRS +3.5 V	1.76	3.44	4.7	5.38×10^{-9}
After	LRS -5 V	2.49	3.04	2.79	5.05×10^{-5}
After	HRS +5 V	2.40	3.07	2.82	6.80×10^{-5}
After (Parallel R=18 kΩ)	HRS +5 V	1.93	1.97	3.5	6.1×10^{-5}
After (Parallel R=18 kΩ)	LRS -5 V	1.96	2.06	3.4	7.22×10^{-5}

Appendix. 4.6

Capacitance (C-*f*) and impedance (Z''-Z') measurement conducted in sample with different HZO thickness. Similar behavior is observed for all samples irrespectively of their thickness.

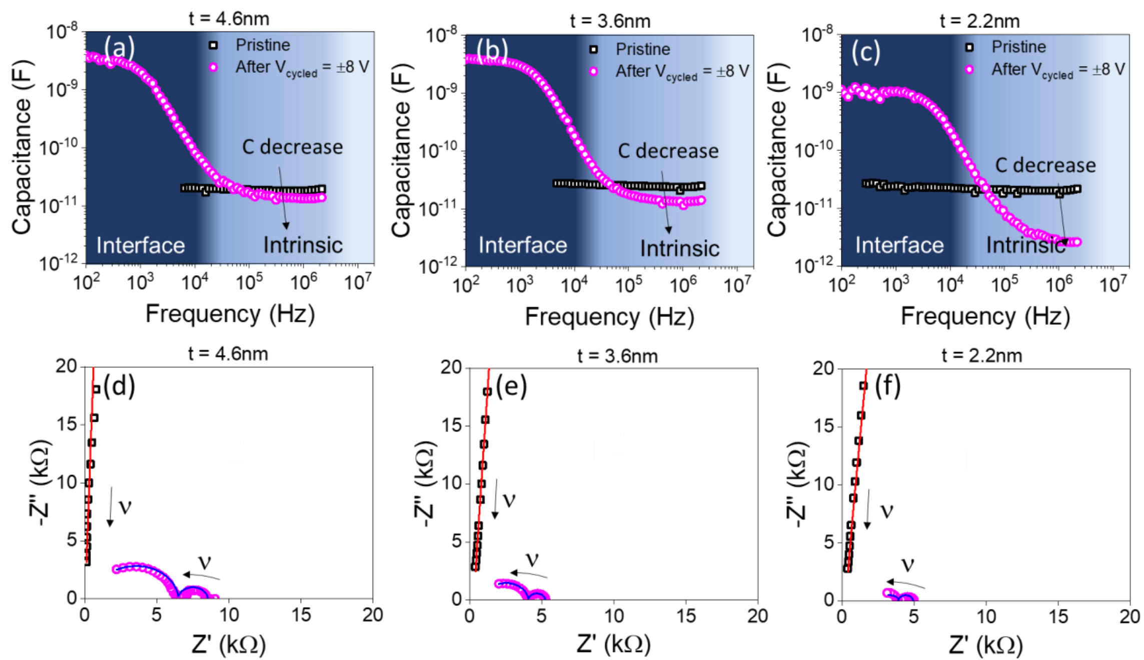

Figure 4.10 Capacitance as a function of frequency in pristine and cycled states for samples with different HZO thickness (a) t = 4.6 nm, (b) t = 3.6 nm, (c) t = 2.2 nm. And each corresponding Nyquist plot (d) t = 4.6 nm, (e) t = 3.6 nm, (f) t = 2.2 nm.

Appendix. 4.7

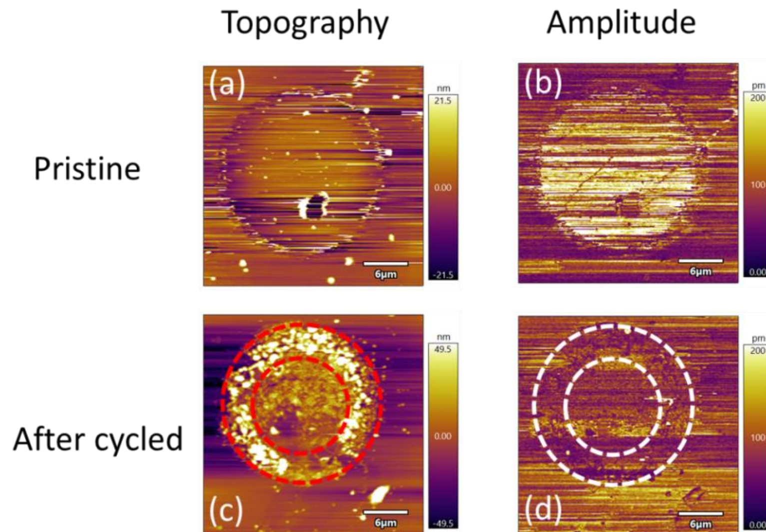

Figure 4.11 PFM topography on Pt electrode region for (a) pristine and (c) after cycled. PFM amplitude on Pt electrode region for (c) pristine and (d) after cycled. For Pt electrode after cycled, a ringed wrinkle was observed from its topography, as shown in the region between two dashed circles in (c), which indicates to a volume expansion caused by filament formation. And the piezo response in this area is considerably lower as shown in its amplitude (d).

Chapter 5. Optical control of resistive switch in BTO FTJs

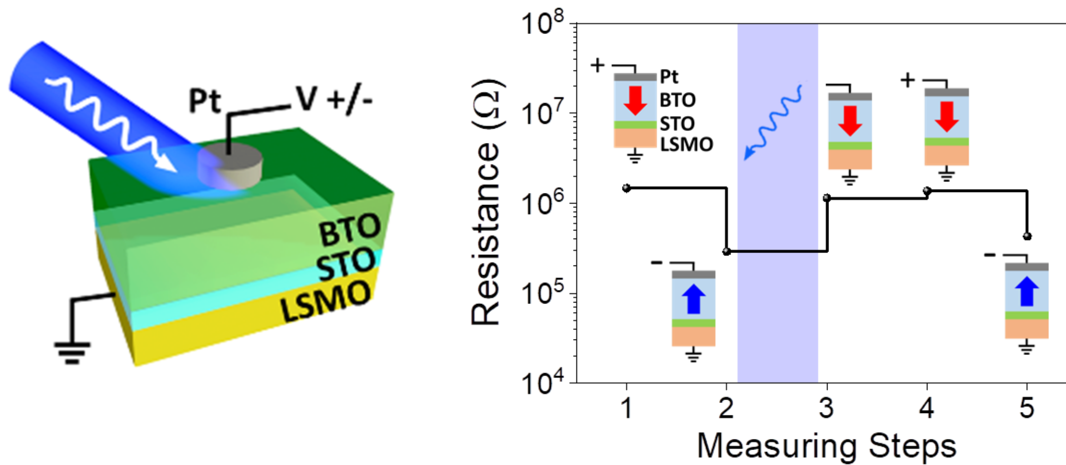

The results of this chapter have been published in "Long, X., Tan, H., Sánchez, F., Fina, I., & Fontcuberta, J. (2021). Non-volatile optical switch of resistance in photoferroelectric tunnel junctions. *Nature Communications*, 12(1), 1–9." from where the figure above is adapted.

Chapter 5. Optical control of resistive switch in BTO FTJs

5.1 Synopsis

Here, we study the polarization and resistance switch of a ferroelectric tunnel junction by visible light and we show how the device can be cycled to store information, which is subsequently read by measuring the tunnel current across the device. In a first realization, an ultrathin epitaxial ferroelectric BTO layer is sandwiched between bottom and top metallic electrodes, LSMO and Pt, respectively. This structure is used to elucidate the presence of E_{IMP} and its direction, and to demonstrate the light-induced (blue light) polarization reversal. Next, the ER is measured. Data analysis allows to disentangle different contributions to ER, namely the contribution related to the ferroelectric polarization reversal, which is prevalent at low voltage and high writing speed, superimposed to the ionic motion contribution, which is dominant in the opposite limits. Measurements under illumination clearly reveal that the resistive switching associated to polarization reversal is very sensitive to photon absorption. Finally, we show that the electric and optical responses of the device are radically improved by engineering the interface between BTO and the LSMO bottom electrode. Indeed, by inserting a nanometric dielectric layer (STO) between the bottom LSMO electrode and the ferroelectric BTO barrier, a larger ER (increased by a factor near 2×10^3 %) and a robust light-induced ON to OFF (LRS to HRS) resistance switch is observed allowing to demonstrate a dual electric-optical control of resistance in a FTJ memory element.

5.2 Sample

STO//LSMO (30 nm)/BTO (4 nm) and STO//LSMO (30 nm)/STO (1 nm)/BTO (4 nm) samples were grown in situ by PLD. Both structures were deposited in a single process. The LSMO layer was grown at 725 °C, at oxygen pressure of 0.1 mbar and 2 Hz of laser frequency. The BTO was grown at 700 °C, at oxygen pressure of 0.02 mbar and 2 Hz. In heterostructure a 1nm STO dielectric layer was grown at 700 °C, at oxygen pressure of 0.02 mbar and 2 Hz. Further experimental details and structural characterization can be found elsewhere.[147] Top Pt electrodes (20 nm thick) were deposited by sputtering through a stencil mask, allowing to obtain arrays of contacts of 20 and 7 μm diameter. The dependence of ER and optical suppression of ER on electrode size has been investigated, fully consistent results are shown in Appendix. 5.20.

5.3 Results

5.3.1 Light induced polarization switching

We first demonstrate the switching of the polarization direction by visible light, in ultrathin 4 nm epitaxial BTO films grown using pulsed-laser deposition (PLD).[147] The BTO layer is deposited on a LSMO (30 nm) conducting film grown on a (001) STO substrate in a single process (see 5.2 Sample). XRD θ-2θ scans of the samples, confirm the excellent quality of the films and its [001]

texture (See Appendix. 5.1). LSMO film is used as bottom electrode and it is grounded in all reported experiments, unless otherwise indicated.

The polarization direction of the as-grown film, inferred by piezoelectric force microscopy (PFM) (Figure 5.1 (a)) is found to be P_{DOWN}, indicating the presence of E_{IMP} pointing downwards. It will be shown below that $E_{IMP} \approx -2.8$ MV/cm, which roughly corresponds to voltage imprint (V_{IMP}) $\approx$ -1.0 V. By application of bias voltage (V = ±8 V) to the microscope tip (See Appendix. 5.2), P_{UP} (black) and P_{DOWN} (yellow) domains are defined (Figure 5.1 (a)), showing the electric control of ferroelectric polarization. The observation of near-zero piezoelectric response and 180° phase shift between domains of opposite polarity in PFM images (See Appendix. 5.3 and Appendix. 5.4) strongly supports their ferroelectric nature[148,149] PFM images have subsequently been collected after illuminating the sample with a blue laser in dark conditions (λ = 405 nm). As shown by data in Figure 5.1 (b), illumination has prompted P_{UP} switching to P_{DOWN}. The illuminating condition can be found in 2.2.4.1 Optical set-up. Control experiments indicated that, in dark, P_{UP} states remain stable, without any obvious change in PFM contrast in at least 6 h (See Appendix. 5.5), implying that spontaneous polarization back-switching is not relevant. Therefore, data in Figure 5.1 demonstrate that light-absorption assisted by E_{IMP}, promotes polarization switching of one of the polarization states (P_{UP}, in our BTO film). In the following, we shall exploit this phenomenon to demonstrate optical control of resistance in BTO FTJs.

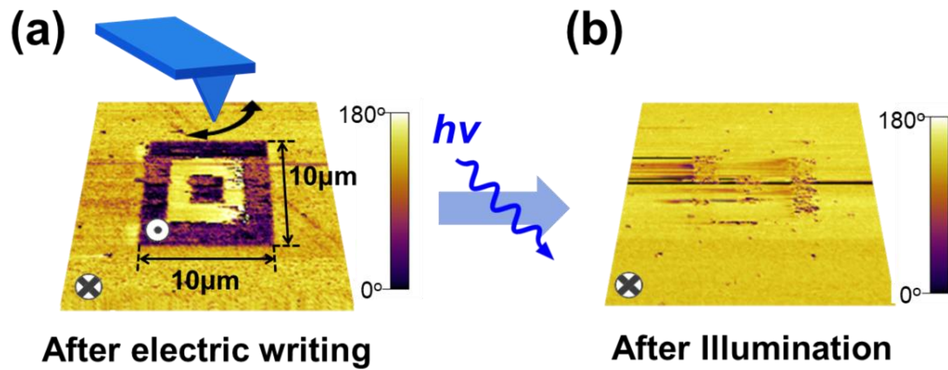

Figure 5.1 Polarization switching by combined action of light and E_{IMP} electric field. PFM phase-maps (30 µm × 30 µm) of BTO film. a P_{DOWN} and P_{UP} regions were written by applying voltage to the tip of -8 or +8 V within (a) 10 µm × 10 µm area in yellow and black regions, respectively. (b) After illumination (blue laser, 10 min) P_{UP} domains are switched back.

5.3.2 Electric field and light control of ER

We turn now to the ER of BTO tunnel barriers on LSMO, using Pt as top electrode (LSMO/BTO/Pt) (sketch in Figure 5.2 (a)). First, we aim at identifying the different mechanisms contributing to the ER in these FTJs. In Figure 5.2 (a), we show an illustrative I(V) curve recorded in dark (black line). It can be appreciated that the I(V) curve displays two current peaks indicated by dashed lines for increasing positive applied voltage at: $V^{+}_{C\text{-}LOW} \approx 3$ V [best seen in Figure 5.2 (a) (inset)] and $V^{+}_{C\text{-}HIGH} \approx 13$ V. In Figure 5.2 (b), we show the junction resistance (R) recorded by varying the writing voltage (V_W). Data were collected at remanence, i.e. after application of a suitable writing triangular voltage pulse of amplitude V_W and duration $\tau_W = 1$ ms. Black symbols in Figure 5.2 (b) correspond to R(V_W) data collected in dark. Loops are stable upon further cycling (See Appendix. 5.6). Two distinguishable voltages, at $V^{+}_{C\text{-}}$

$_{LOW} \approx 3$ V and $V^{+}_{C\text{-}HIGH} \approx 13$ V, can be identified. At $V^{+}_{C\text{-}LOW}$ and $V^{+}_{C\text{-}HIGH}$ there is a sudden increase of resistance; these voltages closely coincide with those where current switching peaks are observed in the I(V) curves (Figure 5.2 (a)). We focus first our attention on the changes of resistance occurring at the $V_W > 0$ region. The existence of two critical voltages ($V^{+}_{C\text{-}LOW}$ and $V^{+}_{C\text{-}HIGH}$) indicates the presence of different switching mechanisms. One can expect that these coexisting mechanisms might have different time response. The fastest mechanism could be related to a pure electronic process, i.e. ferroelectric switching. Figure 5.2 (c) shows the $R(V_W)$ loop recorded using $\tau_W = 100$ μs. A coercive field, $E_C \approx 8.0$ MV/cm (corresponding to $V_C \approx 3.2$ V) and an $E_{IMP} \approx -2.8$ MV/cm (corresponding to $V_{IMP} \approx -1.0$ V) can be extracted. Note that although E_C is comparable to the breakdown field in polycrystalline samples,[150] time-dependent current measurements under constant electric stress and endurance data do not agree for dielectric breakdown at $V^{+}_{C\text{-}LOW} < V_W < V^{+}_{C\text{-}HIGH}$. Instead, equivalent characterization collected for $V_W > V_{C\text{-}HIGH}$ is consistent with the proposed ionic motion scenario although the presence of soft dielectric breakdown after successive cycling cannot be disregarded (See Appendix. 5.7 and Appendix. 5.8). The PFM phase loop (recorded using $\tau_W = 100$ μs) (Figure 5.2 (c)) shows coercive and imprint voltages which are closely coinciding with those extracted from $R(V_W)$ data (vertical dashed lines). The I(V) curves in the low-voltage region ($V_W < V^{+}_{C\text{-}HIGH}$) can be well fitted by an electron tunnel transport model across polarization modulated tunnel barriers (See Appendix. 5.9 and Appendix. 5.10), providing additional support to the ferroelectric origin of the ER in this voltage region. P(V) and I(V) loops (Figure 5.2 (d)) collected in top-top configuration (see 2.2.1 Measurement setup, and the method to extract switching current peak can be found in Appendix. 5.21)

further indicate the ferroelectric nature of the sample. Switching current peaks appear at 5.6 V, which is about twice V_C observed in the $R(V_W)$ loop, as expected from an antiserial connection of ferroelectric capacitors.[151] Polarization value is also in reasonable agreement with bulk values and similar to values obtained in BTO films grown in the same nominal conditions and similar thickness.[152] Therefore, we conclude that the $R(V_W < V^+_{C\text{-}HIGH})$ loops collected at short τ_W (< 1 ms) are governed by ferroelectric polarization switching, which give rise to a LRS (P_{UP}) to HRS (P_{DOWN}) resistive switching and vice versa upon V_W cycling.

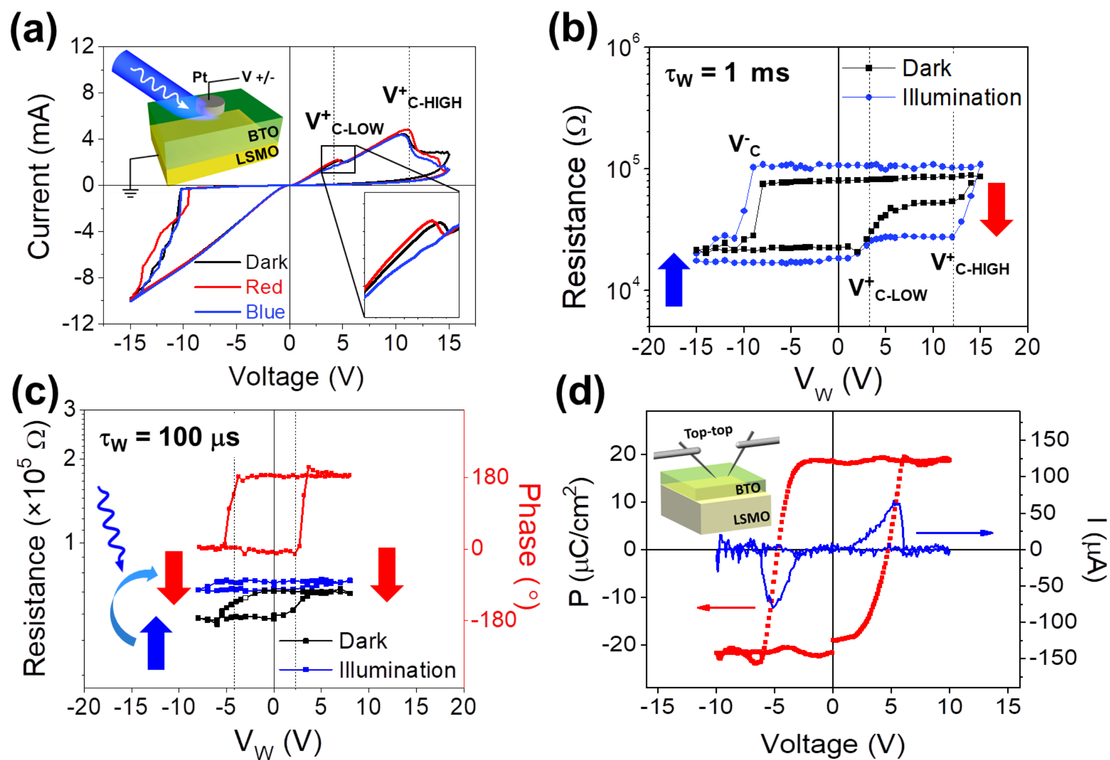

Figure 5.2 Electroresistance under illumination. (a) I(V) loops following the -15 to +15 to -15 V path collected in dark and under illumination (red and blue laser). Inset top-left: Schematic of the measuring configuration. Inset bottom-right: Zoom of the I(V) loops around $V^+_{C\text{-}LOW}$. (b) $R(V_W)$ loops collected using τ_W = 1 ms in dark and under (blue) illumination. Arrows indicates polarization

direction. (c) $R(V_W)$ loops collected using $\tau_W = 100$ μs in dark (black symbols) and under (blue) illumination (blue symbols). The PFM phase-voltage hysteresis loop (red symbols) of the sample (right-bottom axis). Vertical dashed lines indicate the E_C in PFM loop, coinciding with V^+_{C-LOW} and V^-_{C-LOW} in the $R(V_W)$ loop. (d) P(V) and I(V) loop and sketch of the measuring configuration.

The presence of two critical voltages (V^+_{C-LOW}, V^+_{C-HIGH}) in $R(V_W)$ data collected at $\tau_W = 1$ ms in Figure 5.2 (a), allows stabilizing three different resistance states: low (LRS ≈ 30 kΩ) state, intermediate (HRS ≈ 50 kΩ) state at V^+_{C-LOW} and high state, labeled HRS_{ION}, ($HRS_{ION} \approx 90$ kΩ), at V^+_{C-HIGH}. Interestingly, when using a faster writing time, $\tau_W < 500$ μs, the LRS and HRS resistance states are visible in the $R(V_W)$ loops but the HRS_{ION} state is absent in all tested junctions (See Appendix. 5.11 and Appendix. 5.12). One might suspect that a slower resistive switching mechanism, not responsive to fast writing pulses (≤ 500 μs), is related to an ionic migration process.[153,154] Taking $\tau_W = 500$ μs as the diffusion time of ions across the BTO film thickness to reach the interface under $V^+_{C-HIGH} \approx 13$ V, a mobility ≈ 2.5×10^{-9} cm^2 V^{-1} s^{-1} is estimated. This estimate is within the range of values reported for the motion of oxygen vacancies motion in BTO at room temperature[155] and it is orders of magnitude smaller than typical electron mobility in similar oxides (mobility ≈ 1 cm^2 V^{-1} s^{-1}), suggesting defect migration is the most probable mechanism.[156–160]

The change of resistance occurring at $V_W < 0$ (after the $V_W > 0$ excursion) and particularly the abrupt reduction of resistance observed at $V^-_C \approx -10$ V (Figure 5.2 (a) (b)), makes indiscernible the electronic and ionic transport channels. Analogous abrupt change of resistance at $V_W < 0$ was reported in other BTO-

based FTJs[154,161] and it was interpreted in terms of ferroelectric domain avalanches stimulated by the asymmetric voltage drop across the junctions.

Now, we turn to the electrical characterization of the FTJs under illumination conducted by using blue (λ = 405 nm, E = 3.06 eV) and red (λ = 638 nm, E = 1.94 eV) lasers, near and well below BTO bandgap (E_g = 3.3 eV),[162] respectively. A FTJ capacitor was completely exposed to the laser beam, as sketched in Figure 5.2 (a). The I(V) characteristics recorded under red and blue light are shown in Figure 5.2 (a). Strikingly, it is observed that the current peak at $V^+_{C\text{-}LOW}$ is suppressed when the junction is illuminated by the blue laser. In contrast, I(V) curves recorded under red laser and dark are almost identical. These results indicate that the suppression of the polarization switching, which we recall is at the origin of the observed current peak at $V^+_{C\text{-}LOW}$, results from photocarriers generated at the BTO layer by the blue laser. This is confirmed by the absence of polarization switching by red light, observed by PFM (See Appendix. 5.13). Thermal effects, in a 4 nm BTO film, would have similar effects for both wavelengths, in contrast to observation, thus suggesting to have a minor role on the I(V) photoresponse. The contribution of LSMO photoconductance has been verified, being it negligible and thus suggesting that LSMO contribution in the ferroelectric switching polarization is not relevant (See Appendix. 5.14). In Figure 5.2 (b), the $R(V_W)$ loop collected (τ_W = 1 ms) under blue light is shown. It can be observed that, under illumination, the ER at $V^+_{C\text{-}LOW}$ is largely suppressed. Instead, $V^+_{C\text{-}HIGH}$ remains and signals the onset of a large change of resistance. These observations indicate that the LRS to HRS switching resulting from polarization reversal is suppressed by illumination. Instead, the ionic-like conduction channel at $V^+_{C\text{-}HIGH}$ persists and governs the ER, giving rise to the HRS_{ION} state. Figure 5.2 (c) shows that the resistance of

the HRS obtained by voltage control ($V_W < V^+_{C\text{-}HIGH}$) is coincident with that measured under illumination (blue symbols), which confirms that polarization is switched from P_{UP} to P_{DOWN} by the blue laser as schematized in Figure 5.2 (c). An identical behavior is found when measuring the ER in dark and under illumination of junctions with BTO barriers of different thicknesses (≈ 2 and 5 nm) (See Appendix. 5.10). As the polarization has been already switched by light, the $R(V_W)$ loops collected with $V_W < V^+_{C\text{-}HIGH}$ under blue light, display a very reduced ER, which is in agreement with the absence of the switching peak in the I(V) data under blue light (Figure 5.2 (a)). All loops collected under light in the $V_W < V^+_{C\text{-}HIGH}$ voltage range and using the same τ_W , show a similar ER suppression (See Appendix. 5.15). Moreover, it is observed that some junctions display non-reversible photoresponse (See Appendix. 5.15), as reported in ferroelectric single crystals and thin films,[163,164] and attributed to charge trapping. It thus follows that, to take full advantage of the photoresponsive ER in FTJs, the ionic transport channel should be mitigated or suppressed. It will be shown in the following that engineered interfaces allow to overcome this limitation.

5.3.3 Enhanced optical control of ER

Aiming at suppressing ionic contributions (possibly oxygen vacancies) to the ER and eventually obtaining fully polarization-controlled tunnel barrier suitable for optical resistive switching, we have introduced a dielectric blocking layer (STO, 1 nm thick) between the LSMO bottom electrode and the BTO layer (LSMO/STO/BTO), as sketched in Figure 5.3 (a). It is expected that this

dielectric layer could have a double benefit. First, limiting ionic motion across the LSMO/BTO interface and second, blocking the flow of photocarriers through the circuit while allowing photocarriers in BTO to screen P, thus the polarization-related tunnel barrier or Schottky barrier at BTO interfaces will remain sensitive to photocarriers. The STO thickness (1 nm) is selected to be thin enough to allow tunneling across the whole device. Figure 5.3 (b) displays the $R(V_W)$ loop collected in a junction in this hybrid structure LSMO/STO/BTO (τ_W = 100 μs) in dark (black symbols) and under illumination (blue symbols). Loops are stable upon further cycling (See Appendix. 5.16). Four important features can be observed. First, the ER in dark increases by a factor near 2×10^3 % compared to data in Figure 5.3 (c), and it is robust under constant cycling (See Appendix. 5.17). Indeed, the change of resistance is of about 500 % in the LSMO/STO/BTO (Figure 5.3 (b)) while it was of ≈ 30 % in LSMO/BTO junctions (Figure 5.3 (c)). This enhancement results from the larger asymmetry of the electronic potential profile across the device. A similar approach had been used earlier to improve ER in ferroelectric tunnel barriers.[73][74] Moreover, whereas two critical ($V^+_{C\text{-}LOW}$ and $V^+_{C\text{-}HIGH}$) fields, related to polarization reversal and ionic motion, respectively, were observed in LSMO/BTO junctions, only the $V^+_{C\text{-}LOW}$ remains apparent in the $R(V_W)$ loops of the LSMO/STO/BTO hybrid junctions. This observation confirms that the STO layer contributes to suppress the ionic channel and the HRS_{ION} state[74] (See Appendix. 5.18). Second, it is found that the E_{IMP} increases by about a factor 2 (from -1 V in the LSMO/BTO junction (Figure 5.3 (c)) to -2 V in the LSMO/STO/BTO (Figure 5.3 (b))). The EIMP increase also contributes to stabilize a HRS (P_{DOWN}), that consistently with the notation in previous section we still denote as HRS, without compromising the ER magnitude. Third, under illumination, the

polarization-related ER is completely suppressed and the system remains in the HRS. This observation is crucial as it indicates that, although ferroelectric polarization is suppressed, E_{IMP} induces non-ferroelectric (paraelectric) polarization parallel to P_{DOWN} under illumination. And fourth, the $R(V_W)$ loop after illumination (open symbols) is very similar to the one measured before illumination (black symbols), which indicates the robustness of the ferroelectric controlled ER. To confirm the effect of light on the LSMO/STO/BTO structure, PFM images of LSMO/STO/BTO were collected in dark and after illumination. First, after writing with $V_W = \pm 8$ V ferroelectric domains with opposite polarity, a PFM phase image was collected (Figure 5.3 (c), left panel). The PFM contrast among P_{UP}/P_{DOWN} regions is obvious although smaller than in the PFM of the LSMO/BTO sample (Figure 5.1 (b)) due to the more relevant charging effects[149] in the LSMO/STO/BTO structure (see Appendix. 5.3). After illumination using the blue laser, PFM images were collected again. It can be appreciated in Figure 5.3 (c) (right panel) that the contrast between P_{UP} and P_{DOWN} has significantly decreased compared with the image collected in dark, indicating light-induced P_{UP} polarization suppression. Contrast profiles shown in Figure 5.3 (c) (bottom panel) provide a direct evidence of P_{UP} suppression by (blue laser) light. P(V) and I(V) loops (Figure 5.3 (d)) collected in top-top configuration (see 2.2.1 Measurement setup, and the method to extract switching current peak can be found in Appendix. 5.21) further indicate the ferroelectric nature of the sample. Switching current peaks appear at 8.4 V, which is close to two times V_C ($\approx$ 4.4 V) from $R(V_W)$ loop, as expected.[151] The reduced polarization compared with the LSMO/BTO sample is expectedly smaller due to different electrostatic boundary conditions of the BTO layer.

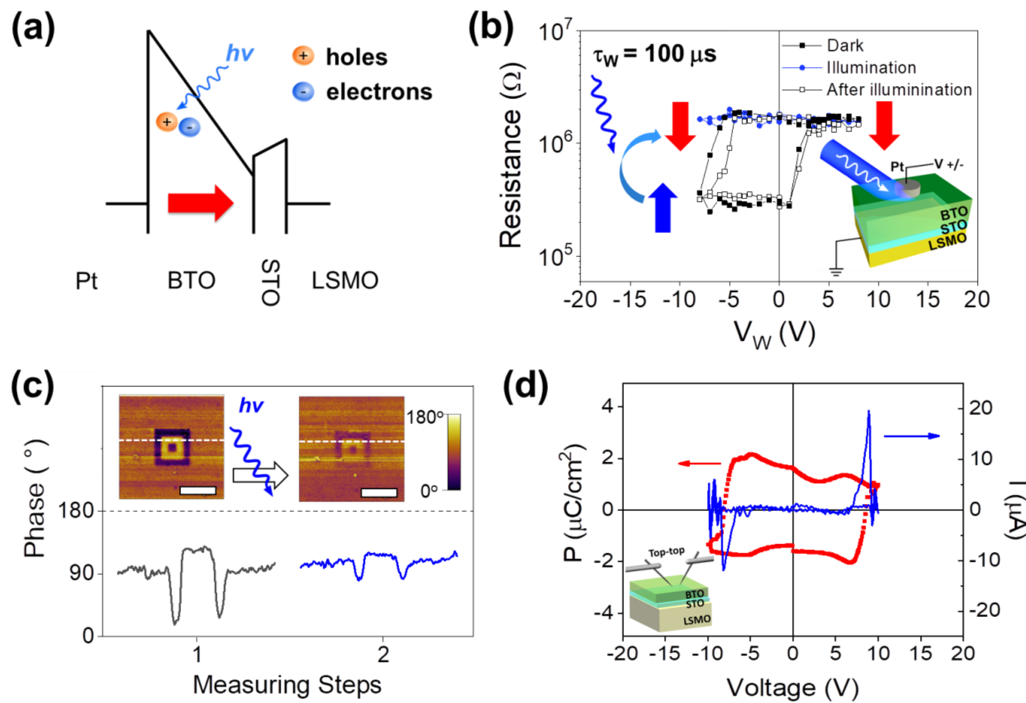

Figure 5.3 Electroresistance of dielectric/ferroelectric heterostructures under illumination. (a) Sketch of the layer stacking with a polarized BTO barrier. (b) $R(V_W)$ loop collected using $\tau_W = 100\ \mu s$ in dark (black solid and open circles) and under illumination (blue symbols). (c) Out-of-plane PFM phase images obtained after writing P_{DOWN} and P_{UP} domains (applied voltage to the tip of +8 V (inner yellow region) and -8 V (black region)), respectively (left image) and after illuminating the LSMO/STO/BTO sample (right image). Scale bars correspond to 10 µm. Bottom, phase-profiles along the white dashed lines in the corresponding images. (d) P(V) and I(V) loop and sketch of the measuring configuration.

The LSMO/STO/BTO hybrid structure allows a reversible (light-on/light-off) ER response. Therefore, combined voltage–illumination protocols can be used to handle the non-volatile resistance state (memory) of the device. To illustrate this prospect, we show in Figure 5.4 the sequence of stimuli (V_W ($\tau_W = 100\ \mu s$), blue-laser light) acting on the FTJ and the subsequent resistance states. In Figure 5.4 (a), a HRS (P_{DOWN}) is first written by applying a $V_W = +8$ V pulse (step 1);

after a LRS (P_{UP}) state is written by a V_W = -8 V pulse (step 2); the HRS (P_{DOWN}) is recovered (step 3) after illumination of the sample while the sample is unbiased. Afterwards, it is observed that applying V_W = +8 V the HRS (P_{DOWN}) state does not change as expected (step 4). The LRS (P_{UP}) is recovered (step 5) by applying V_W = -8 V. Thus LRS optically switch to HRS. Reciprocal results are shown in Figure 5.4 (b). In this case, it is observed that HRS (P_{DOWN}) does not switch under illumination. Data in Figure 5.4 illustrates in the clearest way how light-induced polarization reversal can be used to control the memory state of the device. Similar results are obtained in different devices (See Appendix. 5.19).

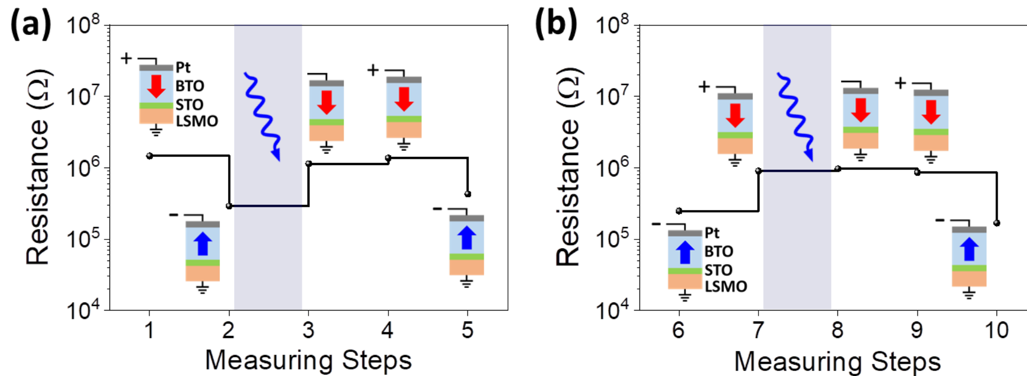

Figure 5.4 Electro-optical control of resistance. Resistance measured under different electric and optical stimulus sequence. Initial states at LRS and HRS in (a) and (b), respectively. Notice (blue shaded areas) that P_{UP} states are reversed by light and resistance switches from LRS to HRS, whereas P_{DOWN} states are insensitive to light. In this example: V_W = ±8 V. Optical illumination is marked with symbol. Arrows indicate polarization direction.

Figure 5.5 (a) demonstrates the remarkable retention of the electrically and/or optically written LRS and HRS states of the device. The resistance of the ON/OFF states, electrical written using voltages pulses of -8 V for LRS and +8

V for HRS, are recorded as a function of the time elapsed after electrical writing. Figure 5.5 (a) also illustrates the retention of the HRS induced by light, after writing with -8 V. All light-induced resistive switching experiments reported above, were performed using fixed illumination conditions (see 2.2.4.1 Optical set-up) that were selected to completely switch the LRS to HRS state. Fine-tuning (memristive-like) of optical switch is achieved by reduction of laser power and illumination time. Figure 5.5 (b) illustrates the LRS-to-HRS resistance switching dependence on illumination time when the laser power is reduced to 0.1 W/cm^2. Interestingly, under these conditions, the resistance of the device can be continuously varied from LRS to HRS. Naturally, the switching is faster when increasing the laser power (See Figure 6.4 (b) in Chapter 6).

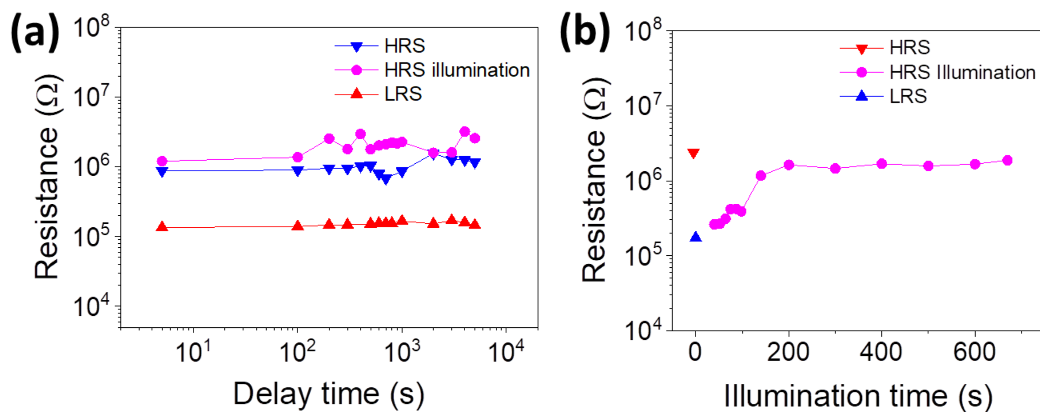

Figure 5.5 Retention and optical modulation of resistance. (a) Retention of the voltage (τ_W = 100 µs) and light written HRS states and LRS state in a junction on STO//LSMO/BTO/STO/Pt. (b) Evolution of the resistance of the junctions under illumination, from LRS to HRS. Data (blue circles) are collected as function of illumination time using a laser power of 0.1 W/cm^2. Each plot also includes the resistance of the LRS and HRS measured in dark (up blue and down red, respectively). Arrows indicate the direction of the polarization of the ferroelectric barrier.

5.4 Conclusion

We have shown that the combined action of E_{IMP} and optical stimulus is used to switch ferroelectric polarization and concomitantly, the resistance state in a FTJ. Robust optical-electric switching is found in the LSMO/STO/BTO (DE/FE) heterostructures, demonstrating that the optical control of resistance is non-volatile. These hybrid DE/FE heterostructures appear to mitigate ionic-like conducting channels across the FTJs and improving ER and stability compared to the junctions based on LSMO/BTO bilayer. The results presented here demonstrate a novel dual stimulus (voltage/light) control of the memory state of ferroelectric junctions. The optical switch sets resistance state as stable as the electrically set; in addition, appropriate selection of illumination time and power allows fine-tuning of the final resistance state, i.e. memristive behavior. The observed optical control, based on polarization switching, relies on the existence of an E_{IMP} that is dictated by the BTO deposition conditions. Alternative sources can be envisaged to mimic E_{IMP} and unbalance ad hoc P_{UP} and P_{DOWN} states without requiring changing the polarity by V_W. They may offer alternatives and may be more practical ways to achieve full optical control of polarization in FTJs. Pivotal for the operation of the device are the photocarriers required to suppress the ferroelectric polarization, here obtained by photoabsorption in BTO. The large bandgap of BTO implies that photobsorption is mainly dictated by defects in the film, of limited absorbance. It is clear that larger efficiency could be obtained by exploiting narrower gap ferroelectrics, such as BFO or hexagonal manganite, both having bandgaps in the visible range.

5.5 Appendix

Appendix. 5.1 Structure characterization

Figure 5.6 shows the XRD θ-2θ scans for the STO//LSMO/BTO/Pt and STO//LSMO/STO/BTO/Pt samples. The BTO (002) reflection is well visible in both cases together with the LSMO (002). Traces of reflections of polycrystalline Pt are also observed. The BTO peak broadness results from its thickness, which is approximate 4 nm. Note that the difference in the presence or not of the Pt(111) peak is because in one case the beam was focused on the Pt electrodes and not in the other.

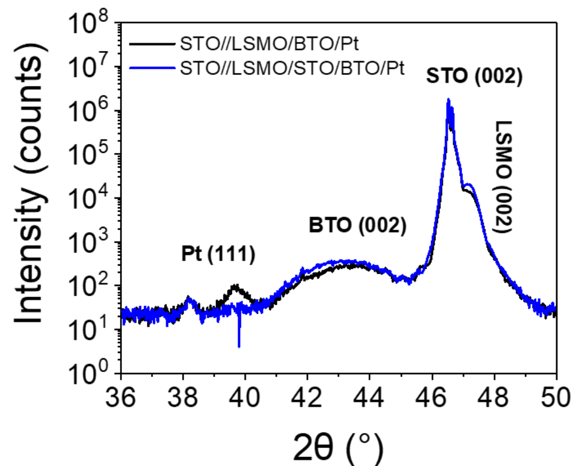

Figure 5.6 Structural characterization. XRD θ-2θ scans for samples: STO//LSMO/BTO/Pt and STO//LSMO/STO/BTO/Pt.

Appendix. 5.2 Electric writing in PFM experiments

Figure 5.7 shows the 10 × 10 μm^2 region where the positive (+8 V in white) or negative (-8 V in dark) was applied to define regions with P_{DOWN} and P_{UP} states,

respectively. The bias voltage was applied while performing a single PFM image.

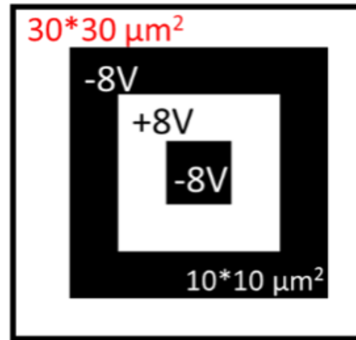

Figure 5.7 Electric writing in PFM experiments. The electric writing was done by applying bias voltage (V = +8, -8 V for white and black, respectively) at the PFM tip in a region of 10 × 10 μm^2, while reading in a region of 30 × 30 μm^2 with zero tip bias. The electric pattern was defined in a single PFM pass.

Appendix. 5.3 Extended PFM characterization I

Figure 5.8 shows PFM amplitude and phase image for written regions in the LSMO/BTO sample, respectively. It can be observed that the phase contrast is 180° and the amplitude is constant across the sample except at the ferroelectric domain walls, as expected for a ferroelectric material. Some regions with lower amplitude signal out from ferroelectric domain walls are observed due to tip bad electrical contact. Equivalent data is shown for the LSMO/STO/BTO sample (Figure 5.8 (c),(d)). It can be observed that both images show contrast with reduced from 180° phase contrast in the phase image. This effect is ascribed to the better insulating properties of the STO/LSMO/BTO sample, which result in greater charging effects which hidden genuine ferroelectric signal as discussed in previous works.[149]

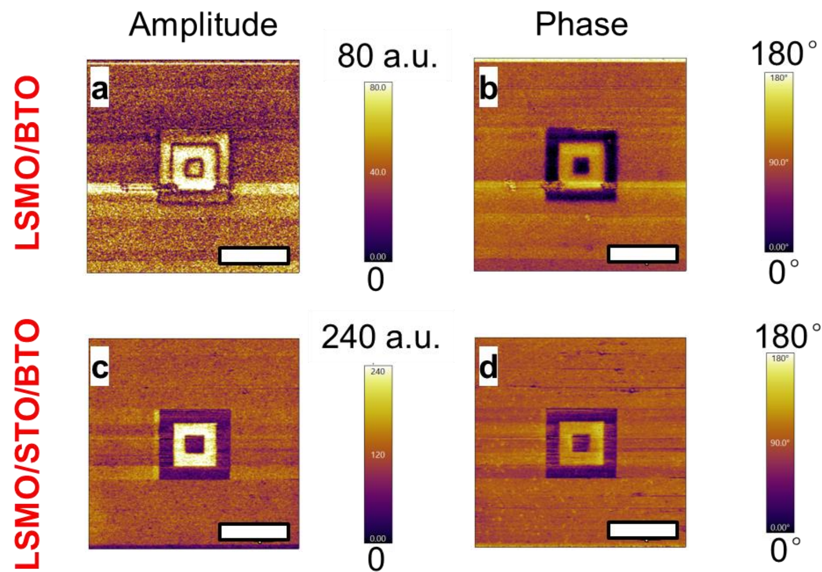

Figure 5.8 Charging effects in LSMO/STO/BTO sample. (a) amplitude and (b) phase images of both LSMO/BTO sample. (c) amplitude and (d) phase images of LSMO/STO/BTO sample.

Appendix. 5.4 Extended PFM characterization II

Figure 5.9 (a) shows PFM phase images and profiles collected just after electric writing and after 20 min delay time in dark for the STO//LSMO/BTO sample. The delay time was fix to 20 min, because it is similar to the time between PFM images shown in Figure 5.1. It can be observed that the PFM phase contrast is constant among all the collected images/profiles indicating that the polarization retention is high, and disregarding the reduction of polarization contrast shown in Figure 5.1 to the action of depolarization fields. Similar set of data is shown in Figure 5.9 (b) for the STO//LSMO/STO/BTO sample. It can be also observed that the phase contrast is constant comparing the images/profiles collected just after and after waiting 20 min delay time, denoting good retention and disregarding the influence of poor polarization retention in the data shown in Figure 5.3 (c). The non-180° phase contrast is discussed in Appendix. 5.3.

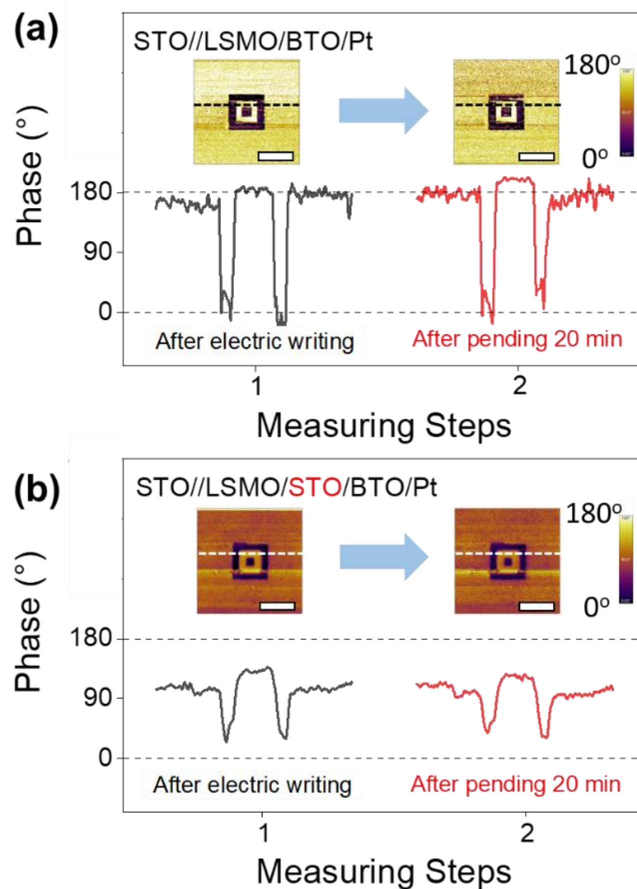

Figure 5.9 PFM extended characterization. Out-of-plane domain PFM phase images for both (a) LSMO/BTO and (b) LSMO/STO/BTO samples, obtained just after writing P_{DOWN} (inner yellow region) and P_{UP} domains (black region), respectively (left image) and after pending in dark for 20 min (right image). The lines scans shown in the bottom correspond to PFM phase profiles along the dashed lines in the corresponding images for each sample. Scale bar corresponds to 10 μm.

Appendix. 5.5 Time dependence of the phase-contrast in PFM

Figure 5.10 (a)(b)(c) show PFM phase images collected after writing with (±8 V), either immediately (Original) and after waiting for 1 h and 6 h, respectively. It can be observed that the phase contrast is preserved (Figure 5.10 (d)) and the

dark regions slightly expand with time (Figure 5.10 (e)) as expected from the presence of E_{IMP}.

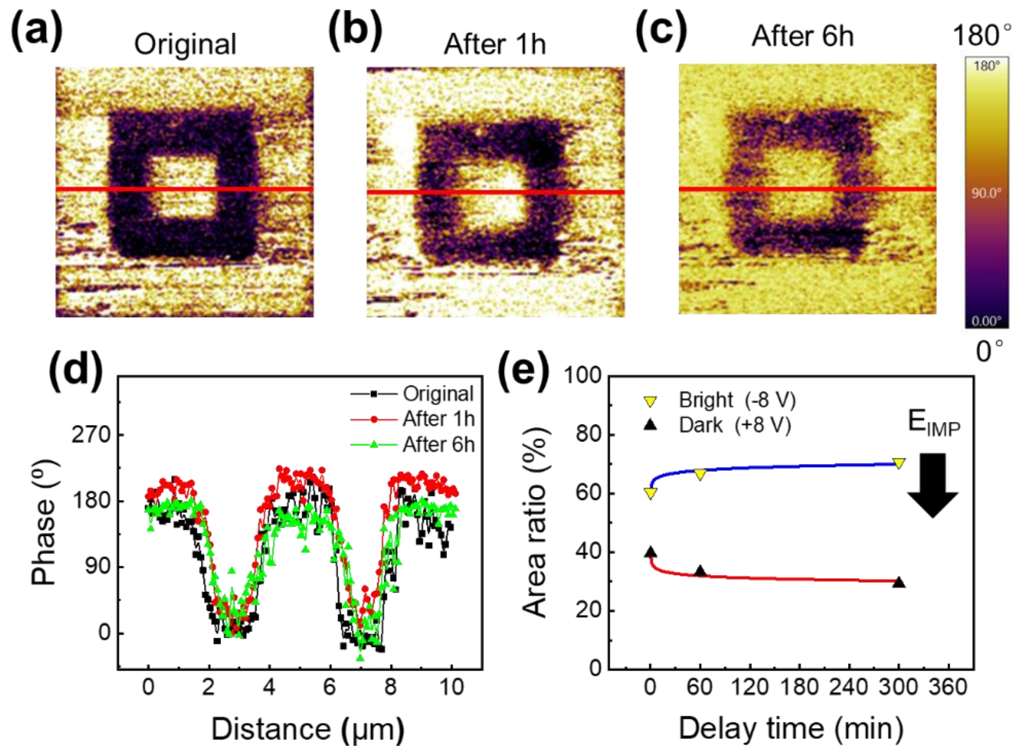

Figure 5.10 PFM phase contrast retention. PFM phase images collected after electrical lithography with +8 (bright) and -8V (dark) for the LSMO/BTO sample. (a)(b)(c) Data collected freshly after writing (original); after 1 h and after 6 h, respectively. (d) Line scans (red lines in panels a-c) of the phase-contrast of images in (a,b,c). (e) Dependence on delay time since electrical writing of relative area ratio of dark/bright areas [= $area_{dark/bright}$/(total area)]. Lines are guides for the eye.

Appendix. 5.6 Reproducibility of the measured ER loops in STO//LSMO/BTO/Pt

Figure 5.11 shows illustrative $R(V_W)$ loops recorded using different writing times and in different junctions, in STO//LSMO/BTO/Pt sample. Observation

of these loops clearly reveal than the main features are well reproducible during the first cycles.

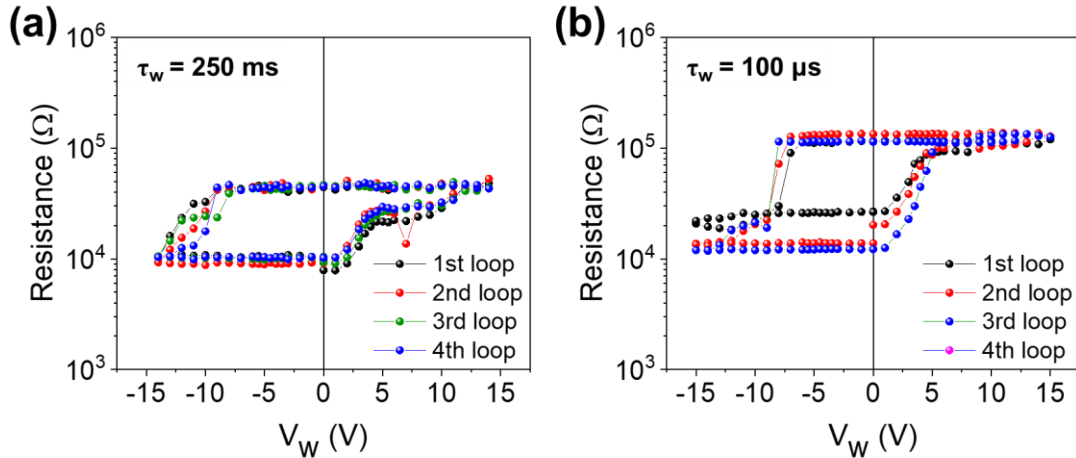

Figure 5.11 R(V_W) loop stability. Illustrative examples of the reproducibility of the major ER loops in two different junctions in a STO//LSMO/BTO/Pt sample as a function of the writing time: (a) 250 ms and (b) 100 μs. Data show the reproducibility of ER loops over several cycles of operation.

Appendix. 5.7 Time dependent current characterization

Figure 5.12 shows illustrative current versus time measurements after prepolarizing the sample with a voltage pulse V_W = -15 V and setting a voltage near $V^+_{C\text{-}LOW}$ (= 3 V) and $V^+_{C\text{-}HIGH}$ (= 10 V) in the LMSO/BTO sample. It can be observed that the current flowing under V = 3V is nearly constant. Instead, the current flowing under V = 10 V shows a gradual reduction, with a time constant of about ≈ 1 s. Although, the time scale of the latter result might be compatible with soft breakdown, we should emphasize that we observe a reduction of current, that is an increase of the device resistance, which is opposite to the resistance decrease observed when SBD occurs in $BaTiO_3$.[165]

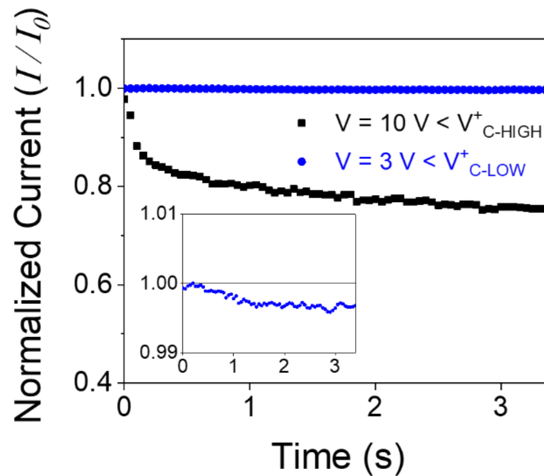

Figure 5.12 Time dependent current experiments. Time dependence of the normalized current for applied voltages near $V^{+}_{C\text{-}LOW}$ (= 3 V) and $V^{+}_{C\text{-}HIGH}$ (= 10 V) for the LSMO/BTO sample. Zoom of the time dependence of the normalized current for applied voltages near $V^{+}_{C\text{-}LOW}$ (= 3 V).

Appendix. 5.8 ER endurance in LSMO/BTO sample

HRS and LRS states obtained sequentially by the application of hundreds of ±8 V pulses ($V_{C\text{-}LOW}$ > 8V < $V_{C\text{-}HIGH}$) are shown for the LSMO/BTO sample in Figure 5.13 (a). As shown in the manuscript, at this rather voltage, ionic conduction contribution is of little relevance for ER. The data collected for up to 200 cycles demonstrate that the two resistance states remain relatively constant and are well distinguishable. In other words, the device can be robustly switched. The observed variations of resistance can be ascribed to electrical noise and mechanical instabilities. In Figure 5.13 (b), HRS and LRS states obtained sequentially by the application of much larger voltage pulses (±15 V) are shown. Notice that V = +15 V is well above $V_{C\text{-}HIGH}$, where ionic motion is predominant. We observe that the junction degrades fast, after 20 cycles for BTO. This fast degradation is in agreement with the proposed ionic conduction

mechanism but, a soft dielectric breakdown after several cycles, cannot be excluded.

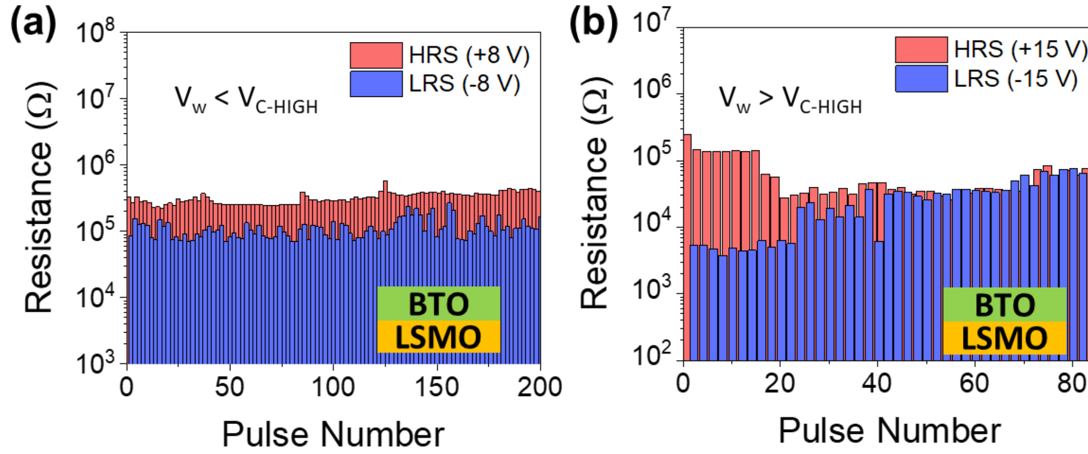

Figure 5.13 Endurance for LSMO/BTO sample. (a) Endurance of HRS states and LRS states written by ±8 V in a junction of STO//LSMO/BTO/Pt sample. (b) Endurance of HRS states and LRS states written by ±15 V in a junction of STO//LSMO/BTO/Pt sample.

Appendix. 5.9 Tunneling current analysis

Figure 5.14 (a) shows I(V) characteristics in the low-voltage region (0.5 V) for the indicated LRS (written either by -8 or -15 V), HRS ($V_W = +8$ V) and HRS_{ION} ($V_W = +15$ V) states and data fitting. The fittings are obtained by minimizing the χ^2 value accounting for the difference between the experimental values and the fitted ones [$\chi^2 = \sum(\text{experimental-fitted})^2$] using the equation:[50,166]

$$J \cong C \frac{\exp\left\{\alpha(V)\left[\left(\Phi_2 - \frac{eV}{2}\right)^{3/2} - \left(\Phi_1 + \frac{eV}{2}\right)^{3/2}\right]\right\}}{\alpha^2(V)\left[\left(\Phi_2 - \frac{eV}{2}\right)^{1/2} - \left(\Phi_1 + \frac{eV}{2}\right)^{1/2}\right]^2} \times \sinh\left\{\frac{3}{2}\alpha(V)\left[\left(\Phi_2 - \frac{eV}{2}\right)^{1/2} - \left(\Phi_1 + \frac{eV}{2}\right)^{1/2}\right]\frac{eV}{2}\right\}$$

Equation 5.1

where $C = -\left(4em^{*}m_{e}\right)/(9\pi^{2}\hbar^{3})$ and $\alpha(V) \equiv \left[4d\left(2m^{*}m_{e}\right)^{1/2}\right] \Big/ \left[3\hbar\left(\Phi_{1} + eV - \Phi_{2}\right)\right]$, and m_e corresponds to the electron mass, m^* to its effective mass (fixed to 1), e to its charge, d to the tunneling thickness and Φ_1 and Φ_2 corresponding to the LSMO/BTO and BTO/Pt interfaces, respectively.

In Figure 5.14 (b) it is sketched the band alignment of isolated materials (values are obtained according to refs.[167–170]) and in Figure 5.14 (c) the band alignment of the junction. The values obtained are similar to those obtained by the described data fitting, which are summarized in Table 5.1. It can be observed that the fitted values of Φ_1 (0.5 ~ 0.6 eV) and Φ_2 (1.4 ~ 1.8 eV) corresponding to the LSMO/BTO and BTO/LSMO interfaces, respectively are in agreement with those obtained from band alignment analysis Φ_1 = 1 eV and Φ_2 = 1.8 eV. The discrepancy is attributed to the high modulation of d parameter, accounting for tunneling thickness, which dominates in the shape of the fitted I(V) curves. Overall data in Figure 5.14 indicates tunneling transport across the film thickness.

Attempts to fit I(V) characteristics using Fowler-Nordheim tunneling (FNT) and Thermionic injection (TI) following the equations described in Pantel et al.[171] It turns out that good fits can be obtained by using the TI model and the extracted barrier energies are almost identical (≈ 0.5 V) for both barrier sides. A barrier of ≈ 0.5 V for the BTO/Pt interface is much smaller than that expected from simple estimates of the barrier height on the basis of work function of Pt and electron affinity of BTO. We had therefore concluded that the fits using FNT and TI models were not meaningful.

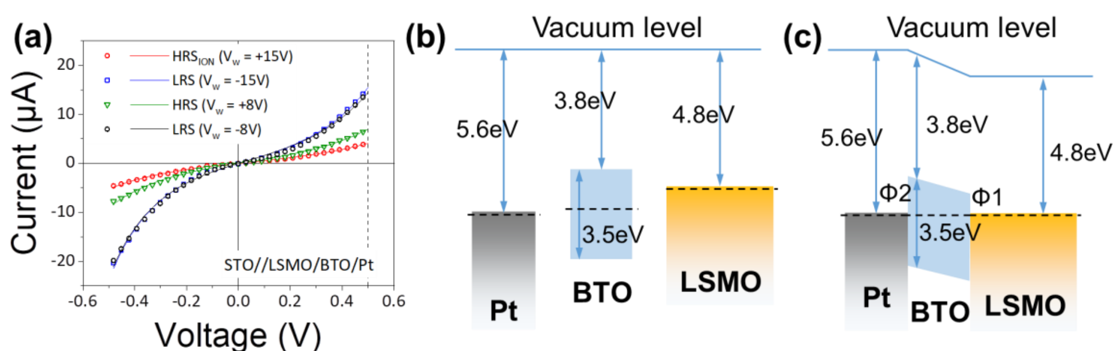

Figure 5.14 Tunneling current and barrier analysis. (a) I(V) characteristics measured at room temperature on BTO junction of 4 nm. The I(V) curves were measured for different resistance state: HRS_{ION} (V_W = +15 V), LRS (V_W = -15 V, -8 V), and HRS (V_W = +8 V). All the τ_W used here was constantly 1ms. (b) Sketch of the band structure before contact. (c) Sketch of band structure in the equilibrium state after contact.

Table 5.1 Fitting parameters obtained from I(V) curves in Figure 5.14 (a).

V_W (V)	Φ_1 (eV)	Φ_2 (eV)	d (nm)
-15 V	0.5	1.5	4.7
-8 V	0.5	1.4	4.7
+8 V	0.5	1.4	5.2
+15 V	0.6	1.8	4.9

Appendix. 5.10 Thickness dependence of the tunneling current in LSMO/BTO

Figure 5.15 shows the resistance of junctions of several samples of different thickness grown in nominally the same conditions to that reported in the main text and its dependence of the polarization direction dictated by writing pulses of V_W = ±5 V. It can be appreciated that, for both polarization states (up and down triangles), the resistance increases roughly exponentially with thickness.

We also include the resistance values at the HRS obtained by suitable illumination (circles). The coincidence of HRS obtained by voltage pulses and illumination is remarkable.

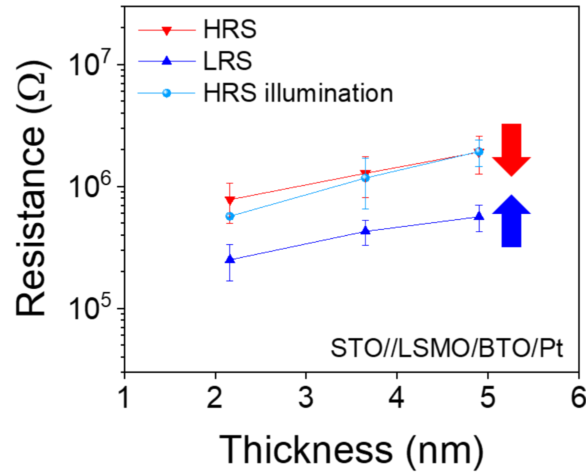

Figure 5.15 Resistance of samples of different thickness. Resistance dependence on BTO thickness of the voltage (downward red triangle) and light (blue circles) written HRS states and LRS (upward blue triangle) state in STO//LSMO/BTO/Pt sample. Error bars correspond to standard deviation of 5 measurements.

Appendix. 5.11 ER dependence on τ_W

Figure 5.16 (a-e) shows the $R(V_W)$ loops collected for different τ_W. In Figure 5.16 (f), LRS, HRS and HRS_{ION} states, corresponding to resistance measured after V_W = -15, +8 and +15 V, respectively, dependence on τ_W is plotted. It can be observed that the two resistance states LRS and HRS are visible irrespective of τ_W, while the HRS_{ION} only appears at $\tau_W > 500$ μs.

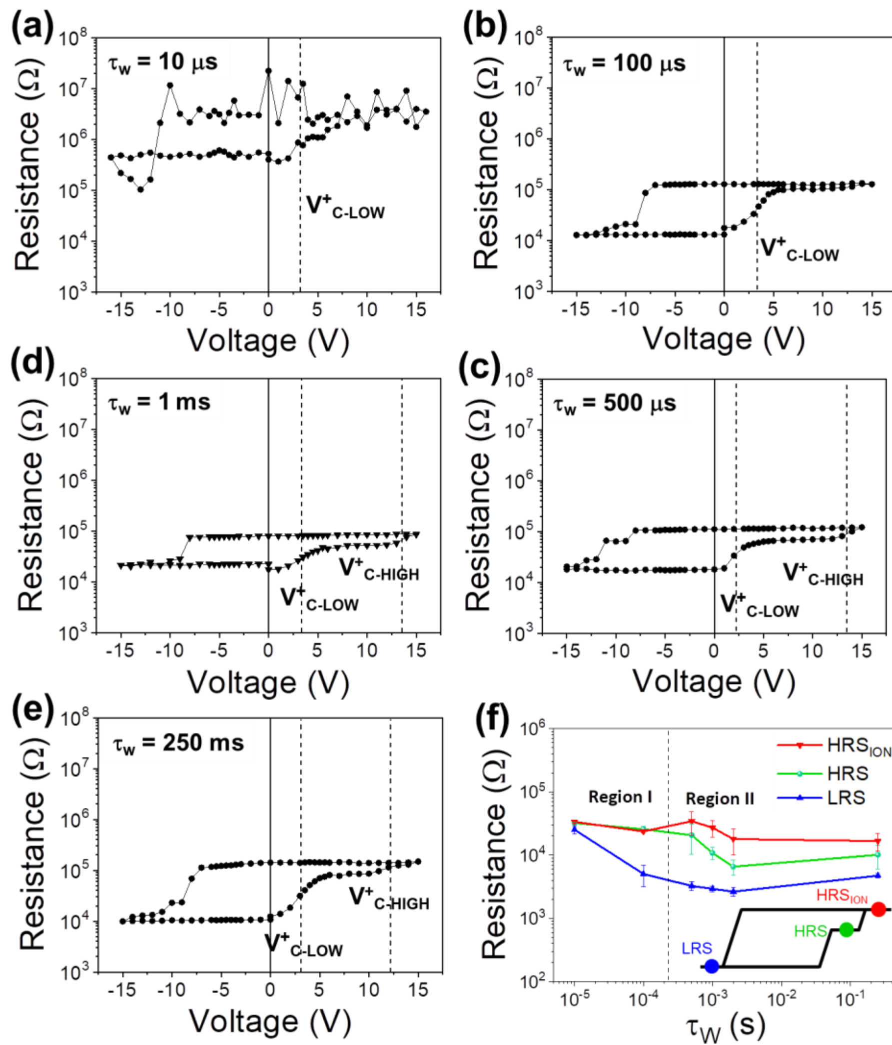

Figure 5.16 ER dependence on τ_W. $R(V_W)$ loops (from -15 V to 15 V) were collected in a series of writing time (τ_W from 10^{-5} s to 0.25 s), in the LSMO/BTO sample: (a-e). (f). Dependence of HRS_{ION} (red), LRS (blue) and HRS (green) on τ_W. The plot is divided into two regions depending on whether HRS_{ION} is absent or not. Error bars correspond to standard deviation of 5 measurements.

Appendix. 5.12 ER dependence on τ_W in several junctions

Figure 5.17 shows ER dependence on τ_W in four junctions, which show similar behavior of data shown in Figure 5.16 (f), although some variability in the absolute resistance values is observed.

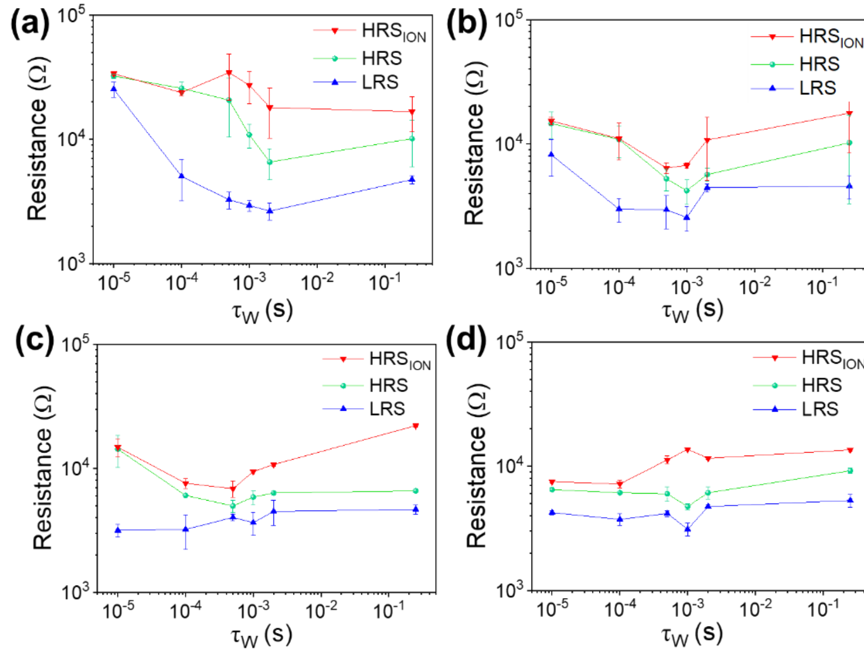

Figure 5.17 ER dependence on τ_W in several junctions. Dependence of different resistance state (HRS_{ION}, red; LRS, blue; HRS, green) on writing time recorded in 4 junctions. Error bars correspond to standard deviation of 5 measurements.

Appendix. 5.13 PFM characterization under red laser illumination

In Figure 5.18 (a)(b)(c), PFM-phase images just after, 10 min after and after 10 min of red (λ = 638 nm, E = 1.94 eV, 9 W/cm^2) laser illumination after electrical writing, respectively, are shown. No change is observed. LSMO is expected to absorb red light due to its small bandgap of 0.6 eV.[172] Instead, BTO is not expected to not absorb light due to its greater bandgap (E_g = 3.3 eV),[162] much above E = 1.94 eV. Thus, if LSMO has a relevant role in the polarization

switching under blue light illumination, the polarization switching should be reproducible under red illumination. Instead, if BTO has a relevant role in the polarization switching under blue illumination, the polarization switching is expected to not be reproducible under red illumination. Therefore, the results summarized in Figure 5.18 (a)(b)(c) disregard important contribution from LSMO bottom electrode in the polarization switching under blue illumination. The results shown in Supplementary Figure 5.18 also disregard important contribution of thermal effects, which should be similar for red and blue illumination.

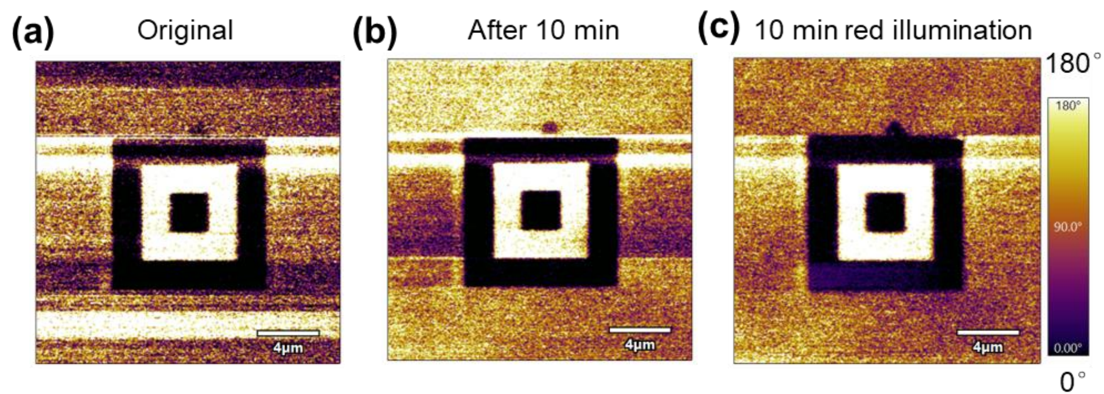

Figure 5.18 PFM phase contrast under red illumination. (a) PFM phase images collected just after electrical lithography with +8 (bright) and -8 V (dark). (b) PFM phase images collected 10 min after electrical lithography with +8 (bright) and -8 V (dark). for the LSMO/BTO sample. (c) PFM phase images collected after 10 min illumination with red light red (λ = 638 nm, E = 1.94 eV, 9 W/cm^2) after electrical lithography with +8 (bright) and -8V (dark).

Appendix. 5.14 Photoconductance of the bottom electrode (LSMO)

We have measured the dependence of the resistivity of LSMO on illumination by using the same conditions (same power and wavelength) than used in the experiments reported in the manuscript. Using a 4-probe configuration, the

resistance of the bottom layer in dark and under illumination has been recorded. In Figure 5.19, below we show the results. The resistivity is ≈ 1 mΩ·cm in agreement in literature data for similar films. Any photoresistance in our films is below noise level (<< 1 mΩ·cm). This observation excludes a contribution of LSMO photoconductance to the resistance changes observed in the manuscript.

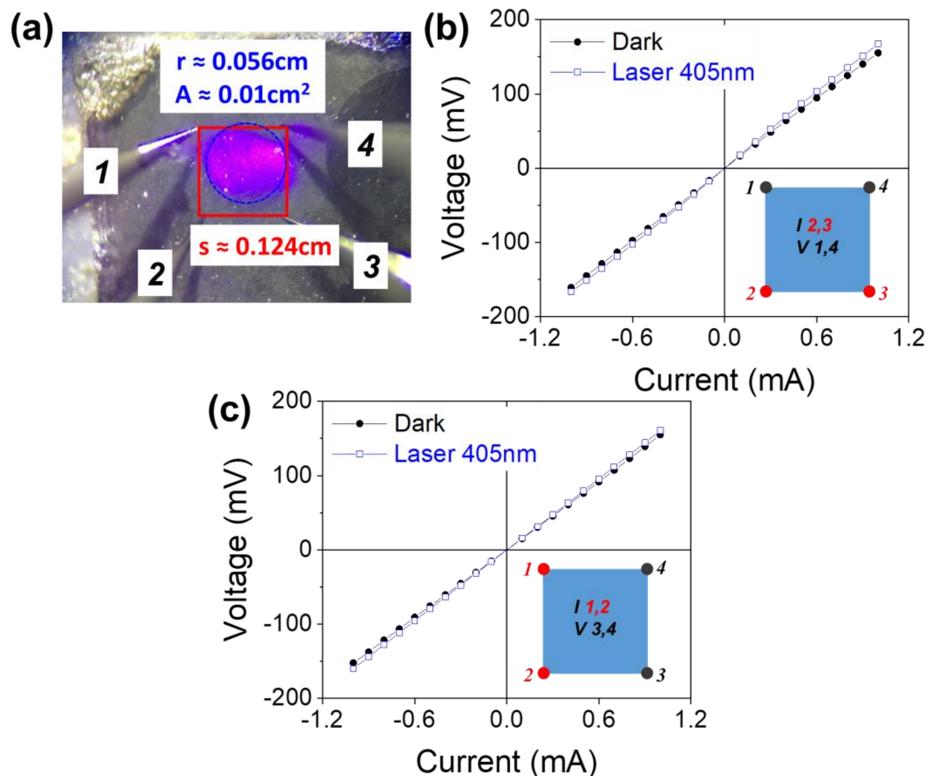

Figure 5.19 (a) Experimental set up to measure the LSMO film resistivity in the LSMO/BTO sample. Four needles adjacent to an array of 4 neighboring 4 Pt are used to measure in 4 probe configuration the LSMO resistivity. (b)(c) I(V) measurements recorded in two different configurations, obtained by permuting current and voltage probes. Date recorded in dark (black symbols) and under illumination (blue symbols) are shown in (b) and (c).

Appendix. 5.15 Resistance drop under illumination

Figure 5.20 shows $R(V_W)$ loops measured sequentially in dark (black solid squares), under illumination (blue solid circles) and after illumination (black solid squares) in 3 different junctions of STO//LSMO/BTO/Pt sample. It can be observed that the loop collected under illumination always show less contrast that in dark conditions irrespectively if the loop is collected before or after illumination. It can be also observed that the loop measured in dark after illumination is not the same than the one measured before, indicating some irreversibility during the illumination process discussed in the main text.

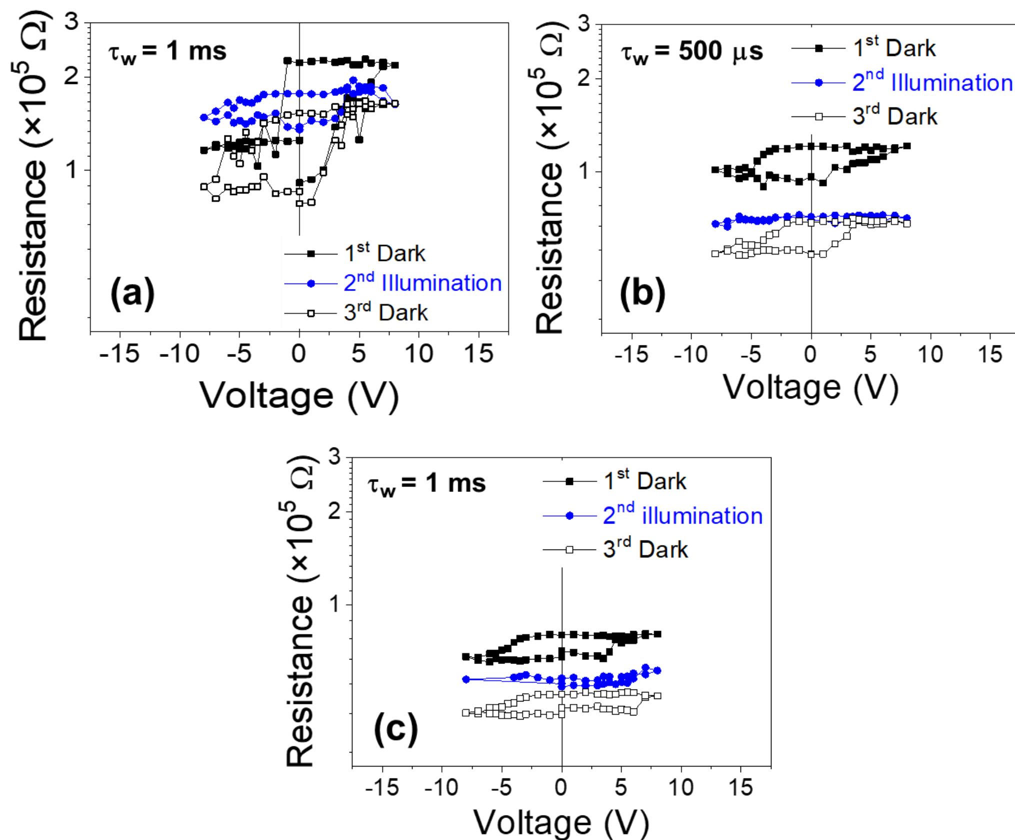

Figure 5.20 Non-reversible photoresponse. $R(V_W)$ loops collected (-8V ~ 8V) in LSMO/BTO samples following the sequence: dark → illumination → dark.

Appendix. 5.16 Reproducibility of the measured ER loops in heterostructures

Figure 5.21 shows illustrative $R(V_W)$ loop recorded loops recorded using different writing times (τ_W = 1 μs, 2 ms) and in different junctions, in STO//LSMO/STO/BTO/Pt heterostructures. Observation of these loops clearly reveal than the main features are well reproducible.

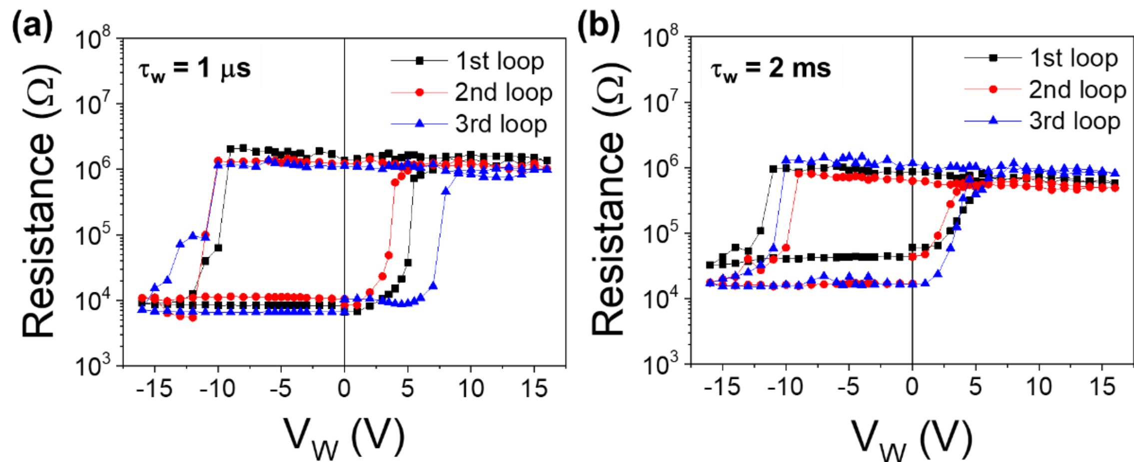

Figure 5.21 $R(V_W)$ loop reproducibility. Illustrative examples of the reproducibility of the major ER loops in two different junctions in a STO//LSMO/STO/BTO/Pt sample for different writing time: (a) 1 μs, (b) 2 ms. Data show the reproducibility of ER loops over several cycles of operation.

Appendix. 5.17 ER endurance in LSMO/BTO sample

HRS and LRS states obtained sequentially by the application of hundreds of ±8V pulses (V_{C-LOW} < 8V < V_{C-HIGH}) are shown for the LSMO/STO/BTO sample in Figure 5.22. As shown in the manuscript, at this rather voltage, ionic conduction contribution is negligible for ER. The data collected for up to 200 cycles demonstrate that the two resistance states remain constant and are well distinguishable. In other words, the device can be robustly switched. The

observed variations of resistance can be ascribed to electrical noise and mechanical instabilities.

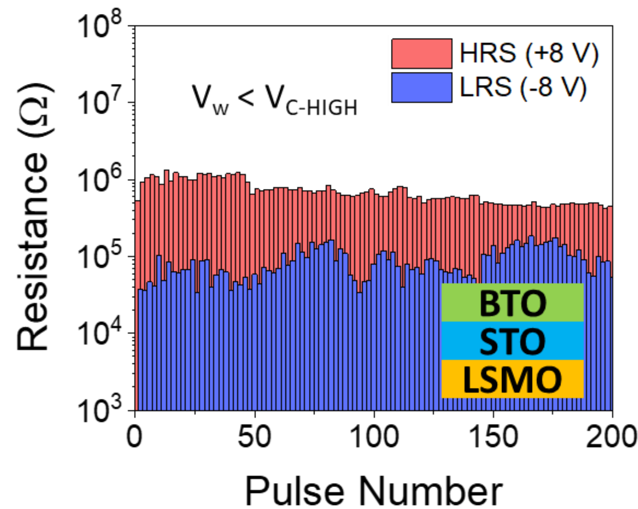

Figure 5.22 Endurance for LSMO/BTO sample. Endurance of HRS states and LRS states written by ±8 V in a junction of STO//LSMO/STO/BTO/Pt sample.

Appendix. 5.18 Suppression of ionic effect in LSMO/STO/BTO sample

Figure 5.23 shows $R(V_W)$ loops collected for indicated τ_W for the LSMO/STO/BTO sample. It can be observed that the $V^{+}_{C\text{-}LOW}$ is well-visible, whereas the $V^{+}_{C\text{- }HIGH}$ is not, indicating the suppression of the HRS_{ION} state. This indicates that the introduction of the STO dielectric layer contributes to mitigate the ionic effect.

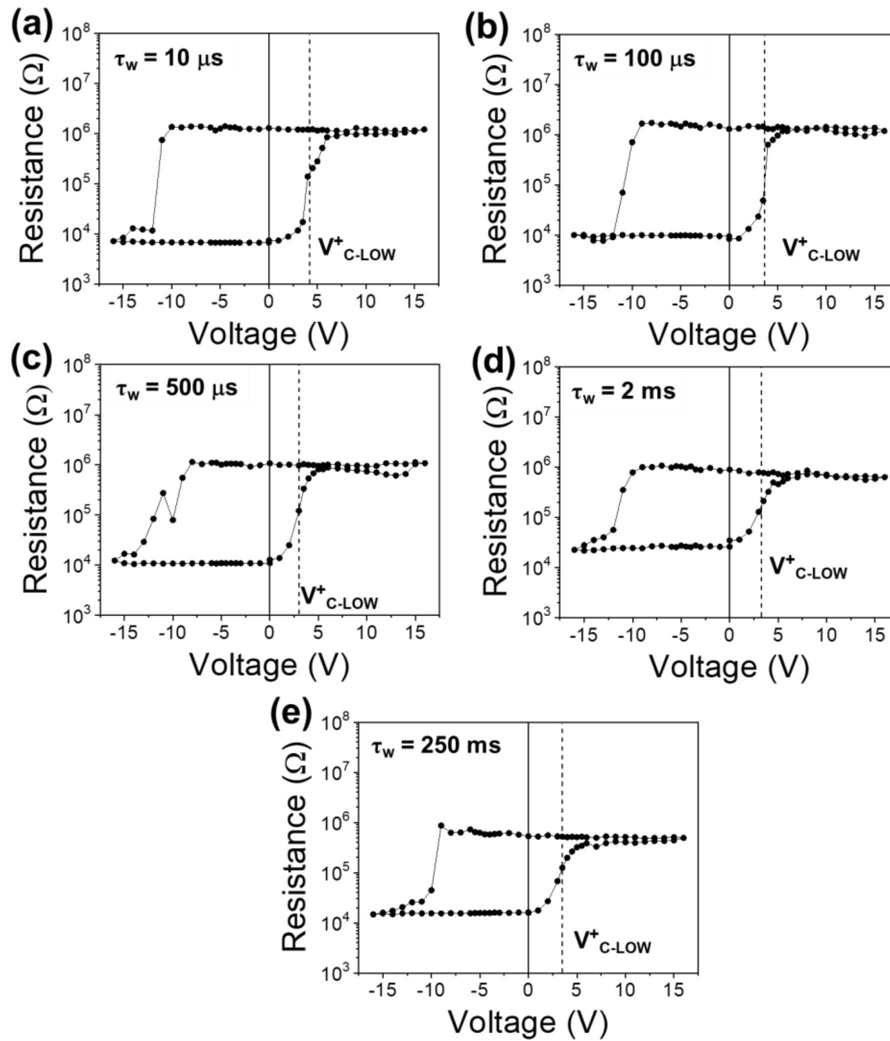

Figure 5.23 Suppression of ionic effect in LSMO/STO/BTO sample. (a-e) $R(V_W)$ loops collected for indicated τ_W for the LSMO/STO/BTO sample.

Appendix. 5.19 Reproducibility of photoinduced switching

In Figure 5.24, we depict the resistance obtained after electrical and optical writing for several junctions. Although, as mentioned in the main manuscript, absolute resistance values display some sample-to-sample variability, the optical switch of resistance is systematic observed.

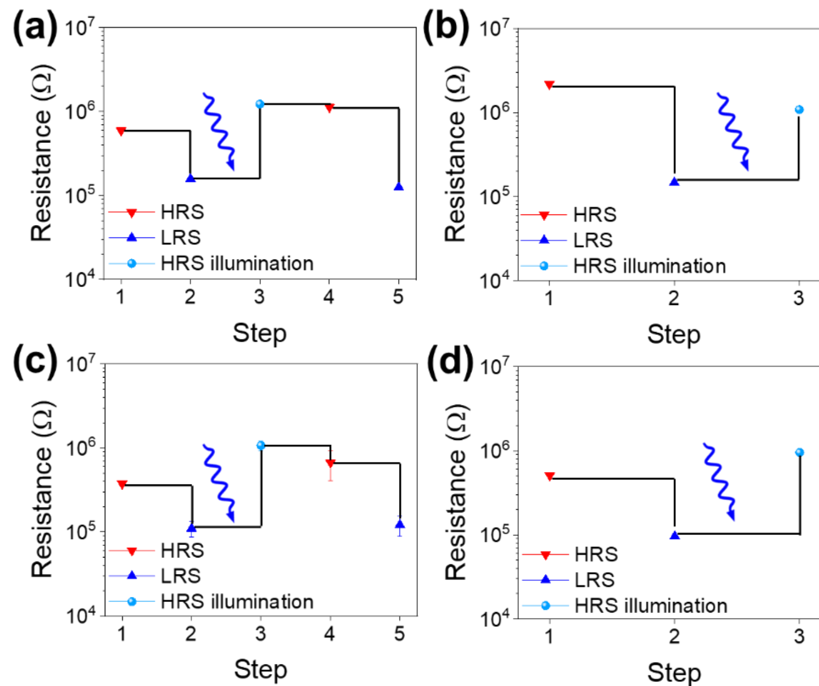

Figure 5.24 Optical switch stability for different junctions. (a-d) Resistance states obtained sequentially after electrical and optical stimuli (as indicated) for several junctions, respectively. In this example: $V_W = \pm 8$ V. Illumination is performed with the same condition to Figure 5.4.

Appendix. 5.20 Dependence of ER and optical suppression of ER on junction area

In Figure 5.25, we show data for STO//LSMO/STO/BTO/Pt. The switching response is clearly observed using both electrodes (Figure 5.25 (a)) and in the corresponding ER loops (Figure 5.25 (b)). In Figure 5.26, additional data collected in different junctions of 7 μm size in STO//LSMO/STO/BTO/Pt hetersostructure is shown. Data corresponding to the junctions of 20 μm size shown in Figure 5.26 (b) is also included for comparison. In data in Figure 5.25 and Figure 5.26 it can be appreciated that junction resistance and the ER are larger in the smaller junctions, as commonly found. This is typically related to

the existence of non-switchable low-resistance channels in the barriers. The fact that the effect is area-dependent disregards filamentary conduction as triggering mechanism of the found effect. In Figure 5.27, the ER suppression under illumination for electrodes of different sizes is shown. It can be observed that the suppression under illumination is robust, irrespectively of the electrode size.

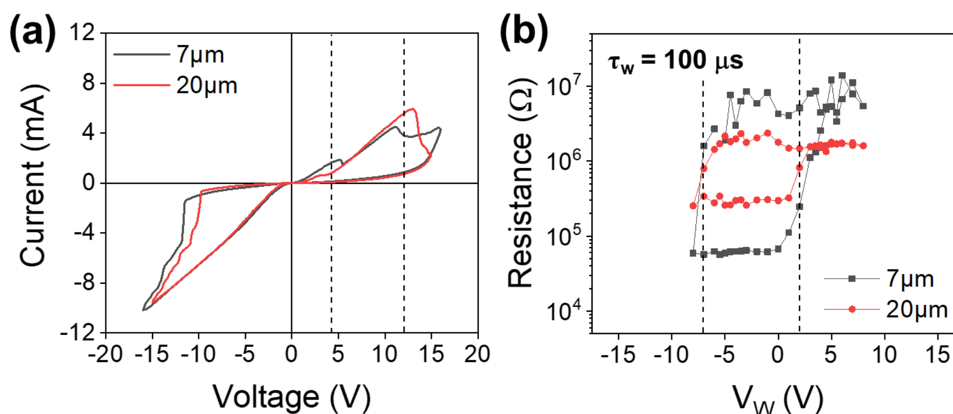

Figure 5.25 Dependence of ER on electrode area for STO/BTO sample. (a) Illustrative examples of the I(V) curves and (b) ER recorded in dark in junctions in STO//LSMO/STO/BTO/Pt having electrodes with diameter of 7 μm and 20 μm, as indicated.

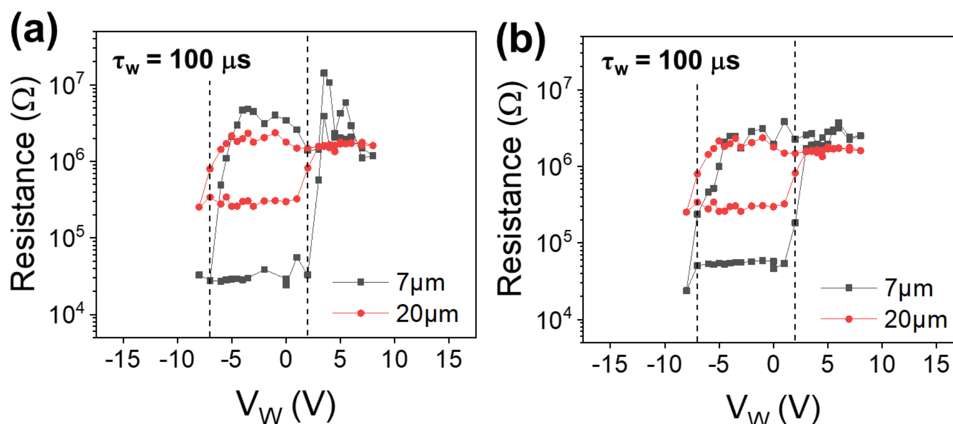

Figure 5.26 Dependence of ER on electrode area for STO/BTO sample. (a),(b) Illustrative ER loops recorded in dark in different junctions, respectively, in

STO//LSMO/STO/BTO/Pt having electrodes with diameter of 7 μm, as indicated. Reference loop obtained in the representative 20 μm junction of Figure 5.25 (b) is also included in both panels.

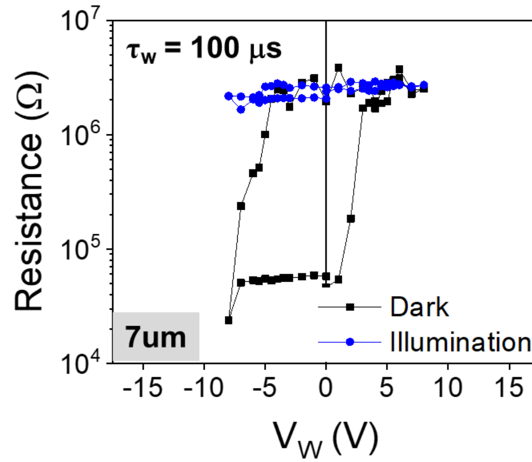

Figure 5.27 Dependence of optical switch on electrode area for STO/BTO sample. Illustrative ER loops recorded in dark and under illumination in electrodes with diameter of 7 μm of STO//LSMO/STO/BTO/Pt sample.

Appendix. 5.21 Leakage subtraction

In Figure 5.28, we show ferroelectric characterization performed on both LSMO/BTO and LSMO/STO/BTO samples. I(V) characteristics collected at 5 kHz in top-top configuration show important leakage contribution. Superimposed to it clear ferroelectric current switching peaks are observed (enclosed by circles). Its contribution has been isolated by fitting the leakage contribution to an exponential dependence and subtracting it from the raw data. Free of leakage I(V) and P(V) loops shown in Figure 5.2 (d) and Figure 5.3 (d) for the LSMO/BTO and LSMO/STO/BTO samples, respectively are obtained.

The reasonable polarization values obtained indicate that ferroelectric nature of the observed current switching peaks.

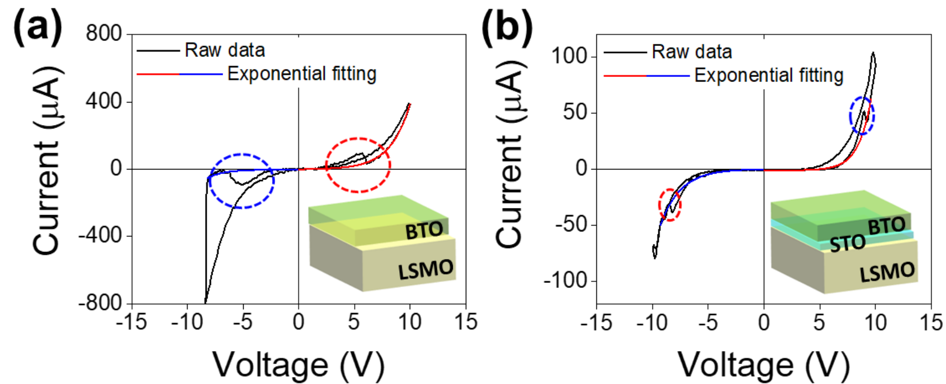

Figure 5.28 Leakage subtraction. (a) Illustrative examples of the I(V) curves collected at 5 kHz for the LSMO/BTO sample. The leakage contribution has been fitted by exponential curve. This contribution has been removed from the I(V) characteristics and the subtracted curve is shown in Figure 5.2 (d). (b) Equivalent to (a) data for the LSMO/STO/BTO sample. The subtracted curve is shown in Figure 5.3 (d).

Chapter 6. Disentangle physical origin of light induced resistive switch

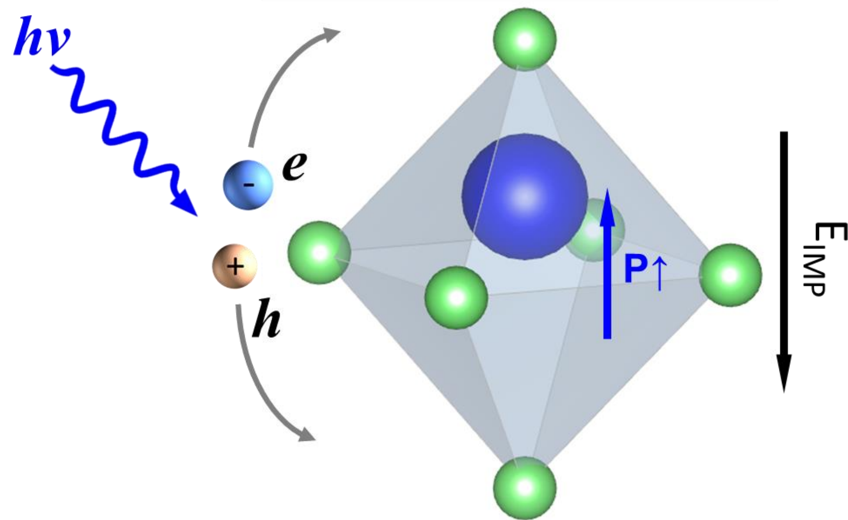

The results of this chapter is an extension to Chapter 5. The work has been submitted, entitled "Disentangling electronic and thermal contributions to the observed light-induced resistance switching in $BaTiO_3$ ferroelectric tunnel junction".

Chapter 6. Disentangle physical origin of light induced resistive switch

6.1 Synopsis

As presented in Chapter 5, optical switching of polarization in ferroelectric $BaTiO_3$ (BTO) films and subsequent reversal of low-resistance state (LRS) to high-resistance (HRS) state in ferroelectric tunnel junctions. In this chapter, we aim at disclosing the prevalent mechanism for optically-induced polarization reversal. We study the role of the wavelength of light on the observed response, explore the time-dependence of the photoresponse and elucidate the impact of possible thermal effects. We conclude that the effect is mainly dominated by photogenerated charges rather than heating and we discussed why large light intensity or long illumination times are required to observe the optical polarization/resistance switch of ferroelectric tunnel device.

6.2 Sample

All samples mentioned in this work were grown in-situ by PLD, with structures denoted as: STO//LSMO (30 nm)/BTO (4 nm) (results shown in Supporting Information), STO//LSMO (30 nm)/STO (1 nm)/BTO (4 nm) (denoted as STO/BTO), and STO//LSMO (30 nm)/BTO (70 nm). Both samples were deposited in a single process. Detailed PLD conditions have been introduced in Chapter 5. Top Pt electrodes (20 nm thick) were deposited by sputtering through a stencil mask, allowing obtaining arrays of circular contacts of 20 μm diameter, and square contacts of 60×60 μm^2.

6.3 Results

6.3.1 Light-induced ER suppression

ER loops were collected in dark and under illumination in a LSMO/STO/BTO (4 nm)/Pt junction, with a top Pt circular electrode (diameter 20 m), as illustrated in Figure 6.1 (inset). The ER loop measured in dark (Figure 6.1, squares) shows a HRS ($\sim 6 \times 10^5\ \Omega$) corresponding to polarization down (P_{DOWN}, towards LSMO), and a LRS ($\sim 2 \times 10^5\ \Omega$) corresponding to polarization up (P_{UP}, towards Pt) with ER = (HRS - LRS)/LRS ≈ 200 %. Note the obvious existence of an imprint field, as revealed by the shift towards negative voltage of the ER loop (blue vertical line). The imprint field is -4.4 MV/cm towards LSMO indicating that P_{DOWN} is the most stable state. The ER loop collected under illumination using a $\lambda = 405$ nm laser beam of power density of 9 W/cm^2 is also shown (Figure 6.1, circles). It can be readily appreciated that ER is virtually suppressed, definitely smaller (ER ≈ 0) than the ER recorded in dark. Note also that the resistance value of the ER loop collected under illumination roughly equals to the HRS of the ER loop in dark. Finally, ER loop is collected again in dark (Figure 6.1 , triangles). It can be observed that ER loop recovers its initial shape with magnitude (ER ≈ 200 %).

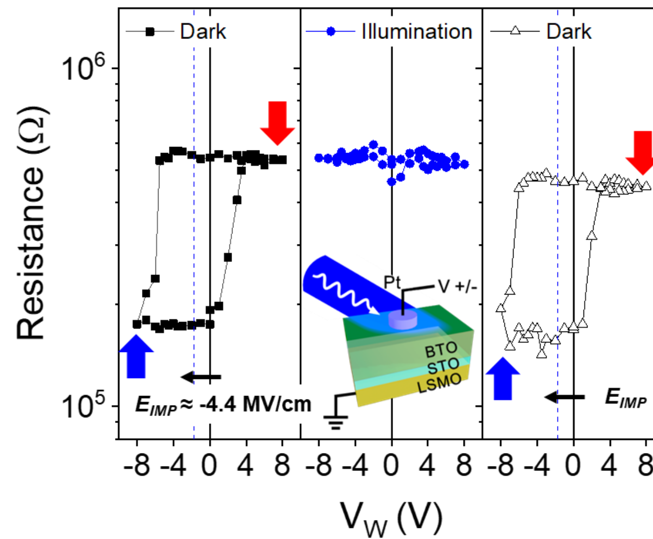

Figure 6.1 R(V_W) loops collected using τ_W = 100 μs in STO/BTO junction (inset sketch of the structure), collected with the following sequence: (1) dark (black solid symbols, left pannel); (2) under (blue, λ = 405 nm, 9 W/cm^2) illumination (blue symbols, middle pannel); (3) dark again (black open symbols, right pannel). Red and blue arrows indicate polarization direction, and blue dash line indicates the center of the ER loop measured in dark and indicates the existence of an imprint field (pointing towards the bottom electrode (black arrow) (E_{IMP} ≈ -4.4 MV/cm).

6.3.2 Resistive switching dependence on wavelength

Resistance as a function of time [R(t)] has been measured when the sample was illuminated using different light wavelength (blue λ = 405 nm, red λ = 638 nm) [sketches Figure 6.2 (a,b)]. Pre-poling was conducted in dark before illumination, by using a trapezoid pulse of amplitude V_W = +/- 8 V and τ_W = 100 μs, to set a specific initial state [either HRS(P_{DOWN}) or LRS(P_{UP}) indicated by red/blue triangles in Figure 6.2 (c,d,e,f)]. The power density for each light

wavelength is fixed at 1.4 W/cm^2, time of illumination lasts for ~200 s [blueish background in Figure 6.2 (c,d,e,f)]. In Figure 6.2 (c), we show the R(t) after setting the LRS. Data shows that under blue illumination the resistance gradually rises from initial LRS to a final HRS that closely coincide with the HRS dark value at ~100 s. In sharp contrast, when a HRS is set in dark, illumination does not modify at all the resistance state, i.e. it remains at HRS [Figure 6.2 (d)]. Considering that resistance of these ferroelectric tunnel junctions is determined by the remnant polarization, the results shown in Figure 6.2 (c,d) indicate that light has induced a polarization reversal from P_{UP} to a final state P_{DOWN}. Importantly, the polarization direction in the final state (P_{DOWN}) is coherent with the direction of imprint field (pointing down towards LSMO). In Figure 6.2 (e,f), we plot R(t) of similar experiments but collected using the red light. Irrespectively if the initial state is set to LRS or HRS, light does not appear to produce any significant change. Direct evidence of light induced reversal of the remnant polarization from P_{UP} to P_{DOWN} but in the reverse case, has also been observed in a LSMO/BTO (4 nm) sample using PFM (see Appendix. 6.1). The resistance recorded under a sequence of different electric/optical (red and blue) stimuli has revealed that resistance switch to HRS (P_{DOWN}) is only produced under blue light if LRS is set (P_{UP}) (see Appendix. 6.2). Therefore, the light wavelength and the initially set state determine the occurrence of resistance switch under illumination.

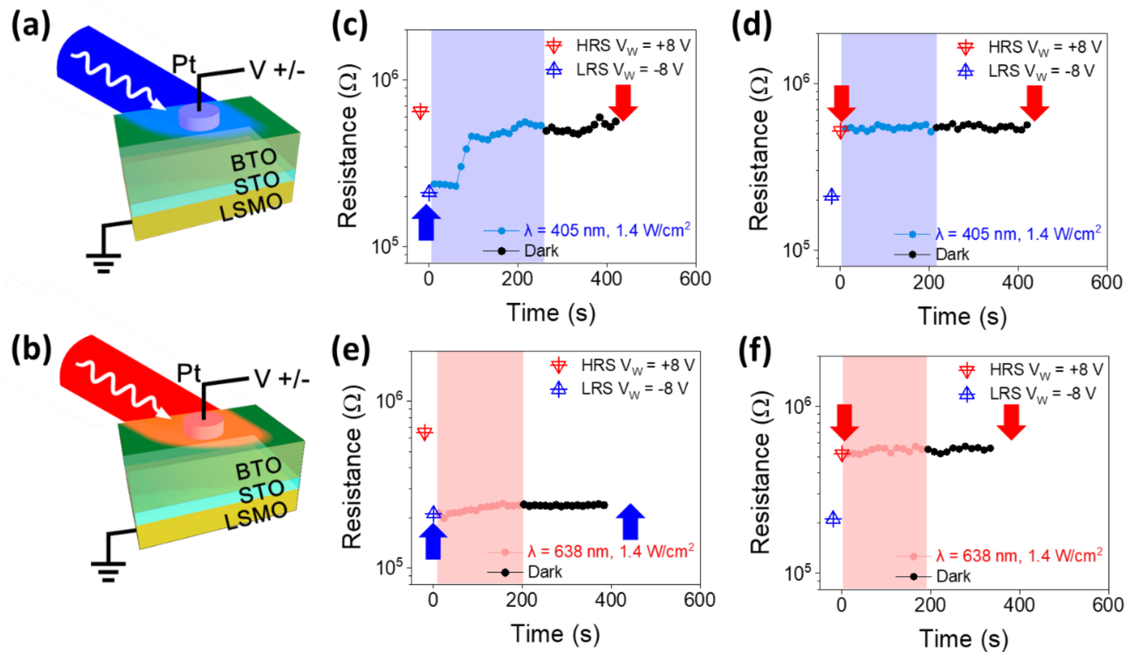

Figure 6.2 (a,b) Sketch of the sample and electric configuration under different illumination conditions, both with blue and red light. (c,d) Resistance data collected as function of time initially starting from HRS or LRS (up blue and down red triangles) respectively. In both cases, resistance was recorded and the illumination period (200 s) with blue light ($\lambda = 405$ nm, 1.4 W/cm^2) is indicated with a blueish background in each panels, and then continuously recorded in dark for a period of time. (e,f) Idem for red illumination ($\lambda = 638$ nm, 1.4 W/cm^2) during the time laps indicated by the reddish background.

6.3.3 Photoresponse dependence on wavelength

In order to further investigate the photoresponse dependence on wavelength, we measured photocurrent generated under blue and red-light illumination. Figure 6.3 (a) shows the short-circuit photocurrent as function of time. Data shows that under blue illumination [blueish region in Figure 6.3 (a)] a clear $j_{sc} \approx 12$ μA/cm^2 develops. The I-V curve under illumination is shown in Appendix. 6.3. Instead,

no short circuit photocurrent develops under red illumination [reddish region in Figure 6.3 (a)] for blue illumination. Note that the generated photocurrent is very small and thus it does not affect significantly the measured resistance (corresponding to a current density of ≈ 150 mA/cm^2) shown in Figure 6.1 and Figure 6.2. The difference in photo response depending on the used wavelength, is expected from the fact that blue light wavelength is 3.06 eV, near BTO bandgap (E_g = 3.3 eV). Although, the photon energy is somewhat smaller than the bandgap of BTO, deep or shallow levels can contribute to a significant photon absorption.[173–175] In the case of red light, with photon energy 1.9 eV, photoabsorption and thus photocarrier generation should be much depressed, which is consistent with the absence of short-circuit photocurrent. Besides, the absence of any effect of the device resistance when using red illumination indicates that photon-induced thermal effects are also negligible. Therefore, polarization reversal under illumination (blue) is neither ruled by thermal effects. Complementary finite elements calculation of photoinduced thermal effects allows us to conclude that the sample temperature increase could not larger than 4 °C, thus the temperature increase unlikely produces any polarization reversal (see Appendix. 6.6). In summary, a plausible scenario is sketched in Figure 6.3 (b), where the energy profile of the LSMO/BTO/STO/Pt device is depicted. The direction of the imprint field E_{IMP} and the initial state of polarization P_{UP} (LRS) is indicated. The electron-hole pairs generated by blue photons within BTO come to screen P_{UP} and P is switched to P_{DOWN} following E_{IMP}.

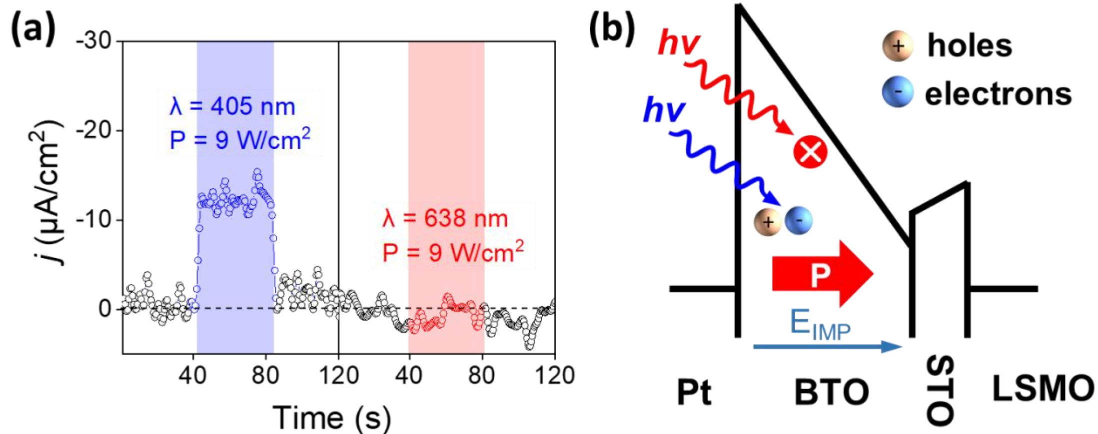

Figure 6.3 (a) Photoresponse in the LSMO/STO/BTO/Pt heterostructure junction, respectively to blue and red light. The light power was fixed at 9 W/cm^2. (b) Sketch of the same heterostructure demonstrating the possibility of near bandgap excitation that can happen in BTO film only triggered by blue light (λ = 405 nm, E = 3.06 eV) but not by red light (λ = 638 nm, E = 1.9 eV).

6.3.4 Response speed dependence

An additional salient observation in Figure 6.2 (c), is the remarkably slow switching process (≈ 100 s). This slow response is not expected from photovoltaic response, because carrier generation is an exceedingly faster process.[176] To get a hint into the ultimate reason for this relatively slow process, we compare the photoinduced change of resistance in BTO ferroelectric capacitors where the thickness of the photoabsorbing layer (BTO) largely differs. In Figure 6.4 (a), we show data collected in a LSMO/STO/BTO (4 nm)/Pt and LSMO/BTO (70 nm)/Pt junctions, under blue photon illumination at 0.1 W/cm^2 power density. Note that the STO (1 nm) layer is not present in the thicker film, which does not affect the conclusions discussed as follows.

Consistent with results of Figure 6.2 (c), for the 4 nm BTO junction, an illumination time of ≈ 100 s is needed to switch gradually from LRS to HRS. In contrast, the 70 nm BTO junction respond faster to illumination and the required time for LRS to HRS transit is of only ≈ 70 s. Note that in this thicker film resistance is most probably controlled by the Schottky barrier height, which itself is modulated by the ferroelectric polarization, rather than tunneling.[171] In any event, data above suggest that concentration of photocarrires, which is ultimately limited by the BTO thickness, is a crucial parameter to account for the different time response. An additional insight can be derived from R(t) measurements under different laser power. In Figure 6.4 (b) we show R(t) data collected in STO/BTO (4nm) junction at different power density: 0.1, 1.2, and 9 W/cm^2. Data clearly shows that by increasing light power, the time scale for resistance state change shortens from ~200 s to ~50 s. Similar effects are observed in the BTO (70 nm) capacitors (See Appendix. 6.4).

Therefore, Figure 6.4 (a,b) shows that faster change of resistance is observed in thicker BTO film and using higher light power intensity. Therefore, it can be inferred that the total amount of photogenerated charges is a relevant parameter determining the time scale for polarization and resistance switching under illumination, because photogenerated charges increase both for thicker BTO films and when using larger light power density. These results agree with data shown in Figure 6.4 (c), where it is shown that the short-circuit photocurrent increases with power and sample thickness. According to earlier reports by Dimos and Warren and Land and Peercy[177–186] photogenerated charges play a role as screening polarization in perovskite materials.

To evaluate the role of the photogenerated charges in the photoresponse, we have calculated the charge generated under illumination, using reported absorption and efficiency of BTO films (α = 500 cm^{-1} and η = 0.6 %)[187] following the procedure described in Appendix. 6.5. Figure 6.4 (d) shows the calculated time-dependent accumulated charge density (Q/A) under the electrodes of surface A, using a blue photons and 0.1 W/cm^2 power density for a 70 nm and 4 nm films. Accumulated charge is obtained from the integration through time of the simulated photocurrent. For 70 nm film, the illumination time to achieve P ≈ 25 μC/cm^2, which is similar to the remnant polarization of bulk BTO, is about ≈ 30 s, which indicate that the time to screen the polarization of bulk BTO would be τscreen ≈ 30 s. For the 4 nm film τ_{screen} ≈ 500 s is obtained. The different τscreen values obtained in thick and thin BTO capacitors are fully consistent with experimental values. In Figure 6.4 (e), the accumulated charge on time dependence for different light power is shown. For 9 W/cm^2 the τ_{screen} ≈ 10 s is obtained, whereas for 1.2 W/cm^2, τ_{screen} ≈ 50 s and for 0.1 W/cm^2, τ_{screen} ≈ 700 s. The trend and order of magnitude of results shown in Figure 6.4 (d,e) coincides with those shown in Figure 6.4 (a,b), despite absorption and efficiency of the characterized films can differ to the tabulated one. In Figure 6.4 (f), accumulated charge for different α and η values is shown. We can see that the modification of both parameters has an important impact on τ_{screen}. In particular, τ_{screen} decreases with efficiency and absorption increase. This result also gives the hint about obtaining faster optical switching of resistance using more absorbing / more efficient ferroelectric materials.

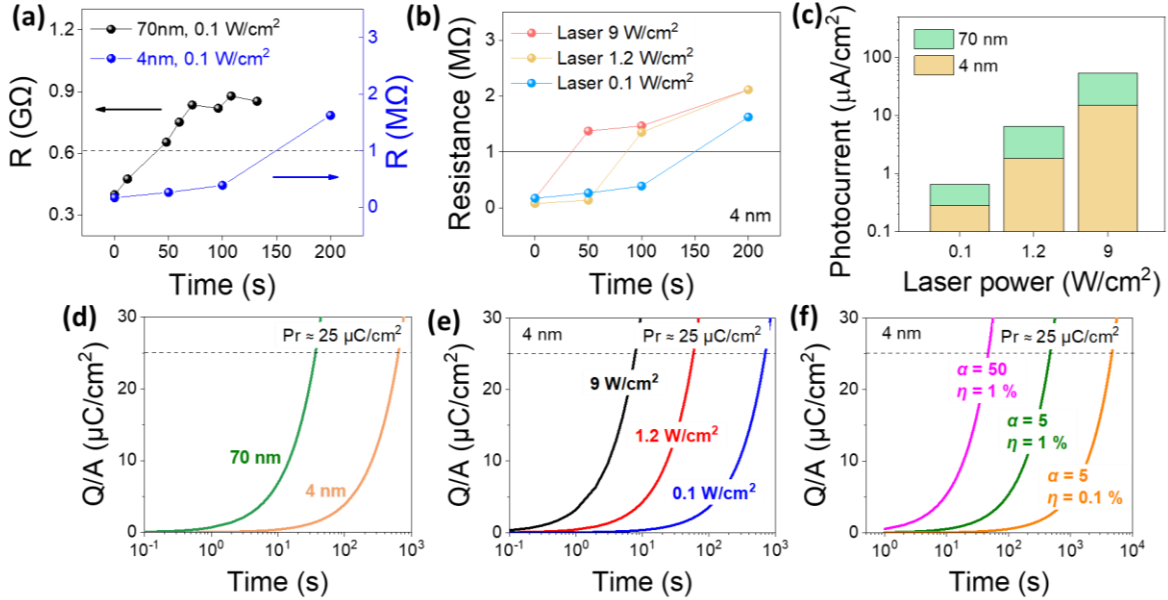

Figure 6.4 (a) Resistance data collected as function of illumination time with different BTO thickness (4, 70 nm), illumination power is fixed at 0.1 W/cm². Initial LRS is defined by a pre-poling pulse (-8 V, 100 μs); (b) Resistance data collected as function of illumination time with different light power (0.1, 1.2, 9 W/cm²) in 4 nm BTO heterojunction; The resistance value for both cases were extracted at a reading voltage of 0.5 V. (c) Photocurrent dependence on BTO thickness (4, 70 nm) and light power (0.1, 1.2, 9 W/cm²); (d) Simulation of Q/A value as a function of time in BTO film with different thickness (4, 70 nm), with fixed 0.1 W/cm² and assuming α = 500 cm⁻¹, η = 0.6 %; (e) Simulation of Q/A value as a function of time in 4 nm BTO film varying by light power (0.1, 1.2, 9 W/cm²), assuming α = 500 cm⁻¹, η = 0.6 %; (f) Simulation of remnant of Q/A value in 4 nm BTO film with different absorption (α) and efficiency (η) parameters, with a fixed 9 W/cm².

6.4 Conclusion

We have studied light induced polarization switching and concomitant resistance changes in BTO-based capacitors where BTO layer is thin enough (≈

4 nm) to allow tunnel transport or thick enough (≈ 70 nm) to impose interface-limited conductance, f.i. Schottky barriers. In both cases it has been shown that, in presence of an imprint field, photoabsorption promotes a unidirectional resistance switch from LRS to a HRS, that we have attributed to polarization reversal. Wavelength dependent experiments indicate that the observed light-induced polarization reversal suppression is related to photovoltaic effect, and it is operational using highly energetic photons (blue) but it is absent while using less energetic photons (red). Moreover, data and simulations show that a possible thermal contribution to polarization reversal is negligible. We have shown that the relatively slow time response of polarization and resistance switching (of the order of 100 s) results from the reduced photon absorption of BTO at blue (3.06 eV) as the bandgap of BTO is 3.3 eV and poor photon-carrier conversion efficiency. This study shall be a guidance for future implementation and development on fast optically controlled memristor or visual neural networks.

6.5 Appendix

Appendix. 6.1

Figure 6.5 (a) shows PFM phase image collected after electrical lithography. Bias voltage of V = +/- 8 V was applied to the PFM tip in contact with the sample surface before obtaining the displayed image to define the inner bright and dark regions, respectively. Therefore, dark region corresponds to polarization pointing up and bright region to polarization pointing down. Notice

that the outer region has not been biased and thus it corresponds to the as-grown state with polarization pointing down. In Figure 6.5 (b), the image was collected in the same region after illuminating the sample (λ = 405 nm, 9 W/cm^2, τ_{light} = 600 s). It can be observed that the dark regions with polarization pointing up now has become brighter indicating that in these regions the polarization have almost switched towards down (completely lost contrast between bright and dark region), which corresponds to the as-grown polarization state as E_{IMP} discussed in the main text. However, such a change does not happen when replacing illumination condition with a red light (λ = 638 nm, 9 W/cm^2, τ_{light} = 600 s). As shown in Figure 6.5 (c,d), there is no substantial change in PFM image before and after illumination. From these results, it can be concluded that: (1) the blue illumination has triggered P_{UP} switch to P_{DOWN}; (2) while the illumination of red light does not trigger such a change.

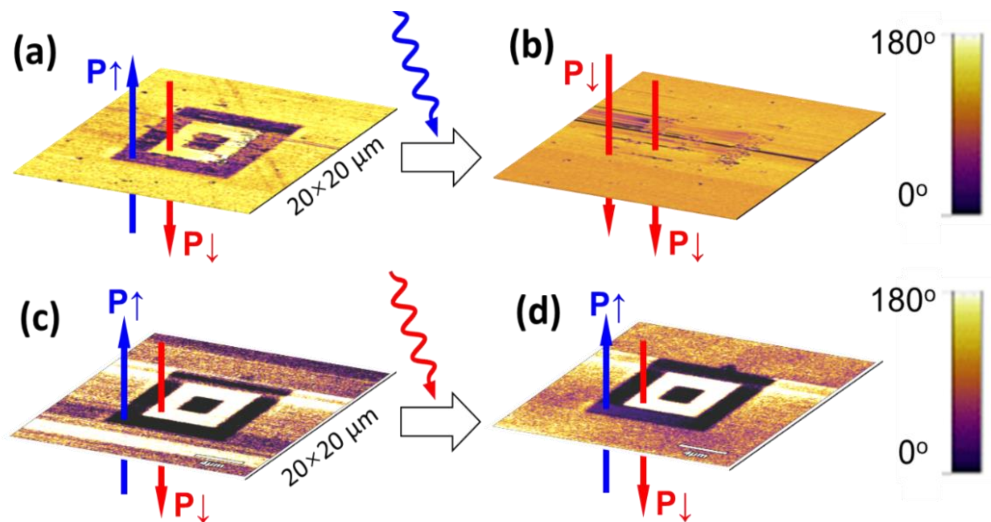

Figure 6.5 (a,c) P_{UP} and P_{DOWN} region were written by applying voltage to the tip -8 V or +8 V, corresponding to dark and bright regions respectively. (b) Idem after illuminating with blue light (λ = 405 nm, 9 W/cm^2). (d) Idem after illuminating with red light (λ = 638 nm, 9 W/cm^2).

Appendix. 6.2

Resistance operation in LSMO/STO/BTO/Pt heterostructure junction, under a series sequence of stimuli [V_W (τ_W = 100 μs), blue-light, red-light]. In Figure 6.6 (a), a HRS (P_{DOWN}) state is written by V_W = +8 V pulse (step 1); then a LRS (P_{UP}) is written by a V_W = -8 V pulse (step 2); LRS remains the same level after illumination of red light (step 3) and remains the same level in dark (step 4); HRS recovered (step 5) after illumination of blue light and remains in HRS in dark (step 6); repeating the previous operation from step 3 to step 5 in the following step 6 to step 9, and any substantial change is not observed. Notice that except step 1 and step 2, the rest are conducted while sample is not prepoled, and the time interval between each step is 200 s. Similarly, in Figure 6.6 (b), a LRS (P_{UP}) state is written by V_W = -8 V pulse (step 1); then a HRS (P_{DOWN}) is written by V_W = +8 V pulse (step 2); then the rest operation was following the same protocol as in Figure 6.6 (a), and no substantial change has been observed. These data illustrate that optically switch from LRS (P_{UP}) to HRS (P_{DOWN}) only occurs using blue light.

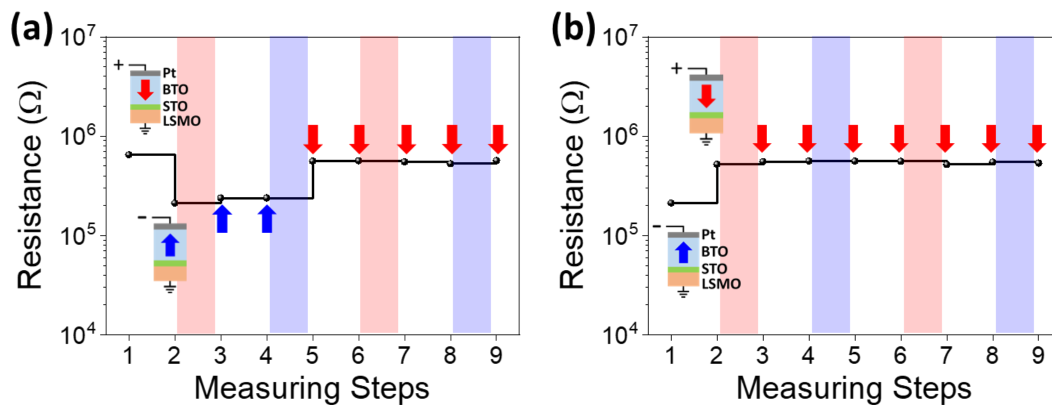

Figure 6.6 Initial state at LRS and HRS are shown in (a) and (b) respectively, and the time interval from step to step is 200 s. Optical illumination is denoted with rectangular transparent strips with color red and blue, representing red light (λ = 638 nm) and blue light (λ = 405 nm). Arrows indicate polarization direction. Notice that a light-induced resistance switch only occurs with blue layer and the previous state is at LRS, as shown in (a) from step 4 to 5.

Appendix. 6.3

Current-voltage measurement was conducted in LSMO/STO/BTO/Pt heterostructure junction, respectively in dark and under blue light illumination (λ = 405 nm, 9 W/cm^2). *j*-V curves are shown in Figure 6.7. Notice that in dark $j_{sc} \approx 0$ under zero bias, while with illumination $j_{sc} \approx -15$ $\mu A/cm^2$ under zero bias. The small j_{sc} discrepancy with the data shown in Figure 6.3 (a) is due to the slightly different illumination limited by the experimental set-up.

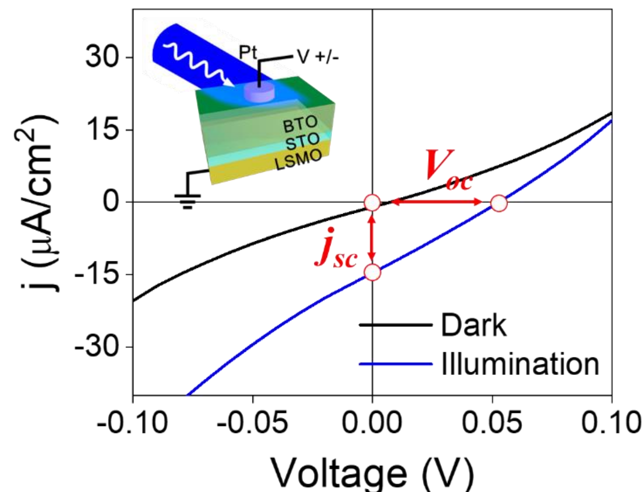

Figure 6.7 Current-voltage curves obtained with and without illumination (black line: dark, blue line: under blue light). Red arrows indicate intercept shift in both axis, which represents the open-circuit voltage (V_{oc}) and short-circuit current (j_{sc}) respectively. Inset sketch shows measurement configuration.

Appendix. 6.4

Resistance data collected as function of illumination time with different BTO thickness (4, 70 nm), with illumination power (9 W/cm^2, 1.2 W/cm^2). In Figure 6.8 (a) resistance changes recorded respectively in two samples when using higher power (9 W/cm^2) show: 70 nm sample needs ~25 s to complete the switch from LRS to HRS; while 4 nm sample needs > 50 s. In Figure 6.8 (b) resistance changes recorded respectively in two samples when using higher power (1.2 W/cm^2) show: 70 nm sample need ~50 s to complete the switch from LRS to HRS; while in 4 nm sample it takes >100 s. Thus, the resistance switch is always faster in a thick BTO sample than in a thinner sample.

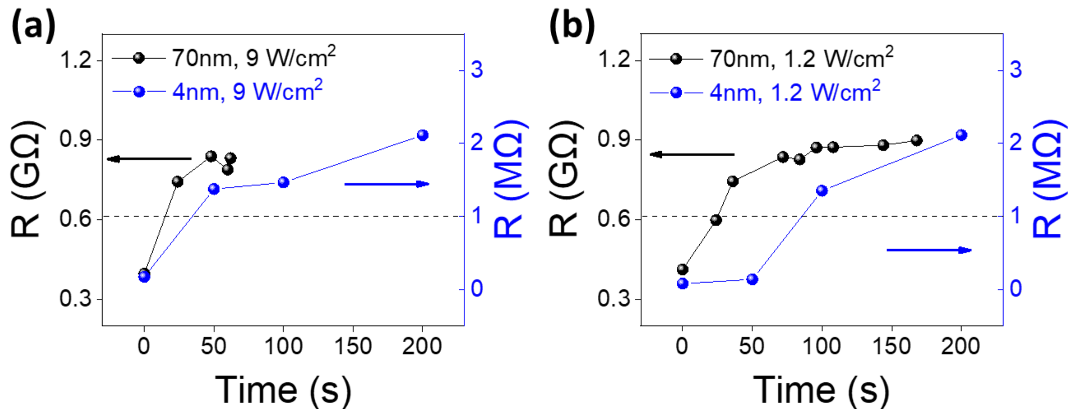

Figure 6.8 Resistance data collected as function of illumination time with different BTO thickness (4, 70 nm), with illumination power (a) 9 W/cm^2 and (b) 1.2 W/cm^2. Initial LRS is defined by a pre-poling pulse (-8 V, 100 μs).

Appendix. 6.5

Simulation based on the model of light absorption and photovoltalic conversion has been conducted to interpret how photogenerated charges dominate response speed. It is known that the concept attenuation describes a gradual reduction of light intensity (W/cm^2) when propagating through a media. The mathematic relation between attenuated light intensity and initial value is following:

$$I(x) = I(0)e^{-\alpha x} \qquad \textit{Equation 6.1}$$

where *I(0)* represents the initial intensity of light before propagating through a medium. The implication of x is a distance that light has transmitted in a media, here x value is determined by the thickness of BTO films (x = 4, 70 nm). And α is the absorption coefficient (cm^{-1}) which describes how far a specific wavelength light can penetrate through a media before completely absorbed. The remnant light intensity *I(x)* can be calculated according to the equation, so light intensity absorbed by BTO film is denoted as *I(0)-I(x)*. Take into account that light energy was absorbed in BTO films and consequently converted into electrical energy, thus we introduce the photovoltaic conversion equation shown as below:

$$j_{ph} = \frac{\eta \cdot e}{\hbar \cdot v} \times \{I(0) - I(x)\} \qquad \textit{Equation 6.2}$$

where *I(0)-I(x)* represents the absorbed light power density (W/cm^2) as mentioned above. The internal quantum efficiency η (%) is defined as the ration of the number of photogenerated carriers to the number of absorbed photons. Then e is the charge of electron, $\hbar$ is the Planck constant (4.14×10^{-15} eV·s), and v is the frequency of blue light (7.41×10^{14} Hz). Then photocurrent j_{ph} (A/cm^2)

can be calculated and charge density (Q/A, μC/cm^2) is obtained from integration of j_{ph} thought time. Assuming these photogenerated charges accumulate by time and screen the remnant polarization (P ≈ 25 μC/cm^2), thus we are able to estimate response speed with given values of sample thickness and laser power.

Appendix. 6.6

To further crosscheck the possible contribution of heating in the reported resistance change temperature distribution maps has been simulated. On them a power heat source (diameter 250 μm) of 9 W/cm^2 is simulated in the STO (001)//LSMO/STO/BTO system on the top of a PVC stage surrounded by air T_{amb} = 20.15 °C. The initial temperature of the model is equal to T_{amb} (20.15 °C). We see from the simulated result in Figure 6.9 (a) that there is a thermal gradient from beam center to the rest part of the model, but the temperature change is limited to 4 °C. Figure 6.9 (b) shows the temperature dependence on time of A and B points market in Figure 6.9 (a). It can be inferred that within τ_{light} = 1000 s temperature rises and after it saturates. We find that on point A the ΔT ≈ 4 ℃ while on point B the ΔT ≈ 2 ℃. Notice that the result is based on a prerequisite that we presume all light fluence can be completely absorbed by the sample.

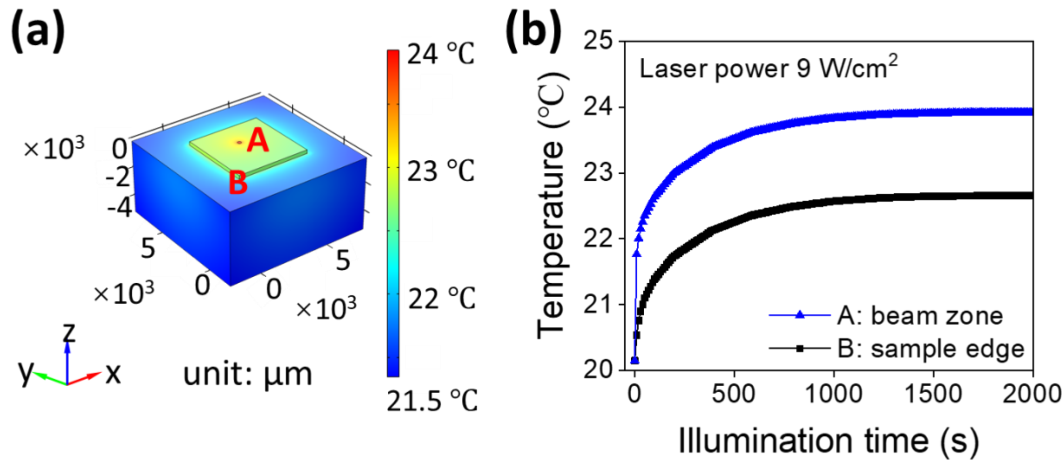

Figure 6.9 (a) Temperature distribution (in Celsius degree) of the STO (001)/LSMO/STO/BTO sample (5 mm×5 mm×0.25 mm) on an non-transparent stage (polyvinyl chloride plastic, 10 mm×10 mm×5 mm), after illuminating for 2000 s with light (9 W/cm²), assuming light power can be absorbed completely by the system. Points A and B are indicating the light beam zone (diameter 250 µm) and sample edge respectively. (b) Temperature vs time track under illumination, on points A (beam zone) and B (sample edge). The initial state of system is a room temperature (20.15 ℃). The ΔT ≈ 2 ~ 4 ℃ after illuminating sample 2000 s, indicating that thermal effect in this case is limited.

Finite-element thermal model following time-dependent heat transfer equation for heat transfer in solids (omitting the heat convection of air) is:

$$\rho C_P \frac{\partial T}{\partial t} = \nabla \cdot (k \nabla T) + Q \qquad \textit{Equation 6.3}$$

where ρ is the material density (g/cm^3); C_P is the heat capacity (J/(kg·K)); k is the thermal conductivity (isotropic, W/(K·m)); Q is the heat source, which is equivalent to the absorbed energy from the illumination (assuming power fluence can be completely absorbed). And meanwhile a boundary condition of

surface-to-ambient radiation should be taken into consideration, as described in the following equation:

$$-n\cdot\left(-k\nabla T\right)=\varepsilon\sigma\left(T_{amb}^{4}-T^{4}\right) \quad \textit{Equation 6.4}$$

where the left part $-n\cdot(-k\nabla T)$ represents the integral of total heat flux over all external boundaries, ε is the surface emissivity, σ is the Stefan–Boltzmann constant (5.67×10^{-8} $W\cdot m^{-2}\cdot K^{-4}$), and T_{amb} is the ambient temperature. All key parameters used in thermal simulation are listed in Table 6.1.

Table 6.1 Physical parameters for COMSOL thermal simulation in Figure 6.9.

	ρ (g/cm³)	**k (W/(K·m))**	**C_p at 300K (J/(kg·K))**	**ε (emissivity)**
BTO	6.02	6	450	0.9
LSMO	5.6	2.8 - 4	545.4	-
STO	5.12	11.1	530	0.8
PVC	1.35	0.17	840	0.91

Chapter 7. Conclusion

This thesis reports investigations on electroresistance of ferroelectric tunnel junctions based on HZO and BTO, in view of their potential application as non-volatile memory and optically tunable memristors, respectively. The targeted objectives in this thesis have been completed and hereby concluded as below:

(i) Firstly, similar to the case of thicker HZO films, by introducing 1 nm STO capping layer higher resistance and increased ER are obtained in the ultrathin HZO FTJs. Moreover, the STO capped FTJs demonstrate improved endurance and less dispersion of ER (improved yield). This implies that the use of suitable dielectric capping layer can substantially suppress the grain boundary ionic transport, although capping layer leads to higher defects concentration near HZO/STO interface region according to XPS characterization study.

(ii) Secondly, by applying suitable large voltage, soft breakdown occurs which leads to a reduction of resistance in HZO FTJs. A series study indicates that breakdown induces conductive channel formation, which lowers junction resistance and produces a concomitant capacitance drop. This latter fact is ascribed to a non-ferroelectric region generated by breakdown. Still, after breakdown, HZO films remains ferroelectric.

(iii) STO/BTO stack was adopted to fabricate FTJs, which enable optical absorption in visible light range. Samples have shown obvious existence of imprint fields (E_{IMP}), which breaks the P_{UP}/P_{DOWN} symmetry favoring one of the polarization orientations. A repeated switching between HRS and LRS can be triggered by appropriate combination of electrical/optical stimulus. Furthermore, the STO/BTO FTJs have shown optical memristive behavior,

under suitable illumination condition.

(iv) Finally, a detailed study has revealed that the physical origin of light induced resistive switch in BTO films is related to photovoltaic effect. The switch from LRS to HRS is triggered by light with suitable wavelength (photon energy). In addition, the response time is found to be related to laser power and BTO thickness. It is concluded that LRS/HRS switching is due to light-induced changes of polarization screening requirements.

All conclusions here will pave ways for implementing desired functions such as non-volatile storage and neuromorphic computing, with FTJs as basic elements.

Chapter 8. Outlook

This thesis has systematically investigated the potential application of non-volatile and tunable memories by using ultrathin FTJs. Still there are interesting points which deserves further investigation. Here we mention:

(i) In spite of the advantages mentioned in the summary above, unfortunately the introduction of dielectric capping layer leads to a poor retention, due to the emergence of depolarization field. Thus, it is proposed that more attention should be focused on the retention properties of HZO/STO FTJs.

(ii) Soft breakdown induced by large voltage application offers an effective method to reduce overall resistance of HZO FTJs, while preserving ferroelectricity with a reduced LRS/HRS ration. Therefore, future exploration has to target on how to avoid soft-breakdown.

(iii) For the STO/BTO optically tunable memories, further efforts can be done to enhance photoresponse by optimizing photoabsorption while preserving polarization and leakage in the films. This implies a systematic and careful combined work of growth and device characterization.

Bibliography

[1] S. Boyn, S. Girod, V. Garcia, S. Fusil, S. Xavier, C. Deranlot, H. Yamada, C. Carrétéro, E. Jacquet, M. Bibes, A. Barthélémy, J. Grollier, *Appl. Phys. Lett.* **2014**, *104*, 052909.

[2] T. Mikolajick, S. Slesazeck, M. H. Park, U. Schroeder, *MRS Bull.* **2018**, *43*, 340.

[3] M. A. Alam, M. Si, P. D. Ye, *Appl. Phys. Lett.* **2019**, *114*, 090401.

[4] J. S. Meena, S. M. Sze, U. Chand, T. Y. Tseng, *Nanoscale Res. Lett.* **2014**, *9*, 1.

[5] R. Guo, W. Lin, X. Yan, T. Venkatesan, J. Chen, *Appl. Phys. Rev.* **2020**, *7*.

[6] Y. Jiang, E. Parsonnet, A. Qualls, W. Zhao, S. Susarla, D. Pesquera, A. Dasgupta, M. Acharya, H. Zhang, T. Gosavi, C. C. Lin, D. E. Nikonov, H. Li, I. A. Young, R. Ramesh, L. W. Martin, *Nat. Mater. 2022 217* **2022**, *21*, 779.

[7] T. Y. Wang, J. L. Meng, Z. Y. He, L. Chen, H. Zhu, Q. Q. Sun, S. J. Ding, D. W. Zhang, *Nanoscale Res. Lett.* **2019**, *14*.

[8] T. Zhang, K. Yang, X. Xu, Y. Cai, Y. Yang, R. Huang, *Phys. status solidi – Rapid Res. Lett.* **2019**, *13*, 1900029.

[9] S. Dai, Y. Zhao, Y. Wang, J. Zhang, L. Fang, S. Jin, Y. Shao, J. Huang, *Adv. Funct. Mater.* **2019**, *29*, 1.

[10] S.-R. Zhang, L. Zhou, J.-Y. Mao, Y. Ren, J.-Q. Yang, G.-H. Yang, X. Zhu, S.-T. Han, V. A. L Roy, Y. Zhou, S. Zhang, J. Mao, Y. Ren, X. Zhu, Y. Zhou, L. Zhou, J. Yang, G. Yang, S. Han, V. A. L Roy, *Adv. Mater. Technol.* **2019**, *4*, 1800342.

[11] X. Wang, W. Xie, J.-B. Xu, X. Wang, J.-B. Xu, W. Xie, *Adv. Mater.* **2014**, *26*, 5496.

[12] S. D. W. Law, W. C., & Wong, *Emerging Non-volatile Memory Technologies*; Springer Singapore, 2021.

[13] L. Chen, T. Y. Wang, Y. W. Dai, M. Y. Cha, H. Zhu, Q. Q. Sun, S. J. Ding, P. Zhou, L. Chua, D. W. Zhang, *Nanoscale* **2018**, *10*, 15826.

[14] Y. Yang, Z. Xi, Y. Dong, C. Zheng, H. Hu, X. Li, Z. Jiang, W. C. Lu, D. Wu, Z. Wen, *ACS Appl. Mater. Interfaces* **2020**, *12*, 56300.

[15] T. Schenk, M. Pešić, S. Slesazeck, U. Schroeder, T. Mikolajick, *Reports Prog. Phys.* **2020**, *83*, 086501.

[16] 2013 International Technology Roadmap for Semiconductors (ITRS) - Semiconductor Industry Association.

[17] W. Banerjee, *Electron. 2020, Vol. 9, Page 1029* **2020**, *9*, 1029.

[18] L. Crippa, R. Micheloni, I. Motta, M. Sangalli, *Memories Wirel. Syst.* **2008**, 29.

[19] M. Zheng, J. Tucek, F. Qin, M. Lillibridge, *11th USENIX Conf. File Storage Technol. (FAST 13)* **2013**, 271.

[20] A. Tal, *M-Systems Flash Disk Pioneers Newark* **2002**.

[21] B. De Salvo, C. Gerardi, R. Van Schaijk, S. A. Lombardo, D. Corso, C. Plantamura, S. Serafino, G. Ammendola, M. Van Duuren, P. Goarin, W. Y. Mei, K. Der Van Jeugd, T. Baron, M. Gély, P. Mur, S. Deleonibus, *IEEE Trans. Device Mater. Reliab.* **2004**, *4*, 377.

[22] R. Harris, Is ReRAM the end of NAND flash? | ZDNET **2012**.

[23] J. Hoffman, X. Pan, J. W. Reiner, F. J. Walker, J. P. Han, C. H. Ahn, T. P. Ma, *Adv. Mater.* **2010**, *22*, 2957.

[24] A. M. Ionescu, *Nat. Nanotechnol.* **2012**, *7*, 83.

[25] V. Garcia, M. Bibes, *Nat. Commun. 2014 51* **2014**, *5*, 1.

[26] A. E. Pereda, D. P. Purpura, *Nat. Rev. Neurosci. 2014 154* **2014**, *15*, 250.

[27] D. Kuzum, S. Yu, H. S. Philip Wong, *Nanotechnology* **2013**, *24*, 382001.

[28] V. M. Ho, J. A. Lee, K. C. Martin, *Science (80-.).* **2011**, *334*, 623.

[29] Y. Chen, Artificial synapses based on the photoconductance of laalo3/srtio3 quantum wells, Universitat Autònoma de Barcelona, 2019.

[30] W. Xu, H. Cho, Y.-H. Kim, Y.-T. Kim, C. Wolf, C.-G. Park, T.-W. Lee, W. Xu, H. Cho, Y. Kim, Y. Kim, C. Wolf, C. Park, T. Lee, *Adv. Mater.* **2016**, *28*, 5916.

[31] L. Chua, *Appl. Phys. A 2011 1024* **2011**, *102*, 765.

[32] H. L. Park, Y. Lee, N. Kim, D. G. Seo, G. T. Go, T. W. Lee, *Adv. Mater.* **2020**, *32*, 1903558.

[33] D. Ielmini, H. S. P. Wong, *Nat. Electron. 2018 16* **2018**, *1*, 333.

[34] S. Gil Kim, J. Su Han, H. Kim, S. Young Kim, H. Won Jang, S. G. Kim, J. S. Han, H. Kim, H. W. Jang, S. Y. Kim, *Adv. Mater. Technol.* **2018**, *3*, 1800457.

[35] M. Cervo Sulzbach, H. Tan, S. Estandía, J. Gàzquez, F. Sánchez, I. Fina, J. Fontcuberta, *ACS Appl. Electron. Mater.* **2021**, *3*, 3657.

[36] Z.-D. Luo, X. Xia, M.-M. Yang, N. R. Wilson, A. Gruverman, M. Alexe, *ACS Nano* **2020**, *14*, 746.

[37] T. Li, A. Lipatov, H. Lu, H. Lee, J. W. Lee, E. Torun, L. Wirtz, C. B. Eom, J. Íñiguez, A. Sinitskii, A. Gruverman, *Nat. Commun.* **2018**, *9*.

[38] H. Markram, J. Lübke, M. Frotscher, B. Sakmann, *Science* **1997**, *275*, 213.

[39] Y. Dan, M. M. Poo, *Science (80-.).* **1992**, *256*, 1570.

[40] G. Q. Bi, M. M. Poo, *J. Neurosci.* **1998**, *18*, 10464.

[41] J. Boyn, S., Grollier, J., Lecerf, G., Xu, B., Locatelli, N., Fusil, S., Girod, S., Carrétéro, C., Garcia, K., Xavier, S. and Tomas, *Rev. Med. Suisse* **2017**, *13*, 878.

[42] L. Esaki, R. B. Laibowitz, P. J. Stiles, *IBM Tech. Discl. Bull.* **1971**, *13*, 2161.

[43] M. Dawber, K. M. Rabe, J. F. Scott, *Rev. Mod. Phys.* **2005**, *77*, 1083.

[44] T. Tybell, C. H. Ahn, J. M. Triscone, *Appl. Phys. Lett.* **1999**, *75*, 856.

[45] D. D. Fong, G. B. Stephenson, S. K. Streiffer, J. A. Eastman, O. Aucielo, P. H. Fuoss, C. Thompson, *Science (80-.).* **2004**, *304*, 1650.

[46] J. Junquera, P. Ghosez, *Nat. 2003 4226931* **2003**, *422*, 506.

[47] A. V. Bune, V. M. Fridkin, S. Ducharme, L. M. Blinov, S. P. Palto, A. V. Sorokin, S. G. Yudin, A. Ziatkin, *Nat. 1998 3916670* **1998**, *391*, 874.

[48] E. Y. Tsymbal, H. Kohlstedt, *Science (80-.).* **2006**, *313*, 181.

[49] V. Garcia, S. Fusil, K. Bouzehouane, S. Enouz-Vedrenne, N. D. Mathur, A. Barthélémy, M. Bibes, *Nat. 2009 4607251* **2009**, *460*, 81.

[50] A. Gruverman, D. Wu, H. Lu, Y. Wang, H. W. Jang, C. M. Folkman, M. Y. Zhuravlev, D. Felker, M. Rzchowski, C. B. Eom, E. Y. Tsymbal, *Nano Lett.* **2009**, *9*, 3539.

[51] R. Guo, L. You, Y. Zhou, Z. S. Lim, X. Zou, L. Chen, R. Ramesh, J. Wang, *Nat. Commun. 2013 41* **2013**, *4*, 1.

[52] S. S. Cheema, D. Kwon, N. Shanker, R. dos Reis, S. L. Hsu, J. Xiao, H. Zhang, R. Wagner, A. Datar, M. R. McCarter, C. R. Serrao, A. K. Yadav, G. Karbasian, C. H. Hsu, A. J. Tan, L. C. Wang, V. Thakare, X. Zhang, A. Mehta, E. Karapetrova, R. V. Chopdekar, P. Shafer, E. Arenholz, C. Hu, R. Proksch, R. Ramesh, J. Ciston, S. Salahuddin, *Nat. 2020 5807804* **2020**, *580*, 478.

[53] N. W. Ashcroft, N. D. Mermin, *Solid state physics*; Saunders College, Philadelphia., 1976; Vol. 30.

[54] M. Stengel, D. Vanderbilt, N. A. Spaldin, *Nat. Mater. 2009 85* **2009**, *8*, 392.

[55] J. G. Simmons, *J. Appl. Phys.* **2004**, *34*, 1793.

[56] T. Shimizu, K. Katayama, T. Kiguchi, A. Akama, T. J. Konno, O. Sakata, H. Funakubo, *Sci. Reports 2016 61* **2016**, *6*, 1.

[57] S. Mueller, J. Mueller, A. Singh, S. Riedel, J. Sundqvist, U. Schroeder, T. Mikolajick, *Adv. Funct. Mater.* **2012**, *22*, 2412.

[58] S. Estandía, N. Dix, J. Gazquez, I. Fina, J. Lyu, M. F. Chisholm, J. Fontcuberta, F. Sánchez, *ACS Appl. Electron. Mater.* **2019**, *1*, 1449.

[59] J. Müller, U. Schröder, T. S. Böscke, I. Müller, U. Böttger, L. Wilde, J. Sundqvist, M. Lemberger, P. Kücher, T. Mikolajick, L. Frey, *J. Appl. Phys.* **2011**, *110*, 114113.

[60] X. Sang, E. D. Grimley, T. Schenk, U. Schroeder, J. M. Lebeau, *Appl. Phys. Lett.* **2015**, *106*, 162905.

[61] M. H. Park, Y. H. Lee, T. Mikolajick, U. Schroeder, C. S. Hwang, *MRS Commun.* **2018**, *8*, 795.

[62] M. H. Park, Y. H. Lee, H. J. Kim, Y. J. Kim, T. Moon, K. Do Kim, S. D. Hyun, T. Mikolajick, U. Schroeder, C. S. Hwang, *Nanoscale* **2018**, *10*, 716.

[63] J. Lyu, I. Fina, J. Fontcuberta, F. Sánchez, *ACS Appl. Mater. Interfaces* **2019**.

[64] B. Max, M. Hoffmann, S. Slesazeck, T. Mikolajick, *IEEE J. Electron Devices Soc.* **2019**, *7*, 1175.

[65] Y. Liu, A. V. Ievlev, L. Collins, N. Borodinov, A. Belianinov, J. K. Keum, M. Wang, M. Ahmadi, S. Jesse, K. Xiao, B. G. Sumpter, B. Hu, S. V. Kalinin, O. S. Ovchinnikova, *Adv. Opt. Mater.* **2019**, *7*, 1901451.

[66] F. Liu, Photoresponse of ferroelectric BaTiO3 thin films, 2017.

[67] M. Acosta, N. Novak, V. Rojas, S. Patel, R. Vaish, J. Koruza, G. A. Rossetti, J. Rödel, *Appl. Phys. Rev.* **2017**, *4*, 041305.

[68] P. Maksymovych, S. Jesse, P. Yu, R. Ramesh, A. P. Baddorf, S. V. Kalininl, *Science (80-.).* **2009**, *324*, 1421.

[69] Y. Yin, Q. Li, *J. Mater.* **2017**, *3*, 245.

[70] J. P. Velev, J. D. Burton, M. Y. Zhuravlev, E. Y. Tsymbal, *npj Comput. Mater. 2016 21* **2016**, *2*, 1.

[71] M. Y. Zhuravlev, Y. Wang, S. Maekawa, E. Y. Tsymbal, *Appl. Phys. Lett.* **2009**, *95*, 1.

[72] Y. Z. Wu, S. Ju, Z. Y. Li, *Appl. Phys. Lett.* **2010**, *96*, 252905.

[73] L. Wang, M. R. Cho, Y. J. Shin, J. R. Kim, S. Das, J. G. Yoon, J. S. Chung, T. W. Noh, *Nano Lett.* **2016**, *16*, 3911.

[74] M. C. Sulzbach, S. Estandía, J. Gàzquez, F. Sánchez, I. Fina, J. Fontcuberta, *Adv. Funct. Mater.* **2020**, *30*, 1.

[75] V. M. Fridkin, **1979**, *9*.

[76] J. L. Wang, B. Vilquin, N. Barrett, *Appl. Phys. Lett.* **2012**, *101*, 092902.

[77] F. Liu, I. Fina, G. Sauthier, F. Sánchez, A. M. Rappe, J. Fontcuberta, *ACS Appl. Mater. Interfaces* **2018**, *10*, 23968.

[78] J. Y. Wang, G. Liu, D. Sando, V. Nagarajan, J. Seidel, *Appl. Phys. Lett.* **2017**, *111*, 092902.

[79] J. Y. Wang, W. Zhai, B. C. Luo, K. X. Jin, C. L. Chen, *Solid State Commun.* **2014**, *187*, 10.

[80] L. A. Delimova, V. S. Yuferev, I. V. Grekhov, P. V. Afanasjev, G. P. Kramar, A. A. Petrov, V. P. Afanasjev, *Appl. Phys. Lett.* **2007**, *91*, 112907.

[81] A. N. Kolmogorov, *Bull. Acad. Sci. USSR, Math. Ser* **1937**, *1*, 355.

[82] M. Avrami, *J. Chem. Phys.* **1940**, *8*, 212.

[83] Y. Ishibashi, Y. Takagi, *J. Phys. Soc. Japan* **1971**, *31*, 506.

[84] J. Guo, W. Chen, H. Chen, Y. Zhao, F. Dong, W. Liu, Y. Zhang, *Adv. Opt. Mater.* **2021**, *9*, 2002146.

[85] D. Kundys, A. Cascales, A. S. Makhort, H. Majjad, F. Chevrier, B. Doudin, A. Fedrizzi, B. Kundys, *Phys. Rev. Appl.* **2020**, *13*, 064034.

[86] M. M. Yang, M. Alexe, *Adv. Mater.* **2018**, *30*, 1.

[87] Z. D. Luo, D. S. Park, M. M. Yang, M. Alexe, *ACS Appl. Mater. Interfaces* **2019**, *11*, 8276.

[88] S. Pal, N. V. Sarath, K. S. Priya, P. Murugavel, *J. Phys. D. Appl. Phys.* **2022**, *55*, 283001.

[89] Z. Huang, P. Li, Z. Fan, H. Fan, Q. Luo, C. Chen, D. Chen, M. Zeng, M. Qin, Z. Zhang, X. Lu, X. Gao, J.-M. Liu, *Phys. status solidi – Rapid Res. Lett.* **2018**, *12*, 1770401.

[90] Y. Yuan, Z. Xiao, B. Yang, J. Huang, *J. Mater. Chem. A* **2014**, *2*, 6027.

[91] V. Sivakumar, S. Kumar, C. Ross, al -, T. Mukai, T. Fujita, S. Tsukui, J. Zhang, J. M. McGraw, H. M. Christen, G. Eres, *J. Phys. Condens. Matter* **2008**, *20*, 264005.

[92] J. Schou, *Appl. Surf. Sci.* **2009**, *255*, 5191.

[93] L. Pintilie, I. Vrejoiu, D. Hesse, M. Alexe, *J. Appl. Phys.* **2008**, *104*, 114101.

[94] J. Lyu, Epitaxial Ferroelectric Thin Films on Si (001): strain tuning of BaTiO 3 and stabilization of polar phase in Hf 0 . 5 Zr 0 . 5 O 2, 2019.

[95] a. S. GmbH, *User Manual of TF Analyzer 2000*; 2000.

[96] M. Qian, Resistive switching in nanometric BaTiO 3 ferroelectric junctions, 2018.

[97] M. C. Sulzbach, Resistive Switching in Hf0.5Zr0.5O2 ferroelectric tunnel junctions, 2021.

[98] J. F. Scott, *J. Phys. Condens. Matter* **2007**, *20*, 021001.

[99] R. Meyer, R. Waser, K. Prume, T. Schmitz, S. Tiedke, *Appl. Phys. Lett.* **2005**, *86*, 142907.

[100] I. Fina Martínez, Ferroelectricity and magnetoelectric coupling in magnetic ferroelectrics and artificial multiferroic heterostructures, 2012.

[101] I. Fina, L. Fábrega, E. Langenberg, X. Mart, F. Sánchez, M. Varela, J. Fontcuberta, *J. Appl. Phys.* **2011**, *109*, 074105.

[102] J. F. Scott, L. Kammerdiner, M. Parris, S. Traynor, V. Ottenbacher, A. Shawabkeh, W. F. Oliver, *J. Appl. Phys.* **1998**, *64*, 787.

[103] X. Long, H. Tan, S. Estandía, J. Gazquez, F. Sánchez, I. Fina, J. Fontcuberta, *APL Mater.* **2022**, *10*, 031114.

[104] W. Slurzberg, M., & Osterheld, *Essentials of Electricity for Radio and Television*; New York, McGraw-Hill, 1950.

[105] L. Callegaro, **2013**.

[106] Lessons In Electric Circuits -- Volume II (AC) - Chapter 4.

[107] A. M. Lord, J. E. Evans, C. J. Barnett, J. K. Kim, Y. S. Choi, D. W. Lee, I. Miccoli, F. Edler, H. Pfnür, P. Pfnür, C. Tegenkamp, *J. Phys. Condens. Matter* **2015**, *27*, 223201.

[108] L. J. van der Pauw, *Philips Tech. Rev.* **1958**, *20*.

[109] W. Hamouda, A. Pancotti, C. Lubin, L. Tortech, C. Richter, T. Mikolajick, U. Schroeder, N. Barrett, *J. Appl. Phys.* **2020**, *127*, 0.

[110] S. Hofmann, Springer Series in Surface Sciences; Springer Berlin Heidelberg: Berlin, Heidelberg, 2013; Vol. 49.

[111] X-Ray Photoelectron Spectroscopy (XPS) Surface Analysis Technique.

[112] M. J. Edgell, D. R. Baer, J. E. Castle, *Appl. Surf. Sci.* **1986**, *26*, 129.

[113] P. Gelius, U.; Wannberg, B.; Nakayama, Y.; Baltzer, Photoemission: from the Past to the Future. *EPSL Publ.* **1992**.

[114] E. O. Filatova, A. S. Konashuk, S. S. Sakhonenkov, A. A. Sokolov, V. V. Afanas'ev, *Sci. Reports 2017 71* **2017**, *7*, 1.

[115] J. Azadmanjiri, J. Wang, C. C. Berndt, A. Kapoor, D. M. Zhu, A. S. M. Ang, V. K. Srivastava, *Phys. Chem. Chem. Phys.* **2017**, *19*, 11881.

[116] S. Tanuma, C. J. Powell, D. R. Penn, *Surf. Interface Anal.* **2011**, *43*, 689.

[117] Y. Waseda, E. Matsubara, K. Shinoda, *X-Ray Diffr. Crystallogr.* **2011**.

[118] N. Dix, F. Sánchez Barrera, J. Fontcuberta i Griñó, J. Rodríguez Viejo, Universitat Autònoma de Barcelona. Departament de Física., Institut de Ciència de Materials de Barcelona., Preparation and characterization of biferroic nanostructures with magneto-electric coupling, 2017.

[119] D. Pesquera, X. Marti, V. Holy, R. Bachelet, G. Herranz, J. Fontcuberta, *Appl. Phys.*

Lett. **2011**, *99*, 221901.

[120] A. Gruverman, M. Alexe, D. Meier, *Nat. Commun. 2019 101* **2019**, *10*, 1.

[121] A. Alexe, M., Gruverman, **2004**.

[122] S. Kalinin, A. Gruverman, *Scanning Probe Microsc.* **2007**, *2*, 1.

[123] P. D. Nellist, *Scanning Transmission Electron Microscopy*; Springer, New York, NY: New York, NY, 2007.

[124] O. A. Shenderova, D. M. Gruen, *Ultrananocrystalline diamond : synthesis, properties and applications*; William Andrew, 2012.

[125] C. A. English, J. M. Hyde, G. Robert Odette, G. E. Lucas, L. Tan, *Struct. Alloy. Nucl. Energy Appl.* **2019**, 103.

[126] R. A. Shanks, *Nanostructured Polym. Blends* **2014**, 15.

[127] J. Rose, *Front. Nanosci.* **2015**, *8*, 217.

[128] S. Estandia, Thin Films and BaTiO 3 / SrTiO 3 Superlattices Saúl Estandía Rodríguez Doctoral Thesis in Materials Science, 2021.

[129] J. Lyu, I. Fina, R. Solanas, J. Fontcuberta, F. Sánchez, *Appl. Phys. Lett.* **2018**, *113*, 082902.

[130] M. C. Sulzbach, S. Estandía, X. Long, J. Lyu, N. Dix, J. Gàzquez, M. F. Chisholm, F. Sánchez, I. Fina, J. Fontcuberta, *Adv. Electron. Mater.* **2020**, *6*, 1.

[131] F. Ambriz-Vargas, G. Kolhatkar, M. Broyer, A. Hadj-Youssef, R. Nouar, A. Sarkissian, R. Thomas, C. Gomez-Yáñez, M. A. Gauthier, A. Ruediger, *ACS Appl. Mater. Interfaces* **2017**, *9*, 13262.

[132] F. Ambriz-Vargas, G. Kolhatkar, R. Thomas, R. Nouar, A. Sarkissian, C. Gomez-Yáñez, M. A. Gauthier, A. Ruediger, *Appl. Phys. Lett.* **2017**, *110*, 093106.

[133] B. Prasad, V. Thakare, A. Kalitsov, Z. Zhang, B. Terris, R. Ramesh, *Adv. Electron. Mater.* **2021**, *7*, 2001074.

[134] Y. Goh, J. Hwang, Y. Lee, M. Kim, S. Jeon, *Appl. Phys. Lett.* **2020**, *117*, 242901.

[135] L. Porte, L. Roux, J. Hanus, *Phys. Rev. B* **1983**, *28*, 3214.

[136] B. J. Rodriguez, C. Callahan, S. V. Kalinin, R. Proksch, *Nanotechnology* **2007**, *18*, 475504.

[137] S. Estandía, N. Dix, M. F. Chisholm, I. Fina, F. Sánchez, *Cryst. Growth Des.* **2020**, *20*, 3801.

[138] G. Bersuker, D. C. Gilmer, D. Veksler, P. Kirsch, L. Vandelli, A. Padovani, L. Larcher, K. McKenna, A. Shluger, V. Iglesias, M. Porti, M. Nafría, *J. Appl. Phys.* **2011**, *110*.

[139] T. Song, S. Estandía, H. Tan, N. Dix, J. Gàzquez, I. Fina, F. Sánchez, *Adv. Electron. Mater.* **2022**, *8*, 2100420.

[140] V. Hippel, A. R., *Dielectrics and Waves*; John Wiley & Sons, Inc., New York, 1954.

[141] R. Schmidt, In *Ceramic Materials Research Trends*; 2007; p. 321.

[142] T. Song, H. Tan, N. Dix, R. Moalla, J. Lyu, G. Saint-Girons, R. Bachelet, F. Sánchez, I. Fina, *ACS Appl. Electron. Mater.* **2021**, *3*, 2106.

[143] M. Cazorla, S. Aldana, M. Maestro, M. B. González, F. Campabadal, E. Moreno, F. Jiménez-Molinos, J. B. Roldán, *J. Vac. Sci. Technol. B, Nanotechnol. Microelectron. Mater. Process. Meas. Phenom.* **2019**, *37*, 012204.

[144] W. Zhu, F. He, J. Hayden, Q. Tran, J. I. Yang, P. Tipsawat, B. Foley, T. N. Jackson, J.-P. Maria, S. Trolier-McKinstry, **2022**.

[145] U. Schroeder, M. H. Park, T. Mikolajick, C. S. Hwang, *Nat. Rev. Mater. 2022 78* **2022**, *7*, 653.

[146] B. Max, M. Hoffmann, S. Slesazeck, T. Mikolajick, *Eur. Solid-State Device Res. Conf.* **2018**, *2018-Septe*, 142.

[147] E. Khestanova, N. Dix, I. Fina, M. Scigaj, J. M. Rebled, C. Magén, S. Estradé, F. Peiró, G. Herranz, J. Fontcuberta, F. Sánchez, *Adv. Funct. Mater.* **2016**, *26*, 6446.

[148] Z. Guan, Z. Z. Jiang, B. B. Tian, Y. P. Zhu, P. H. Xiang, N. Zhong, C. G. Duan, J. H. Chu, *AIP Adv.* **2017**, *7*, 095116.

[149] S. Kim, D. Seol, X. Lu, M. Alexe, Y. Kim, *Sci. Reports 2017 71* **2017**, *7*, 1.

[150] J. F. Scott, M. Azuma, C. A. P. De Araujo, L. D. McMillan, M. C. Scott, T. Roberts, *http://dx.doi.org/10.1080/10584589408018661* **2011**, *4*, 61.

[151] F. Liu, I. Fina, R. Bertacco, J. Fontcuberta, *Sci. Rep.* **2016**, *6*, 1.

[152] G. Radaelli, D. Gutiérrez, M. Qian, I. Fina, F. Sánchez, L. Baldrati, J. Heidler, C. Piamonteze, R. Bertacco, J. Fontcuberta, G. Radaelli, D. Gutiérrez, M. Qian, I. Fina, F. Sánchez, J. Fontcuberta, L. Baldrati, R. Bertacco, J. Heidler, C. Piamonteze, *Adv. Electron. Mater.* **2016**, *2*, 1600368.

[153] Q. Hang Qin, L. Äkäslompolo, N. Tuomisto, L. Yao, S. Majumdar, J. Vijayakumar, A. Casiraghi, S. Inkinen, B. Chen, A. Zugarramurdi, M. Puska, S. van Dijken, Q. H. Qin, L. Äkäslompolo, L. D. Yao, S. Majumdar, J. Vijayakumar, A. Casiraghi, S. Inkinen, B. B. Chen, S. van Dijken, N. Tuomisto, A. Zugarramurdi, M. Puska, *Adv. Mater.* **2016**, *28*, 6852.

[154] M. Qian, I. Fina, F. Sánchez, J. Fontcuberta, *Adv. Electron. Mater.* **2019**, *5*, 1.

[155] H. I. Yoo, M. W. Chang, T. S. Oh, C. E. Lee, K. D. Becker, *J. Appl. Phys.* **2007**, *102*, 093701.

[156] N. G. Eror, D. M. Smyth, *J. Solid State Chem.* **1978**, *24*, 235.

[157] N. -H CHAN, R. K. SHARMA, D. M. SMYTH, *J. Am. Ceram. Soc.* **1981**, *64*, 556.

[158] R. Waser, *J. Am. Ceram. Soc.* **1991**, *74*, 1934.

[159] S. Zafar, R. E. Jones, B. Jiang, B. White, V. Kaushik, S. Gillespie, *Appl. Phys. Lett.* **1998**, *73*, 3533.

[160] Y. B. Nian, J. Strozier, N. J. Wu, X. Chen, A. Ignatiev, *Phys. Rev. Lett.* **2007**, *98*, 146403.

[161] A. Chanthbouala, V. Garcia, R. O. Cherifi, K. Bouzehouane, S. Fusil, X. Moya, S. Xavier, H. Yamada, C. Deranlot, N. D. Mathur, M. Bibes, A. Barthélémy, J. Grollier, *Nat. Mater. 2012 1110* **2012**, *11*, 860.

[162] S. H. Wemple, *Phys. Rev. B* **1970**, *2*, 2679.

[163] A. S. Makhort, F. Chevrier, D. Kundys, B. Doudin, B. Kundys, *Phys. Rev. Mater.* **2018**, *2*, 012401.

[164] A. Quattropani, A. S. Makhort, M. V. Rastei, G. Versini, G. Schmerber, S. Barre, A. Dinia, A. Slaoui, J. L. Rehspringer, T. Fix, S. Colis, B. Kundys, *Nanoscale* **2018**, *10*, 13761.

[165] S. B. Desu, I. K. Yoo, *J. Electrochem. Soc.* **1993**, *140*, L133.

[166] W. F. Brinkman, R. C. Dynes, J. M. Rowell, *J. Appl. Phys.* **1970**, *41*, 1915.

[167] M. Cardona, *Phys. Rev.* **1965**, *140*, A651.

[168] S. Piskunov, E. Heifets, R. I. Eglitis, G. Borstel, *Comput. Mater. Sci.* **2004**, *29*, 165.

[169] D. W. Reagor, S. Y. Lee, Y. Li, Q. X. Jia, *J. Appl. Phys.* **2004**, *95*, 7971.

[170] J. Hölzl, F. K. Schulte, H. Wagner., *Solid surface physics*; Springer-Verlag Berlin Heidelberg New York, Germany, 2006; Vol. 85.

[171] D. Pantel, M. Alexe, *Phys. Rev. B - Condens. Matter Mater. Phys.* **2010**, *82*, 1.

[172] H. S. Lee, H. H. Park, *Adv. Condens. Matter Phys.* **2015**, *2015*.

[173] V. V. Laguta, A. M. Slipenyuk, I. P. Bykov, M. D. Glinchuk, M. Maglione, D. Michau, J. Rosa, L. Jastrabik, *Appl. Phys. Lett.* **2005**, *87*, 022903.

[174] M. L. Moreira, M. F. C. Gurgel, G. P. Mambrini, E. R. Leite, P. S. Pizani, J. A. Yarda, E. Longo, *J. Phys. Chem. A* **2008**, *112*, 8938.

[175] M. Choi, F. Oba, I. Tanaka, *Appl. Phys. Lett.* **2011**, *98*, 172901.

[176] P. Würfel, U. Würfel, *Physics of solar cells: from basic principles to advanced concepts*; John Wiley & Sons., 2016.

[177] W. L. Warren, D. Dimos, *Appl. Phys. Lett.* **1998**, *64*, 866.

[178] W. L. Warren, D. Dimos, *J. Non. Cryst. Solids* **1995**, *187*, 448.

[179] W. L. Warren, C. H. Seager, D. Dimos, E. J. Friebele, *Appl. Phys. Lett.* **1998**, *61*, 2530.

[180] W. L. Warren, D. Dimos, B. A. Tuttle, G. E. Pike, R. W. Schwartz, P. J. Clews, D. C. McIntyre, *J. Appl. Phys.* **1998**, *77*, 6695.

[181] P. S. Peercy, C. E. Land, *IEEE Trans. Electron Devices* **1981**, *28*, 756.

[182] P. S. Peercy, C. E. Land, *Nucl. Instruments Methods Phys. Res.* **1983**, *209–210*, 1167.

[183] P. S. Peercy, C. E. Land, *Nucl. Instruments Methods* **1981**, *182–183*, 787.

[184] C. E. Land, P. S. Peercyt, *Ferroelectrics* **1982**, *45*, 25.

[185] C. E. Land, P. S. Peercy, *Ferroelectrics* **1978**, *22*, 677.

[186] D. Dimos, W. L. Warren, M. B. Sinclair, B. A. Tuttle, R. W. Schwartz, *J. Appl. Phys.* **1998**, *76*, 4305.

[187] A. Zenkevich, Y. Matveyev, K. Maksimova, R. Gaynutdinov, A. Tolstikhina, V. Fridkin, *Phys. Rev. B - Condens. Matter Mater. Phys.* **2014**, *90*, 1.

[188] B. Max, T. Mikolajick, M. Hoffmann, S. Slesazeck, In *2019 IEEE 11th International Memory Workshop, IMW 2019*; Institute of Electrical and Electronics Engineers Inc., 2019.

[189] Y. J. Kim, M. H. Park, Y. H. Lee, H. J. Kim, W. Jeon, T. Moon, K. Do Kim, D. S. Jeong, H. Yamada, C. S. Hwang, *Sci. Reports 2016 61* **2016**, *6*, 1.

[190] J. Lyu, I. Fina, R. Solanas, J. Fontcuberta, F. Sánchez, *Sci. Rep.* **2018**, *8*, 1.

[191] J. Lyu, S. Estandía, J. Gazquez, M. F. Chisholm, I. Fina, N. Dix, J. Fontcuberta, F. Sánchez, *ACS Appl. Mater. Interfaces* **2018**, *10*, 25529.

List of Samples

	Material	Code
Chapter 3	STO//LSMO/HZO (2.2 nm)/Pt	A210511_03
	STO//LSMO/HZO (2.2 nm)/STO1/Pt	A210511_01
	GSO//LSMO/HZO (2.2 nm)/Pt	A210511_04
	GSO//LSMO/HZO (2.2 nm)/STO1/Pt	A210511_02
Chapter 4	Si//buffer*/LSMO/HZO (2.2 nm)/Pt	A190118_01
	Si//buffer/LSMO/HZO (3.6 nm)/Pt	A190117_02
	Si//buffer/LSMO/HZO (4.6 nm)/Pt	A180814_01
	Si//buffer/LSMO/HZO (4.6 nm)/Pt	A180814_02
Chapter 5	STO//LSMO/BTO (4 nm)/Pt	A180604_01
	STO//LSMO/STO/BTO (4 nm)/Pt	A170727_03
Chapter 6	STO//LSMO/STO (1nm)/BTO (4 nm)/Pt	A170727_03
	STO//LSMO/BTO (70 nm)/Pt	A160715_01

* Here buffer layer contains YSZ, CeO_2 and LNO, see ref.[94]

List of Figures

Figure 1.1 Hierarchy of the memory classification, depicted according to these references[4,17,23–25] Three categories are marked with colored background: (1) Typical volatile memory; (2) Non-volatile memory with mature technique; (3) Emerging non-volatile memory, with a subset of "FeNVM" marked with dash line box. 23
Figure 1.2 Comparison between biological synapse and artificial synapse. Taken from ref.[34] 25
Figure 1.3 Resistance dependence on the number of pulses (N_P) in ultrathin HZO FTJ, mimicking the potentiation/depression process. Taken from ref.[35] 26
Figure 1.4 Potentiation/depression process implemented synergistically by electrical/optical stimulus, in a WS_2/PZT optoelectronic synapse. This device is a three terminal transistor, where Au source/drain were fabricated through photolithography, e-beam evaporation and lift-off. The current flowing through WS_2 channel was detected. Electrical pulses applied at the bottom gate $SrRuO_3$ (SRO), optical pulses illuminated at the WS_2 region. Taken from ref.[36] 27
Figure 1.5 (a) Sketch of pre- and post-neurons connected by a synapse. The synaptic transmission is modulated by the time interval (Δt) of two neuron spikes. (b) Measurements of STDP in a $BiFeO_3$ (BFO) FTJ. Modulation of the device conductance (ΔG) as a function of the delay (Δt) between pre- and post-synaptic spikes. Taken from ref.[41] 29
Figure 1.6 Energy barrier profile of a metal 1/ferroelectric/metal 2 (M1/FE/M2) structure, showing different change distribution (screening length $\delta 1$, $\delta 2$) in interfacial region for two polarization direction (right and left). As a consequence, the average barrier height changes (between Φ_- and Φ_+) lead to a change in the tunneling resistance. Taken from ref.[25] 32
Figure 1.7 (a)-(d) Dependence of the domain variation on the power intensity and irradiation time; (e) Schematic of the mechanism of photovoltaic effect in the heterojunction composed of LSMO and poled PZT. Taken from ref.[78] .. 37
Figure 1.8 (a) Schematic diagram of sample structure and experimental geometry; (b)(d) The PFM phase and (c)(e) amplitude images obtained before and after UV illumination. Taken from ref.[37] 38

Figure 1.9 (a) Schematic illustration of the device showing the light-controlled resistance state writing and the electrical reading. The PFM image shows ferroelectric P_{UP} and P_{DOWN} in PZT layer. Note that LSMO/PZT/Pt-tip FTJ is connected to a PV cell (Pt/BFO/Pt); (b) Switching the polarity of the photocurrent by rotating the light polarization between −45° and 45°. (c) Resulting resistance states in the FTJ after the photodriven AFM tip writing, indicating a resistive switching memory function. Taken from ref.[87] 40
Figure 2.1 Sketch of a plano-parallel capacitor: (a) basic M1/FE/M2 structure and derived structure (b) M1/FE/DE/M2 and (c) M1/DE/FE/M2 with extra dielectric layer inserted. Here M1 represents bottom electrode and M2 represents top electrode. 43
Figure 2.2 Pulsed laser deposition system utilized in ICMAB thin film laboratory: (a) A diagram of the PLD equipment structure and its working mechanism. (b) Plasma plume generated by ablating ceramic target with laser. 44
Figure 2.3 (a) Sketch of typical DC magnetron sputtering process. Optical microscopy of Pt electrode with different shape and size: (b) Circular with diameter of 20 μm; (c) Square with dimension of 60 μm × 60 μm. 45
Figure 2.4 Wirings scheme for FE-module (taken from aixACT TFAnalyzer 2000 manual[95]). In our work, a Lakeshore EMPX-HP multifunctional probe station (marked with light blue background in scheme) was used to mount and connect samples, more details can be found elsewhere[96]. Coaxial cables connecting between devices and probe station are using earth ground on the shield. Sample is connected by using virtual ground on its bottom electrode. 47
Figure 2.5 Electrode connection configuration for (a) top-bottom and (c) top-top; I-V data and equivalent circuit of each configuration (b)top-bottom and (d)top-top in an example of LSMO/2.2 nm-HZO/Pt junction. 48
Figure 2.6 (a)Sketch of V-t pulses applied on a ferroelectric junction for tunnel resistance measurement. (b) Reading I-V recorded after pre-poling with V_W = +8 V and -8 V pulse (τ_W = 100 μs) in STO//LSMO/4nm-BTO/Pt junction. The tunnel resistance is calculated by V_R = 0.5 V, indicated with a black dash line. 50
Figure 2.7 (a) Sketch of variation 1; (b) Resistance dependence on writing pulse amplitude V_W obtained from the sequence (a).(c) Sketch of variation 2; (d) Resistance dependence on writing time τ_W obtained from the sequence (c)... 52

Figure 2.8 (a) Sketch of variation 3, (b) Representative resistance loop obtained from the sequence in (a), with fixed τ_W = 100 μs and V_{max} = +/- 5 V. 53
Figure 2.9 (a) Sketch of variation 4: a sequence of writing pulses with alternating positive and negative V_W and fixed τ_W. (b) Endurance measurement obtained by following the sequence in (a) with 300 pulses. 54
Figure 2.10 (a) Sketch of variation 5: recording I-V after writing pulse with different delay time (τ_{D1} and τ_{D2}). (b) The evolution of resistance in maximum delay time 5000 s. Both HRS and LRS were recorded. 55
Figure 2.11 (a) Sketch of the voltage pulse sequence used for measurement with frequency ν_0 using DHM mode (b) I-V curve obtained from (a). It is possible to identify coercive voltages (V_C^-, V_C^+) and dielectric displacement current (I_{DE}) and switching current (I_{FE}). (c) The integration of current in time results in the polarization curve P-V. Taken from ref.[97] 56
Figure 2.12 (a) Typical pulse sequence of the PUND technique, τ_D is the delay time interval between one pulse and another; (b) Representation of current response corresponding to PUND sequence; (c). Final I-V curve obtained by (I_P - I_U) and (I_N - I_D). Now the only current contribution visible is related to ferroelectric switching. Taken from ref.[97] 58
Figure 2.13 (a) Sketch of pulses applied in a cycle training; (b) Representative I-V curves measured with triangular signal 2.5V 1Hz in pristine state and after cycling 10^4 times, inset is the log scale current versus voltage in small range -0.5 V ~ +0.5 V; (c) Representative ER loops measured in pristine state and after cycling 10^4 times, with maximum writing voltage V_{max} = +/- 5 V and writing time τ_W = 100 μs. 59
Figure 2.14 (a) Sketch of measurement under blue laser illumination in an example of STO//LSMO/BTO/Pt junction. (b) Photoresponse in LSMO/BTO/Pt junction, light blue region indicates an epoch between light on and light off. The laser power is fixed at 9 W/cm^2. 61
Figure 2.15 Current-voltage curves obtained with and without illumination (black line in dark, blue line illuminated with blue light 9 W/cm^2). Red arrows indicate intercept shift in both axis, which represents the open-circuit voltage (V_{oc}) and short-circuit current (I_{sc}) respectively. Data collected in a LSMO/STO/BTO/Pt heterostructure junction. 62
Figure 2.16 Sketches of AC circuit, phase angle and waveform for pure resistor (R), capacitor (C) and inductor (L). Taken from ref.[106] 64

Figure 2.17 (a) A sketch of a complex impedance panel. (b)Typical Nyquist plot (Z''-Z') for ideal capacitor (C), non-ideal capacitor (constant phase element, CPE), and a complicated circuit with parallel resistor and capacitor (R1||C1-R2||C2). Inset with their circuit..64
Figure 2.18 (a) Scheme of a four-probe configuration; (b) Representative data of a STO//30 nm-LSMO/4 nm-BTO stack: Recording $V_{4,3}$ as a function of $I_{1,2}$ (orange data points); Or recording $V_{1,4}$ as a function of $I_{2,3}$ (black data points). Inset in (b) shows how measurement was conducted on different position. ...66
Figure 2.19 Sketch of basic components of XPS system, where MCD is acronym of multi-channel detector. Taken from ref.[111] 69
Figure 2.20 Sketch of X-ray beam projection (ellipse, long diameter 3.5 mm, short diameter 0.5mm) on sample (square, ~5 mm × 5 mm), optical microscopic photo shows the central Pt electrode array region (diameter ~1mm)..............70
Figure 2.21 A comparison of C 1s peak position shift (to standard C 1s E_b = 284.8 eV): (a) Without flood gun treatment; (b) With flood gun treatment: 9 V 0.2 mA. Tests done on the same group of samples, grown on GSO (001) (pseudocubic setting) substrates. 72
Figure 2.22 (a) Sketch of XPS probe depth with emission angle θ = 0° and θ ≠ 0°, where l represents a distance that photoelectrons travel through the sample, while d represents a probe depth vertical to sample plane; (b) Emission angle dependence (θ = 0°, 45°, 60°) of the attenuated intensity (I_S) respect its value at the surface (c) Integral calculation based on I_S - depth curve (θ = 0°), a proportion of 1 nm shallow area dividing total area is estimated to be 39%; (d) Similar calculation done based on I_S - depth curve (θ = 60°). 74
Figure 2.23 Core level spectrum measured without flood gun treatment: (a) C 1s, (b) Pt 4f. And after treated with electron flood gun (5V 0.1mA): (c) C 1s, (d) Pt 4f. The solid line in (a) (c) is corresponding to the standard binding energy of C 1s (284.8 eV). Red dash line represents the original C 1s peak position without flood gun treatment, with red arrow indicating a binding energy shift after the flood gun treatment. Solid line in (b) (d) is corresponding to the standard binding energy of Pt 4f 7/2 (metallic, 71 eV). Doublet peaks in Pt 4f are due to spin orbit splitting. 75
Figure 2.24 (a) Hf 4f core level spectrum of representative sample, raw data and Shirley background. I_1 and I_2 are the background intensity at two sides. I_{max} indicates the peak to background intensity. (b) XPS signal after normalization,

Hf 4f spectrum of two different representative samples in the upper panel, and the corresponding Shirley background lines are shown in the bottom panel. . 76
Figure 2.25 XPS fitting quality with different fitting method: upper panel, without Hf 3+; bottom panel, with Hf 3+. The open square data points are the raw data. 77
Figure 2.26 Axes and degrees of freedom for rotation in an XRD measurement. Taken from ref.[97] 79
Figure 2.27 XRD pattern of epitaxial BTO film with 300 pulses by PLD. Sample was grown on a STO (001) substrate, Pt was deposited on the surface. Red line is a simulation of Laue interference fringes. 80
Figure 3.1(a)–(c) Sketches of the junction structure without/with dielectric capping. (d) Illustrative example of the training effect. The I–V characteristics before/after training in the STO//HZO sample. (e) and (f) I–V characteristics of STO//HZO and STO//HZO/STO1 and GSO//HZO and GSO//HZO/STO1 substrates, respectively. Data shown in panels (e) and (f) have been collected in trained devices. The insets in (e) and (f) display data in the semi-log scale. . 86
Figure 3.2 (a) and (b) Resistance vs writing voltage (V_W) of bare and capped HZO samples grown on STO and GSO substrates, respectively. Up/Down symbols indicate positive/negative writing voltages, respectively. 87
Figure 3.3 Electroresistance of HZO and HZO/STO1 grown on (a) and (b) STO and (c) and (d) GSO, electrically written with V_{max} = 2.5 V (a) and (c) and V_{max} = 5 V (b) and (d), respectively. (e) Comparison of LRS and HRS states obtained after V_W writing of bare and capped samples 89
Figure 3.4 (a) and (b) Distribution of the normalized LRS and HRS resistance values (R_N/R_{mean}) measured in a set of 15 junctions on STO//HZO and STO//HZO/STO1 samples, respectively. R_{mean} is the mean value of the $\{R_N\}$ distribution. (c) and (d) Endurance of the representative junctions on STO//HZO and STO//HZO/STO1 samples, respectively, measured up to 300 writing/reading cycles for the STO//HZO sample and 1250 for the STO//HZO/STO1. 91
Figure 3.5 (a) and (b) Distribution of the normalized LRS and HRS resistance values (R_N/R_{mean}) measured in a representative set of junctions on GSO//HZO and GSO//HZO/STO1 samples, respectively. (c) and (d) Endurance of the representative junctions on GSO//HZO and GSO//HZO/STO1 samples, respectively, measured up to 1250 writing/reading cycles. Data with zoomed-in view of scales are shown in the insets of (c) and (d). 92

Figure 3.6 XPS Hf 4f core spectra of STO//HZO (a) and STO//HZO/STO1 (b) samples recorded at various emission angles. The vertical dashed lines indicate the expected positions of the Hf-4$f_{7/2}$ line of Hf^{4+} and Hf^{3+} and the position of the O 2s line. (c) XPS Ti 2p spectra collected at various emission angles. The vertical dashed lines indicate the expected positions of the Hf-4$f_{7/2}$ line of Hf^{4+} and Hf^{3+} and the position of the O 2s line. (d)-(f) Zoomed-in view of the XPS spectra recorded at different emission angles, with the deconvolution of Hf^{4+} and Hf^{3+} (blue areas) and O 2s (orange area) lines for STO//HZO (bottom panels) and STO//HZO/STO1 (top panels) samples. 95
Figure 3.7 (a) STO//HZO/STO1 film. A HAADF image of the LSMO bottom electrode, the HZO film, the STO-1 nm capping film, and the Pt top electrode. In order to clearly image the conformal covering of the HZO film by STO, the right side inset shows an enlarged region with the corresponding Ti L-edge chemical map (in faded yellow) from EELS superimposed onto the HAADF image. The location of the grain boundaries (GBs) is marked with yellow arrows. (b) From the top to the bottom, the HAADF image, Pt, Sr, Ti, Hf, and Zr chemical maps corresponding to a larger horizontal area than the one shown in (a).. 97
Figure 3.8 (a,b) PFM amplitude and phase loops for the STO//HZO and STO//HZO/STO1 samples. Note that the horizontal shift of the loop along the negative voltage indicates the presence of ferroelectric imprint field. It appears larger than in the case that the ER loops shown in Figure 3a, b, which are measured with large metallic top electrodes, due to the worse contact of the PFM tip. (c,d) PFM amplitude images for the STO//HZO and STO//HZO/STO1 samples after writing with ± 8 V in the indicated regions. The outer region corresponds to the pristine state. (e,f) PFM phase images for the STO//HZO and STO//HZO/STO1 samples showing 180° phase contrast. The performed characterization is fully consistent with the ferroelectric character of these ultrathin films. Note that the fact that similar response is observed in sample where the surface is HZO or STO denotes the absence of important surface chemistry effects, because both materials are expected to have a very different response on this regard. Piezoelectric force microscopy (PFM) measurements were performed with an MFP-3D microscope (Oxford Instrument Co.) using the Budget Sensors silicon (n-type) cantilevers with Pt coating (Multi75E- G). To achieve better sensitivity, the dual AC resonance tracking (DART) method was employed. [B. J. Rodriguez, C. Callahan, S. V. Kalinin, and R. Proksch, Dual-frequency resonance-tracking atomic force microscopy, Nanotechnology

18, 475504 (2007)].[136] PFM voltage hysteresis loops were always performed at remanence using a dwell time of 100 ms. 99
Figure 3.9 I-V of pristine and trained stated of a device in STO//HZO/STO1 sample. 100
Figure 3.10 I-V of pristine and trained stated of a device in (a) GSO//HZO and (b) GSO//HZO/STO1 samples, respectively. 100
Figure 3.11 Resistance ON (LRS) and OFF (HRS) of 15 junctions of (a) STO//HZO and (b) STO//HZO/STO1 samples, respectively. 101
Figure 3.12 Resistance ON (LRS) and OFF (HRS) of 15 junctions of (a) GSO//HZO and (b) GSO//HZO/STO1..101
Figure 3.13 Hf 4f XPS spectra of GSO//HZO and GSO//HZO/STO1..........102
Figure 3.14 Dependence on emission angle of oxygen and Hf 3+ contributions. Whereas oxygen shows a no dependence, Hf is more reduced at the surface in the capped sample. 102
Figure 4.1 (a) Sketch of the 4.6 nm HZO film on LSMO on buffered Si with Pt top electrodes and its electrical contact configuration. (b) XRD 2θ-χ frame and integrated scan of the sample. Integrated along χ scan (±5° around χ = 0°) zoom around HZO (111) is also included, corresponding to θ-2θ scan. (c) XRD pole figure around asymmetric Si, CeO_2 YSZ, LSMO (111) and o-HZO (−111) reflections. 106
Figure 4.2 (a) I-V loops collected before using at indicated voltages in a consecutive manner. (b) I-V loops collected at different frequency. (c) $R(V_W)$ data of samples with increasing different V_W pulse amplitude and indicated τ_W.(d) ER loop before (top) and after breakdown (bottom). The ER loops are collected at V_{max} = 3.8 V and 5 V respectively (e) P-V and I-V loops collected in the pristine state. (f) I-V loop collected after breakdown. 111
Figure 4.3 (a) Capacitance as a function of frequency in the pristine and cycled states. (b) Nyquist plot of the impedance of pristine and after cycling. Equivalent circuit model for (c) pristine state when ferroelectric capacitor is insulating (Rb ↑ ↑) and (d) after cycled when ferroelectric capacitor becomes leaky (Rb ↓ ↓)...114
Figure 4.4 (a) Thickness extracted from the data fitting using the procedure indicated in the text versus the nominal thickness of different samples before and after correcting the device are using the area extracted from broken devices shown in panel (c). (b) Wide view of the Pt electrodes. (c) Zoom of the Pt top electrodes. In yellow, broken devices. (d) Sketch of the two ferroelectric and

non-ferroelectric contributions extracted from capacitance measurements analysis. 116
Figure 4.5 XRD θ-2θ scans of a Si(001)/buffer layer/LSMO/HZO stack in range of 2θ = 20° ~ 80°, with a zoomed region around the HZO (111) (2θ = 25° ~ 40°). 118
Figure 4.6 R(V_W) data of samples with different HZO thickness (t = 2.2, 3.6, 4.6 nm). The down triangle symbol (▽) represents positive prepoling while the up triangle symbol (△) represents negative prepoling. The writing time for all prepoling are the same τ_W = 100 µs. 119
Figure 4.7 R-V loops collected up to V_{max} = 3.8V, 8V and 5V sequentially in samples with different HZO thickness (a) 3.6 nm and (b) 2.2 nm. And zoomed loops of the 1st (top) and 3rd (bottom) collected respectively for two samples (a) 3.6 nm and (b) 2.2 nm. 120
Figure 4.8 (a) Resistance after application of V_W of indicated amplitude versus τ_W. (b) Resistance after application of V_W of indicated amplitude versus cycles of amplitude V_W , τ_W = 100 µs in the collected data of (a) and (b)...............121
Figure 4.9 (a,b) I-V curves collected respectively after writing with V_W = +3.5 V and V_W = -3.5 V as indicated for the (b) pristine state, and V_W = +5 V and V_W = -5 V for (c) after V_{cycled} = ±8 V. (c) Dependence of ON and OFF resistance states on the HZO thickness for pristine and after V_{cycled} = ±8 V. 122
Figure 4.10 Capacitance as a function of frequency in pristine and cycled states for samples with different HZO thickness (a) t = 4.6 nm, (b) t = 3.6 nm, (c) t = 2.2 nm. And each corresponding Nyquist plot (d) t = 4.6 nm, (e) t = 3.6 nm, (f) t = 2.2 nm. 123
Figure 4.11 PFM topography on Pt electrode region for (a) pristine and (c) after cycled. PFM amplitude on Pt electrode region for (c) pristine and (d) after cycled. For Pt electrode after cycled, a ringed wrinkle was observed from its topography, as shown in the region between two dashed circles in (c), which indicates to a volume expansion caused by filament formation. And the piezo response in this area is considerably lower as shown in its amplitude (d). ...124
Figure 5.1 Polarization switching by combined action of light and E_{IMP} electric field. PFM phase-maps (30 µm × 30 µm) of BTO film. a P_{DOWN} and P_{UP} regions were written by applying voltage to the tip of -8 or +8 V within (a) 10 µm × 10 µm area in yellow and black regions, respectively. (b) After illumination (blue laser, 10 min) P_{UP} domains are switched back. 129

Figure 5.2 Electroresistance under illumination. (a) I(V) loops following the -15 to +15 to -15 V path collected in dark and under illumination (red and blue laser). Inset top-left: Schematic of the measuring configuration. Inset bottom-right: Zoom of the I(V) loops around $V^{+}_{C\text{-}LOW}$. (b) $R(V_W)$ loops collected using $\tau_W = 1$ ms in dark and under (blue) illumination. Arrows indicates polarization direction. (c) $R(V_W)$ loops collected using $\tau_W = 100$ μs in dark (black symbols) and under (blue) illumination (blue symbols). The PFM phase-voltage hysteresis loop (red symbols) of the sample (right-bottom axis). Vertical dashed lines indicate the E_C in PFM loop, coinciding with $V^{+}_{C\text{-}LOW}$ and $V^{-}_{C\text{-}LOW}$ in the $R(V_W)$ loop. (d) P(V) and I(V) loop and sketch of the measuring configuration. 131
Figure 5.3 Electroresistance of dielectric/ferroelectric heterostructures under illumination. (a) Sketch of the layer stacking with a polarized BTO barrier. (b) $R(V_W)$ loop collected using $\tau_W = 100$ μs in dark (black solid and open circles) and under illumination (blue symbols). (c) Out-of-plane PFM phase images obtained after writing P_{DOWN} and P_{UP} domains (applied voltage to the tip of +8 V (inner yellow region) and -8 V (black region)), respectively (left image) and after illuminating the LSMO/STO/BTO sample (right image). Scale bars correspond to 10 μm. Bottom, phase-profiles along the white dashed lines in the corresponding images. (d) P(V) and I(V) loop and sketch of the measuring configuration. 137
Figure 5.4 Electro-optical control of resistance. Resistance measured under different electric and optical stimulus sequence. Initial states at LRS and HRS in (a) and (b), respectively. Notice (blue shaded areas) that P_{UP} states are reversed by light and resistance switches from LRS to HRS, whereas P_{DOWN} states are insensitive to light. In this example: $V_W = \pm 8$ V. Optical illumination is marked with symbol. Arrows indicate polarization direction. 138
Figure 5.5 Retention and optical modulation of resistance. (a) Retention of the voltage ($\tau_W = 100$ μs) and light written HRS states and LRS state in a junction on STO//LSMO/BTO/STO/Pt. (b) Evolution of the resistance of the junctions under illumination, from LRS to HRS. Data (blue circles) are collected as function of illumination time using a laser power of 0.1 W/cm^2. Each plot also includes the resistance of the LRS and HRS measured in dark (up blue and down red, respectively). Arrows indicate the direction of the polarization of the ferroelectric barrier... 139

Figure 5.6 Structural characterization. XRD θ-2θ scans for samples: STO//LSMO/BTO/Pt and STO//LSMO/STO/BTO/Pt. 141
Figure 5.7 Electric writing in PFM experiments. The electric writing was done by applying bias voltage (V = +8, -8 V for white and black, respectively) at the PFM tip in a region of 10 × 10 μm^2, while reading in a region of 30 × 30 μm^2 with zero tip bias. The electric pattern was defined in a single PFM pass.... 142
Figure 5.8 Charging effects in LSMO/STO/BTO sample. (a) amplitude and (b) phase images of both LSMO/BTO sample. (c) amplitude and (d) phase images of LSMO/STO/BTO sample. 143
Figure 5.9 PFM extended characterization. Out-of-plane domain PFM phase images for both (a) LSMO/BTO and (b) LSMO/STO/BTO samples, obtained just after writing P_{DOWN} (inner yellow region) and P_{UP} domains (black region), respectively (left image) and after pending in dark for 20 min (right image). The lines scans shown in the bottom correspond to PFM phase profiles along the dashed lines in the corresponding images for each sample. Scale bar corresponds to 10 μm. 144
Figure 5.10 PFM phase contrast retention. PFM phase images collected after electrical lithography with +8 (bright) and -8V (dark) for the LSMO/BTO sample. (a)(b)(c) Data collected freshly after writing (original); after 1 h and after 6 h, respectively. (d) Line scans (red lines in panels a-c) of the phase-contrast of images in (a,b,c). (e) Dependence on delay time since electrical writing of relative area ratio of dark/bright areas [= $area_{dark/bright}$/(total area)]. Lines are guides for the eye. 145
Figure 5.11 $R(V_W)$ loop stability. Illustrative examples of the reproducibility of the major ER loops in two different junctions in a STO//LSMO/BTO/Pt sample as a function of the writing time: (a) 250 ms and (b) 100 μs. Data show the reproducibility of ER loops over several cycles of operation. 146
Figure 5.12 Time dependent current experiments. Time dependence of the normalized current for applied voltages near $V^+_{C\text{-}LOW}$ (= 3 V) and $V^+_{C\text{-}HIGH}$ (= 10 V) for the LSMO/BTO sample. Zoom of the time dependence of the normalized current for applied voltages near $V^+_{C\text{-}LOW}$ (= 3 V). 147
Figure 5.13 Endurance for LSMO/BTO sample. (a) Endurance of HRS states and LRS states written by ±8 V in a junction of STO//LSMO/BTO/Pt sample. (b) Endurance of HRS states and LRS states written by ±15 V in a junction of STO//LSMO/BTO/Pt sample. 148

Figure 5.14 Tunneling current and barrier analysis. (a) I(V) characteristics measured at room temperature on BTO junction of 4 nm. The I(V) curves were measured for different resistance state: HRS_{ION} (V_W = +15 V), LRS (V_W = -15 V, -8 V), and HRS (V_W = +8 V). All the τ_W used here was constantly 1ms. (b) Sketch of the band structure before contact. (c) Sketch of band structure in the equilibrium state after contact. 150
Figure 5.15 Resistance of samples of different thickness. Resistance dependence on BTO thickness of the voltage (downward red triangle) and light (blue circles) written HRS states and LRS (upward blue triangle) state in STO//LSMO/BTO/Pt sample. Error bars correspond to standard deviation of 5 measurements. 151
Figure 5.16 ER dependence on τ_W. $R(V_W)$ loops (from -15 V to 15 V) were collected in a series of writing time (τ_W from 10^{-5} s to 0.25 s), in the LSMO/BTO sample: (a-e). (f). Dependence of HRS_{ION} (red), LRS (blue) and HRS (green) on τ_W. The plot is divided into two regions depending on whether HRS_{ION} is absent or not. Error bars correspond to standard deviation of 5 measurements. 152
Figure 5.17 ER dependence on τ_W in several junctions. Dependence of different resistance state (HRS_{ION}, red; LRS, blue; HRS, green) on writing time recorded in 4 junctions. Error bars correspond to standard deviation of 5 measurements. 153
Figure 5.18 PFM phase contrast under red illumination. (a) PFM phase images collected just after electrical lithography with +8 (bright) and -8 V (dark). (b) PFM phase images collected 10 min after electrical lithography with +8 (bright) and -8 V (dark). for the LSMO/BTO sample. (c) PFM phase images collected after 10 min illumination with red light red (λ = 638 nm, E = 1.94 eV, 9 W/cm^2) after electrical lithography with +8 (bright) and -8V (dark). 154
Figure 5.19 (a) Experimental set up to measure the LSMO film resistivity in the LSMO/BTO sample. Four needles adjacent to an array of 4 neighboring 4 Pt are used to measure in 4 probe configuration the LSMO resistivity. (b)(c) I(V) measurements recorded in two different configurations, obtained by permuting current and voltage probes. Date recorded in dark (black symbols) and under illumination (blue symbols) are shown in (b) and (c). 155
Figure 5.20 Non-reversible photoresponse. $R(V_W)$ loops collected (-8V ~ 8V) in LSMO/BTO samples following the sequence: dark → illumination → dark. 156

Figure 5.21 $R(V_W)$ loop reproducibility. Illustrative examples of the reproducibility of the major ER loops in two different junctions in a STO//LSMO/STO/BTO/Pt sample for different writing time: (a) 1 μs, (b) 2 ms. Data show the reproducibility of ER loops over several cycles of operation. 157
Figure 5.22 Endurance for LSMO/BTO sample. Endurance of HRS states and LRS states written by ±8 V in a junction of STO//LSMO/STO/BTO/Pt sample. 158
Figure 5.23 Suppression of ionic effect in LSMO/STO/BTO sample. (a-e) $R(V_W)$ loops collected for indicated τ_W for the LSMO/STO/BTO sample. 159
Figure 5.24 Optical switch stability for different junctions. (a-d) Resistance states obtained sequentially after electrical and optical stimuli (as indicated) for several junctions, respectively. In this example: V_W = ±8 V. Illumination is performed with the same condition to Figure 5.4..160
Figure 5.25 Dependence of ER on electrode area for STO/BTO sample. (a) Illustrative examples of the I(V) curves and (b) ER recorded in dark in junctions in STO//LSMO/STO/BTO/Pt having electrodes with diameter of 7 μm and 20 μm, as indicated. 161
Figure 5.26 Dependence of ER on electrode area for STO/BTO sample. (a),(b) Illustrative ER loops recorded in dark in different junctions, respectively, in STO//LSMO/STO/BTO/Pt having electrodes with diameter of 7 μm, as indicated. Reference loop obtained in the representative 20 μm junction of Figure 5.25 (b) is also included in both panels...161
Figure 5.27 Dependence of optical switch on electrode area for STO/BTO sample. Illustrative ER loops recorded in dark and under illumination in electrodes with diameter of 7 μm of STO//LSMO/STO/BTO/Pt sample. 162
Figure 5.28 Leakage subtraction. (a) Illustrative examples of the I(V) curves collected at 5 kHz for the LSMO/BTO sample. The leakage contribution has been fitted by exponential curve. This contribution has been removed from the I(V) characteristics and the subtracted curve is shown in Figure 5.2 (d). (b) Equivalent to (a) data for the LSMO/STO/BTO sample. The subtracted curve is shown in Figure 5.3 (d). 163
Figure 6.1 $R(V_W)$ loops collected using τ_W = 100 μs in STO/BTO junction (inset sketch of the structure), collected with the following sequence: (1) dark (black solid symbols, left pannel); (2) under (blue, λ = 405 nm, 9 W/cm^2) illumination (blue symbols, middle pannel); (3) dark again (black open symbols, right

pannel). Red and blue arrows indicate polarization direction, and blue dash line indicates the center of the ER loop measured in dark and indicates the existence of an imprint field (pointing towards the bottom electrode (black arrow) (E_{IMP} $\approx$ -4.4 MV/cm).. 167

Figure 6.2 (a,b) Sketch of the sample and electric configuration under different illumination conditions, both with blue and red light. (c,d) Resistance data collected as function of time initially starting from HRS or LRS (up blue and down red triangles) respectively. In both cases, resistance was recorded and the illumination period (200 s) with blue light (λ = 405 nm, 1.4 W/cm^2) is indicated with a blueish background in each panels, and then continuously recorded in dark for a period of time. (e,f) Idem for red illumination (λ = 638 nm, 1.4 W/cm^2) during the time laps indicated by the reddish background. 169

Figure 6.3 (a) Photoresponse in the LSMO/STO/BTO/Pt heterostructure junction, respectively to blue and red light. The light power was fixed at 9 W/cm^2. (b) Sketch of the same heterostructure demonstrating the possibility of near bandgap excitation that can happen in BTO film only triggered by blue light (λ = 405 nm, E = 3.06 eV) but not by red light (λ = 638 nm, E = 1.9 eV). 171

Figure 6.4 (a) Resistance data collected as function of illumination time with different BTO thickness (4, 70 nm), illumination power is fixed at 0.1 W/cm^2. Initial LRS is defined by a pre-poling pulse (-8 V, 100 μs); (b) Resistance data collected as function of illumination time with different light power (0.1, 1.2, 9 W/cm^2) in 4 nm BTO heterojunction; The resistance value for both cases were extracted at a reading voltage of 0.5 V. (c) Photocurrent dependence on BTO thickness (4, 70 nm) and light power (0.1, 1.2, 9 W/cm^2); (d) Simulation of Q/A value as a function of time in BTO film with different thickness (4, 70 nm), with fixed 0.1 W/cm^2 and assuming α = 500 cm^{-1}, η = 0.6 %; (e) Simulation of Q/A value as a function of time in 4 nm BTO film varying by light power (0.1, 1.2, 9 W/cm^2), assuming α = 500 cm-1, η = 0.6 %; (f) Simulation of remnant of Q/A value in 4 nm BTO film with different absorption (α) and efficiency (η) parameters, with a fixed 9 W/cm^2. 174

Figure 6.5 (a,c) P_{UP} and P_{DOWN} region were written by applying voltage to the tip -8 V or +8 V, corresponding to dark and bright regions respectively. (b) Idem after illuminating with blue light (λ = 405 nm, 9 W/cm^2). (d) Idem after illuminating with red light (λ = 638 nm, 9 W/cm^2). 176

Figure 6.6 Initial state at LRS and HRS are shown in (a) and (b) respectively, and the time interval from step to step is 200 s. Optical illumination is denoted

with rectangular transparent strips with color red and blue, representing red light ($\lambda = 638$ nm) and blue light ($\lambda = 405$ nm). Arrows indicate polarization direction. Notice that a light-induced resistance switch only occurs with blue layer and the previous state is at LRS, as shown in (a) from step 4 to 5........................... 178
Figure 6.7 Current-voltage curves obtained with and without illumination (black line: dark, blue line: under blue light). Red arrows indicate intercept shift in both axis, which represents the open-circuit voltage (V_{oc}) and short-circuit current (j_{sc}) respectively. Inset sketch shows measurement configuration.... 178
Figure 6.8 Resistance data collected as function of illumination time with different BTO thickness (4, 70 nm), with illumination power (a) 9 W/cm^2 and (b) 1.2 W/cm^2. Initial LRS is defined by a pre-poling pulse (-8 V, 100 μs). 179
Figure 6.9 (a) Temperature distribution (in Celsius degree) of the STO (001)/LSMO/STO/BTO sample (5 mm×5 mm×0.25 mm) on an non-transparent stage (polyvinyl chloride plastic, 10 mm×10 mm×5 mm), after illuminating for 2000 s with light (9 W/cm^2), assuming light power can be absorbed completely by the system. Points A and B are indicating the light beam zone (diameter 250 μm) and sample edge respectively. (b) Temperature vs time track under illumination, on points A (beam zone) and B (sample edge). The initial state of system is a room temperature (20.15 ℃). The $\Delta T \approx 2{\sim}4$ ℃ after illuminating sample 2000 s, indicating that thermal effect in this case is limited............ 182

List of Tables

Table 2.1 The measured C 1s binding energy (E_b , eV) depending on different flood gun condition, and the relative shift (ΔE_b) compared to a standard C 1s peak (E_b =284.8 eV). Tests done on sample GSO//HZO/AlO_x. 71
Table 4.1 Barrier parameters extracted from fittings are shown in Figure 4.9 (b)(c), including effective thickness (t_{eff}), barrier height for both interfaces (Φ_{LSMO} and Φ_{Pt}), and the fitting quality chi^2. Exclusively for status after breakdown, both conventional Brinkman model and an improved Brinkman model with parallel resistance (fixed R = 18kΩ). 122
Table 5.1 Fitting parameters obtained from I(V) curves in Figure 5.14 (a). . 150
Table 6.1 Physical parameters for COMSOL thermal simulation in Figure 6.9. 183

List of Abbreviations

NVM	Non-volatile memory
RAM	Random-access memory
DRAM	Dynamic random-access memory
CPU	Central processing unit
NAND	NOT AND
CMOS	Complementary Metal Oxide Semiconductor
ReRAM	Resistive random access memory
PCM	Phase change memory
MRAM	Magnetic random access memory
STT-RAM	Spin-transfer torque random access memory
FeRAM	Ferroelectric random access memory
FeNVM	Non-volatile ferroelectric memory
1T1C	One transistor and one capacitor
STDP	Spike-time dependent plasticity
FTJ	Ferroelectric tunnel junction
FE	Ferroelectric
DE	Dielectric
FNT	Fowler-Nordheim tunneling
TER	Tunneling electroresistance
ER	Electroresistance
HRS	High resistive state
LRS	Low resistive state
KAI	Kolmorogov-Avrami-Ishibashi
HZO	$Hf_{0.5}Zr_{0.5}O_2$
BTO	Barium titanate
STO	$SrTiO_3$
GSO	$GdScO_3$
LSMO	$La_{2/3}Sr_{1/3}MnO_3$
PZT	$PbZr_xTi_{1-x}O_3$
SRO	$SrRuO_3$
BFO	$BiFeO_3$

TSO	$TbScO_3$
pc	Pseudocubic
ALD	Atomic layer deposition
PLD	Pulse laser deposition
AC	Alternating current
DC	Direct current
MM	Main modulus
DHM	Dynamic hysteresis mode
DLCC	Dielectric leakage current compensation
PUND	Positive-Up-Negative-Down
UV	Ultraviolet
PV	Photovoltaic
PFM	Piezoresponse force microscopy
ph-PFM	Photo-assisted piezoresponse force microscopy
XPS	X-ray photoelectron spectroscopy
XRD	X-ray diffraction
STEM	Scanning transmission electron microscopy
HAADF	High angle dark field imaging
EELS	Energy electron loss spectroscopy

List of Publications

[1] Sulzbach, M. C., Estandía, S., Long, X., Lyu, J., Dix, N., Gàzquez, J., Chisholm, M. F., Sánchez, F., Fina, I., & Fontcuberta, J. (2020). Unraveling Ferroelectric Polarization and Ionic Contributions to Electroresistance in Epitaxial $Hf_{0.5}Zr_{0.5}O_2$ Tunnel Junctions. *Advanced Electronic Materials*, *6*(1), 1–8.

[2] Long, X., Tan, H., Sánchez, F., Fina, I., & Fontcuberta, J. (2021). Non-volatile optical switch of resistance in photoferroelectric tunnel junctions. *Nature Communications*, 12(1), 1–9.

[3] Long, X., Tan, H., Estandía, S., Gazquez, J., Sánchez, F., Fina, I., & Fontcuberta, J. (2022). Enhanced electroresistance endurance of capped $Hf_{0.5}Zr_{0.5}O_2$ ultrathin epitaxial tunnel barriers. *APL Materials*, 10(3), 031114.

[4] Long, X., Tan, H., Sánchez, F., Fina, I., & Fontcuberta, J. Disentangling electronic and thermal contributions to the observed light-induced resistance switching in $BaTiO_3$ ferroelectric tunnel junction. **(**Submitted to *Journal of Applied Physics*)**.**

[5] Long, X., Tan, H., Sánchez, F., Fina, I., & Fontcuberta, J. Ferroelectric electroresistance after breakdown in Epitaxial $Hf_{0.5}Zr_{0.5}O_2$ Tunnel Junctions**.** (Submitted to *ACS Applied Electronic Materials*).

List of Communications

6th - 7th June, 2019

Universitat Autònoma de Barcelona

4th Scientific Meeting of BNC-b Students (JPhD2019)

Oral presentation: "CMOS compatible Hafnium Zirconium Oxide tunnel junctions for data storage"

31st August - 4th September, 2020

Conference of the Condensed Matter Divisions and Condensed Matter Physics Division (CMD2020GEFES, online)

Oral presentation: "Optically controlled ON/OFF operation in barium titanate ferroelectric tunnel junction"

17th - 18th September, 2020

Institut de Ciència de Materials de Barcelona (ICMAB-CSIC)

5th Scientific Meeting of BNC-b Students (JPhD2020)

Oral presentation: "Optically controlled ON/OFF operation in barium titanate ferroelectric tunnel junction"

22nd - 23rd October, 2020

Optically Controlled Ferroelectric Memristors School (OPTOFEM2020, online)

Attendee

11th - 13th April, 2021

Materials Challenges for Memory Conference (MCFM2021, online)

Poster contribution: "Disentangling electronic and thermal contributions to the observed light-induced resistance switching in $BaTiO_3$ ferroelectric tunnel junction"

30th May - 1st June, 2022

Spring Meeting European Materials Research Society (EMRS2022, online)

Oral presentation: "Disentangling electronic and thermal contributions to the observed light-induced resistance switching in $BaTiO_3$ ferroelectric tunnel junction"

27th June - 1st July, 2022

Tours, France

International Symposium on Applications of Ferroelectrics (IEEE ISAF2022)

Oral presentation: "Impact of dielectric capping layer on electroresistance endurance of ultrathin ferroelectric $Hf_{0.5}Zr_{0.5}O_2$ tunnel barriers"